
Doctoral

Science

2008-01-01

Digital close range photogrammetry in motor vehicle accident reconstruction

Fiona Coyle
Technological University Dublin

Follow this and additional works at: <https://arrow.tudublin.ie/sciendoc>



Part of the [Physics Commons](#)

Recommended Citation

Coyle, Fiona. (2008). *Enhanced absorption metal oxides for photocatalytic applications*. Technological University Dublin. doi:10.21427/D7K59M

This Theses, Ph.D is brought to you for free and open access by the Science at ARROW@TU Dublin. It has been accepted for inclusion in Doctoral by an authorized administrator of ARROW@TU Dublin. For more information, please contact yvonne.desmond@tudublin.ie, arrow.admin@tudublin.ie, brian.widdis@tudublin.ie.



This work is licensed under a [Creative Commons Attribution-NonCommercial-Share Alike 3.0 License](#)

Digital Close Range Photogrammetry in Motor Vehicle Accident Reconstruction

Fiona Coyle B.Sc.

**A thesis submitted for the award of Doctor of Philosophy to
Dublin Institute of Technology**



Supervisors

Dr. Vincent Toal

Dr. Denis P. Wood

Centre for Industrial and Engineering Optics

School of Physics

Dublin Institute of Technology

February 2008

ABSTRACT

Road traffic accidents are consistently in the top ten causes of deaths world-wide. In order to reduce the number of fatalities caused by traffic collision, better knowledge and understanding of the sequence of events prior to and during a traffic accident, i.e. Accident Reconstruction, is required, so it is important to obtain detailed quantitative information about the damage sustained by the crashed vehicle(s). The research reported here was aimed at developing a fast and accurate method of measuring the damage. Digital Close Range Photogrammetry is the technique chosen for obtaining vehicle profiles from which accurate measurements of crush damage could be made.

These profiles can provide valuable information about the collision. They can be used to find the orientation(s) of the vehicle(s) at the moment of impact. The orientation of the vehicle is used to determine the direction of the principal force acting on the vehicle as a function of the relative velocity vector. The depth of the damage sustained can be measured from the profile; this is used to calculate the energy absorbed by the structure from which the pre-impact speed can be calculated.

The photogrammetric measuring method is compared with other techniques, for accuracy and speed. A direct comparison is made with the results obtained from Coordinate Measuring Machine and tape measurements. Consideration is given to errors that arise from the reconstruction of three-dimensional space from two-dimensional images. The optimal lighting conditions for best results are studied and results are discussed. In addition the repeatability of photogrammetric modelling is evaluated. The technique is applied to vehicles involved in collisions; the

photogrammetric models are used to determine the profile of what the vehicles struck and the pre-impact speeds.

It is concluded that close range digital photogrammetry is a fast, accurate (12.4mm) and inexpensive (€2000) method of measuring crush damage and hence of considerable benefit in accident investigation

Declaration

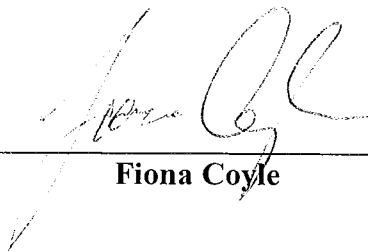
I certify that this thesis which I now submit for examination for the award of PhD, is entirely my own work and has not been taken from the work of others save and to the extent that such work has been cited and acknowledged within the text of my work.

This thesis was prepared according to the regulations for postgraduate study by research of Dublin Institute of Technology and has not been submitted in whole or in part for another award in an Institute.

The work reported on in this thesis conforms to the principles and requirements of the institute's guidelines for ethics in research.

The Institute has permission to keep, lend or copy this thesis in whole or in part, on condition that any such use of the material of the thesis be duly acknowledged.

Signature _____



Fiona Coyle

Date 11 JUNE 2008

Acknowledgements

I would like to thank my supervisors, Dr. Vincent Toal (Dublin Institute of Technology) and Dr Denis P. Wood (Denis Wood Associates) for their advise, encouragement, support and practical help.

I wish to thank Colin, Vicki and all at Denis Wood Associates, Eamonn Donnelly and Kevin Mooney from the Department of Spatial Planning, Maurice Murphy from the Department of Construction Management and Technology, Sgt. Colm Finn and his colleagues in the Garda road traffic division, for their advise and help.

I wish to thank the Institute of Traffic Accident Investigators, especially their event organisers Tony Foster, Bob Seston, Andy Salt, Michael Corrigan and Ian Smith, AREC group, Dr. Heinz Burg, TNO, Ton Versmissen and DSD Linz, for allowing me to attending their staged collisions and examine the vehicles. I would also like to acknowledge the assistance of Haley Ash, Jennifer Commins, Kathleen Canniffe, Robert Rice and Kevin Ryan during the examination of the vehicles.

I also wish to thank Dr. James Walsh and Linda Casey for reading my thesis.

Special thanks to my colleagues in the Centre for Industrial and Engineering Optics and the School of Physics in Dublin Institute of Technology, to my family especially my father and sister and all my friends for their encouragement and support.

Contents

Abstract	i
Declaration	iii
Acknowledgements	iv
Contents	1
List of illustrations	5
List of Tables	13
Chapter 1 Introduction	15
Chapter 2 Collisions	19
2.1 Collisions in One Dimension	19
2.2 Elastic, Inelastic and Plastic Collisions	20
2.3 Collisions in Two Dimensions	22
2.4 Friction	26
2.5 Rotation	27
2.6 Vehicles during Collision Impact	27
Chapter 3 Pre-impact Speed from Crush Measurements	31
3.1 Energy Absorption	31
3.2 Specific Energy Absorption Capacity (SEAC)	35
3.3 Energy Equivalent Speed (V_{EES})	36
3.4 Eccentric Collisions	38
3.5 T-style Collisions	40
3.6 Impact Orientation	42

Chapter 4 Crush Depth Measurement and Crush Profile	45
4.1 Traditional Methods of measuring Crush Depth	47
4.1.1 Crush Deformation Jig	47
4.1.2 Base – Line Technique	48
4.1.3 Theodolite and Electronic Measuring Device (EMD)	50
4.2 Review of Alternative methods of measuring Crush Depth	53
4.2.1 3D Laser Scanning	53
4.2.2 Laser Trackers	56
4.2.3 Digital Photogrammetry	59
 Chapter 5 Photography	 64
5.1 Pinhole Camera	64
5.2 Camera Lens	66
5.3 Depth of Field	68
5.4 Photographic Film	69
5.5 Digital Photography	69
5.6 Charged-Couple Device (CCD) Sensors	70
5.7 Photogrammetric Cameras	72
5.8 Camera Calibration (PhotoModeler Method)	74
5.9 Photographing Vehicles	75
 Chapter 6 Photogrammetry	 76
6.1 History of Photogrammetry	76
6.2 Digital Photogrammetry	77
6.3 Photographic Geometry	78
6.3.1 Geometry of a Single Photograph	78
6.3.2 Stereo Photography	80
6.3.3 Geometry of Multiple Photographic Frames	83
6.3.4 Geometric error of locating a point in space from two photographs	86
6.3.5 Exterior and Image Orientation	90
6.4 Mathematics of Photogrammetry	93
6.4.1 Collinearity Equations	93

6.4.2 Bundle Adjustment and Complete Collection of Collinearity Equations	100
6.5 PhotoModeler	102
6.5.1 PhotoModeler Requirements	102
6.5.2 Creating a Model of a Vehicle's Crush Profile	105
6.5.3 Merging of Vehicle Models	108
6.5.4 Crush Measurement	110
 Chapter 7 Test Programme	 112
7.1 Computational Study of Photogrammetric Modelling Process	112
7.2 Photogrammetric Measurement of Simple Objects	119
7.2.1 Short Pipes (Range 0.5m – 1m)	120
7.2.1A PhotoModeler and Coordinate Measuring Machine	123
7.2.1B Tape measurements and Coordinate Measuring Machine	127
7.2.1C PhotoModeler and Tape Measurements (Short Lengths)	130
7.2.2 Long Pipes (Order of Magnitude of a Vehicle, Range 0.7m – 4m)	133
7.2.3 Summary of Results of Modelling Simple Objects	140
7.2.4 Comparison of Pipe measurements with Computational Model measurements	141
7.3 Photogrammetric measurement of complex objects - vehicles.	144
7.3.1 Overcast Lighting Conditions	146
7.3.2 All Lighting Conditions	149
7.3.3 Summary of Results of Modelling Complex Objects	151
7.3.4 Comparison of Vehicle measurements with Computational Model measurements	151
7.4 Consistency of Creating Photogrammetric Models with PhotoModeler	156
 Chapter 8 Speed Calculations and Photogrammetric Vehicle Models	 162
8.1 Photogrammetric Vehicle Models	163
8.1.1 Saab 93 Side to Pole	163
8.1.2 Saab 93 – Front	165
8.1.3 Toyota Corolla	166
8.1.4 Opel Corsa	168

8.2 Staged Two Vehicle Collisions, Orientation and Speed Calculations	171
8.2.1 Orientation of Vehicles	172
8.2.2 Calculation of Speed of Bullet Vehicle	178
Chapter 9 Conclusions	185
References	196
Appendix A	203
Appendix B	222
Appendix C	227
Appendix D	243
List of Publications	248

List of Illustrations

Figure 1.1 Principal Direction Of Force (PDOF) when two vehicles collide	18
Figure 2.1 Over view of an eastbound car colliding with a northbound van	24
Figure 2.2 Regions involved in frontal collisions	29
Figure 3.1 The geometry of two vehicles colliding at an angle γ	39
Figure 3.2 Shows the distances from the centre of gravity to the point of impact, in the x and y directions (p and q) for a side struck vehicle	40
Figure 4.1 Crush Deformation Jig in place at side of a damaged vehicle	48
Figure 4.2 Base – Line in place at front of a vehicle	49
Figure 4.3 Crush Depth Measurements	50
Figure 4.4 Total Station	51
Figure 4.5 Vehicle Profile created in AutoCAD with Total Station Coordinates	52
Figure 4.6 RIEGL LMS-Z390	55
Figure 4.7 Components of Riegl Scanner	55
Figure 4.8 Schematic diagram of an Interferometer	57
Figure 5.1 Pinhole Camera	65
Figure 5.2 Path of Light in Pinhole Camera	65
Figure 5.3 Geometry of lens camera	66

Figure 5.4 Camera Lens	67
Fig 5.5 Tri-colour Filtered CCD	71
Fig 5.6 Path of light through a CCD	71
Figure 5.7 PhotoModeler Camera Calibration Slide	74
Fig 6.1 Single Photographic Frame Geometry	79
Fig 6.2 Photographic Scale	80
Figure 6.3 Stereoscopic depth perception	81
Figure 6.4 Schematic diagram of a stereoscope	82
Fig 6.5 Parallax	84
Fig 6.6 Adjacent Camera Locations	85
Fig 6.7 Locating point A in 3D space	85
Figure 6.8 “Side on”, object parallel to photographs	87
Figure 6.9 “End on”, object perpendicular to photographs	87
Figure 6.10 Area of possible location of a point in 3D space	88
Figure 6.11 Location of mis-tagged object point i.e. modelled object point	90
Fig 6.12 Orientation of image space and object space	91

Figure 6.13 Recommended Camera Locations	103
Figure 7.1 Images of targets	113
Figure 7.2 Object points 1 and 2, and Modelled object points 1 and 2 are parallel to the common view of two photographs, “Side-on”	114
Figure 7.3 Object points 1 and 2, and Modelled object points 1 and 2 are perpendicular to the common view of two photographs, “End-on”	115
Figure 7.4 Graph of Computational Model generated results for Side-on situation, the positive trend in the results shows that the lengths computed by the computational model are longer than the actual lengths	116
Figure 7.5 Mean Computational Model results generated for Side-on situation, the positive trend in the results shows that the lengths computed by the computational model are longer than the actual lengths	117
Figure 7.6 Graph of Computational Model generated results for End-on situation, the positive increasing trend in the results shows that the lengths computed by the computational model are longer than the actual lengths and the difference between the two gets larger as the actual length increases	118
Figure 7.7 Mean Computational Model results generated for End-on situation, the positive increasing trend in the results shows that the lengths computed by the computational model are longer than the actual lengths and the difference between the two gets larger as the actual length increases	118
Figure 7.8. Target at end of pipe	120
Figure 7.9. Pipes of various lengths attached to frame	121

Figure 7.10. Pipes on table of CMM	122
Figure 7.11 Plot of PhotoModeler measurements (PM) against the Coordinate Measuring Machine measurements (CMM)	124
Figure 7.12 Plot of Difference (PM – CMM) against CMM measurements	125
Figure 7.13A Frequency Histogram of Differences (PhotoModeler – CMM measurements)	126
Figure 7.13B Cumulative Distribution of Differences (PhotoModeler – CMM measurements)	126
Figure 7.14 Plot of Tape measurements against the Coordinate Measuring Machine measurements (CMM)	127
Figure 7.15 Plot of Difference (Tape – CMM) against CMM measurements	128
Figure 7.16A Frequency Histogram of Differences (Tape – CMM measurements)	129
Figure 7.16B Cumulative Distribution of Difference (Tape – CMM measurements)	129
Figure 7.17 Plot of PhotoModeler measurements (PM) against the tape measurements	130
Figure 7.18 Plot of Difference (PM – Tape) against Tape measurements	131
Figure 7.19A Frequency Histogram of Differences (PhotoModeler – Tape measurements)	132
Figure 7.19B Cumulative Distribution of Differences (PhotoModeler – Tape measurements)	132

Figure 7.20 Arrangement of pipes with dimensions in order of magnitude of vehicles	133
Figure 7.21 Plot of PhotoModeler measurements against average tape measurements for long pipes	134
Figure 7.22 Plot of Difference (PM – Tape) against Tape measurements	135
Figure 7.23A Frequency Histogram of Differences (PhotoModeler – Tape measurements) Long pipes	136
Figure 7.23B Cumulative Distribution of Differences (PhotoModeler – Tape measurements) Long pipes	136
Figure 7.24 Plot of PhotoModeler measurements against average tape measurements, for both long and short pipes.	137
Figure 7.25 Plot of Difference (PM – Tape) against Tape measurements, for both long and short pipes.	138
Figure 7.26A Frequency Histogram of Differences (PhotoModeler – Tape measurements) both Short and Long pipes	139
Figure 7.26B Cumulative Distribution of Differences (PhotoModeler – Tape measurements) both Short and Long pipes	139
Figure 7.27A Difference (PM – True) against True length, Long pipe test (pink) and Computational Model side-on programme (blue).	141
Figure 7.27B Difference (PM – True) against True length, Long pipe test (pink) and Computational Model end-on programme (blue).	142

Figure 7.28 Cumulative distribution long pipe test and computational model end-on	143
Figure 7.29 Undamaged vehicle	144
Figure 7.29A Overcast Lighting Conditions	145
Figure 7.29B Sunny Lighting Conditions	145
Figure 7.29C Dusk Lighting Conditions	146
Figure 7.30 Plot of Difference (PM – Tape) against Tape measurements, for vehicle in overcast lighting conditions.	147
Figure 7.31A Frequency Histogram of Differences (PhotoModeler – Tape measurements) for Vehicle modelled in Overcast Lighting	148
Figure7.31B Cumulative Distribution for Vehicles modelled in Overcast Lighting	148
Figure 7.32 Plot of Difference (PM – Tape) against Tape measurements, for vehicle in all lighting conditions.	149
Figure 7.33A Frequency Histogram of Differences (PhotoModeler – Tape measurements) for Vehicles Modelled in All Lighting	150
Figure7.33B Cumulative Distribution for Vehicles modelled in All Lighting	150
Figure 7.34 Comparison of Overcast Vehicle and Computational model, end-on results	152
Figure 7.35 Cumulative Distributions for Overcast vehicle (pink) and Computational model, end-on (blue)	153

Figure 7.36 Comparison of All lighting Vehicle and Computational Model end-on results	154
Figure 7.37 Cumulative Distributions for All vehicle (pink) and Matlab end-on (blue)	155
Figure 7.38 Cumulative Distributions for All vehicle (pink) and computational model end-on increasing error (blue)	156
Figure 7.39 Merged vehicle models	157
Figure 8.1 Saab 93 that collide with a Pole	163
Figure 8.2 Merged before and after photogrammetric models of Saab	164
Figure 8.2A Crush damage sustained by Saab 93 and estimation of object struck	164
Figure 8.3 Saab 93 that collided with deformable barrier	165
Figure 8.4 Merged before and after photogrammetric models of Saab	166
Figure 8.5 Toyota Corolla	167
Figure 8.6 Merged before and after photogrammetric models of Corolla	168
Figure 8.6A Crush damage sustained by Corolla and estimation of object struck	168
Figure 8.7 Opel Corsa (with Bumper, hiding extent of damage)	169
Figure 8.8 Opel Corsa (without Bumper, all damage visible)	169
Figure 8.9A Merged before photogrammetric model and after with bumper photogrammetric model of Corsa	170

Figure 8.9B Merged before photogrammetric model and after without bumper photogrammetric model of Corsa	170
Figure 8.10 Collision 1 (Jaguar S-Type – Jaguar XJ)	173
Figure 8.11 Collision 2 (Mondeo – Vectra)	174
Figure 8.12 Collision 3 (Mondeo – Vectra)	175
Figure 8.13 Collision 4 (Mondeo – Vectra)	176

List of Tables

Table 3A Mean relationships between Energy Equivalent Speed and the ratio of crush depth damage to pre-impact length	38
Table 3B Guide for investigators at first examination of vehicles	38
Table 4A Summary of measuring techniques	63
Table 7A Comparison of results for different methods of measuring	123
Table 7B Summary of Pipe Results	140
Table 7C Summary of Pipe Results	151
Table 7D Results of remodelling test	158
Table 7E Summary of photogrammetric accuracy	160
Table 8A Summary of Collision Tests	172
Table 8B Orientation of Vehicles	177
Table 8B(i) Ueyama's Orientation of Vehicles	177
Table 8C Summary of Vehicle Measurements and Masses	179
Table 8D Average Crush Measurements and Standard Deviation due to measuring from photogrammetric model	180
Table 8E Single Crush Measurements and Standard Deviation due to measuring from photogrammetric model	180
Table 8F Summary of Bullet Vehicle Pre-Impact Speeds (Average Crush)	181

Table 8G Summary of Bullet Vehicle Pre-Impact Speeds (Single Crush)	181
Table 8H Comparison of Average and Single Crush Speed Results	182
Table 8I Differences due to different crush measurement selection	182
Table 8J Summary of Bullet Vehicle Pre-Impact Speeds (Average Crush), Standard Deviation due to photogrammetric modelling and speed calculation	183
Table 8K Summary of Bullet Vehicle Pre-Impact Speeds (Single Crush), Standard Deviation due to photogrammetric modelling and speed calculation	184

Chapter 1 INTRODUCTION

The high numbers of fatal accidents on Irish roads keep the subject of road safety to the fore in people's minds. In 2000, 415 people were killed in 362 fatal accidents, in 2001, 411 in 360 accidents and in 2002, 376 in 346 accidents on Irish roads [1]. World wide in 2002 there were almost 1.2 million deaths from road traffic accident injuries, of which over 70% were male. The fourth leading cause of mortality among adults aged 15 – 59 was road traffic injuries (the top three being HIV/AIDS, Ischaemic heart disease and tuberculosis [2]). In the United States, traffic deaths from 1977 through 1988 exceeded all US battle deaths in all wars over a 200-year period from the revolutionary war (1775) through the Vietnam War (1975). In addition injuries from traffic accidents out-number deaths by a factor of 70 [3]. The introduction of penalty points in Ireland in October 2002 and reduction of some speed limits in January 2005 are examples of the authorities' attempts to deter people from unsafe driving. However the threat of fines and increased insurance premiums does not seem to be reducing the number of fatal / serious accidents on our roads. Therefore new ways of encouraging drivers to drive more safely and ways of protecting vehicle occupants are needed.

Accident investigation can help both safe driving and occupant protection. In order to improve the protection of the vehicle's occupants, knowledge of what happens to a vehicle during a collision is required. Research studies of accidents have lead to the development of safety devices such as seatbelts and airbags. It has also lead to the development of accident avoidance devices such as ABS brakes and reversing sensors.

On the deterrent side of accident investigation if drivers are aware that their last action, or in deed inaction, before the collision can be accurately discovered, they may drive with more care as the chances of them being held accountable and perhaps prosecuted by the authorities are increased.

This project focuses on the creation of three-dimensional models of the vehicle(s) and of the object struck in collisions. The crush damage sustained by the vehicle(s) is then measured from the model and used to estimate the pre-impact speed of the bullet vehicle (the striking vehicle). The models of the vehicle(s) and struck object can be orientated at the point of impact, to establish the direction the vehicle(s) were travelling in prior to the collision. This gives the operator insight into the collision sequence and probable cause, and can also identify any secondary collisions.

Of course fatal accidents are to the fore, but non-fatal accidents are also very important. Reported to and recorded by An Garda Síochána in 2002 were 6,279 accidents, which resulted in 9,206 people being injured (25 times the number of people killed on Irish roads). In 2002 the estimated cost of a serious injury accident was €168,461 and €16,142 for a minor injury accident and the typical material damage accident was valued at €1,758, while the cost of a fatal accident was estimated at €1,357,489. The total cost of accidents on Irish roads in 2002 was estimated to be €728 million [1].

The aim of this project is to develop a low cost, fast and accurate method of measuring the damage caused to a vehicle during a collision using digital photogrammetry. Determining the limitations of digital photogrammetry and the accuracy achievable is key to this project. The damage sustained by the vehicle is measured from a “crush

profile”, a 3D model of the damage, by over-laying models of the vehicle before and after the collision. The vehicle(s) may also be orientated by fitting together the damage profiles of the vehicle and the object or vehicle that was struck.

The depth of the damage can be measured from the crush profile; this is used to calculate the energy absorbed by the structure, from which the pre-impact speed can be calculated. Chapter 3 explains how to calculate the pre-impact speed of a vehicle from crush depth. The formulae and relationships given in chapter 3 were assumed to be reliable and no investigation of them was carried out during this project. The relationships were used to obtain pre-impact speeds of the bullet vehicles, for comparison to the known speeds of staged collisions examined. Fitting the models together gives the orientation of the vehicles, which is used to determine the angle between the principal axes of the vehicles at impact, and thus the direction of the principal force acting on the vehicles. The paths of travel of the vehicles can be determined from the angle of the vehicles at the impact; combining this path with a site map and information from the accident scene, may reveal the cause of the collisions. The direction of the principal force and of the velocity vector are the direction of the vector additions of the force vectors of each of the vehicles involved in the collision (Figure 1.1). The passengers in the vehicles will move in the opposite direction, but with the same magnitude of force as the principal force within the vehicles (Figure 1.1).

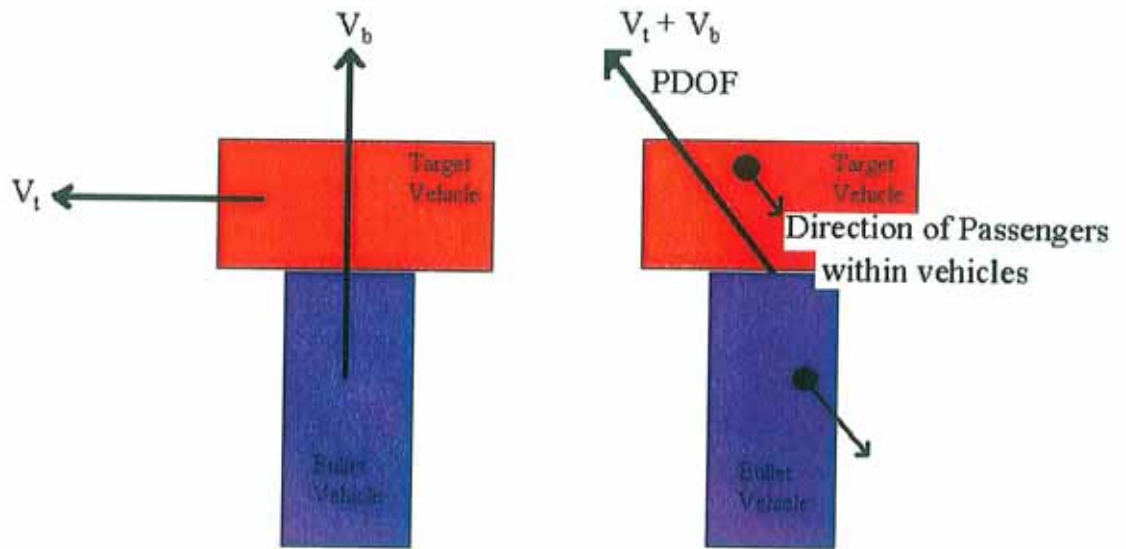


Figure 1.1 Principal Direction Of Force (PDOF) when two vehicles collide

The 3D models are created using digital photogrammetry and PhotoModeler software. Details of how to create a model are given in chapter 6. Once the 3D model has been created, it is a permanent record of the vehicle's post collision condition, which can be viewed from any angle. Therefore there is no need for the vehicle to be kept for legal inspection, which means the vehicle can be destroyed or returned to the owner for repair and continued use.

Chapter 2 COLLISIONS

Collisions are constantly happening all around us, be they visible or not, from intermolecular collisions to pile-ups on the motorways. They all must obey the laws of Physics. Collisions are generally explained using particles or points colliding, and any object can be described as a single point once that point is the centre of gravity. The centre of gravity is the point in an object through which the force of gravity acts.

Weaver [4] defines a collision as, “an event that produces finite velocity changes in the particles involved, consisting of a short duration contact”.

Damask [5] defines a collision, “as when two objects in motion collide, there is an interaction of forces and acceleration at the point of the collision”.

Serway [6] defines a collision as, “an event of two particles coming together for a short period of time and producing impulsive forces on each other”.

Wood [7] defines a collision as “when a car runs into a fixed object (or another vehicle) exchange of momentum occurs over a very short time period”.

2.1 Collisions in One Dimension

The time duration of the collision is very small. The average acceleration, a_{avg} , that a particle experiences over the impact's duration Δt is $a_{avg} = \frac{\Delta v}{\Delta t}$, where change in

velocity, Δv , is finite and Δt the duration is very small. Therefore the acceleration will be very large and the forces on the individual bodies (particles) extremely large. The average velocity of a particle is $v_{avg} = \frac{\Delta x}{\Delta t}$, where Δx is the change in position of the particle over the duration of the impact [7].

$$\Delta x = v_{avg} \Delta t$$

2.1

v_{avg} is finite, Δt is very small, therefore Δx during a collision is also very small, there is no significant change in a particle's location during a collision event; a collision takes place at a point in space [7].

Momentum is the product of mass and velocity. All collisions must obey the law of the conservation of momentum. That is the total momentum of a system just before the collision equals the total momentum of a system just after the collision. In general there are three types of collisions 'elastic', 'inelastic', and 'perfectly inelastic' (plastic), and they are distinguished by whether kinetic energy for the system is conserved or not [6].

2.2 Elastic, Inelastic, and Plastic Collisions

The coefficient of restitution, e , is defined as the ratio of the rebound speed of the vehicle, V_r , to the pre impact speed or approach speed of the vehicle, V_a , both along its original direction of travel, $e = \frac{-V_r}{V_a}$ [8].

When the coefficient of restitution equals one ($e = 1$), the kinetic energy loss of the collision is zero, the collision is elastic. Snooker-ball collisions and the collisions of air

molecules with the walls of a container at ordinary temperatures are highly elastic. In general collisions in the micro-world are elastic.

When the coefficient of restitution is less than one ($e < 1$) total kinetic energy is not conserved, the collision is inelastic. Some of the kinetic energy is converted into thermal energy, to potential energy when the object is deformed, and to rotational energy [6].

When the coefficient of restitution equals zero ($e = 0$), the collision is plastic, the vehicles remain together after the collision, the two objects collide and stick together after the collision, and move with some common velocity [6].

Vehicle collisions are inelastic collisions and are often plastic collisions. As with all collisions momentum is always conserved, but kinetic energy is not. The sum of the momenta of vehicles involved in the collision before the collision is equal to the sum of the momenta of vehicles after the collision. The kinetic energy of the vehicles is not conserved; some of the kinetic energy of the vehicles before the collision is converted to sound energy, to deformation energy (potential energy associated with the deformation of the vehicles), to thermal energy with the heating of the metal and rubber tyres, and to rotational energy associated with the spinning of the vehicles [7]. Also some of the kinetic energy of the vehicles is passed to the passengers in the vehicles and their movement within the vehicles.

For an inelastic collision of two objects, of masses M_1 and M_2 with velocities before the collision of v_{i1} and v_{i2} , and the velocities after the collision being v_{f1} and v_{f2} , the momentum relationship is written as [6]:

$$M_1 v_{i1} + M_2 v_{i2} = M_1 v_{f1} + M_2 v_{f2} \quad \mathbf{2.2}$$

For inelastic collisions kinetic energy is not conserved, therefore:

$$\frac{1}{2} M_1 v_{i1}^2 + \frac{1}{2} M_2 v_{i2}^2 \neq \frac{1}{2} M_1 v_{f1}^2 + \frac{1}{2} M_2 v_{f2}^2 \quad \mathbf{2.3}$$

2.3 Collisions in Two Dimensions

For a collision of two particles, total momentum is conserved in each direction, of x, y and z. Collisions generally take place on a two-dimensional surface. Therefore there are two component equations for the conservation of momentum [6]:

$$\begin{aligned} M_1 v_{i1x} + M_2 v_{i2x} &= M_1 v_{f1x} + M_2 v_{f2x} \\ M_1 v_{i1y} + M_2 v_{i2y} &= M_1 v_{f1y} + M_2 v_{f2y} \end{aligned} \quad \mathbf{2.4 \text{ a \& b}}$$

Serway [6] recommends the following problem solving strategy when dealing with collision problems.

1. Set up a coordinate system and define velocities with respect to this system.
2. Sketch this coordinate system, drawing and labelling all velocity vectors and all other information given.
3. Write down the expressions for the x and y components of the momentum of each object before and after the collision.
4. Write expressions for the total momentum in x direction before and after collision, equate these two expressions. Repeat this for y direction.

Note: it is the momentum of the system that is the constant, not the momentum of the individual objects.

Momentum of the system is constant; therefore momentum is constant in any direction.

5. (A) If the collision is inelastic (generally vehicle collisions are), kinetic energy is not conserved.

(B) If the collision is totally inelastic (vehicles stick together and don't separate before coming to rest), the final velocities (velocity after collision) of the two objects are equal.

(C) If the collision is elastic (not common in vehicle collisions), kinetic energy is constant, kinetic energies before and after the collision can be equated, giving another relationship between the velocities.

6. Solve equations for the unknown quantities.

Applying the above strategy to the following problem [6] results as follows:

A 1500kg car travelling east with a speed of 25.0m/s collides with a 2500kg van travelling north at a speed of 20.0m/s. Find the direction and magnitude of the velocity of the wreckage after the collision assuming that the vehicles undergo a perfectly inelastic collision, i.e. they stick together.

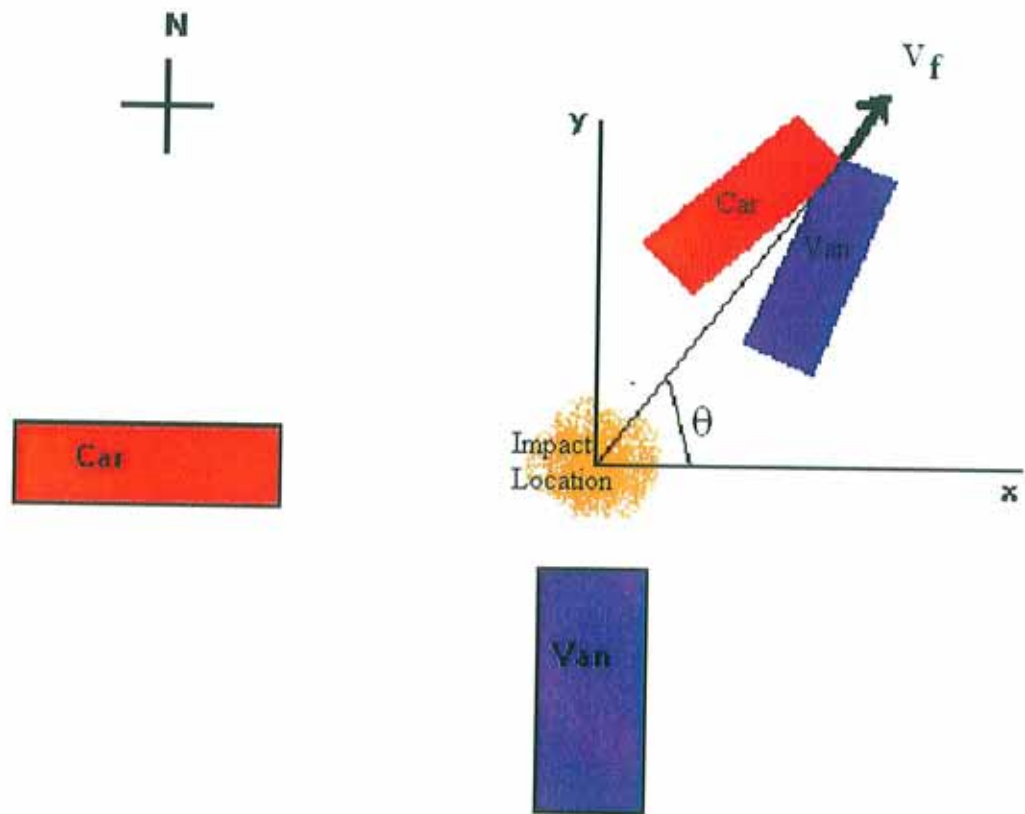


Figure 2.1 Over view of an eastbound car colliding with a northbound van.

Choose east to be along the positive x direction and north to be along the positive y direction. Before the collision the only object having momentum in the x direction is the 1500kg car. Thus the magnitude of the total initial momentum of the system (car plus van) in the x direction is

$$\sum P_{xi} = \text{Mass} \times \text{Velocity} = (1500\text{kg})(25.0\text{m/s}) = 3.75 \times 10^4 \text{ kg} \cdot \text{m/s} \quad 2.5$$

Assume that the wreckage moves at an angle θ to the x direction and velocity v after the collision. The magnitude of the total momentum in the x direction after the collision is

$$\sum P_{xf} = \text{Mass} \times \text{Velocity} = (4000\text{kg})v \cos \theta \quad 2.6$$

Because the total momentum in the x direction is constant, we can equate these two expressions to get

$$3.75 \times 10^4 \text{ kg} \cdot \text{m} / \text{s} = (4000 \text{ kg})v \cos \theta \quad 2.7$$

Similarly, the total initial momentum of the system in the y direction is that of the 2500kg van

$$\sum P_{yi} = \text{Mass} \times \text{Velocity} = (2500 \text{ kg})(20.0 \text{ m} / \text{s}) = 5.00 \times 10^4 \text{ kg} \cdot \text{m} / \text{s} \quad 2.8$$

Applying conservation of momentum to the y direction, we have

$$\begin{aligned} \sum P_{yi} &= \sum P_{yf} \\ 5.00 \times 10^4 \text{ kg} \cdot \text{m} / \text{s} &= (4000 \text{ kg})v \sin \theta \end{aligned} \quad 2.9$$

Dividing total momentum in the y direction (equation 4.3.6) by total momentum in the x direction (4.3.4), we get

$$\begin{aligned} \tan \theta &= \frac{5.00 \times 10^4}{3.75 \times 10^4} = 1.33 \\ \theta &= 53.1^\circ \end{aligned} \quad 2.10$$

When this angle is substituted into the equation 4.3.6, the value of v is

$$v = \frac{5.00 \times 10^4 \text{ kg} \cdot \text{m} / \text{s}}{(4000 \text{ kg}) \sin 53.1^\circ} = 15.6 \text{ m} / \text{s} \quad 2.11$$

However the conservation of momentum is not enough to completely describe vehicle collisions. Damask [5], states “The principal limitation to the use of momentum in accident reconstruction is that, while conservation of momentum occurs, it is not always possible to express all post-impact momentum contributions.” For example if a vehicle collides with a solid wall, after the collision the deformation of the vehicle can be seen and measured, as can any rebound of the vehicle. However the vibrations of the wall and the road around the vehicle, which absorbs energy, may be felt by bystanders but cannot be measured. Chapter 3 contains details of how a vehicle’s pre-impact speed can be estimated from the crush deformation sustained by the vehicle.

2.4 Friction

When two bodies are in contact with each other, there is a force acting along the surface of the contact areas between the bodies, whenever one body moves or tries to move over the other [6]. This force is called friction and is opposite in direction to that of the relative movement of the body. Friction can be either detrimental or absolutely essential. Friction is detrimental to the pistons and cylinder walls of a vehicle's engine; therefore oil is used to reduce the wear and tear on these moving parts. However friction is essential between the vehicle's tyres and the road surface, as without friction there would be no traction, which moves the vehicle.

The tread design on a tyre helps to preserve friction between the tyre surface and the road surface. The coefficient of friction between tyres and wet or oily roads is much less than the coefficient when the road is dry, as the tyre is no longer sliding on the road alone but also against the lubricating material. For tyres with tread, water on the roadway typically reduces the coefficient of friction by 25% [5]. The wet-road reduction is much greater for well-worn tyres, while there is no practical difference between the dry-road coefficient of friction for well-treaded tyres and bald tyres [5].

When a body is at rest, the force to be overcome to start it moving is the static frictional force (F_s). When a body is moving the frictional force is called the kinetic frictional force or the sliding frictional force (F_k). The coefficients of the static and kinetic frictional forces are denoted by μ_s and μ_k respectively and are defined by $\mu_s = F_s / N$ and $\mu_k = F_k / N$, where N is the normal force, which equals the weight of the body [6].

2.5 Rotation

External forces can cause an object to move in a curved path and/or spin (rotational motion). Rotational motion is a factor in nearly every motor vehicle accident. When the net external force on a vehicle as a result of a collision is not directed towards the vehicle's centre of mass, the vehicle will spin during its post-impact trajectory. Just as linear motion has linear momentum, rotation motion has angular momentum, which is also conserved. Rotation is discussed further in section 3.6.

2.6 Vehicles during Collision Impact

What happens to a car during impact depends on the type of impact, whether it is a frontal, side, rear or full-width impact. 60% of fatal accidents are frontal collisions and a further 25% are side collisions [7]. Therefore this research has concentrated on frontal and front to side collisions.

When a collision happens there is only a very short period of time, from when first contact is made until the car stops moving or disengages contact. Momentum is only exchanged during this period of time and therefore the forces and deceleration are very high. It is also during this time that deformation occurs.

Dynamic Deformation, C_d , is the instantaneous deformation (crush or difference between the length of the vehicle at an instant during the collision process and its length before contact occurred). This deformation increases until a maximum is reached, C_{dmax} , but this deformation is not the deformation that will be seen after the crash, as,

when the maximum is reached the structure then rebounds. The rebound process has two stages, a strong spring followed by a weak spring. Energy is returned to the car and rebound velocity generated during the strong spring phase and the majority of the structural recovery occurs in the weak spring phase [7]. The residual (permanent) deformation, C_{res} , is what will be seen after the collision (this may be slight in the case of low speed collisions due to bumper flexibility and spring back). A crush profile is the permanently deformed shape of the crushed vehicle. Residual crush is always less than the maximum dynamic crush.

There are three regions/zones (Fig. 2.2) to be considered in frontal collisions, which are distinguished by the magnitude of crushing force that they experience. The first region is the extreme front of the vehicle as far as the engine. The second region is the engine and the rear of the front of the vehicle and the third region is the passenger compartment [9] [10].

The first region requires the least amount of force for deformation to occur while the second region requires the highest amount of crushing force. First the bumper crushes, followed by the compression of the front struts (front of the wing as far as the shock absorber). There is a peak in the crushing force as the front struts undergo plastic or permanent collapse. Once the resistance of the structure is overcome, the front buckles and the force drops to zero. The crushing force rises as the engine, its sub-frame, front suspension components, and rear elements of the front structure are crushed. The force rises sharply to a peak due to the sudden deceleration of the engine block. The force then drops and oscillates about a mean level [7].

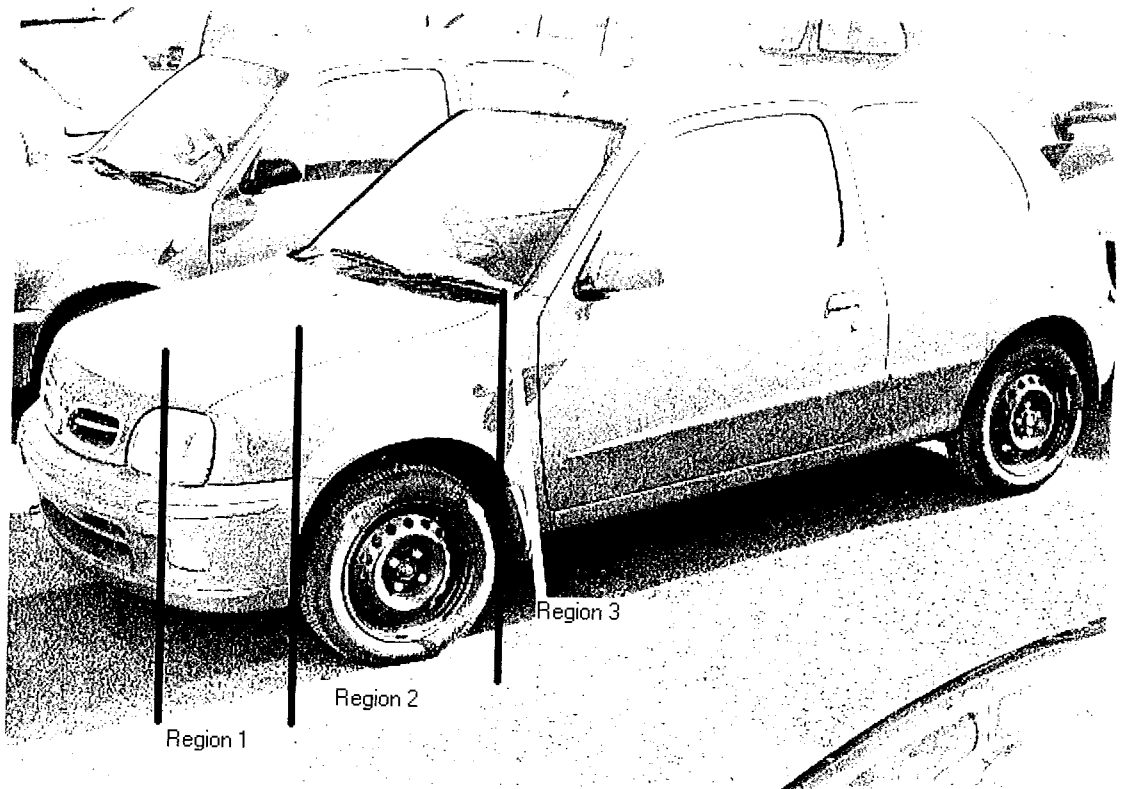


Figure 2.2 Regions involved in frontal collisions

At high speeds, ≥ 55 km/h, in full-width impacts the entire front structure of the vehicle is completely crushed and crushing of the occupant compartment i.e. 'intrusion' begins. Johnson [11] has shown that sequential crushing is a characteristic of dynamic impact. Vehicles, in general, collapse sequentially, from the point of impact rearwards even though some parts of the structure are stronger than others.

In video footage of frontal collisions [12] the first region appears to be crushed before the vehicle begins to decelerate significantly. This is consistent with results from a plot of velocity against crush for a given restitution by Wood, (the given restitution is the amount of spring-back of the deformed structure) who finds that [7], "the curve shows that very substantial crushing takes place before there is any significant reduction in the

speed of the car.” This is a consequence of the dynamics of the event, an outcome from kinematics equations.

Results from barrier impact tests show that vehicles with V_{CCS} (Collision Closing Speed) of 50 km/h, typically sustain residual crush of 10% of the overall length of the vehicle, and that residual crush is 73.5% of the maximum dynamic crush [7]. In a single vehicle collision, the collision closing speed is simply the approach speed of the vehicle. The collision closing speed of a two vehicle collision, is the combined speed of approach (\bar{V}_1, \bar{V}_2) of both vehicles, $V_{CCS} = |\bar{V}_1 - \bar{V}_2|$.

As vehicles are crushed, some of the kinetic energy of the vehicles is absorbed by their structures. The maximum kinetic energy is absorbed as the maximum dynamic crush takes place. Then some of the initial kinetic energy that was absorbed by the vehicle(s) is returned with the rebound of the structure as it recovers some of its initial shape.

Energy absorption is discussed further in the following chapter.

Chapter 3 PRE-IMPACT SPEED FROM CRUSH MEASUREMENTS

The key to finding the pre-impact speed of a vehicle from the crush damage it has sustained is estimating the amount of energy that the vehicle's structure has absorbed during its deformation. As discussed in the previous chapter vehicle collisions are generally inelastic collisions, the kinetic energy of the vehicle before the collision is not conserved; some of this energy can be transformed into potential energy when the vehicle is permanently deformed. The deformed shape of the vehicle i.e. the crush damage or crush profile can be used to estimate the kinetic energy of the vehicle before the collision and thus the pre-impact speed of the vehicle.

3.1 Energy Absorption

For energy to be absorbed there must be an applied force and crushing in the direction of that force. The total energy absorbed (E) is the displacement (crushing) integral of the applied force (F) [7].

$$E = \int F ds = \int F v dt \quad 3.1$$

where v is the velocity of the vehicle and t is the duration of the deformation period.

J is the magnitude of the impulse imposed on the vehicle. It is the change in momentum of the vehicle [7].

$$J = \langle F \rangle (t_2 - t_1) = M(v_2 - v_1) \quad 3.2$$

where $\langle F \rangle$ is the mean applied force, t_1 and t_2 are the time at the start and end of the application of the force (collision) respectively, M is the mass of the vehicle, v_1 and v_2 are the velocities of the vehicle before and after the application of the force.

Kinetic energy, which the vehicle had prior to the collision, is absorbed by the structure of the vehicles during crushing; maximum absorption occurs when maximum dynamic crush occurs [7]. Then some of the initial kinetic energy that was absorbed by the vehicle(s) is returned to kinetic energy with the movement of the structure as it rebounds and recovers some of its initial shape, and / or as the vehicles separate. The kinetic energy absorbed by the vehicle causes the vehicle's structure to oscillate, which in turn allows the vehicle to recover its shape; the damping force that stops this oscillating, also stops recovery of the vehicle's shape. The net energy absorbed (E_n) in a two-vehicle collision is the total energy of the vehicles as they approach the collision (E_a) minus the energy returned to the vehicles' structures (E_{reb}), as the structures regain some of their initial shape [7].

$$E_n = E_a - E_{reb} \quad 3.3$$

$$E_a = \frac{1}{2} \left(\frac{M_1 M_2}{M_1 + M_2} \right) V_{CCS}^2 \quad 3.4$$

$$E_{reb} \approx e^2 (E_a) \quad 3.5$$

M_1 and M_2 are the masses of the two vehicles involved, V_{CCS} is the collision closing speed and e is the coefficient of restitution. Therefore maximum energy absorption is directly proportional to collision closing speed squared (when the tyre to road interference is ignored) [7].

As stated in section 2.6 the collision closing speed is the approach speed of the vehicle in a single vehicle collision, or the combined approach speeds of both vehicles in a two-vehicle collision. In accident reconstruction the approach or pre-impact speed is often the information that the investigator is looking for, therefore in calculations the collision

closing speed is equated with the energy equivalent speed, V_{EES} . The energy equivalent speed is the speed at which an exemplar vehicle (a vehicle of the same make and model), with no load, must be travelling, before colliding with a flat non-deformable barrier, to absorb the same amount of energy as the actual crashed loaded vehicle that is being investigated [7]. As this vehicle has no load, no passengers or fuel and collides with a non-deformable barrier, it is only the vehicle's structure that can absorb the kinetic energy the vehicle had prior to the collision. Energy equivalent speed is discussed further in section 3.3.

In 1974 Campbell [13] published his paper on an objective technique for estimating the severity of automotive collisions. The vehicle damage and dynamic force-deflection characteristics of the vehicle's structure were used to estimate the energy absorbed in plastic (permanent) deformation of the vehicle. Firstly Campbell [13] collected information on the dynamic force-deflection characteristics, in order to relate the vehicle deformation to the amount of energy absorbed. Various vehicles were crashed into non-deformable barriers in controlled circumstances and graphs of impact speed against residual crush were plotted. This data could then be described by a linear equation,

$$v = b_0 + b_1c \quad \quad \quad \mathbf{3.6}$$

where v is the impact speed (mph), c is crush (inches), b_0 is intercept (mph) and b_1 is the slope (mph/inches). b_0 is the impact speed at which no residual crush is produced, however the significance of this value is reduced, as no collisions were staged at speeds below 15 mph and b_0 is the extrapolation of the slope (b_1) to zero crush. Campbell [13] also found that the force per unit width (f), assuming damage was uniform vertically, as a function of crush was,

$$f = \frac{W}{gw_0} (b_0 b_1 + b_1^2 c) \quad 3.7$$

where W is the standard weight of the vehicle, g is gravitational acceleration, b_0 and b_1 are coefficients from barrier test collisions, c is crush and w_0 is the vehicle's width. Integrating this over the distance crushed, c , gave the energy absorbed per unit width, E_{abs} , and then integrating over vehicle width gave energy absorbed.

$$E_{abs} = \iint fdc dw + \frac{Wb_0^2}{2g} \quad 3.8$$

The last term represents the initial energy absorbed by the vehicle without any residual crush being caused to the vehicle's structure. Substituting equation 3.7 into equation 3.8, results in the following [13],

$$E_{abs} = \frac{W}{gw_0} \int_0^{w_0} \left(b_0 b_1 c + \frac{b_1^2 c^2}{2} \right) dw + \frac{Wb_0^2}{2g} \quad 3.9$$

Equating this energy absorbed with the kinetic energy, the vehicle would have to have had to absorb this amount of energy. $K.E. = \frac{1}{2} \frac{W}{g} (EBS)^2$, where EBS is the velocity of the vehicle for this kinetic energy or the pre-impact velocity of the vehicle involved in the collision being investigated [13]. Therefore

$$(EBS)^2 = \frac{1}{w_0} \int_0^{w_0} (2b_0 b_1 c + b_1^2 c^2) dw + b_0^2 \quad 3.10$$

Various damage patterns can be approximated in terms of crush, as function of width and used in equation 3.10 to evaluate pre-impact velocity of the vehicle. However in order to use this method of calculation, the coefficients b_0 and b_1 must be known for the type of vehicle involved in the collision, i.e. the dynamic force-deflection characteristics must be known for every make and model of vehicle [13]. A solution to this is provided by Wood [7], using specific energy absorption capacity, which gives a general

relationship between energy absorption and all vehicle structures, is discussed in section 3.2.

3.2 Specific Energy Absorption Capacity (SEAC)

The Specific Energy Absorption Capacity (*SEAC*) is the maximum amount of energy per unit mass that the structure could theoretically absorb if it were possible to completely crush the structure over its full length [7].

$(SEAC) = \langle F \rangle \frac{l}{M_k}$, where $\langle F \rangle$ is the average force, l is the overall length, and M_k is the curb (unloaded) mass of the vehicle.

For a simple structure, $\langle F \rangle = \sigma A$ and $M_k = \rho A l$ where A is the cross-sectional area of the structure, σ the mean crumpling stress, and ρ the density of the structure. In this case $\langle F \rangle \frac{l}{M_k} = \frac{\sigma}{\rho}$ and the SEAC can be considered as the ratio of the mean crumpling stress to the density of the structure. SEAC would be identical for different structures provided they had the same density and the same average crumpling stress.

Consider a collision between a vehicle and a full-width, flat rigid barrier; the barrier is not deformable, therefore the vehicle itself, through deformation and deceleration must absorb the entire vehicle's kinetic energy. Ignoring the mass of the barrier and equating the Energy Equivalent Speed, V_{EES} , with the collision closing speed, V_{CCS} , the energy absorbed is,

$$E = \frac{1}{2} M_k V_{EES}^2 = \langle F \rangle C_{res} \quad 3.11$$

where C_{res} is the average residual crush.

Dividing the energy absorbed by the curb mass gives the energy of approach per unit mass or the Specific Energy of Approach, E_{SEA} ,

$$E_{SEA} = \frac{E}{M_k} = \frac{1}{2} V_{EES}^2 = \langle F \rangle \frac{l}{M_k} \ln \left(\frac{1}{\left(1 - \frac{C_{res}}{l} \right)} \right) \quad 3.12$$

The logarithmic term arises from the assumption that the mass is uniformly distributed [7]. This means as the vehicle crumples, the mass remaining to be decelerated decreases as the crushing progresses.

Therefore there is a single relation between V_{EES} and the normalised crush depth C_{res}/l , provided SEAC is the same for different structures [7].

3.3 Energy Equivalent Speed (V_{EES})

A study by Danckert [14] showed the mean crushing force in 50km/h full width barrier tests to be proportional to $M_k^{2/3}$; this implies that the mean crumpling stress is independent of the car size. Hofferberth and Tomassoni [15] showed the average permanent crush deformation to be proportional to $M_k^{1/3}$. A study by Kahane [16] has shown very strong correlations between car mass and length, length and wheelbase, and between width and the mean lengths for the three regions of the front structure of the vehicle (section 2.6). Combining these correlations with mean crumpling stress being independent of vehicle size, strongly suggests that the car population has an SEAC independent of car size and that the relation (3.12) between V_{EES} and C_{res}/l holds true for the car population. Even though the SEAC for individual cars may vary within a

subgroup of the population, the average SEAC for any subgroup will equal the SEAC for any other subgroup of the population. The single relation between V_{EES} and C_{res}/l was found through analysis of data from 202 tests of 67 car types designed between 1950 and 1986. Wood [7] has shown that V_{EES} (km/h) is related to $(C_{res}/l)^{2/3}$ as,

$$V_{EES} = 6.34 + 199.64 \left(\frac{C_{res}}{l} \right)^{2/3} \quad 3.13$$

His analysis of cars designed between 1975 and 1986 gave the relation as,

$$V_{EES} = 7.41 + 191.79 \left(\frac{C_{res}}{l} \right)^{2/3} \quad 3.14$$

A recent study by Wood et al [17] shows that a number of car types representative of the total population manufactured during the 1990's and up to 2001 (last available data) exhibit the same general characteristics. Wood also confirmed SEAC independence of car size in another study into the causative factors of decreasing injury risks with increasing car size. The uniformity and lack of dependence of SEAC on size is the fundamental reason for the higher injury risk in small cars [7].

For full-width, uniform crushing of the front of vehicles equation 3.14 predicts the data, shown in table 3.1 [7]:

V_{EES} (km/h)	C_{res}/l
30	0.05
50	0.10
70	0.20
95	0.32

Table 3A Mean relationships between Energy Equivalent Speed and the ratio of crush depth damage to pre-impact length

The relationships in table 3.1 leads to the following table 3.2, a guide for first examination of a crashed vehicle:

% of length of vehicle crushed	Approximate location of damage
5%	Front strut
10%	Front of engine
20%	(No distinctive point on vehicle)
32%	Leading edge of front door, front structure pushing into occupant compartment.

Table 3B Guide for investigators at first examination of vehicles

3.4 Eccentric Collisions

In the above calculations it was assumed that the vehicle approached its target along a path perpendicular to the barrier plane and that the vehicles' fronts experienced direct rearward crushing. However in reality the majority of collisions are eccentric, non-central. The force vector of the bullet vehicle through the point of impact is not always

directed towards the centre of gravity of the target vehicle, which results in the forces and impulses no longer being directly rearward. Therefore the forces acting on the vehicles can no longer be treated as though they are acting on single points (the vehicles' centers of gravity), angular and rotational velocities must be considered, this is referred to a rigid-body impact theory

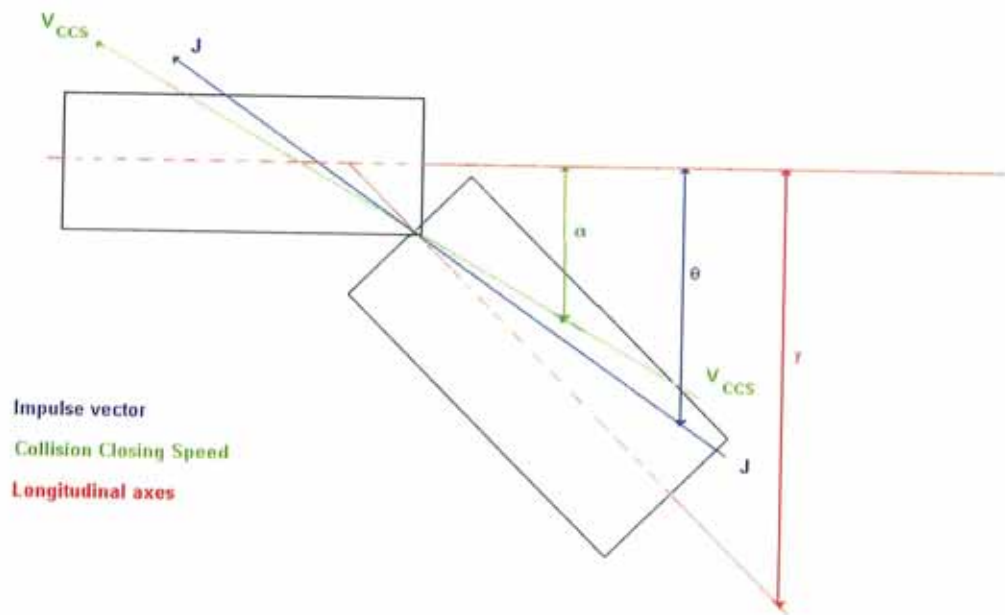


Figure 3.1 The geometry of two vehicles colliding at an angle γ

Figure 3.1 shows two vehicles involved in an eccentric collision, where the angle between the longitudinal axes of the vehicles is γ . Eccentric collisions result in rotation or spinning of the vehicle, after impact. The part of the vehicle which is in contact with the object / other vehicle is stationary. However there are still small longitudinal and transverse velocities, which cause rotation. Wood [7] has found the relationship between rotational velocity, ω , and the longitudinal and transverse components of the

closing speed and the longitudinal and transverse offset distances from the centre of gravity and the vehicle's radius of gyration (equation 3.15) to be

$$\omega = \frac{v_x p - v_y q}{p^2 + q^2 + k^2} \quad 3.15$$

where v_x and v_y are the longitudinal and transverse components of the collision closing speed, p and q are the longitudinal and transverse offset distances from the centre of gravity (fig 3.2), and k is the vehicle's radius of gyration.

3.5 T-style Collisions

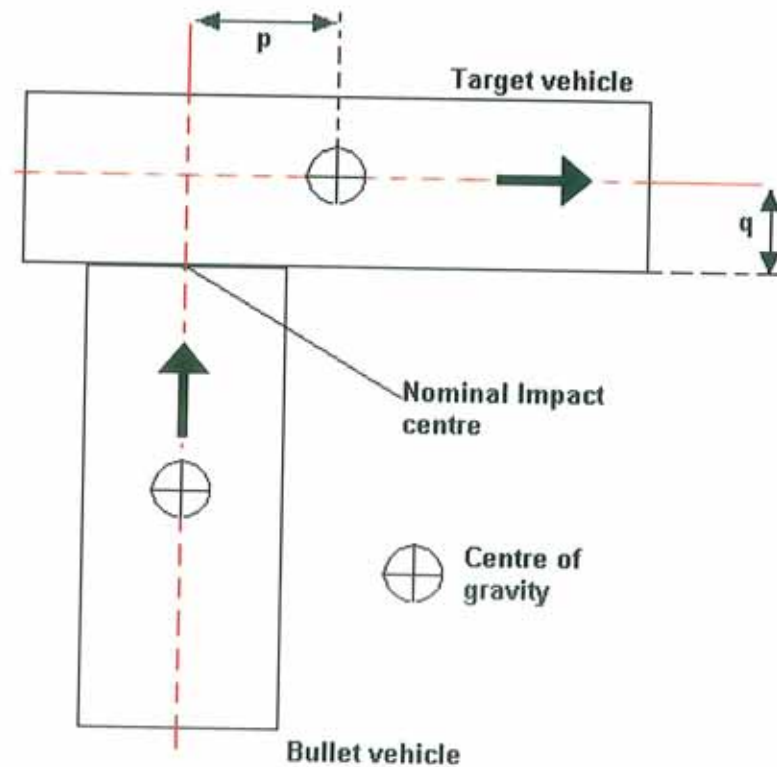


Figure 3.2 Shows the distances from the centre of gravity to the point of impact, in the x and y directions (p and q) for a side struck vehicle

For the case of a T-style collision as shown in figure 3.2, a front to side collision, the ratio of the energies absorbed by the vehicles (bullet and target vehicle) is

$$\frac{E_{target}}{E_{bullet}} = \frac{\langle F_{target} \rangle d_{target}}{\langle F_{bullet} \rangle d_{bullet}} \quad 3.16$$

where d_{target} and d_{bullet} are the depths of the crush deformation on the target and bullet vehicles [7]. $\langle F_{target} \rangle = \langle F_{bullet} \rangle$, the applied force of the impact [7]. Therefore,

$$E_{target} = E_{bullet} \left(\frac{d_{target}}{d_{bullet}} \right) \quad 3.17$$

Therefore, the total energy absorbed (E) by the vehicles is

$$\begin{aligned} E &= E_{target} + E_{bullet} \\ E &= E_{bullet} \left(1 + \frac{d_{target}}{d_{bullet}} \right) \end{aligned} \quad 3.18$$

There are two possible ways of obtaining d_{target} and d_{bullet} . When the vehicles have been orientated and fitted together a single measurement of crush can be measured along the direction of principal force of the collision (taken to be the central line of the bullet vehicle) on both the bullet and target vehicles. Or the average crush depths from across the width of the damage, on both the target and bullet vehicles are d_{target} and d_{bullet} .

E_{bullet} is the energy absorbed by the bullet vehicle alone; a value is estimated for the energy equivalent velocity of the bullet vehicle this using equation 3.14 [7]. This velocity is used in the equation for kinetic energy, $E = \frac{1}{2} Mv^2$, to find E_{bullet} . Equation 3.18 finds the energy absorbed by both vehicles. This value is then used in the equation for kinetic energy, $E = \frac{1}{2} Mv^2$, to find v the pre-impact speed of the bullet vehicle. M is the combined mass of the two vehicles, $M = \frac{m_b m_t}{m_b + m_t}$. m_b is the mass of the bullet

vehicle and m_t is the mass of the target vehicle. Therefore the pre-impact speed of the bullet vehicle, v , taken to be equivalent to the collision closing speed is,

$$v = \sqrt{\frac{2E(m_b + m_t)}{m_b m_t}} \quad 3.19$$

However, when the collision is an eccentric T-style collision, the central force vector of the bullet vehicle does not strike the target vehicle in line with its centre of gravity, it is off-set as in figure 3.2. The mass of the target vehicle must be adjusted to account for the impact not being along the perpendicular lines joining the centres of gravity of the vehicles. In this case, the equivalent mass of the target vehicle, m_{te} is [7]

$$m_{te} = m_t \left(\frac{k^2 + q^2}{k^2 + q^2 + p^2} \right) \quad 3.20$$

Where p and q are the longitudinal and transverse offset distances from the centre of gravity (fig 3.2), and k is the vehicle's radius of gyration. Wood [18] has found that k , the radius of gyration of the vehicle, when it is not measured at the accident site can be estimated by, $k^2 = \frac{0.931}{12}(l^2 + w^2)$, where l is the pre-impact length of the vehicle and w is the pre-impact width.

Therefore, the pre-impact speed of the bullet vehicle, v , in an eccentric T-style collision, using E from equation 3.18, and m_b and m_{te} the corrected masses of the vehicles in the actual collision is;

$$v = \sqrt{\frac{2E(m_b + m_{te})}{m_b m_{te}}} \quad 3.21$$

3.6 Impact Orientation

The orientations of the vehicles just prior to the impact and the direction of the principal force are generally inferred by accident investigators based on measurements taken at the collision site and previous experience of the investigator. Tumbas and Smith [19] found using the results of an experiment that observed investigator error in field measurement, that approximately 70% of the error on the end result of pre-impact speed was contributed by error in the measurement of the direction of the principal direction of force, and only 28% was contributed by error in the measurement of damage or crush. There are also a number of computer packages, which return an estimation of the pre-impact speed when details of the collision are inputted into the programme. The information that these packages require includes the orientation of the vehicles at initial contact, details of the crush profile and the roadway where the collision occurred. Therefore it is essential that the collision configuration be estimated as accurately as possible. Ueyama et al [20], provide a discussion of results obtained from experiments carried out to determine the collision configurations from vehicle crush dynamics and the resulting deformation of the vehicles using a photogrammetric stereo camera system.

Ueyama et al [20] simulated real world situations of twelve intersection collisions with the bullet and target vehicles travelling at speeds of 0, 25, 50 or 70 km/h, with impact angles of 90°, 120°, 150° or 210°. The study found there was very little change in the angle of the bullet and target vehicles until maximum deformation occurred. Therefore assembling (matching together) the deformation models of the damaged bullet and target vehicles with their areas of maximum deformation is the best estimation of the

initial collision angle of impact. They found “an impact angle at the inferred engagement is about $3^{\circ} - 5^{\circ}$ less than that at initial impact in the real world phenomena”. The vehicles involved in the collisions were modelled at horizontal cross sections, every 5cm from 45 cm to 80 cm above ground level. There was very little variation between these models, except that the damage at bumper level was greatest, therefore they concluded that ‘the damage profile is best represented at the level of the bumper’.

Ueyama et al [20] do not give details of the stereo camera they used to create the deformation models in 1991, however with the development of digital cameras and photogrammetric software; photogrammetric stereo cameras have been replaced. This project has been carried out to test the suitability of low cost over the counter equipment for producing vehicle deformation models. A very basic method of orientating the models of the vehicles was developed for this project [21]. Once the models of the outline of the vehicles were created, they were set to the same scale as each other and printed. These images were placed on top of each other and rotated until a best-fit was found; if evidence of direct contact was present (such as transferred paint or scuffing by a rotating wheel) the vehicles were fitted together by matching these contact marks. The point of impact is the centre of area of contact of the two vehicles and the angle of impact is the angle between the longitudinal axes of the two vehicles. Chapter 8 presents examples of vehicles that have been modelled and orientated.

Chapter 4 CRUSH DEPTH MEASUREMENT AND CRUSH PROFILE

The previous chapter has shown that the energy absorbed by a vehicle during a collision can be used to calculate an estimation of the pre-impact speed of the vehicle. In order to find the energy absorbed by the vehicle, the crush damage sustained by the vehicle must be measured. This chapter provides details on the current methods and some alternative techniques to measure crush depth.

Only a short period of time measuring vehicles and their damage is needed to realise that most vehicles have compound contours along their sides and ends, which lead to difficulties for the investigator in deciding what areas of the vehicle have been damaged during the collision and where to start measuring the vehicle's 'Crush Profile'. Crush profile in its simplest form is a top view of the vehicle showing the outline of the crushed and undamaged area of the entire vehicle. Tumbas and Smith [19] set out a measurement protocol for investigators who intended to estimate pre-impact speed from an energy basis stand point [19].

A summary of the protocols is as follows;

- Determine the damaged plane (i.e. front, rear or side).
- Determine the width of the damage. The problem of direct and induced damage is overcome by Tumbas and Smith [19] by recommending that only induced damage that is contiguous to the direct damage be included in the determining of the damage width.
- Determine the level at which damage should be measured. For vehicles involved in front and rear accidents Tumbas and Smith [19] recommend that

crush should be measured at the height of the vehicle frame, as this will have been the site of the major force transfer during the impact. For vehicles involved in side impact collisions the major structural members of a vehicle's side are not limited to the frame rails or body floor but include the doorframe and side door beam. As a result for side crush if there is no hinge, door latch or pillar failure, crush should be measured at various heights within a band of approximately 140mm, each measurement being made at the height of greatest crush. When there is hinge, door latch or pillar failure, then crush should be measured at the sill level and averaged with the above crush measurements.

The above protocol sets out what the crush deformation jig and base-line techniques are used to measure. Tumbas and Smith [19] also give recommendations to how the base line or horizontal rail of the jig should be aligned with vehicles, in most case parallel to the transverse or longitudinal axis of the vehicle, in a plane tangent to the vehicle's extreme pre-crash end or side and at or nearest to the level (height) of crush as possible.

The crush depth measurements which should be used in the calculation of energy absorption is the distance of the damaged point to the base-line, and then account for the free space distance between the base-line and the pre-impact location of the damaged point, by subtracting. Tumbas and Smith [19] say this free space distance is best accounted for with the use of an exemplar (undamaged) vehicle for the pre-impact location of the points.

The number of crush depth measurements across the width of the damage will be determined by the method being used to calculate the energy absorbed. The most

common requirement is to have six measurements, therefore the damaged width is divided into five equal divisions and crush is then measured at each of these equally spaced points [13].

4.1 Traditional Methods of Measuring Crush Depth

After speaking with a number of accident reconstructionists, I have concluded that while they each have their own technique for taking crush measurements. Their techniques are based on variations of the protocols and recommendation set out by Tumbas and Smith [19].

4.1.1 Crush Deformation Jig

The jig consists of a supported horizontal rail with 6 moveable rods attached (Fig 4.1) [22]. The jig is set at a certain distance from an undamaged area of the vehicle (usually the wheel axle centres on the undamaged side in the case of Fig. 4.1). The horizontal rail is adjusted in height to be level with the damaged area (normally bumper height). The moveable rods are evenly spaced across the width of the damaged area on the vehicle.

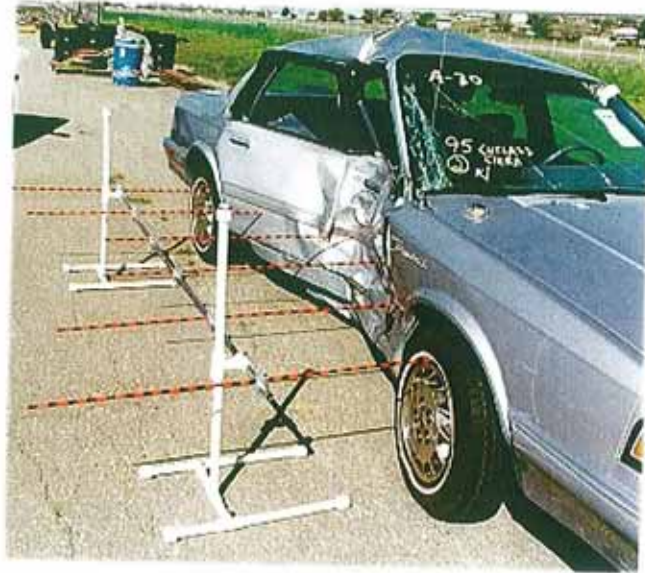


Figure 4.1 Crush Deformation Jig in place at side of a damaged vehicle.

The moveable rods are then moved forward until they make contact with the damaged vehicle. The depth of the crush is then read from increments printed on the rods. These depths are then adjusted to account for the distance the jig was set up away from the vehicle.

4.1.2 Base – Line Technique

In general a reference base line is an adjustable straight rod or rule. For this project a 3 meter multi-fold ruler on height adjustable stands was used at the height (generally bumper height) of the main area of crush damage (Fig 4.2). A reference base line is placed a set distance from the vehicle, a tape measure is used to measure this distance and the distances from the base-line to the crush damage. Bartlett et al [23] found tape measured lengths in the region of 11.7m to have a standard deviation of 7.62mm. Coyle at al [24] found a standard deviation of 0.71 mm when comparing lengths in the range of 0.5m to 1.0m measured with a tape to lengths measured with a Coordinate Measuring

Machine. This base-line technique is used to measure both the damaged and undamaged exemplar vehicle of the same make and model.

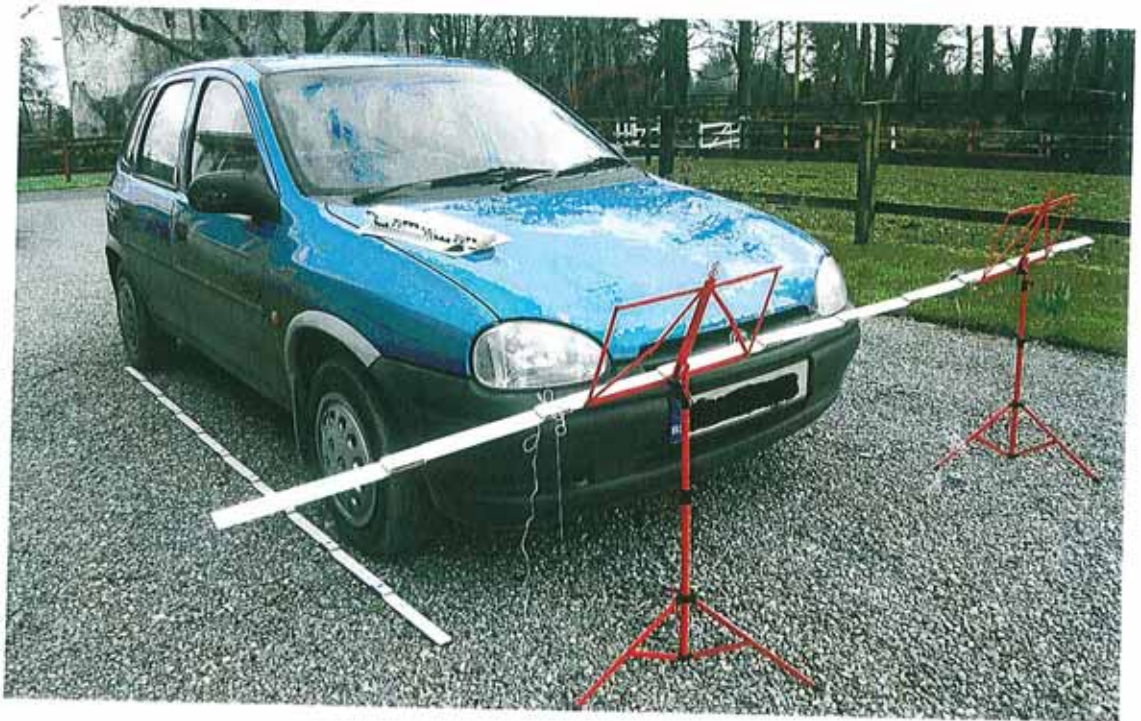


Figure 4.2 Base – Line in place at front of a vehicle

In a frontal collision the set distance is measured from the centre points of the rear wheels. In a side collision, the set distance is measured from the centre points of the wheels on the opposite side to the crush damage. Placing the base-line at this set distance allows it to be placed in the same location for both the damaged and undamaged vehicles. The damaged area of the vehicle is divided into equal lengths, with targets placed on the vehicle and on the base-line to mark the divisions. The distance from a base-line target to its corresponding target on the vehicle is measured, using a measuring tape. These distances are measured on both the damaged and undamaged vehicles and the crush depth at each point is found by subtracting the undamaged measurement from the damaged measurement (Fig 4.3) [25]. This provides

a manually measured crush depth and it takes approximately one hour to set up the base-line and take these measurements (damaged or undamaged vehicle).

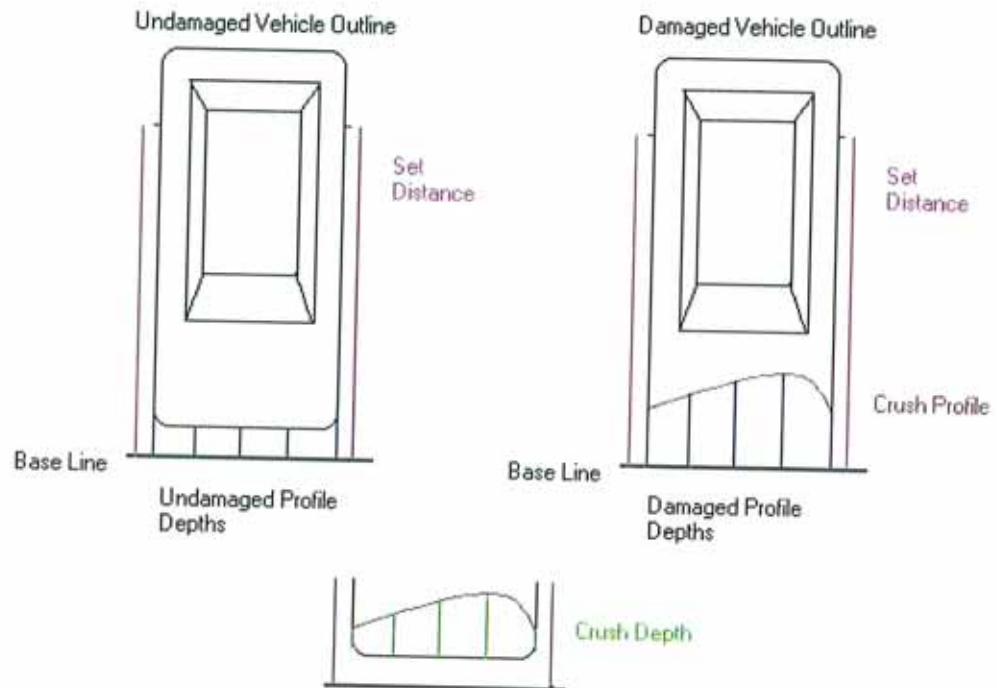


Figure 4.3 Crush Depth Measurements

4.1.3 Theodolite and Electronic Measuring Device

When a more detailed profile of the entire vehicle is required and more time is available, measurements are taken with a theodolite and electronic measuring device. These two instruments are combined in one instrument called a total station (Fig 4.4) [26].



Figure 4.4 Total Station

A theodolite is a calibrated optical instrument used to determine relative positions of points in surveying, navigation and metrology [26]. Depending on the instrument chosen the measurement accuracy ranges from 20mm to 160mm [26]. It consists of a telescope fitted with a spirit level and mounted on a tripod so that it is free to rotate about its vertical and horizontal axes. Graduated scales are used to measure the angles of rotation about the axes. In the electronic measuring device, a laser beam is emitted and hits a target (prism) and is returned to the device. The distance travelled by the beam is then calculated from the return trip time.

The total station is used to find the coordinates of points on the vehicle, which outline the profile of the vehicle. The target, a retro-reflecting prism, is held at each point and the angular separation between any two points can be obtained by noting the rotation of the telescope axis between them. The distances from the station to the points on the

vehicle are obtained by timing the pulses from the electronic measuring device on the station to each point and back. These points are then plotted using a Computer Aided Design (CAD) program to produce a 3D model of the vehicle (Fig 4.5).

The operator decides which points should be included in the outline of the vehicle's profile, which will contain as many or as few points as the operator deems necessary (and has time to collect) to ensure an accurate representation of the actual vehicle. Points can be recorded at varying height levels using this method.

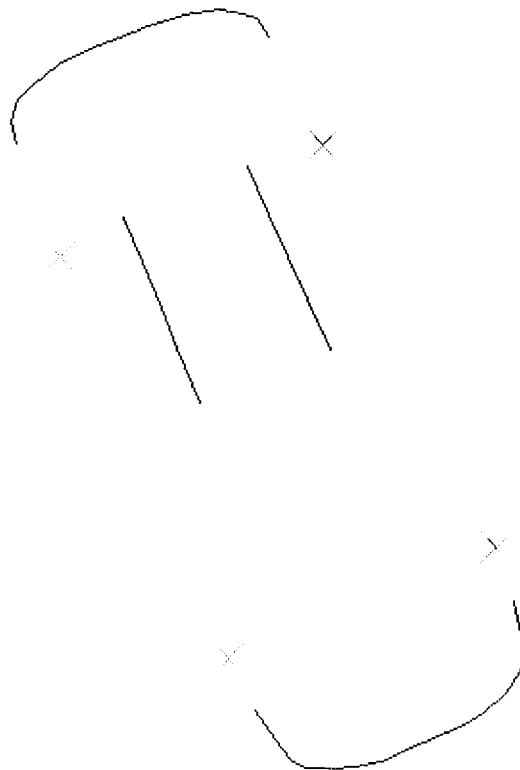


Figure 4.5 Vehicle Profile created in AutoCAD with Total Station Coordinates

4.2 Review of Alternative Methods of Measuring Crush Depth

Section 4.1 gave the details of how crush measurements are commonly taken. This section describes the theory and method behind some new or alternative techniques of crush measurement that are currently being researched and used by some collision investigators. When examining a vehicle the objective of the investigator is to create a 3D profile of the damaged vehicle, so that information about the cause of the accident and pre-impact speed and actions of the vehicle can be discovered. Like the total station the following techniques are traditionally used in areas of modelling and surveying, but more recently have begun to be used in accident reconstruction.

4.2.1 3-D Laser Scanning

Laser scanners are three dimensional, non-contact, high precision, mapping and imaging tools. In Switzerland the Zurich City Police in their investigations of road traffic collisions [27] currently use a laser scanner to create detailed models of the vehicles. The transport research laboratory (TRL) staff in the UK use a Riegl laser scanner in their examination of the vehicles involved in collisions. 3D laser scanners can quickly record range, intensity and colour data over a variable field of view [28]. In general laser scanners work on the principle of emitting a very short pulse of laser light and measuring the transit time for the pulse to travel to the object being scanned and return to the scanner, which gives the distance of the point illuminated by the light, from the scanner. The angle at which the light is emitted is controlled by rotating mirrors or a polygon within the scanner. The angular direction and distance travelled by the pulse of laser light give the 3D position of the point illuminated by each pulse [28].

Points across the entire object are illuminated. The minimum distance between adjacent points is determined by the resolution of the scanner. These points are plotted to produce a mesh outline / scan of the object. In order to add texture or colour to a scan, multiple images of the object are required. These images are obtained from either a camera or a video camera which is attached to the scanner and records images as the scanner is obtaining the 3D coordinates. The mesh outline and images are combined using the operational software of the scanner [28].

Riegl Laser Scanner (LMS-Z390)

At a seminar organised by the school of Geomatics at Dublin Institute of Technology, the terrestrial laser scanning system RIEGL LMS-Z390 (fig 4.6) was demonstrated to the attends. The scanning systems consists of a highly accurate and fast scanner, operating and processing software RiSCAN PRO, and a calibrated and orientated high-resolution digital camera [29]. The RIEGL LMS-Z390 has an accuracy of 2mm [29]. Figure 4.6 shows the scanner upon a supporting tripod, with the camera fitted to the top of the scanner. Figure 4.7 illustrates the different components of the LMS-Z390, the purposes of the components are explained below.



Figure 4.6 RIEGL LMS-Z390

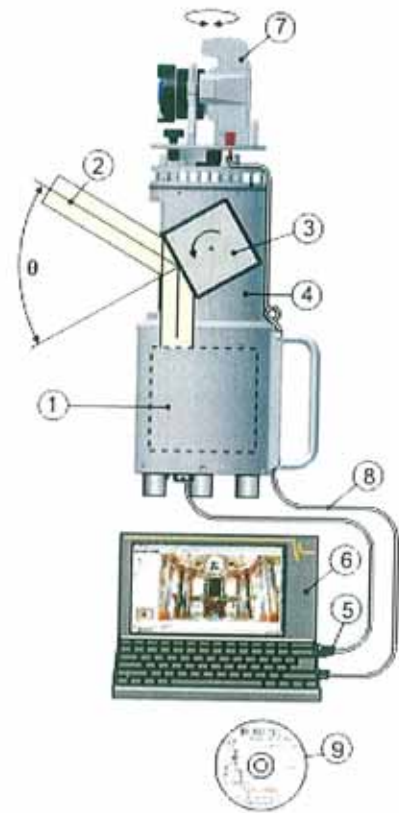


Figure 4.7 Components of Riegl Scanner

Component (1) houses the range-finder electronics of the 3D scanner, which is optimised in order to meet the requirements of high speed scanning (fast laser repetition rate, fast and highly accurate signal processing, and high speed data interface). (2) is the *vertical deflection* ("line scan") of the laser beam, which is directed by (3) a polygon with a number of reflective surfaces. The polygonal mirror rotates continuously at an adjustable speed; it oscillates the laser beam linearly up and down and has a range of 80° . The *horizontal scan* ("frame scan") is provided by rotating the complete optical head (4) up to 360° . Scan data namely: range, angle, signal amplitude and optional timer are transmitted to a laptop (6) via a TCP/IP Ethernet Interface (5). Photographs captured by the camera (7) are fed into the same laptop via USB/firewire interface (8). The RiSCAN PRO software (9) allows the operator to perform a large number of tasks

including sensor configuration, data acquisition, data visualisation, data manipulation, and data archiving. The above explanations for the components of the Riegl scanner are from the manufacturers' literature [29].

3D laser scanners are compared to digital photogrammetry in section 4.3.

4.2.2 Laser Trackers

Laser trackers are distance measurement instrument, they could be used to measure distances at collision sites, or from a base-line to a vehicle surfaces. They are based on the two techniques, laser interferometry and optical encoding to measure azimuth and elevation of a beam-steering mirror [30]. Laser trackers have an accuracy of 60 microns in 15m [26]. In an interferometer the beam of light is split in two, by a beam splitter, a glass plate with a thin layer of silver on one side, at a 45° angle to the incident path of the beam, fig 4.8 [6].

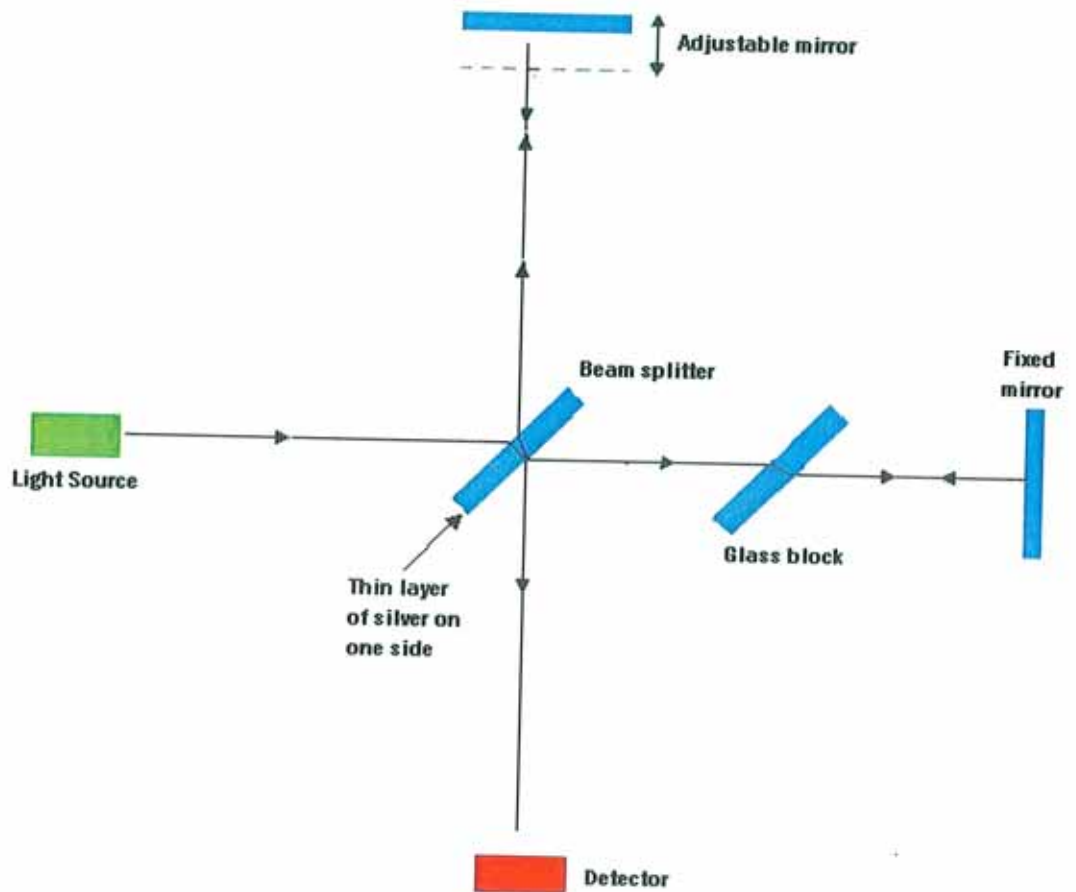


Figure 4.8 Schematic diagram of an Interferometer

Half of the light (measurement beam) is reflected towards an adjustable mirror while the other half (reference beam) passes directly through towards a fixed mirror. The measurement beam hits the adjustable mirror and is reflected back along the same path. The reference beam hits the fixed mirror and is also reflected back along its path. A glass block, of the same thickness, refractive index and chromatic dispersion as the beam splitter is placed between the splitter and the fixed mirror, also at a 45° angle, to ensure that both beams traverse the same optical path in glass, the same number of times. The two beams are recombined at the beam splitter and travel to the detector, where they form an interference pattern. The phase difference, δ , between the beams is

$\delta = 2kS \cos \theta$, where $k = 2\pi/\lambda$, λ is the wavelength, S is the path difference, θ is the angle between the common axis of the two beams and the direction of observation [6] [30] [31]. Interferometers measure displacement from a starting position rather than an absolute measurement of position. The instrument reading is set to zero at the initial position of the adjustable mirror. When the interferometer is used as part of a laser tracker the adjustable mirror is the retroreflector. The retroreflector is then moved to the required point and this displacement is measured relative to the zero position. The distance measured is the optical path, which differs from the physical path by a factor equal to the refractive index of the air [31].

Interferometers measure only displacement along straight lines but combined with a beam-steering mirror, measurements can be made in many directions. Using a feedback loop the laser tracker's beam follows the movements of the retroreflective target. When the target is struck off centre, the beam is reflected back parallel to, but displaced from the incident beam. A two dimensional sensor measures the displacement and the beam-steering mirror is adjusted, to ensure the target is hit in the centre. When the target is struck in the centre, the beam has hit the correct location. The laser tracker follows the retroreflector target at approximately 5m/s, recording the distance, azimuth and elevation; these polar coordinates are then transformed into Cartesian coordinates [30].

Although offering subwavelength precision, laser trackers have a number of limitations. Breaking the beam requires the coordinate system to be reset. The target must physically touch the object. Recorded coordinates are off set from the actual surface, and the size of the retroreflector limits the minimum radius of curvature that can be handled. The scene must remain static as the points are measured. Changes in air

temperature, pressure and humidity affect measurements [30]. These limitations, combined with the length of time required to obtain the profile, make the use of laser trackers impractical for accident reconstruction.

Therefore a highly precise method of recording all the data associated with a collision would be to measure the accident site with a total station or laser tracker and model and measure the vehicles involved with a laser scanner, however the expense of this method would be a major limitation.

4.2.3 Digital Photogrammetry

As stated previously in accident reconstruction measurements are not limited to crush measurements. This project however deals only with crush measurements. In general at a crash site, data is recorded about the location of the vehicle(s), debris and road signs. Also the length of skid marks and lines of sight are recorded. This data is generally gathered by using either surveying method such as total station, or by direct measurements using measuring tapes or laser trackers. More recently this data has begun to be obtained through photogrammetry.

Photogrammetry is currently used by the Zurich City Police to model crash sites [27] and this combined with 3D optical scans of the contact areas and collision damage of the vehicles provides a detailed record of collisions and to enable evaluation.

As stated in section 4.2.1, 3D laser scanners are very expensive, while photogrammetry only requires a good quality digital camera. In 2002, Egan [32], made a comparison of

modelling using a Cryax 2400 3D scanner and Digital Photogrammetry by modelling a row boat by both methods. Eighteen images were taken for the photogrammetry project and three scans were taken and merged together. Preparing the boat with retro-reflective targets (this puts a limit on the number of points that can be included in the photogrammetry model, therefore reducing the detail on the model) and photographing it took two and half hours. Scanning the boat took four hours. Post processing of the photographs took ten hours, while processing the laser scans took only half an hour. However the laser scanner (including Cyclone software) costs \$250,000, while the photogrammetry materials (Kodak DC260 digital camera, Australis software) cost only \$6,500. Egan [32] used the coordinates of the targets from both methods (scanner, photogrammetry) to calculate the inter-target distances and these distances ranged from 2 mm – 10 mm. This is his only reference to measurement accuracy, he found that the two techniques vary but does not conclude that one is more accurate than the other.

The aim of this project as was previously stated is to develop a fast, accurate and low cost method of measuring crush depth damage sustained by a vehicle during a collision. Although digital photogrammetry cannot provide the same detail (resolution) on a model as 3D laser scanning, it is by far the cheaper method and the amount of time required at the scene is less. Digital photogrammetry is fast and inexpensive.

During the construction of a large ship, Fedak [33] compared the measurement accuracy of a Leica TC2002 total station with Digital Photogrammetry (PhotoModeler Pro 4, Fuji film mx-2900 2.3 Mega pixel digital camera). Retro-reflective survey targets were placed on the bow of the ship.

The survey using the total station was done with extra care; the access doors to the area housing the ship were kept closed to stop drafts from thermally distorting the instrument's tripod. Heavy machinery and co-workers were not allowed near the area to avoid vibrations disturbing the instruments. The survey took approximately three hours. The photogrammetry data collection took 20 minutes and did not require any of the above precautions.

As part of the experiment Fedak [33] checked the accuracy of the total station by measuring the coordinates of four targets that were arranged at distances that enveloped the geometry of the ship's bow, from four station locations, producing twenty-four sets of independently measured target separation distances. The root mean square difference between the locations of the coordinates was 0.74mm. The bow width was 18633mm; therefore the accuracy of the total station was in the order of 1: 25000.

Fedak [33] found that the differences between the total station coordinates and photogrammetry coordinates were highly directionally dependent. The correlation between the coordinates of axes which are similar to the plane of the images was much stronger than between those where the axis was generally perpendicular to the plane of the image. Fedak believes this is due to the restricted locations of the camera stations and if additional images were taken, the photogrammetry coordinates would likely be closer to the total station coordinates.

Fedak [33] took the root mean square difference between photogrammetry and total station coordinates along the three axes directions and estimated the accuracy, using the known length of the ship in these directions. He then averaged this accuracy and found

photogrammetry to have an accuracy of 1: 10000, which is suitable for many applications in architecture, model building and some industrial measurements. Fedak concluded that the speed and convenience of the imaging process (of photogrammetry) compared to measuring coordinates with a total station are very attractive.

Suthau et al [34] used photogrammetry to report on the surface of a broken bolt on a railway bridge and found the method had an accuracy of 0.1mm in the x and y directions and 0.2mm in the z direction. Lie et al [35] using stereo photogrammetry found lengths in three dimensions to be within 30mm of the true value. Faig et al [36] found when proper measuring protocol was followed during data collection that measuring crush with photogrammetry was as accurate as traditional methods.

Photogrammetry is discussed in detail in chapter 6. Details of the experiments completed during this project to find the accuracy of photogrammetric measurements with PhotoModeler software are given in chapter 7.

Digital Photogrammetry with PhotoModeler software has been chosen as the fast, accurate, low cost technique to measure crush depth for this project. However without the development of photography, photogrammetry would not be where it is today; photography is discussed in the next chapter.

Table 4A is a summary of the measuring techniques discussed above and their advantages and disadvantages.

Technique	Advantage	Disadvantage
Deformation Jig	Low cost	Time consuming, limited detail
Base – line	Low cost	Time consuming, limited detail
Theodolite & EMD	Medium cost, accurate	Time consuming, limited detail
Laser Scanner	Fast, highly accurate	Expensive
Laser Tracker	Medium cost, accurate	Time consuming, limited detail
Digital Photogrammetry	Low cost, fast, accurate	Limited detail

Table 4A. Summary of measuring techniques

Chapter 5 PHOTOGRAPHY

In order to complete a photogrammetry project, first one needs to capture images of the object to be modelled and measured using photography. The quality of the images used to create the model is key to the accuracy of the model (sections 6.3.4 & 7.2). Leonardo da Vinci discovered the photographic chamber while sheltering from the intense summer sun in a dark room. He noticed that on the wall there was an identical but inverted image of the landscape outside. This resulted in the idea of an obscure chamber, the photographic chamber, which later was developed into the photographic camera [37].

A camera works with the same optical principal as the human eye. Objects are visible to us, when they are illuminated by light (from the sun or a lamp). Light travels from the object through the iris and lens onto the light sensitive retina, where it is converted to an electrical signal and sent via nerves to the brain, where the conception of the object is formed [38].

In a camera the light passes though the aperture and lens and is projected onto photographic film or a charged-coupled device, where the image is stored. The simplest camera is the pinhole camera [38].

5.1 Pinhole Camera

Before the days of mass-produced inexpensive cameras, people would construct their own simple pinhole cameras, using a shoebox, some aluminium foil and photographic

film. A section was cut from one end of the shoebox and replaced with the aluminium foil, a pinhole was put in the centre of the foil and this was now the aperture of the camera. A sheet of photographic film was taped to the other end of the shoebox (fig 5.1). Each visible point on the object being photographed reflected a ray of light that passed through the pinhole aperture and formed a unique image point on the film, see figure 5.2. Pinhole cameras have unlimited depth of field (section 5.3) but require very long exposure times [39].

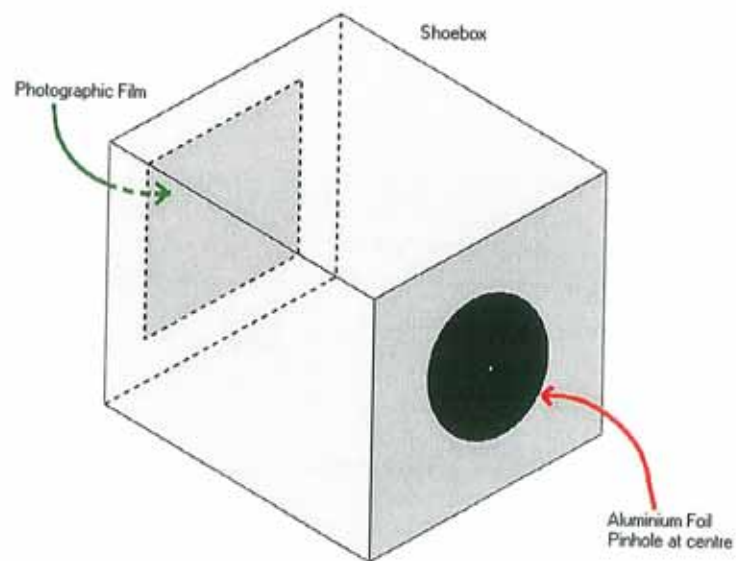
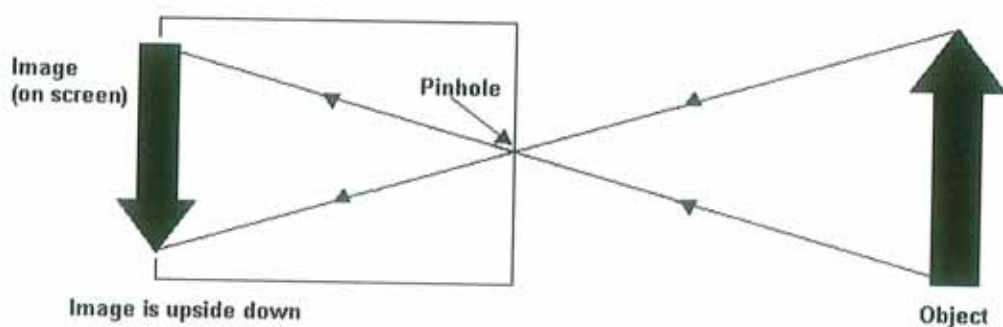


Figure 5.1 Pinhole Camera



5.2 Path of Light in Pinhole Camera [38]

5.2 Camera Lens

In order to reduce the long exposure times, a larger pinhole / aperture was used to allow more light to pass through, however the larger pinhole resulted in blurring of the image. Therefore in modern cameras light from an object passes through a lens and the image is formed on the photographic film, which is located a very short distance from the rear of the lens. Figure 5.3 shows the geometry of the lens camera [40].

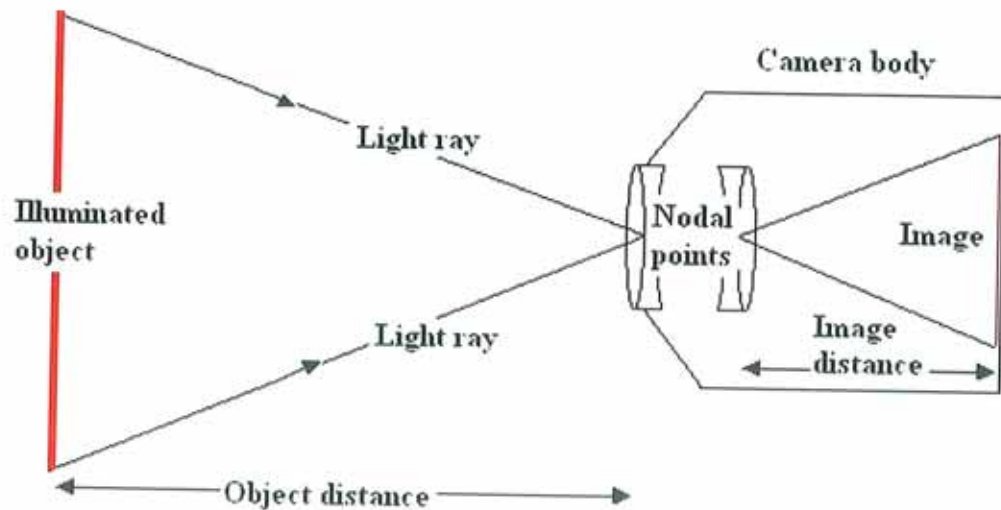


Figure 5.3 Geometry of lens camera [38]

Figure 5.4 shows a camera lens and the path that light takes through it.

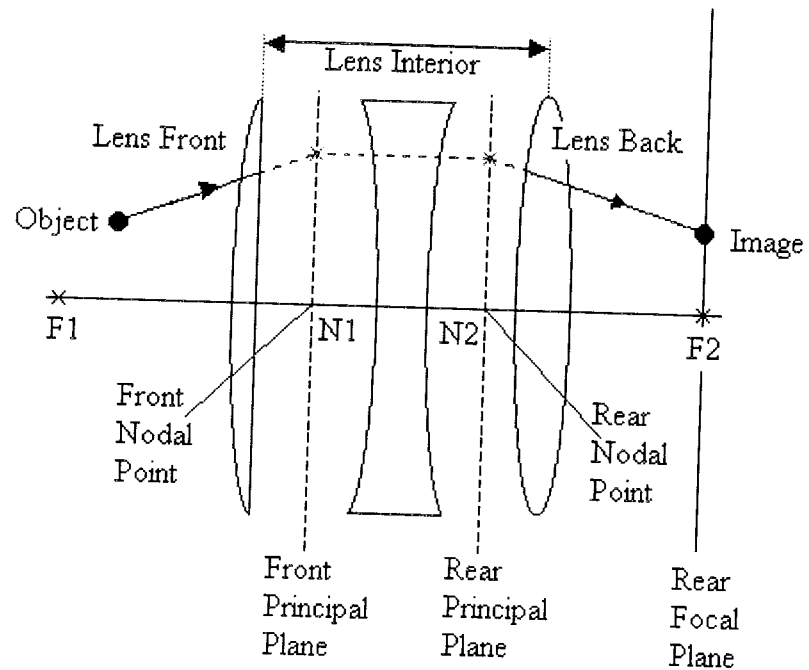


Figure 5.4 Camera Lens [38]

The lens has front and rear focal points, $F1$ and $F2$ and two principal planes, which are planes of unity magnification perpendicular to the lens axis through the nodal points. The front nodal point is the point within the lens at which light is aimed, in order for it to emerge from the lens at the same angle, from the rear nodal point [38]. A light ray from the object enters the front of the lens aimed at the point x on the front principal plane. It emerges from the lens at the same height above or below the optical axis on the rear principal plane on to the rear focal plane [38], which is perpendicular to the lens axis and through the rear focal plane where the photographic film is located.

For photogrammetric calculations, the lens is simplified, the distance between the front and rear nodal points is ignored and the nodal points are treated as one point called the principal point, when this is done the path the light takes is the same for the lens camera and the pinhole camera. Often the lens is further simplified and considered to be a

single point, the perspective centre, at the principal point. Unlike the pinhole camera, the depth of field is restricted with lens cameras.

5.3 Depth of Field

The aperture controls the amount of light reaching the image, by changing the effective diameter of the camera's lens. The shutter speed of the camera controls the amount of time for which light is allowed to reach the film. Shutter speeds are measured in fractions of a second.

The aperture is extremely important for photographs that will be used in photogrammetry, as it determines the depth of field (depth of focus) (*DOF*). The depth of field is the distance between the points nearest (D_N) and furthest from the camera (D_F), which are imaged with acceptable sharpness [41]. $DOF = D_F - D_N$ or

$$DOF = \frac{2Hs^2}{H^2 - s^2},$$
 where H is hyperfocal distance and s is the distance at which the

camera is focused. The hyperfocal distance is found using the focal length (f), f-number

(N) and the circle of confusion (c) of the camera, $H = \frac{f^2}{Nc}$ [40]. The correct aperture to

allow the entire object being photographed for photogrammetric modelling, to be in focus, must be chosen.

5.4 Photographic Film

After the light emitted from the object has passed through the optics of the camera and been focused, it must be recorded. Traditionally the common means of recording imagery was photographic film.

In its simplest form photographic film consists of a light sensitive coating, the emulsion, applied to a plastic or glass base [42]. There may also be an anti-halation layer on the opposite side of the base to the photosensitive side, to prevent reflections from the camera back. The base must not be deformed during exposure or processing, as the geometry of the image will be compromised. The film becomes wet during processing and must be dried uniformly and not subjected to uneven stress as this may lead to non-uniform deformation, which will cause errors in the final results.

The emulsion contains minuscule grains of a light sensitive salt, silver halide. When silver halide crystals are exposed to light, a chemical change occurs and a latent image is formed. When the film is developed, the silver halide crystals are reduced to elemental silver. The intensity of the light striking the film governs the proportion of crystals that change to silver, which is opaque to light, unlike silver halide. Thus the image light intensity is mapped by a spatial variation of opacity (the negative).

5.5 Digital Photography

Over recent years photography has been steadily changing to include electronic methods of recording images. Digital cameras have developed along with developments in semi-

conductor manufacturing; Instead of silver halide coated film, digital cameras contain a light sensitive charged coupled device (CCD) sensor [42]. CCD sensors are composed of thousands or millions of minute electronic elements grouped as a matrix [43]. The number of picture elements (pixels) in the CCD's matrix primarily determines digital image quality and resolution. How the CCD sensor works is explained in the next section.

5.6 Charged-Couple Device (CCD) Sensors

A typical CCD matrix made of light sensitive silicon for colour photography has its microscopic electrical elements overlaid with either a red, green or blue filter, each forming a light-sensitive photosite [44]. Extra green filters are used to bias the light response closer to human eye sensitivity, see figure 5.5. As the light from the object passes through the filters, light of colours that differ from the filter colour are absorbed, so only light the colour of the filter passes through onto the photosite [44], they collectively build up a dot-by-dot picture of the images. The more pixels that the CCD contains the more detailed the resulting picture will be [45].

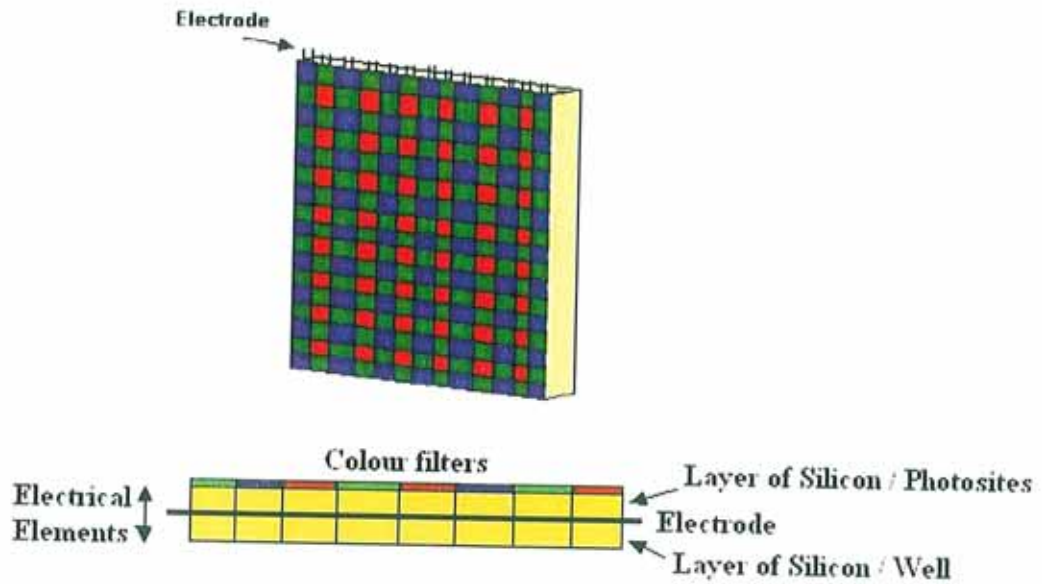


Fig 5.5 Tri-colour Filtered CCD [44]

Light from the object reaching a photosite provides energy, which releases negatively charged electrons from the silicon atoms. Each element has a transparent electronic gate attached, through which the electrons pass. Another layer of silicon directly behind the photosite is receptive to these freed electrons, and acts like a container or well when a voltage is applied via an electrode, see figure 5.6. The negative charge built up during exposure is stored in each well, under each element of the matrix. The amount of stored charge is proportional to the amount of light received by each photosite during exposure [44].

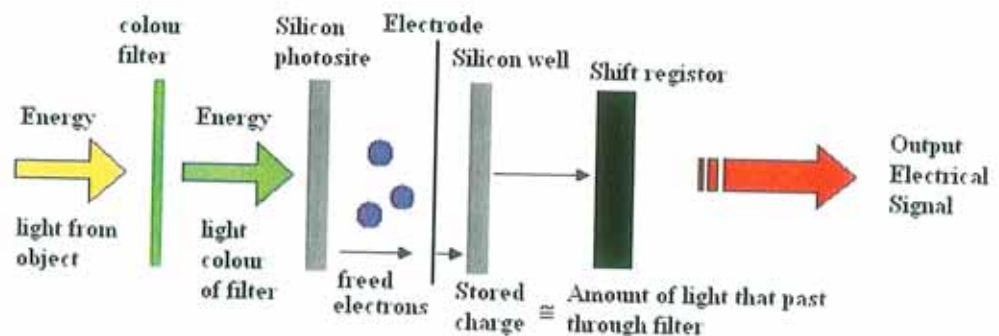


Fig 5.6 Path of light through a CCD [44]

Immediately following exposure all charges simultaneously transfer into adjacent shift registers and are systematically read out of the matrix as electrical signals. The sequence of signals then passes through an analogue to digital converter, which translates the signal into a stepped series, in which each intensity has been assigned a numerical value [44]. The image becomes a grid of points, each one coded with a number in binary form representing the intensity at that point.

5.7 Photogrammetric Cameras

Originally photogrammetry was developed for creating maps using aerial cameras and therefore the first photogrammetric camera were aerial mapping cameras, which have the same components as a standard camera, lens, shutter, magazine and body [46]. The main differences between standard camera and aerial mapping / photogrammetric cameras are that the components of the photogrammetric camera are designed to much higher specifications and designed to maintain their high geometric precision under a wider range of operating conditions. These cameras with high geometric precision are also called metric cameras and standard cameras are referred to as non-metric [47].

In a metric camera, the lens is highly corrected for aberrations and distortions. The shutter controls the film exposure time. The film is housed in a removable magazine, which contains the mechanisms that advance and meter the film and flatten the film during exposure. Film flatness is crucial in photogrammetric camera as it affects the geometric accuracy of the imagery [40]. Originally glass plates were used to flatten the film and avoid deformation, however advance in film materials and platen (film backing

plates) design have made glass plates unnecessary [46]. More recently with developments in digital photography, the issue of film flatness has been removed by electronic methods of recording images. The body of the camera holds the components, motors for film advance and shutter, and has mounting points for attachments to the camera mount. The body is designed to isolate the lens cone and the magazine from excess vibrations.

In the course of this research both metric and non-metric cameras were purchased and used. A Rollei d-7 metric camera was purchased and tried first. It had a fixed focal length of 7mm and the lens was calibrated by the manufacturers for distortions and tilt. However the CCD only had 1.5 Mega-pixels [48], which restricted the amount of enlargement that could be carried out on the images before points of interest were identified and tagged.

An Olympus C5060 zoom digital camera was purchased and used; this standard over-the-counter, non-metric camera was recommended by the manufacturers of the photogrammetric software package that was purchased, PhotoModeler. The Olympus camera had an adjustable focal length 5.7mm to 22.9mm and 5.1 Mega-pixels [49]. Also provided in this software package was the means of calibrating the camera to be used with the software. The Olympus camera was set to its shortest focal length (widest lens angle) and calibrated as set out below. This calibration information was entered into PhotoModeler at the start of each modelling project, for which the photographs were taken with the Olympus camera with its lens set to the shortest focal length.

5.8 Camera Calibration (PhotoModeler Method)

The PhotoModeler package includes calibration software, and a calibration slide (fig 5.7) that must be projected onto a flat surface, alternatively the same image as on the slide may be printed to A4 or A3 size [50] [51]. Full instructions for the calibration of a camera are provided; the following is a summary of the procedure followed.

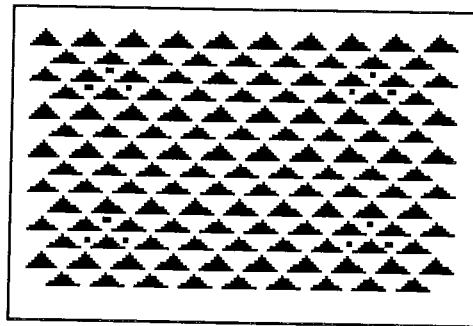


Figure 5.7 PhotoModeler Camera Calibration Slide

The slide was projected onto a flat wall and photographed from surrounding locations as instructed. The four main targets on the slide were tagged in each photograph and PhotoModeler then automatically located and tagged the remaining targets. The diagonal distance between two of the targets was measured and entered into the software, along with the estimated focal length of the camera [50] [51].

Once the calibration programme was processed, a file was created that contained the camera focal length, format size, principal point, lens distortion and image size. The file is used by each PhotoModeler project, which uses this now calibrated camera to photograph the object that is to be modelled.

5.9 Photographing Vehicles

There are a number of precautions that must be taken when taking a photograph, from ensuring the lens is not obstructed to ensuring that the correct exposure is selected for the lighting conditions. These problems are overcome by the experience of the photographer and, with manufacturing improvements in camera design and automatic selection of camera settings, by the camera itself.

Taking photographs for use in PhotoModeler requires more precautions than usual as the photographs must meet the requirements of PhotoModeler. When the object being photographed is a vehicle, one of the major problems that arises is glare from the vehicle's surface. As vehicles have a reflective surface this can reflect the camera's flash, the sun, or any extra lighting used to illuminate the vehicle. PhotoModeler requires photographs to be taken from all around the vehicle [50] [51], which may include facing into the sun, which goes against basic rules of photography.

Photographing the vehicle from locations surrounding the vehicle is just one of the requirements of PhotoModeler, other requirements include ensuring that there are at least six common points in each pair of photographs, and that there is at least one point common to all photographs [50] [51]. Further details of PhotoModeler's requirements are given and discussed in the next chapter.

Chapter 6 PHOTOGRAMMETRY

Photogrammetry is defined as the process of deriving information about an object through measurements made on photographs [37]. Digital photogrammetry is photogrammetry that uses digital images either scanned photographs or photographs from a digital camera. Close – range photogrammetry is the term used when the object being modeled is within 300m of the camera capturing the images [37].

6.1 History of Photogrammetry

Photogrammetry's earliest use can be traced back to Leonardo da Vinci who studied the principles involved in the geometric analysis of pictures in the late 1400s. The main commercial use of photogrammetry is aerial photographic surveying, which was developed, in the late 1800's after the production of usable photographs by Niepce and Daguerre [37]. Laussedat created a photogrammetric apparatus in 1859 [37]. From the rooftops of Paris he photographed objects with two cameras attached to the ends of a bar. From these two photographs bearings could be derived for all points. The intersections of pairs of light rays (from the object point to the image points on the photographs), permitted a point by point reproduction of the object [51]. This point by point intersection technique is called plane table photogrammetry.

In 1907 the first stereoplotter was designed and built in Britain by Thompson [41]. The stereoplotter was the first step in the automation of calculations. In 1915, Gasser [41] in Germany patented his stereoprojector, which utilised anaglyph filters. Two images are superimposed in complementary colours and viewed through filters of corresponding

colours. These were the basis of analog photogrammetric restitution. After modification and refinement, Santani in Italy developed the first mechanical instruments for aerial photogrammetry in 1921 [41].

The invention of the electronic computer in the early 1940s, started a new phase of development in photogrammetry. The British Ordnance Survey is credited with the first operational system of analytical aerotriangulation. In 1953 Schmid and Brown developed the principles of multi-station analytical photogrammetry. Digital components were added to stereoplotters, called computer-assisted stereoplotters, which had increased speed of operation, added flexibility of operation and improved instrument versatility [41].

In 1957, Helava [41] invented the analytical plotter. In the analytical plotter, the coordinate transformation between the image and the map of the area being plotted, is realised by on-line digital computations and servo-control, rather than by optical or mechanical analogy. The analytical reconstruction of the bundle of rays and of the stereomodels generated from the image coordinate readings in analytical plotters, opened new possibilities for close-range photogrammetry.

6.2 Digital Photogrammetry

The development of digital photogrammetry began with the advent of satellites, starting with Sputnik in the USSR in 1957. The development of digital photogrammetry has been parallel with the development of remote sensing. Digital photogrammetry is essentially a sequential process in which either the photographs are first digitised or the

images are captured with a digital camera. The digital data is processed in a computer. Digital photogrammetry uses CCD cameras and image processing techniques to obtain geometric information [41].

For this project the images were captured with either a Rollei d7 metric camera or an Olympus C5060 digital camera. The data was then processed by PhotoModeler software, either PhotoModeler Pro 4 version g or PhotoModeler Pro 5 version 2.2, chapters 7 and 8 contain the results of the models created using photogrammetry, the first pipe experiments were complete with the Rollei camera and PhotoModeler Pro 4 and the remainder of the experiments including all the vehicle models were created with the upgraded camera and software.

6.3 Photographic Geometry

Every photograph represents a two-dimensional perspective projection of the recorded (photographed) three-dimensional object [52]. During projection the third dimension is lost. It is not possible to reconstruct a three dimensional space from a two-dimensional image without assumptions or additional information about the object. That is why photogrammetry requires at least two geometrically different images to reconstruct an object.

6.3.1 Geometry of a Single Photograph

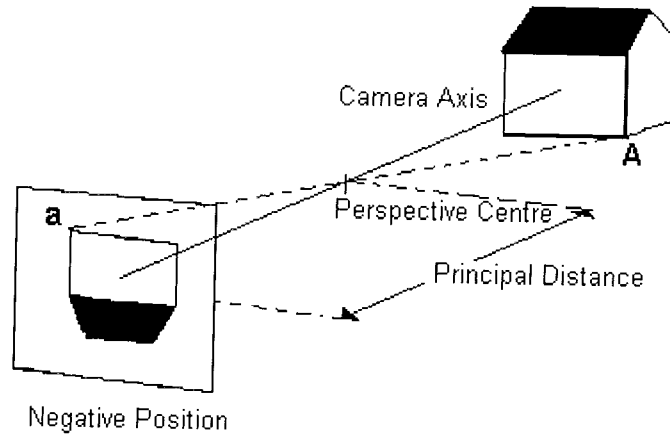


Fig 6.1 Single Photographic Frame Geometry [51]

Figure 6.1 shows a single photographic frame. A single point, the perspective centre, represents the lens of the camera. The distance from the perspective centre to the plane of the image is the principal distance. The distance from the perspective centre to the object point and the focal length of the camera lens determine the principal distance. The image has a negative geometry relative to the object; a right-handed coordinate system in the object space appears left-handed in the negative image. A negative is processed and a photograph is produced, which has the same (positive) geometry as the object.

In a photograph, which is a perspective projection, the scale changes from point to point [52]. This is another reason why measurements cannot be taken from a single photograph.

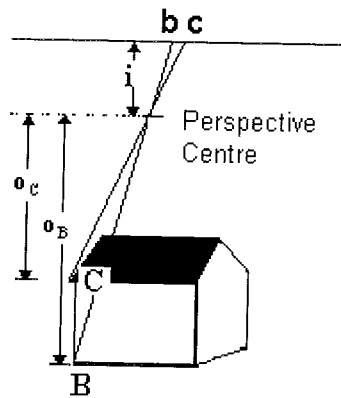


Fig 6.2 Photographic Scale [40]

In figure 6.2, the scale at point C is larger than at point B because B is farther from the perspective centre. The scale of magnification is the image distance (i) divided by the object distance (o_B, o_C), the image distance in a camera is the focal length (f) of the lens.

Therefore the scale at point B is $\left(\frac{f}{o_B}\right)$ and the scale at point C is $\left(\frac{f}{o_C}\right)$ [40].

6.3.2 Stereo Photography

The majority of humans, those capable of viewing with both eyes simultaneously, are said to have binocular vision and their method of judging depth is stereoscopic. Stereoscopic depth perception is of fundamental importance in photogrammetry's development, as it enabled the formation of a three-dimensional model by viewing a pair of over-lapping photographs [40].

When the eyes are focused onto a point the optical axes of both eyes converge onto that point, intersecting at an angle called the parallax angle, which increases with

decreasing distance of the point from the eye. A distance called the eyebase, which for the average adult is between 63 and 69mm, separates the optical axes of the eyes. Figure 6.3 shows the parallax angles ϕ_a and ϕ_b when the eyes are focused on points A and B, distance D_A and D_B from the eyes [40]. The brain automatically and unconsciously associates distance D_A with ϕ_a and D_B with ϕ_b and the distance between these two points is perceived as the difference in these two parallax angles.

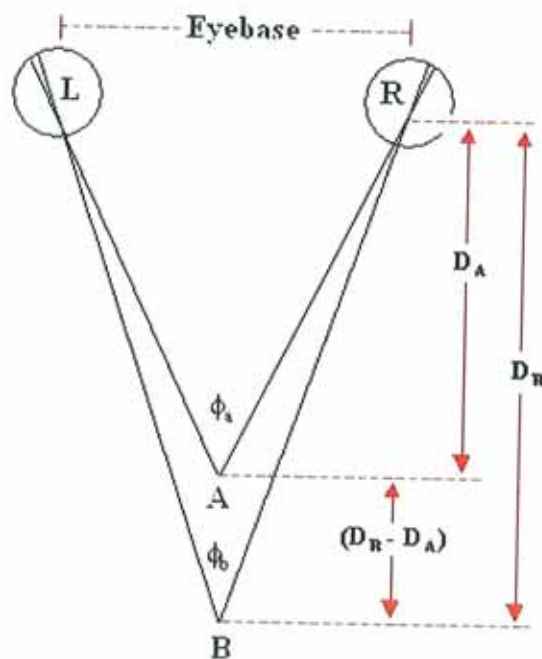


Figure 6.3 Stereoscopic depth perception [40].

In order to create photogrammetric stereomodels the optical geometry in figure 6.3 had to be reproduced. This was achieved by replacing the eyes with two wide-angle lens metric cameras fixed a set distance apart, base distance. The cameras' shutters were tripped simultaneously by a single cable release, to ensure that both cameras capture the object at the same time. The cameras and the base were attached to a tripod and could be raised or lowered and the system was levelled with the levelling head of the tripod. Laussedet developed the first stereo-camera in 1859 [37].

The stereo-camera enabled the geometry of binocular vision to be reproduced, in relation to the camera and object point location. However in order to maximise the effect of stereovision the photographs taken by the cameras needed to be viewed stereoscopically, the photograph taken by the camera on the right by the right eye and the left photograph by the left eye. This difficulty was overcome by the use of stereoscopes.

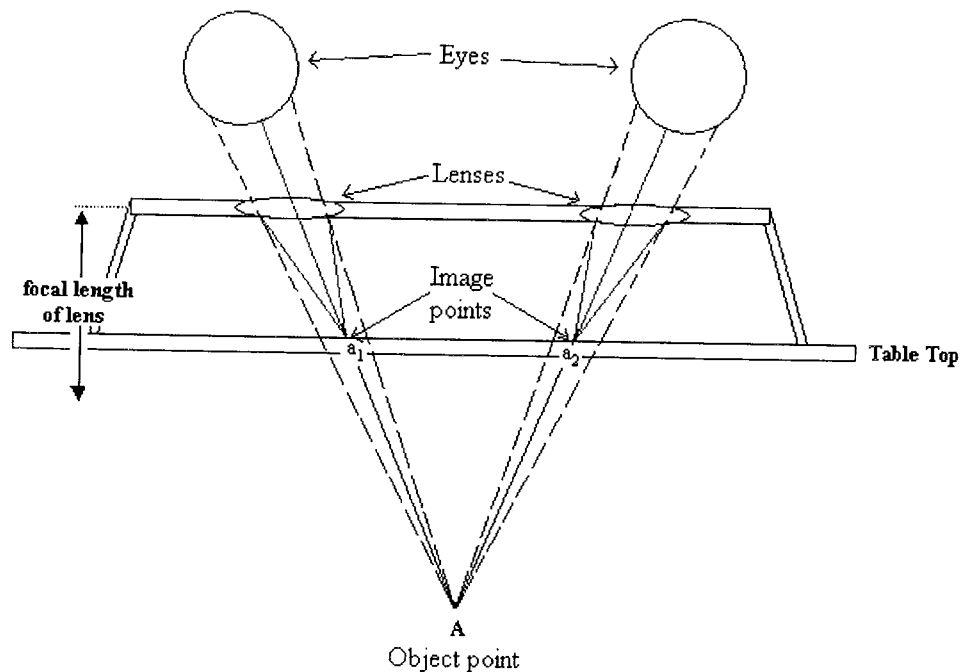


Figure 6.4 Schematic diagram of a stereoscope [40].

In its simplest form, a stereoscope consists of two convex lenses mounted on a frame, figure 6.4 [40]. The photographs are placed on a table, with the common area (overlapping area) slightly less than eyebase apart. The legs of the stereoscope are shorter than the focal length of the lenses. When the stereoscope is placed over the photographs, light rays emanating from points such as a_1 and a_2 (images of the same point on the two photographs) are refracted as they pass through each lens. The eyes

receive these refracted rays and on the basis of the eye focusing associated with these incoming rays, the brain receives the impression that these rays actually originate from a distance greater than that to the tabletop [40].

With advances in computer technology and digital photography, stereoscopic viewing has also advanced. Digital photographs can be polarised and when the viewer wears polarised glasses, the correct eye can then only see the correct photograph. The photographs are displayed on a single computer screen alternating rapidly so that each eye believes it is continuously seeing its photograph.

6.3.3 Geometry of Multiple Photographic Frames

Another phenomenon that allows humans to perceive depth and photogrammetry to recover the third dimension is called parallax. In general linear parallax has two components [40],

$$p_x = x - x'$$

$$p_y = y - y'$$

6.1 a, b

where x, y are the image coordinates on one photograph (generally the left photograph) and x', y' are the image coordinates on the other photograph (generally the right photograph). p_x is the x-parallax, generally in the horizontal direction and p_y is the y-parallax, generally in the vertical direction.

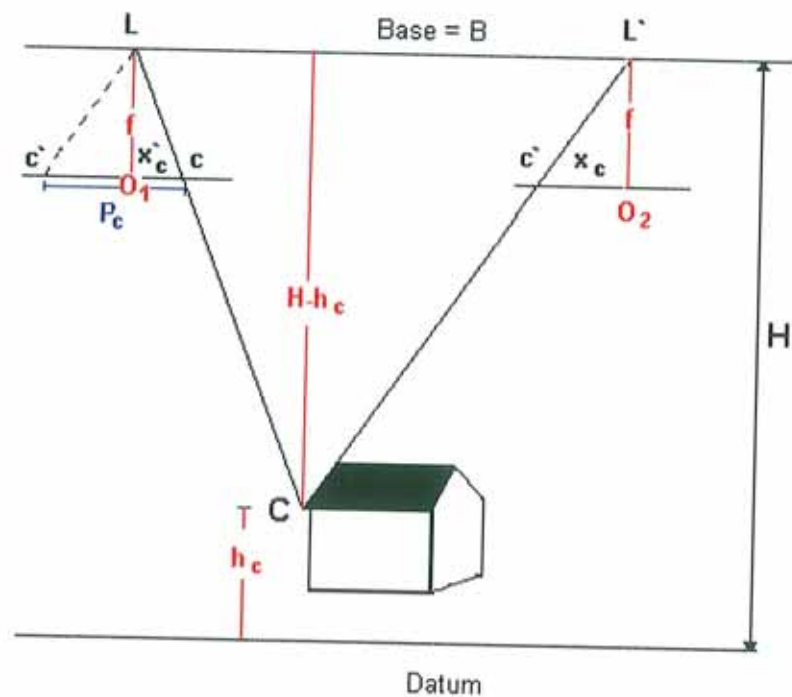


Fig 6.5 Parallax [40]

In figure 6.5 an idealised case is presented, with the photographic images in the positive position (not their true position behind the lens on the photographic paper or CCD chip as the image would be lateral at that position), and with no photographic rotations (the image and object are parallel, there is no tilt on the photograph) and the y-parallax is zero. The lens positions L and L' at the time of photographing are separated by a distance B . The image coordinates are on the positive image position, which is parallel to the base, separated from it by the focal length of the lens.

$$H = \frac{Bf}{p_c} \quad 6.2$$

Where p_c is the distance between the locations of the images of the point C , ($p_c = x_c - x'_c$) and the value H represents the fundamental ability to recover depth or distance from the camera to an object point.

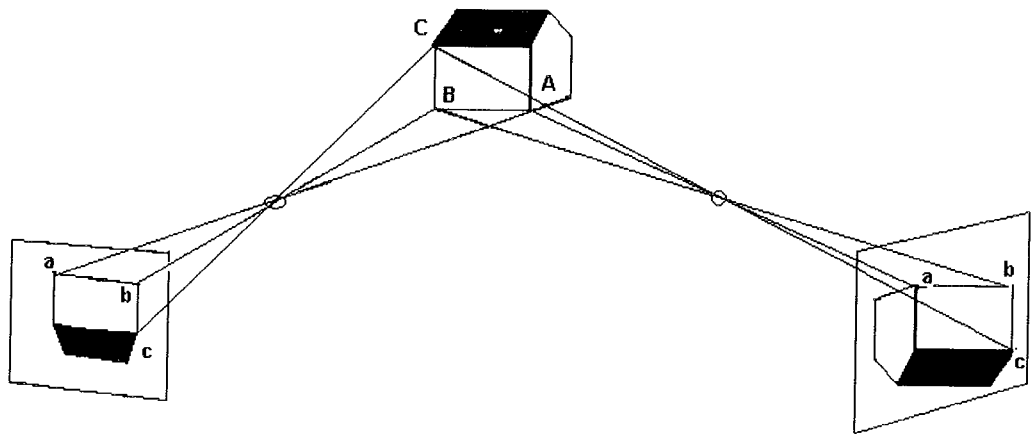


Fig 6.6 Adjacent Camera Locations

The software package being used for this project does not require overlapping photographs but photographs with right angles between each adjacent pair as in figure 6.6. The depth or distance of a point from the camera is found as described in detail in section 6.4.

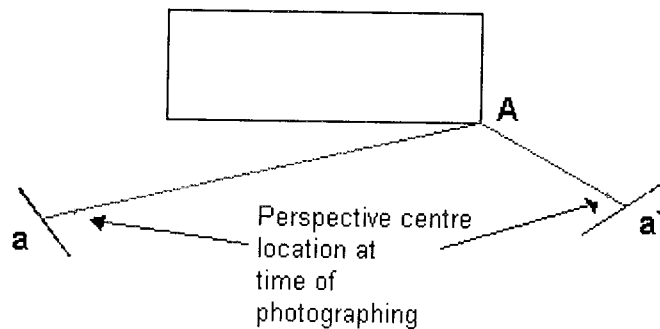


Fig 6.7 Locating point A in 3D space

To find the co-ordinates of point A, the coordinates of the locations of the perspective centre at the time of photographing are used along with the image locations, a and a', to form equations of two straight lines (Figure 6.7); the object point, perspective centre and image point lie on a straight line. This is a simplified version of the treatment of each point of interest captured on the photographic images. Each point on the object

being photographed emits a chief light ray; these are used to develop two equations describing straight lines in space. This pair of equations is called the collinearity equations and will be discussed in more detail in section 6.4.1.

6.3.4 Geometric error of locating a point in space from two photographs

As stated above photogrammetry requires any object point which is to be included on a model to appear in at least two photographs. The operator tags these image points and the photogrammetric software uses these points and the locations of the camera's principal point, when each photograph was taken, to determine the equations of two straight lines running through these points. The point of intersection of these lines is the location of the object point in space. Therefore the object point in space is dependent on the tagging of the image points; any error in tagging the image points results in an error in the calculated location of the object point.

For the purposes of this research, photogrammetry is being used to measure the distance between two points mainly at either end of a plastic pipe or at the front and rear of a vehicle. Measuring the distance between two points in two photographs results in two geometric systems, fig 6.8 and 6.9, as the object points outlining the distances that are to be measured, appear perpendicular or parallel to the common area (area that can be seen in both images) of the adjacent photographs [24].

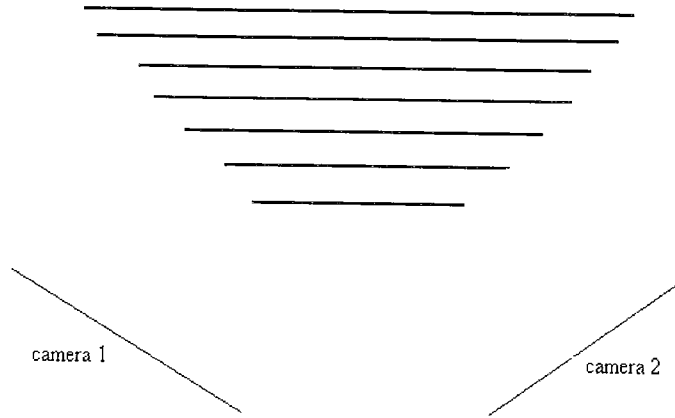


Figure 6.8 “Side on”, object parallel to photographs

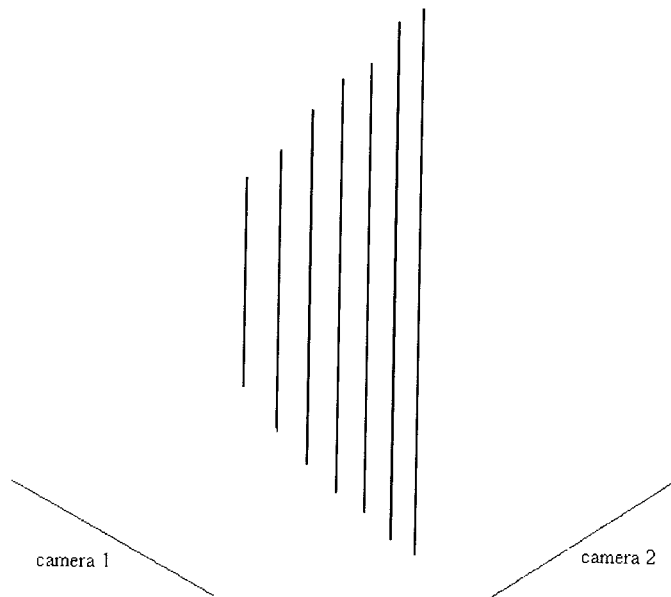


Figure 6.9 “End on”, object perpendicular to photographs

In the perpendicular case, end on, one point is near both photographs, while the other point is further away from both photographs. In the parallel case, side on, each point is near one photograph and further away from the other photograph. The significance of this becomes clear in figure 6.10, which shows the possible area of error around an object point, green dashed line, within which the modelled point could be located when the image points are mis-tagged by the same error to the left and right of the image

point in both photographs. The area of error increases as the object point moves further away from the photographs, even though the size of the mis-tagging does not increase.

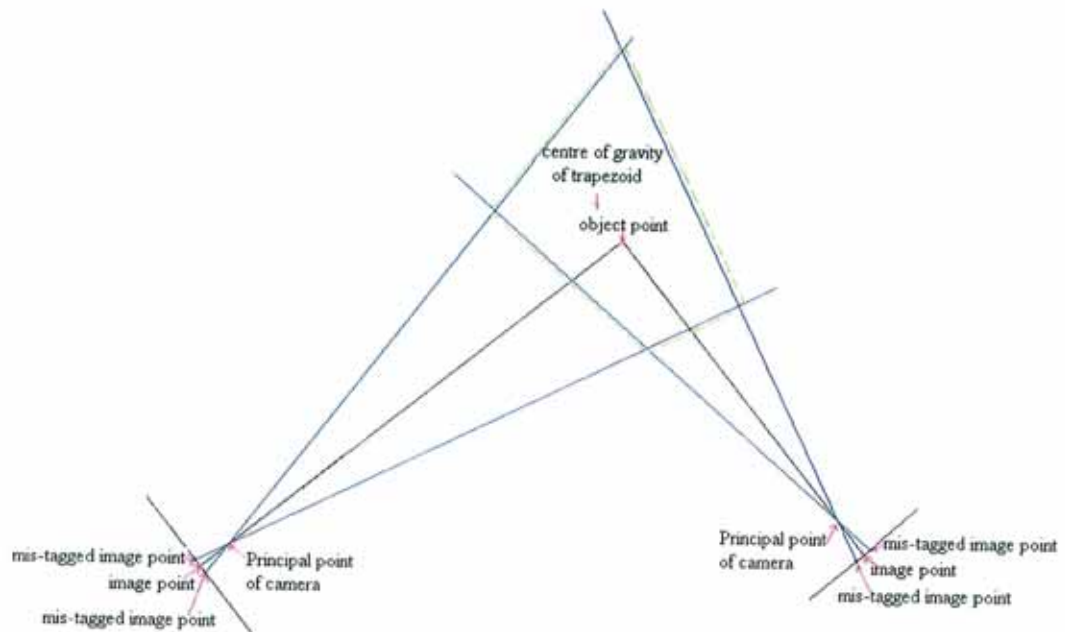


Figure 6.10 Area of possible location of a point in 3D space

However in reality as the object points move away from the photograph, they become more difficult to identify and the operator will have increased difficulty in tagging them. Therefore the size of the mis-tagging error would also increase as the points move away from the photographs, resulting in an even larger area of error, within which the modelled point could be located. The shape formed around the true object point location by the mis-tagging is a trapezoid and the centre of gravity of this shape can be assumed to be the average location of the modelled point, found by repeated tagging and modelling [24]. Thus the photogrammetric software, PhotoModeler, is measuring the distance between the two centres of gravity of the trapezoids corresponding to two object points and one would expect to find that the photogrammetrically measured distance between two points is longer than the actual distance [24]. Also in the end-on case the discrepancy between actual and photogrammetric measurements increases as

the distance between the points gets longer, whereas in the side-on case the discrepancy is constant as the trapezoid shapes formed around both points are similar as each point is near and far from a photograph [24]. This concurs with Fedak [33], he found in his study of the comparison of a total station and photogrammetry that the differences between the total station coordinates and photogrammetry coordinates were highly directionally dependent. The correlation between the coordinates whose axes are similar to the plane of the images was much stronger than between those whose axis was generally perpendicular to the plane of the image.

When modelling objects with complex shapes, placing targets on the surface of the object outlining its profile, guided the operator to the same location in multiple photographs. During the course of this research a number of styles and types of targets were examined, including marks created on the vehicle with non-permanent pens and paper targets of different size, colour and shape. PhotoModeler's subpixel target tagging was also examined, however due to the complex shape of vehicles, subpixel target method was not suitable, the circular targets appeared as eclipses in the photographs and the software could not locate the centre of the target. Therefore it was decided that when preparing a vehicle for photographing, the best procedure was to place triangular targets on the vehicle's surface with the left corner of the target indicating the point of interest that was to be tagged when modelling the vehicle, as the author is right handed. Therefore reducing the possibility of mis-tagging and creating a basis in the geometry of locating the point, as it was the left of the target that was being tagged (if the point was mis-tagged on the image) it would have a negative error, figure 6.11.

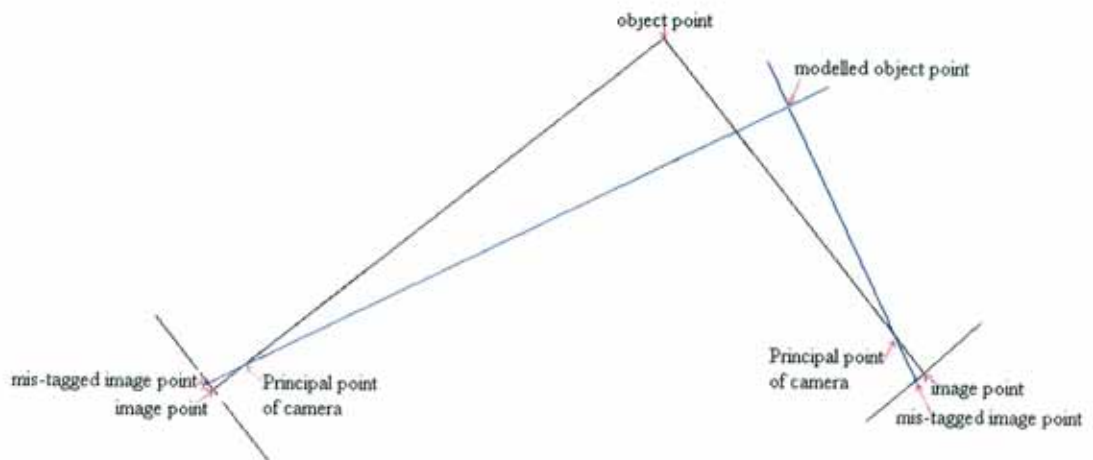


Figure 6.11 Location of mis-tagged object point i.e. modelled object point

This geometric effect was confirmed through experiments carried out using computational model, written in Matlab, a mathematical programming system. This experiment and its results are discussed in the next chapter.

6.3.5 Exterior and Image Orientation

The term ‘exterior orientation’ refers to the position of the camera when the image was taken and to the angular relationship between the image and the object coordinate systems [53]. The object and the image coordinates systems are both right-handed Cartesian coordinate systems. The object coordinates (X, Y, Z) are determined from the measured image coordinates (x, y, z), the z -axis being directed toward the perspective centre; the z coordinate is equal to the principal distance of the camera (figure 6.12)[53]. The principal distance is the distance along the optical axis from the perspective centre to the image plane.

The relationship between image and object coordinates depends on the rotation of the image coordinate system with respect to the object coordinate system and the coordinates of the perspective centre in object space. The rotation of the image coordinate system can be regarded as the three rotations, ω around the X-axis, ϕ around the Y-axis and κ around the Z-axis. The following matrices enable one to convert from the unrotated coordinates to the rotated ones [53];

$$\omega = \begin{pmatrix} 1 & 0 & 0 \\ 0 & \cos\omega & -\sin\omega \\ 0 & \sin\omega & \cos\omega \end{pmatrix} \quad \phi = \begin{pmatrix} \cos\phi & 0 & \sin\phi \\ 0 & 1 & 0 \\ -\sin\phi & 0 & \cos\phi \end{pmatrix} \quad \kappa = \begin{pmatrix} \cos\kappa & -\sin\kappa & 0 \\ \sin\kappa & \cos\kappa & 0 \\ 0 & 0 & 1 \end{pmatrix} \quad \mathbf{6.3 \ a, \ b, \ c}$$

All rotations are defined as positive in the counter clockwise direction. When $\omega=\phi=\kappa=0$, the optical axis is perpendicular to the X – Y plane and the x, y, z axes are parallel to the X, Y, Z axes respectively (figure 6.12).

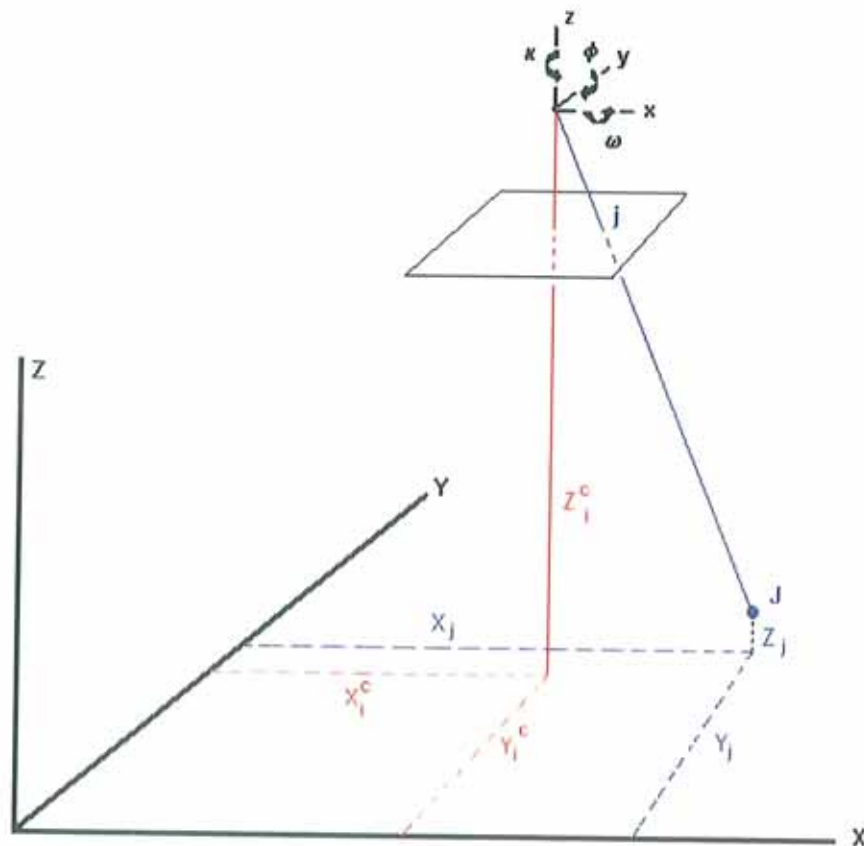


Fig 6.12 Orientation of image space and object space

In figure 6.12, X, Y, Z are the coordinate axes in object space, x, y, z are the axes in image space. ω, ϕ, κ are the rotations around the axes in image space. J is a point in object space and j is its image on photograph i . X_j, Y_j, Z_j are the coordinates of J in object space. X_i^c, Y_i^c, Z_i^c are the object coordinates of the centre point of the image / photograph i [53].

Light travels in straight lines and, assuming all the rays entering a camera through the lens system pass through a single point and that the lens is distortionless, the photograph is a perspective projection (section 6.3.1). A projective relationship exists between the image (photograph) coordinates of the image point and the object coordinates of the object point. Considering the point j on photograph i , this relationship is represented by the following equation [41]:

$$\begin{pmatrix} X_j - X_i^c \\ Y_j - Y_i^c \\ Z_j - Z_i^c \end{pmatrix} = \lambda_{ij} R \begin{pmatrix} x_{ij} - x_p \\ y_{ij} - y_p \\ -f \end{pmatrix} \quad 6.4$$

X_j, Y_j and Z_j are the object space coordinates of the point j . X_i^c, Y_i^c and Z_i^c are the object space coordinates of the centre of the photograph i . x_{ij} and y_{ij} are the image coordinates of the point j on the photograph i . f is the focal length of the lens. x_p and y_p are the coordinates of the principal point, the point where the optical axis of the camera passes through the perspective centre and intersects with the image plane. λ_{ij} is the photograph scale factor at the point j [53]. R is the 3x3 matrix, the product of the matrices ω, ϕ and κ (eqn. 6.3 a, b, c);

$$R = \begin{pmatrix} \cos\phi_i \cos\kappa_i & \cos\omega_i \sin\kappa_i + \sin\omega_i \sin\phi_i \cos\kappa_i & \sin\omega_i \sin\kappa_i - \cos\omega_i \sin\phi_i \cos\kappa_i \\ -\cos\phi_i \sin\kappa_i & \cos\omega_i \cos\kappa_i - \sin\omega_i \sin\phi_i \sin\kappa_i & \sin\omega_i \cos\kappa_i + \cos\omega_i \sin\phi_i \sin\kappa_i \\ \sin\phi_i & -\sin\omega_i \cos\phi_i & \cos\omega_i \cos\phi_i \end{pmatrix} \quad 6.5$$

The projective transformation equations are used to develop the collinearity equations (section 6.4.1) [53].

6.4 Mathematics of Photogrammetry

The most straightforward way to model any physical system is to determine and describe the components involved, and then mathematically express the relationships between them [52]. The mathematical expression of the fact that the object point, the perspective centre and the image point lie on a straight line is the basis of the collinearity adjustment method, as seen in section 6.3.5, which combined with the Bundle method (section 6.4.2) is used by PhotoModeler to solve photogrammetric problems.

6.4.1 Collinearity Equations

The basis of collinearity is that the object point, perspective centre and image point all lie on a straight line. The projective transformation equations are the relationships between image points and object points (section 6.3.5).

$$\begin{pmatrix} x_{ij} - x_p \\ y_{ij} - y_p \\ -f \end{pmatrix} = \frac{1}{\lambda_{ij}} M \begin{pmatrix} X_j - X_i^c \\ Y_j - Y_i^c \\ Z_j - Z_i^c \end{pmatrix} \quad 6.6$$

x_{ij} and y_{ij} are the image coordinates of the point j on the photograph i . f is the focal length of the lens. x_p and y_p are the coordinates of the principal point. λ_{ij} is the photograph scale factor at the point j . X_j , Y_j and Z_j are the object space coordinates of the point j . X_i^c , Y_i^c and Z_i^c are the object space coordinates of the perspective centre of the photograph i [53]. M is the 3x3 matrix, which is R^{-1} ;

$$M = \begin{pmatrix} \cos\phi_i \cos\kappa_i & \cos\omega_i \sin\kappa_i + \sin\omega_i \sin\phi_i \cos\kappa_i & \sin\omega_i \sin\kappa_i - \cos\omega_i \sin\phi_i \cos\kappa_i \\ -\cos\phi_i \sin\kappa_i & \cos\omega_i \cos\kappa_i - \sin\omega_i \sin\phi_i \sin\kappa_i & \sin\omega_i \cos\kappa_i + \cos\omega_i \sin\phi_i \sin\kappa_i \\ \sin\phi_i & -\sin\omega_i \cos\phi_i & \cos\omega_i \cos\phi_i \end{pmatrix}$$

ω_i , ϕ_i , κ_i , are the angles of rotation of photograph 'i' about the x, y and z axes respectively.

These equations reduce to produce the collinearity equations, when the first two equations are divided by the third equation [53]:

$$\begin{aligned} \frac{x_{ij} - x_p}{-f} &= \frac{m_{11}(X_j - X_i^c) + m_{12}(Y_j - Y_i^c) + m_{13}(Z_j - Z_i^c)}{m_{31}(X_j - X_i^c) + m_{32}(Y_j - Y_i^c) + m_{33}(Z_j - Z_i^c)} \\ \frac{y_{ij} - y_p}{-f} &= \frac{m_{21}(X_j - X_i^c) + m_{22}(Y_j - Y_i^c) + m_{23}(Z_j - Z_i^c)}{m_{31}(X_j - X_i^c) + m_{32}(Y_j - Y_i^c) + m_{33}(Z_j - Z_i^c)} \end{aligned} \quad \text{6.7 a and b}$$

Rearranging the above equations (6.7 a and b) produces the two most fundamental equations of analytical photogrammetry, the collinearity equations (6.8 a and b) [53].

$$\begin{aligned} x_{ij} - x_p + \frac{f[m_{11}(X_j - X_i^c) + m_{12}(Y_j - Y_i^c) + m_{13}(Z_j - Z_i^c)]}{m_{31}(X_j - X_i^c) + m_{32}(Y_j - Y_i^c) + m_{33}(Z_j - Z_i^c)} &= 0 \\ y_{ij} - y_p + \frac{f[m_{21}(X_j - X_i^c) + m_{22}(Y_j - Y_i^c) + m_{23}(Z_j - Z_i^c)]}{m_{31}(X_j - X_i^c) + m_{32}(Y_j - Y_i^c) + m_{33}(Z_j - Z_i^c)} &= 0 \end{aligned} \quad \text{6.8 a and b}$$

These two equations describe the orientation and length of the light ray joining the point 'j' on photograph 'i', through the perspective centre of 'i', to the object point 'J' (see Figure 6.12). Every ray of light can be described by two collinearity equations,

therefore a mathematical model of the rays forming a photogrammetric model can be constructed [53].

However before these equations can be used they must be reduced to their linear form.

Let, $x_{ij} = x_{ij}^m + v_{xij}$ and $y_{ij} = y_{ij}^m + v_{yij}$, where x_{ij}^m and y_{ij}^m are the measured image coordinates, v_{xij} and v_{yij} are the corrections need to account for the random error on the measured coordinates [53].

Similarly, let [52] $\omega_i = \omega_i^a + \Delta\omega_i$, $\phi_i = \phi_i^a + \Delta\phi_i$, $\kappa_i = \kappa_i^a + \Delta\kappa_i$, $X_j = X_j^a + \Delta X_j$, $Y_j = Y_j^a + \Delta Y_j$, $Z_j = Z_j^a + \Delta Z_j$, $X_i^c = (X_i^c)^a + \Delta X_i^c$, $Y_i^c = (Y_i^c)^a + \Delta Y_i^c$, $Z_i^c = (Z_i^c)^a + \Delta Z_i^c$ where ω_i^a , ϕ_i^a , κ_i^a , X_j^a , Y_j^a , Z_j^a , $(X_i^c)^a$, $(Y_i^c)^a$ and $(Z_i^c)^a$ are approximations and $\Delta\omega_i$, $\Delta\phi_i$, $\Delta\kappa_i$, ΔX_j , ΔY_j , ΔZ_j , ΔX_i^c , ΔY_i^c and ΔZ_i^c are their corresponding corrections. ^m denotes measurements and ^a denotes approximations.

Assuming these corrections are small and that equations 6.8 a and b are linear over the small intervals between the true values of these parameters and their corresponding approximations, then linearization can be done by Newton's first order approximation as follows [52];

Let

$$F_x = x_{ij} - x_p + \frac{f[m_{11}(X_j - X_i^c) + m_{12}(Y_j - Y_i^c) + m_{13}(Z_j - Z_i^c)]}{m_{31}(X_j - X_i^c) + m_{32}(Y_j - Y_i^c) + m_{33}(Z_j - Z_i^c)}$$

$$F_y = y_{ij} - y_p + \frac{f[m_{21}(X_j - X_i^c) + m_{22}(Y_j - Y_i^c) + m_{23}(Z_j - Z_i^c)]}{m_{31}(X_j - X_i^c) + m_{32}(Y_j - Y_i^c) + m_{33}(Z_j - Z_i^c)}$$

6.9 a and b

Then

$$v_{xij} + \left(\frac{\partial F_x}{\partial \omega_i}\right)^a \Delta\omega_i + \left(\frac{\partial F_x}{\partial \phi_i}\right)^a \Delta\phi_i + \left(\frac{\partial F_x}{\partial \kappa_i}\right)^a \Delta\kappa_i + \left(\frac{\partial F_x}{\partial X_i^c}\right)^a \Delta X_i^c + \left(\frac{\partial F_x}{\partial Y_i^c}\right)^a \Delta Y_i^c$$

$$+ \left(\frac{\partial F_x}{\partial Z_i^c}\right)^a \Delta Z_i^c + \left(\frac{\partial F_x}{\partial X_j}\right)^a \Delta X_j + \left(\frac{\partial F_x}{\partial Y_j}\right)^a \Delta Y_j + \left(\frac{\partial F_x}{\partial Z_j}\right)^a \Delta Z_j + F_x^a = 0$$

$$v_{yij} + \left(\frac{\partial F_y}{\partial \omega_i}\right)^a \Delta\omega_i + \left(\frac{\partial F_y}{\partial \phi_i}\right)^a \Delta\phi_i + \left(\frac{\partial F_y}{\partial \kappa_i}\right)^a \Delta\kappa_i + \left(\frac{\partial F_y}{\partial X_i^c}\right)^a \Delta X_i^c + \left(\frac{\partial F_y}{\partial Y_i^c}\right)^a \Delta Y_i^c$$

$$+ \left(\frac{\partial F_y}{\partial Z_i^c}\right)^a \Delta Z_i^c + \left(\frac{\partial F_y}{\partial X_j}\right)^a \Delta X_j + \left(\frac{\partial F_y}{\partial Y_j}\right)^a \Delta Y_j + \left(\frac{\partial F_y}{\partial Z_j}\right)^a \Delta Z_j + F_y^a = 0$$

6.10 a & b

where F_x^a and F_y^a are the functions F_x and F_y computed with the approximate values, ω_i^a , ϕ_i^a , κ_i^a , $(X_i^c)^a$, $(Y_i^c)^a$, $(Z_i^c)^a$, X_j^a , Y_j^a and Z_j^a [52]. The partial derivatives also use the approximate values. It must be remembered that equations 6.10 a and b are only linear approximations of the exact equations 6.8 a and b. As the approximations near the true values, the difference between equations 6.8 a and b and 6.10 a and b, becomes negligible. Therefore, in computation, the collinearity equations require an iterative solution. The computed corrections (v_{xij} and v_{yij}) from one iteration, are applied to their corresponding approximations and these corrected parameters are then the approximations in the next iteration. The whole iteration process is repeated until the corrections ($\Delta\omega_i$, $\Delta\phi_i$, $\Delta\kappa_i$, ΔX_j , ΔY_j , ΔZ_j , ΔX_i^c , ΔY_i^c and ΔZ_i^c) become negligibly small, or a predefined condition is reached (e.g. $\Delta\omega_i$, $\Delta\phi_i$, $\Delta\kappa_i$ are equal to or less than a predetermined constant) [52] [53].

The software used for this project, PhotoModeler, requires that adjacent pairs of photographs be captured with as close as possible to a 90° angle between them [50] [51]; other requirements of PhotoModeler are given in section 6.4.1. PhotoModeler then has an approximate orientation of these two photographs and uses this and the information about the camera contained in the calibration file, as the first step in the iterative solution of the collinearity equations.

Equations 6.10 a and b can be written in matrix form, as follows [52];

$$\begin{bmatrix} v_{xij} \\ v_{yij} \end{bmatrix} + \begin{bmatrix} b_{11} & b_{12} & b_{13} & b_{14} & b_{15} & b_{16} \\ b_{21} & b_{22} & b_{23} & b_{24} & b_{25} & b_{26} \end{bmatrix} \begin{bmatrix} \Delta\omega_i \\ \Delta\phi_i \\ \Delta\kappa_i \\ \Delta X_i^c \\ \Delta Y_i^c \\ \Delta Z_i^c \end{bmatrix} + \begin{bmatrix} b_{17} & b_{18} & b_{19} \\ b_{27} & b_{28} & b_{29} \end{bmatrix} \begin{bmatrix} \Delta X_j \\ \Delta Y_j \\ \Delta Z_j \end{bmatrix} = \begin{bmatrix} -F_x^a \\ -F_y^a \end{bmatrix} \quad \mathbf{6.11}$$

$$\begin{aligned} b_{11} &= \left(\frac{\partial F_x}{\partial \omega_i} \right)^a, b_{12} = \left(\frac{\partial F_x}{\partial \phi_i} \right)^a, b_{13} = \left(\frac{\partial F_x}{\partial \kappa_i} \right)^a, b_{14} = \left(\frac{\partial F_x}{\partial X_i^c} \right)^a, b_{15} = \left(\frac{\partial F_x}{\partial Y_i^c} \right)^a, b_{16} = \left(\frac{\partial F_x}{\partial Z_i^c} \right)^a, \\ b_{17} &= \left(\frac{\partial F_x}{\partial X_j} \right)^a, b_{18} = \left(\frac{\partial F_x}{\partial Y_j} \right)^a, b_{19} = \left(\frac{\partial F_x}{\partial Z_j} \right)^a \\ b_{21} &= \left(\frac{\partial F_y}{\partial \omega_i} \right)^a, b_{22} = \left(\frac{\partial F_y}{\partial \phi_i} \right)^a, b_{23} = \left(\frac{\partial F_y}{\partial \kappa_i} \right)^a, b_{24} = \left(\frac{\partial F_y}{\partial X_i^c} \right)^a, b_{25} = \left(\frac{\partial F_y}{\partial Y_i^c} \right)^a, b_{26} = \left(\frac{\partial F_y}{\partial Z_i^c} \right)^a, \\ b_{27} &= \left(\frac{\partial F_y}{\partial X_j} \right)^a, b_{28} = \left(\frac{\partial F_y}{\partial Y_j} \right)^a, b_{29} = \left(\frac{\partial F_y}{\partial Z_j} \right)^a \end{aligned}$$

Or simply as;

$$\mathbf{v}_{ij} + \mathbf{B}_{ij} \overset{ce}{\Delta}_i + \mathbf{B}_{ij} \overset{co}{\Delta}_i = \varepsilon_{ij}$$

6.12

Where *ce* denotes corrections to the exterior orientation parameters, and *co* denotes corrections to the object space coordinates, and the elements of ε_{ij} are negligibly small values [52].

In practical use, a number of photographs are taken of the object that is to be modelled. Point 'j' will appear on more than one photograph. Assuming it appears on 'm' photographs, the complete set of collinearity equations generated by its image coordinates on 'm' photographs is [52];

$$\begin{bmatrix} v_{x1j} \\ v_{y1j} \\ v_{x2j} \\ v_{y2j} \\ v_{x3j} \\ \cdot \\ \cdot \\ \cdot \\ v_{xmj} \\ v_{ymj} \end{bmatrix} + \begin{bmatrix} b_{1111} & b_{1112} & \cdot & \cdot & b_{1116} & b_{1211} & \cdot & \cdot & \cdot & b_{1m16} \\ b_{1121} & b_{1122} & \cdot & \cdot & b_{1126} & b_{1221} & \cdot & \cdot & \cdot & b_{1m26} \\ b_{2111} & b_{2112} & \cdot & \cdot & \cdot & \cdot & \cdot & \cdot & \cdot & b_{2m16} \\ b_{2121} & \cdot & \cdot & \cdot & \cdot & \cdot & \cdot & \cdot & \cdot & b_{2m26} \\ \cdot & \cdot & \cdot & \cdot & \cdot & \cdot & \cdot & \cdot & \cdot & \cdot \\ \cdot & \cdot & \cdot & \cdot & \cdot & \cdot & \cdot & \cdot & \cdot & \cdot \\ b_{m111} & b_{m112} & \cdot & \cdot & \cdot & \cdot & \cdot & \cdot & \cdot & b_{mm16} \\ b_{m121} & b_{m122} & \cdot & \cdot & \cdot & \cdot & \cdot & \cdot & \cdot & b_{mm26} \end{bmatrix} \begin{bmatrix} \Delta\omega_1 \\ \Delta\omega_2 \\ \Delta\omega_3 \\ \cdot \\ \cdot \\ \Delta\omega_m \\ \Delta\phi_1 \\ \Delta\phi_2 \\ \cdot \\ \cdot \\ \Delta\phi_m \\ \cdot \\ \cdot \\ \cdot \\ \Delta Z_m^c \end{bmatrix}$$

$$+ \begin{bmatrix} b_{117} & b_{118} & b_{119} \\ b_{127} & b_{128} & b_{129} \\ b_{217} & b_{218} & b_{219} \\ b_{227} & b_{228} & b_{229} \\ \cdot & \cdot & \cdot \\ \cdot & \cdot & \cdot \\ b_{m17} & b_{m18} & b_{m19} \\ b_{m27} & b_{m28} & b_{m29} \end{bmatrix} \begin{bmatrix} \Delta X_j \\ \Delta Y_j \\ \Delta Z_j \end{bmatrix} = \begin{bmatrix} -F_{x1}^a \\ -F_{y1}^a \\ -F_{x2}^a \\ -F_{y2}^a \\ \cdot \\ \cdot \\ -F_{xm}^a \\ -F_{ym}^a \end{bmatrix}$$

6.13

Or simply;

$$\mathbf{v}_j + \mathbf{B}_j^{ce} \Delta + \mathbf{B}_j^{co} \Delta_j = \varepsilon_i$$

6.14

6.4.2 Bundle Adjustment and Complete Collection of Collinearity

Equations

The fundamental basis of the collinearity equations is that the object point, perspective centre and image point all lie on the same straight line. It is the image ray that connects these points. An image (photograph) can be thought of as a bundle of these rays converging at the perspective centre. In section 6.4.1 point 'j' is a point on the images / photographs, but point 'j' is not the only point that would appear and be marked on each of the photographs; all points of interest would be marked. Therefore, assuming that 'n' points appear on 'm' photographs, the complete collection of collinearity equations is [52];

$$\begin{bmatrix} v_{x11} \\ v_{y11} \\ v_{x12} \\ v_{y12} \\ v_{x13} \\ \cdot \\ \cdot \\ \cdot \\ v_{y1n} \\ v_{x21} \\ \cdot \\ \cdot \\ \cdot \\ \cdot \\ v_{xmn} \\ v_{ymn} \end{bmatrix} + \begin{bmatrix} b_{11111} & b_{11112} & \cdot & \cdot & b_{11116} & b_{11211} & \cdot & \cdot & \cdot & b_{11m16} \\ b_{11121} & b_{11122} & \cdot & \cdot & b_{11126} & b_{11221} & \cdot & \cdot & \cdot & b_{11m26} \\ b_{12111} & b_{12112} & \cdot & \cdot & \cdot & \cdot & \cdot & \cdot & \cdot & b_{12m16} \\ b_{12121} & \cdot & \cdot & \cdot & \cdot & \cdot & \cdot & \cdot & \cdot & b_{12m26} \\ \cdot & \cdot & \cdot & \cdot & \cdot & \cdot & \cdot & \cdot & \cdot & \cdot \\ \cdot & \cdot & \cdot & \cdot & \cdot & \cdot & \cdot & \cdot & \cdot & \cdot \\ \cdot & b_{1n111} & b_{1n112} & \cdot & \cdot & \cdot & \cdot & \cdot & \cdot & b_{1nm16} \\ v_{y1n} & b_{1n121} & \cdot & \cdot & \cdot & \cdot & \cdot & \cdot & \cdot & b_{1nm26} \\ v_{x21} & \cdot & \cdot & \cdot & \cdot & \cdot & \cdot & \cdot & \cdot & \cdot \\ \cdot & \cdot & \cdot & \cdot & \cdot & \cdot & \cdot & \cdot & \cdot & \cdot \\ \cdot & \cdot & \cdot & \cdot & \cdot & \cdot & \cdot & \cdot & \cdot & \cdot \\ \cdot & \cdot & \cdot & \cdot & \cdot & \cdot & \cdot & \cdot & \cdot & \cdot \\ \cdot & b_{mn111} & b_{mn112} & \cdot & \cdot & \cdot & \cdot & \cdot & \cdot & b_{mnm16} \\ v_{xmn} & b_{mn121} & b_{mn122} & \cdot & \cdot & \cdot & \cdot & \cdot & \cdot & b_{mnm26} \\ v_{ymn} & \cdot & \cdot & \cdot & \cdot & \cdot & \cdot & \cdot & \cdot & \cdot \end{bmatrix} \begin{bmatrix} \Delta\omega_1 \\ \Delta\omega_2 \\ \Delta\omega_3 \\ \cdot \\ \cdot \\ \Delta\omega_m \\ \Delta\phi_1 \\ \Delta\phi_2 \\ \cdot \\ \cdot \\ \Delta\phi_m \\ \cdot \\ \cdot \\ \cdot \\ \Delta Z_m^c \end{bmatrix} + \begin{bmatrix} b_{11117} & b_{11118} & b_{11119} & b_{11217} & \cdot & \cdot & \cdot & \cdot & b_{11n17} & b_{11n18} & b_{11n19} \\ b_{11127} & b_{11128} & b_{11129} & b_{11227} & \cdot & \cdot & \cdot & \cdot & b_{11n27} & b_{11n28} & b_{11n29} \\ b_{12117} & b_{12118} & b_{12119} & \cdot & \cdot & \cdot & \cdot & \cdot & b_{12n17} & b_{12n18} & b_{12n19} \\ b_{12127} & \cdot & \cdot & \cdot & \cdot & \cdot & \cdot & \cdot & \cdot & \cdot & b_{12n29} \\ \cdot & \cdot & \cdot & \cdot & \cdot & \cdot & \cdot & \cdot & \cdot & \cdot & \cdot \\ \cdot & \cdot & \cdot & \cdot & \cdot & \cdot & \cdot & \cdot & \cdot & \cdot & \cdot \\ b_{1n117} & \cdot & \cdot & \cdot & \cdot & \cdot & \cdot & \cdot & \cdot & \cdot & b_{1nm19} \\ b_{1n127} & \cdot & \cdot & \cdot & \cdot & \cdot & \cdot & \cdot & \cdot & \cdot & b_{1nm29} \\ b_{21117} & \cdot & \cdot & \cdot & \cdot & \cdot & \cdot & \cdot & \cdot & \cdot & b_{21n19} \\ b_{21127} & \cdot & \cdot & \cdot & \cdot & \cdot & \cdot & \cdot & \cdot & \cdot & b_{21n29} \\ \cdot & \cdot & \cdot & \cdot & \cdot & \cdot & \cdot & \cdot & \cdot & \cdot & \cdot \\ \cdot & \cdot & \cdot & \cdot & \cdot & \cdot & \cdot & \cdot & \cdot & \cdot & \cdot \\ \cdot & \cdot & \cdot & \cdot & \cdot & \cdot & \cdot & \cdot & \cdot & \cdot & \cdot \\ b_{mn117} & \cdot & \cdot & \cdot & \cdot & \cdot & \cdot & \cdot & \cdot & \cdot & b_{mnm19} \\ b_{mn127} & \cdot & \cdot & \cdot & \cdot & \cdot & \cdot & \cdot & \cdot & \cdot & b_{mnm29} \end{bmatrix} \begin{bmatrix} \Delta X_1 \\ \Delta Y_1 \\ \Delta Z_1 \\ \cdot \\ \cdot \\ \Delta X_2 \\ \cdot \\ \cdot \\ \cdot \\ \Delta X_n \\ \Delta Y_n \\ \Delta Z_n \\ \cdot \\ \cdot \\ \cdot \\ \Delta X_n \\ \Delta Y_n \\ \Delta Z_n \end{bmatrix} = \begin{bmatrix} -F_{x11}^a \\ -F_{y11}^a \\ -F_{x12}^a \\ -F_{y12}^a \\ \cdot \\ \cdot \\ -F_{x1n}^a \\ -F_{y1n}^a \\ -F_{x21}^a \\ \cdot \\ \cdot \\ \cdot \\ -F_{xmn}^a \\ -F_{ymn}^a \end{bmatrix} \quad \mathbf{6.15}$$

Or simply;

$$\mathbf{v} + \mathbf{B} \overset{ce}{\Delta} + \mathbf{B} \overset{co}{\Delta} = \boldsymbol{\varepsilon} \quad \mathbf{6.16}$$

Using the above complete collinearity equations, three-dimensional coordinates can be found for every point of interest that appears on at least two photographs. All 'n' points do not have to appear on all 'm' photographs. During computation unmarked points are ignored [52].

6.5 PhotoModeler

PhotoModeler® is a Microsoft Windows® program that helps one to extract measurements and 3D models from photographs. By using a camera as an input device, PhotoModeler allows the capture of accurate detail in a very short time. It then organises the model building process as one traces over the photographs on screen [50] [51].

To use PhotoModeler, one or more photographs of a scene or an object are taken. The photographs are displayed on screen and the operator marks each photograph with the mouse, tracing and tagging features of interest. PhotoModeler then combines the data and locates the marked features in three dimensions. The marks become accurately measured points, lines, curves, cylinders or surfaces in a single, unified 3D space. The result is a 3D model that can be transferred to any graphics or CAD program [51].

6.5.1 PhotoModeler Requirements

In order for PhotoModeler to produce a good quality model, a number of requirements must be satisfied when preparing and photographing the object (vehicle) and marking the points of interest on the photographs. Although the PhotoModeler manual gives

guidelines, it was found that if these guidelines were not followed the photogrammetric models did not process, therefore they are listed here as requirements.

As mentioned in section 6.5, PhotoModeler recommends there to be as close as possible to a 90° angle between pairs of adjacent photographs [50] [51]. This assures an optimal starting point for the iterative solution to the collinearity equations. Figure 6.12 shows the recommended locations of the camera for the first four photographs of a vehicle. These first four photographs are enough to create a model of the basic shape of the vehicle; more photographs can later be added to add more detail to the model, if required.

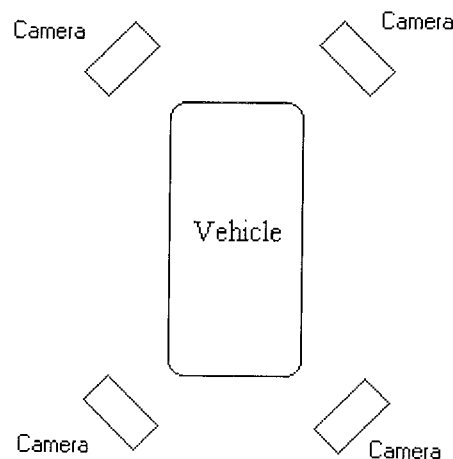


Figure 6.13 Recommended Camera Locations

These locations also ensure that the next requirement is met. Any point of interest that is to be included on the model must appear in at least two photographs [50] [51]. Taking the photographs from the locations indicated in figure 6.13 results in a side and a front or rear of the vehicle being in each photograph, and each side, front and rear appears in two of the initial first four photographs.

The next requirement is the number of common or tie points in adjacent photographs. There must be at least six common points in adjacent photographs [50] [51], in order to solve the collinearity equations. This requirement can be accounted for when preparing the vehicle for photographing by placing at least six targets on the centre area of the sides, front and rear, so that at least six common points are clearly visible in each pair of adjacent photographs. Also at least one common point must appear in all the photographs [50] [51]. Solutions to this requirement are to use the tip of the radio aerial (if it is on the roof of the vehicle) or place a cone on top of the vehicle, and the tip of the cone will be visible in all the photographs. Along with the six common points in each part of adjacent photographs, targets were placed all over the vehicle highlighting points of interest that outlined the vehicle's overall shape and the crush pattern. The targets used were small bright triangles and they were placed on the vehicle in such a manner that the left tip of the triangle was indicating the point that was to be tagged in all the photographs that it appeared in.

In order to scale the model, it is required that the distance between two points on the model be known [50] [51]. For this project a 3m rule was placed next to the vehicle and the ends of this rule were marked and included in the model [25]. After creating the model these two points are selected and PhotoModeler was informed that the distance between them is 3m.

An obvious but fundamental requirement to produce a high quality model, is accurate marking and cross referencing of points of interest on and between photographs. This is the reason why targets are placed on the vehicle before photographing. As vehicle's

surfaces are smooth and curved for better aerodynamics, it is very difficult to definitely identify the corner of the vehicle or points across large relatively flat areas such as the bonnet or doors. Therefore artificial points are added to the vehicle's surface. For this project paper triangles with an adhesive back and bright colours that contrasted with the vehicle's colour, were placed on the vehicle. The operator could then mark an apex of the triangle on each photograph it appeared on and cross-reference these points. This process was repeated for each triangle that had been placed on the vehicle. The targets (triangles) were placed on the vehicle in such a manner as to highlight the vehicle's shape and particular points of interest.

In order to mark the targets accurately, good quality photographs are required. Photographic quality is most affected by the quality of the camera and, in the case of digital photography, the number of pixels in the image. Focus and lighting conditions have a major effect on the quality of the photographs and in turn on the accuracy of the models that are produced from these photographs. Chapter 7 presents the results of experiments to determine the effect of lighting conditions on the accuracy of measurements obtained by photogrammetry and PhotoModeler.

6.5.2 Creating a Model of a Vehicle's Crush Profile

The operator must prepare the damaged vehicle before photographing it, by ensuring there is enough room around the vehicle for the photographer at the positions indicated in figure 6.13, with a full view of the vehicle. Then they must place the targets on the vehicle; the targets should be placed all around the vehicle to outline the vehicle's overall shape and dimensions [54]. Targets are placed at the centres of the wheels,

along the gutter lines, and on the radio aerial. If the radio aerial cannot be seen from all around the vehicle, a cone should be placed on the roof of the vehicle, so that it can be seen from all around the vehicle (as it must appear in all photographs).

Once the photogrammetric models are created they can be viewed from different view points and measurements can be made between any two points on the model. If models of an undamaged and a damaged vehicle of the same manufacture and model are created they can be merged together or superimposed on top of each other in order to measure crush damage. To insure it is possible to superimpose the models, care should be taken when placing the targets on the undamaged area of the damaged vehicle, so that the targets can be placed at the same points on the undamaged vehicle, to insure a good merge of the two models, PhotoModeler's merging process is discussed further in section 6.5.3.

The width of the damaged area should then be divided into equal sections and a target placed at the boundary of each of these sections, at the approximate impact height, generally the bumper height. These targets are then the points $C_1 - C_5$, where crush depth is measured and used to evaluate the pre-impact speed. The 3m rule was placed next to the vehicle, targets at the ends of this rule were used to scale the models of the vehicles.

The operator then photographs the vehicle, ensuring that the camera lens focal length is set at the value for which it was calibrated. Initially photographs should be taken at the positions indicated in figure 6.13. Extra photographs are then taken of the vehicle, especially of the damaged area. The operator must ensure that there is as close as

possible to a 90° angle between adjacent pairs of photographs (the first iteration of the collinearity equations assumes that there is an angle of 90° between pairs of adjacent photographs). The quality of the photographs can be checked on the camera's screen or a laptop if possible. More photographs are then taken if necessary, and the photographs are downloaded to a computer and saved.

The operator must then process the photographs using the photogrammetric software (PhotoModeler). A new PhotoModeler file is opened and the initial first four photographs of the vehicle are imported [51]. A photograph is opened and the apex of each of the targets that are clearly visible in this photograph is tagged. The adjacent photograph is opened and the tagging process is repeated. This is repeated for all the photographs.

The operator then selects the referencing option from PhotoModeler's menu, and two adjacent photographs are opened on screen. The operator clicks on a marked point in one photograph and then finds and clicks on this point in the other photograph. PhotoModeler then gives these two points the same reference ID number [51]. After two adjacent photographs have been cross-referenced, the model is then processed, by clicking on the processing tab. This orients the photographs and gives 3D coordinates to all the points that appear on both photographs. This is repeated for all pairs of adjacent photographs.

Once the photographs have been orientated and all the points of interest have been processed, the model can be viewed in the 3D viewer. It will be the correct shape but not the correct size. The model needs to be scaled. The operator must select the points

marking the ends of the rule and select the scaling tab from PhotoModeler's menu and input the length of the rule, i.e. 3m. The model file is then saved with a distinctive name.

The above steps can be repeated for a vehicle of the same make and design model but undamaged, so that models of the damaged and undamaged vehicles can then be overlaid; to produce a clear model of the damaged sustained by the vehicle during the collision.

6.5.3 Merging of Vehicle Models

As seen in section 3.3, the measurements that are required to estimate the pre-impact speed of a vehicle, are its pre-impact length and the crush depth. The crush depth is the distance (perpendicular to a vehicle's longitudinal or lateral axis) that the pre-impact surface of the vehicle has moved during the collision (chapter 4). Therefore it was felt that the best way of measuring the crush depth was to overlay models of the vehicle before and after the collision. The crush depth could then be seen and measured on one model.

To overlay the before and after models in PhotoModeler, the project merge option is used. Project merge is useful for very large projects with a large number of photographs that are more easily handled as smaller projects, or for projects divided among multiple staff [51], or, in this case, overlaying before and after projects.

In order to merge the before and after models in PhotoModeler, the following steps must be completed; the two models are selected, the order in which they are selected is important as the first model (before collision model) will be the base onto which the other (after collision model) is merged. The key element to merging models is to ensure they share the same coordinate system and scale [51]. Therefore the next step is to perform a coordinate transformation to the models to ensure they are the same. There are three methods of transformation, they are:

‘No Transform’; which as the name suggests, does not perform a transformation, as this method is only used when the models have been created using control points, that have set the same coordinate system for both models [51].

‘Translation’; PhotoModeler does not rotate the models, but translates all 3D data by specified X, Y, Z values. This method is used when both the models have been scaled and rotated, and need to be offset from each other by a known distance [51].

‘Named -- Point Match’; PhotoModeler performs a match between the points on the two models that have the same names (defined by the operator and case sensitive). It computes the best least-squares coordinate system fit (translation, scale and rotation) and applies this transform to the models being merged, i.e. the second model selected (after collision model) [51]. Therefore the scale and rotation on the second model are adjusted from its original. This method is used when there is overlap between the models, but control points were not used. There must be at least four 3D points with the same names for this method to work [51].

The Named-Point Match is the method used to overlay the before and after models of the vehicle. When the operator has created the before and after models, the undamaged area of the after model is examined and the points in this area are given unique names. They then look at the same area on the before model and give the corresponding points the same name as the after model. PhotoModeler matches the models at these points during the merging processes.

The merge is executed and PhotoModeler produces a new model with the after model of the vehicle overlaid onto the before model of the vehicle.

6.5.4 Crush Measurement

The crush profile is viewed in the 3D viewer. There are two methods of measuring crush depth that can be used to find the pre-impact speed. The first method is to divide the width of the damaged area and its original shape (that can be seen on the crush profile) into equal sections, (normally 5 sections) distinguished by points $C_1 - C_6$ on both the undamaged and damaged models of the vehicle. The operator then measures the crush depths, the measurement tab is clicked, C_1 is selected on the damaged and undamaged models and PhotoModeler gives the distances between them. This is the amount C_1 has moved as a result of the collision, the crush depth at C_1 . This is repeated for $C_2 - C_6$. These measurements are then averaged to give the mean residual crush depth. For the second method a single measurement is taken along the central line of the bullet vehicle and also along this line when the two vehicles are fitted together at their point of impact. The pre-impact length and width of the vehicle can also be

measured from the model. These measurements are then used in the crush energy formulae to estimate the energy absorbed and the pre-impact speed (section 3.3) or in a crash simulation package such as PC-Crash or ED-Crash. Chapter 8 presents results of photogrammetric models of vehicles created.

Chapter 7 TEST PROGRAMME

This chapter describes the tests that were carried out to evaluate the accuracy of digital photogrammetric modelling using the software chosen for this project (PhotoModeler), and the results of the tests. The following are the objectives of the test programme:

- Determination of the effect that the process of creating a photogrammetric model has on the accuracy of the measured dimensions of the object.
- Determination of the accuracy with which PhotoModeler can measure simple objects through;
 - Comparison of dimensions measured with PhotoModeler, a Tape measure and a Coordinate Measuring Machine (CMM).
 - Comparison of dimensions in the order of magnitude of a vehicle's dimensions measured with PhotoModeler and a Tape measure.
- Determination of the effects of different lighting conditions on modelling accuracy.
- Determination of the repeatability of modelling with PhotoModeler.

7.1 Computational Study of Photogrammetric Modelling Process

The coordinates of a point on a model are the coordinates of the point of intersection of two straight lines running from the images of the point on the photographs through the principal point of the camera (chapter 6). Any error in selecting the image of the point on the photograph results in an error in the location of the point on the model (section 6.3.4). Therefore it is good practice to place highly visible targets on the object to highlight the points of interest. Throughout this research triangular targets were placed

on the objects being modelling with the left tip of the target (the author being right-handed) indicating the point of interest.

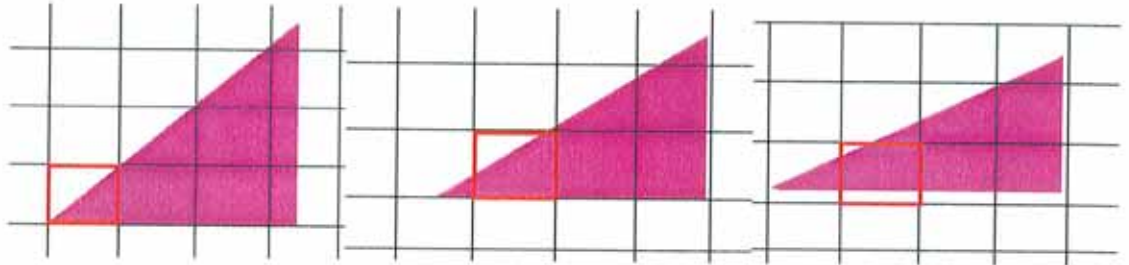


Figure 7.1 Images of targets.

Figure 7.1 shows images of target used on a grid of pixels and some of the possible locations of the left tip of the target that is to be tagged. The red boxes outline the pixels which would be recognised as the left tip as they are the first pixels to contain 50% or more of the target colour. As it was the left of the triangular target that was being tagged in the photographs, the pixel containing 50% or more will be either the true pixel location of the tip or the pixel to the right of the tip on the object. The images shown in figure 7.1 are positive images of the object. While in the geometrical mathematics of calculating the equation of the straight line from the image point through the principal point of the camera to the object point; it is the location of the image point on the negative that is used. Therefore it is the reverse of the images shown and the error in selecting the image point on the photograph of the target is in the negative direction away from the true location of the image point. This error is referred to as “mis-tagging”.

For the purposes of this research, it is the distance between two points that is of interest. In general when two points are viewed from two photographs, there are two geometrical

set ups (section 6.3.4); the distance between the points is measured along a straight line parallel (“side-on”) or perpendicular (“end-on”) to the common area of the photographs. Figure 7.2 shows the set up for the “side-on” case and figure 7.3 for the “end-on” case, and the location of the incorrect object point, the modelled point, when the image point is mis-tagged [24]. The object points and the distance between them are shown in red and the modelled point and the distance between them are shown in green.

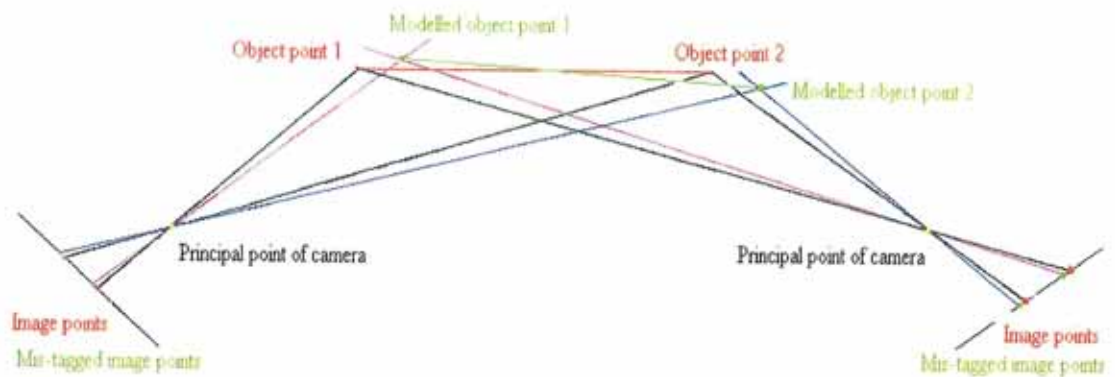


Figure 7.2 Object points 1 and 2, and Modelled object points 1 and 2 are parallel to the common view of two photographs, “Side-on”

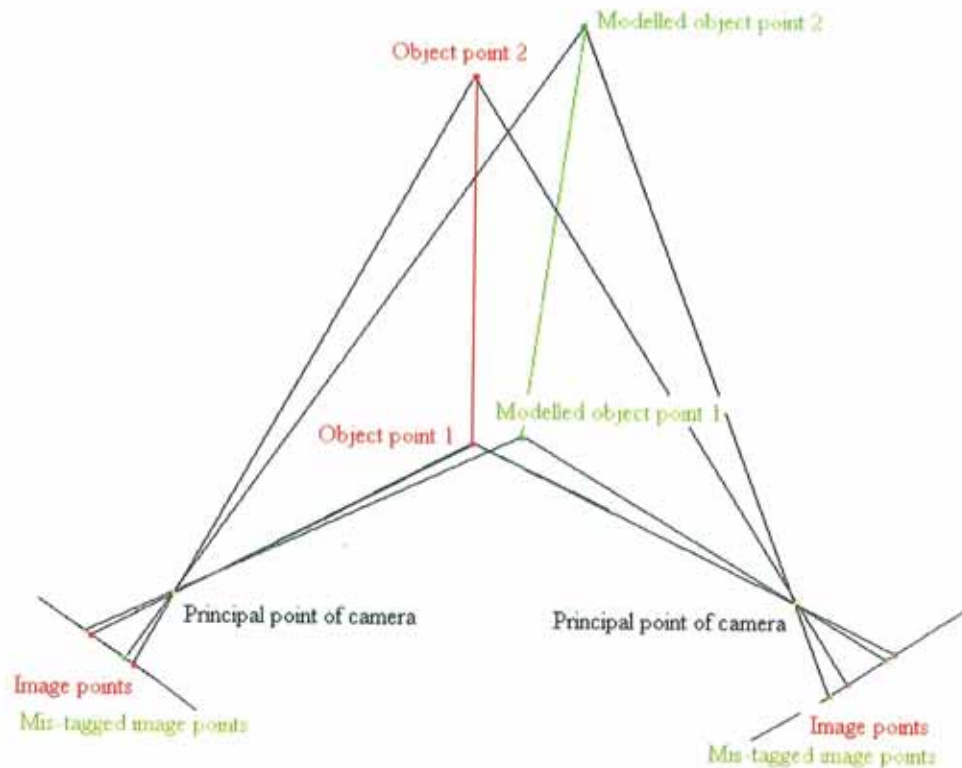


Figure 7.3 Object points 1 and 2, and Modelled object points 1 and 2 are perpendicular to the common view of two photographs, “End-on”

A programme (appendix A) was written in Matlab, a numerical computing environment and programming language, to carry out the calculations to find the point of intersection of the two lines running from the image points through the principal point of the camera, i.e. the location of the object point, and the points of intersection of the lines that run from the mis-tagged image points through the principal point of the camera, i.e. the modelled object point. The main points to note are that the principal point of the first camera location is fixed, as is the focal length of the camera, the angles of both image planes and the orientations of the camera are randomly generated, as are the object points and the distances between them. The size of the mis-tagging error is randomly chosen to be either -1, -2 or -3 pixels from the true image of the object. The negative error arises from the protocol of selecting the left of the targets placed on the

object being modelled. The programme calculates the distance between the object points, that is the actual length, and the calculated length is the distance between the two modelled object points. The difference between the actual and calculated lengths will be referred to as the computational difference, throughout this chapter. The programme was run, to return 10000 lengths, the distances between two object points, for both side-on and end-on situations [24]. Figure 7.4 shows a graph of the computational differences (calculated – actual lengths) plotted against the actual distances between the two object points for the side-on situation. Figure 7.5 shows a graph of the mean computational differences of these measurements, when the data obtained from the computational model programme is split into 100 bins of 40mm and the mean value of the data within each bin is found.

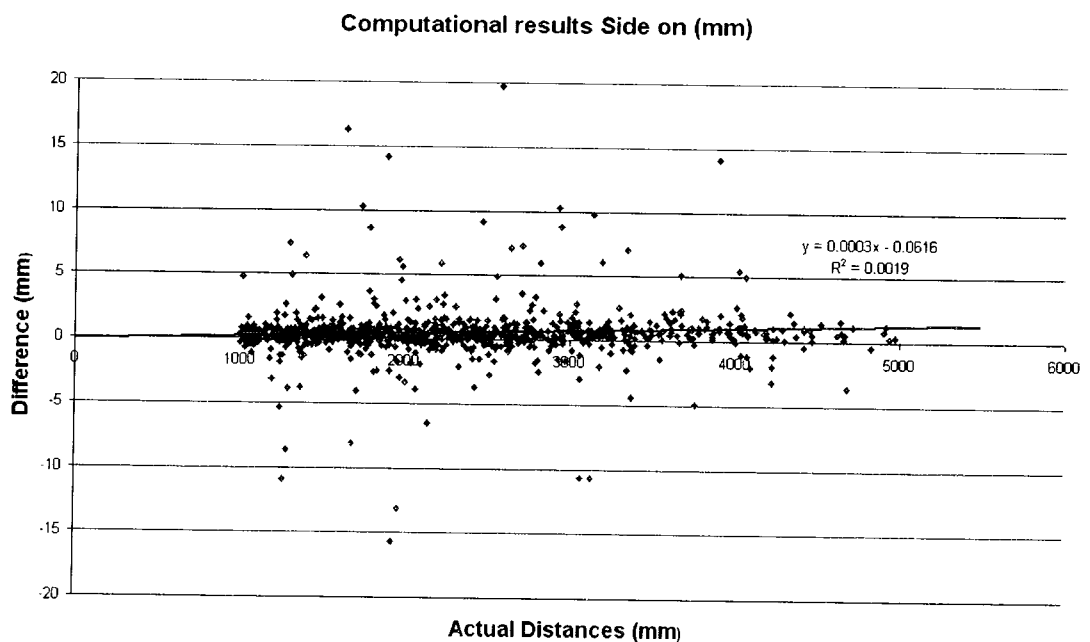


Figure 7.4 Graph of Computational Model generated results for Side-on situation, the positive trend in the results shows that the lengths computed by the computational model are longer than the actual lengths

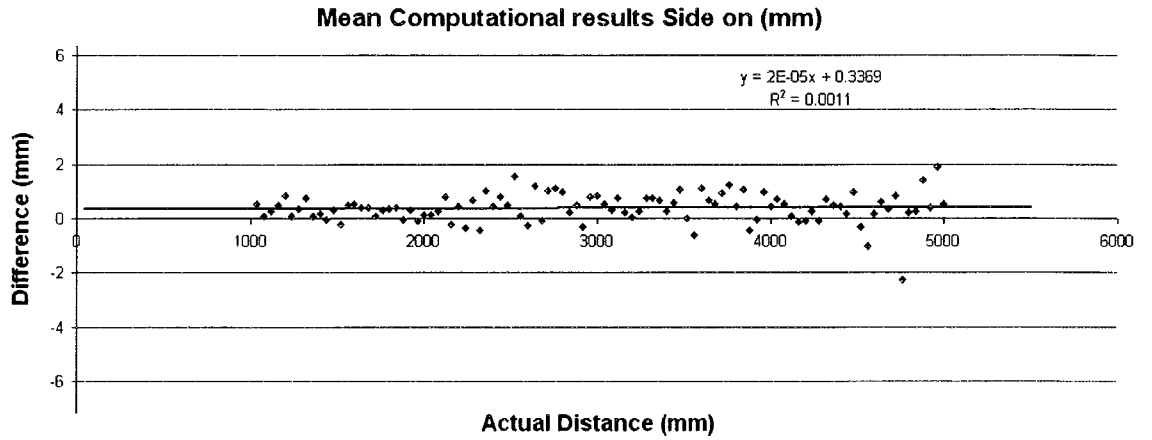


Figure 7.5 Mean Computational Model results generated for Side-on situation, the positive trend in the results shows that the lengths computed by the computational model are longer than the actual lengths

Figure 7.6 shows a graph of the computational differences plotted against the actual distances between the two object points for the end-on situation. Figure 7.7 shows a graph of the mean computational differences for these measurements, when the data obtained from the computational model programme is split into 100 bins of 40mm and the mean value of the data within each bin is found.

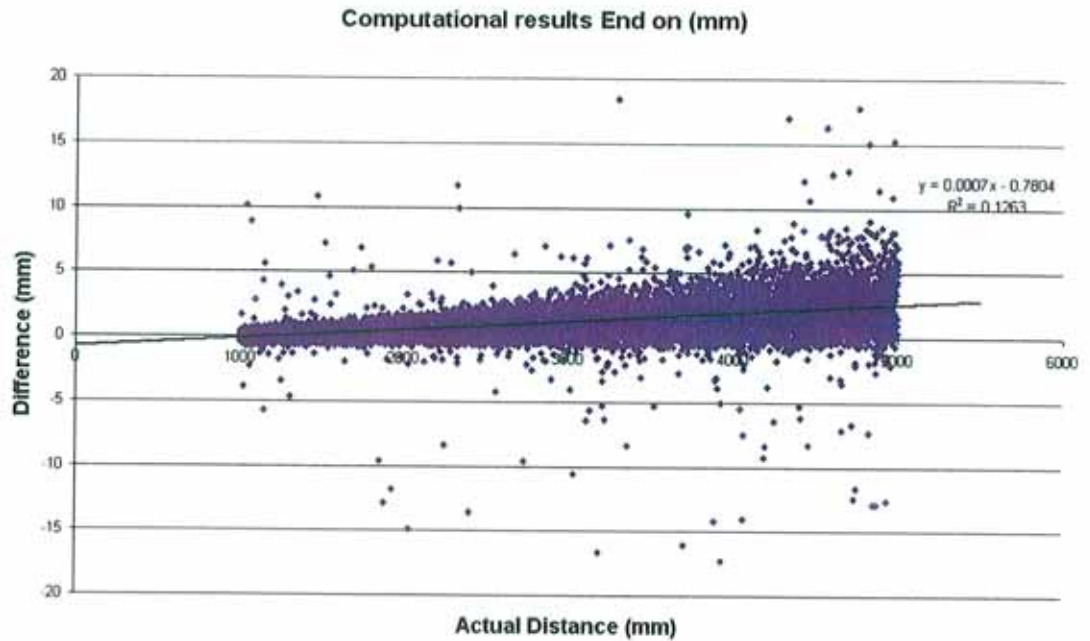


Figure 7.6 Graph of Computational Model generated results for End-on situation, the positive increasing trend in the results shows that the lengths computed by the computational model are longer than the actual lengths and the difference between the two gets larger as the actual length increases

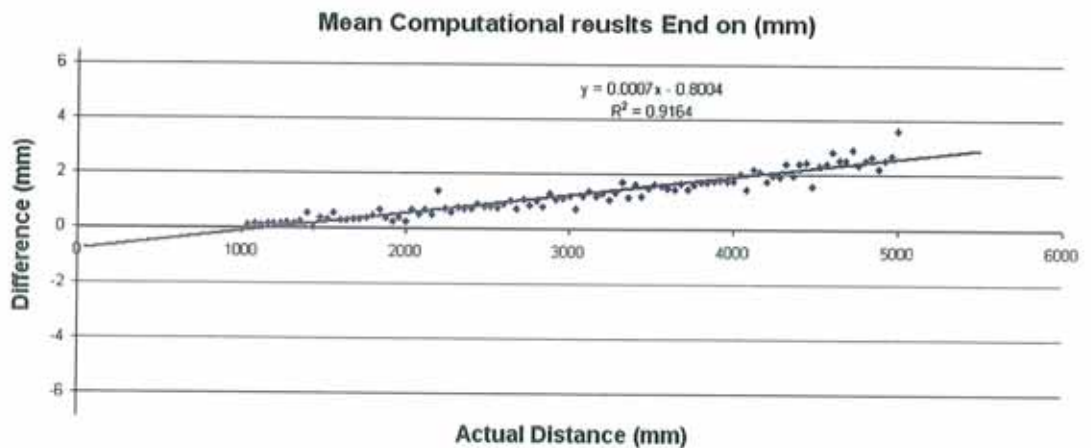


Figure 7.7 Mean Computational Model results generated for End-on situation, the positive increasing trend in the results shows that the lengths computed by the computational model are longer than the actual lengths and the difference between the two gets larger as the actual length increases

The results from the End-on case have a noticeable trend that increases as the actual distance between the points increases. This is caused by the fact that as an object point moves further away from the two camera locations, the difference between the true and the modelled location of the object increases. In the Side-on case, this increasing trend does not occur, because as the object moves away from one photograph it moves closer to the other photograph.

When the mean graphs are viewed, it is clearer and easier to see that the error associated with mis-tagging results in the distance between points on a PhotoModeler model being measured longer than the actual distance, when the points are modelled from two photographs (the trend lines are above zero). Therefore as a result of geometry and selecting the pixel(s) left of the target highlighting points of interest, PhotoModeler measures lengths that are longer than their true values [24]. The following experiments were carried out, to see if this is true in practical use and to establish the accuracy to which a length can be photogrammetrically measured.

7.2 Photogrammetric Measurement of Simple Objects

As stated previously to create a model of an object with PhotoModeler, the operator must tag all the points of interest that are to be included in the model in all the photographs in which they appear and cross reference them. The more precisely the operator tags the locations of the points, the better the quality of the model that will be produced.

For the purposes of this experiment a simple object is defined as an object whose entire outline / profile is clearly visible in each of the photographs taken to create the model. Hollow pipes arranged in different configurations were chosen. In order to ensure the same point was always being tagged at the ends of the pipes in all the photographs, targets were placed at the ends of each of the pipes being modelled (fig 7.8). When the pipes were being measured by other methods (Coordinate Measuring Machine, tape measure) the targets were still in place and also used to define the ends of the pipes by these other measurement methods.



Figure 7.8. Target at end of pipe.

7.2.1 Short Pipes (Range 0.5m – 1m)

In this experiment the actual lengths of the pipes were measured using a Coordinate Measuring Machine (CMM). Five pipes of different lengths (given in table 7A) were attached to a frame (fig 7.9). Targets were placed at the ends of each of the pipes to ensure the same point was marked in all four photographs of the arrangement of pipes [24] [55].

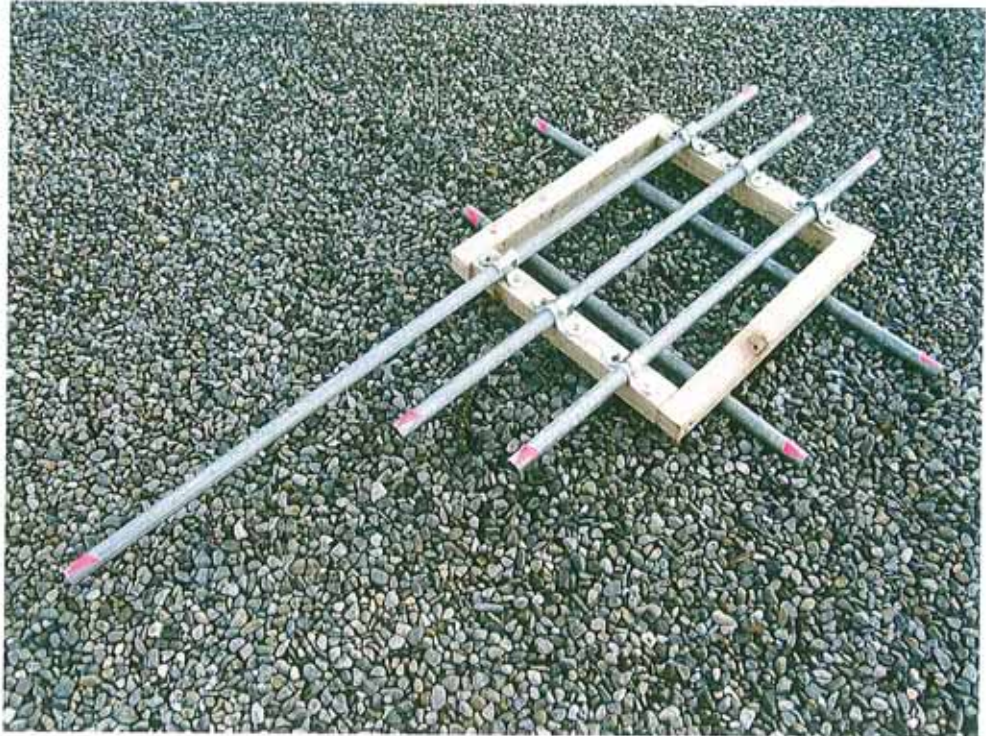


Figure 7.9. Pipes of various lengths attached to frame.

Mr. Jim O'Donnell of the National Metrology Laboratory, Enterprise Ireland, Glasnevin, Dublin 9 made the CMM measurements. The CMM has a measurement accuracy of one micron, 1×10^{-6} m [56]. The pipes were placed on the table of the CMM (fig 7.10). The size of the table restricted the lengths of the pipes that could be used, whereas the experiment detailed in section 7.2.2, used pipes equivalent in length to a vehicle's dimensions. The coordinates of the targets at the ends of the pipes were found. Then using coordinate geometry (straight-line distance between two points), the lengths of the pipes were found. These lengths are the "Actual Lengths" in table 7A [24] [55].

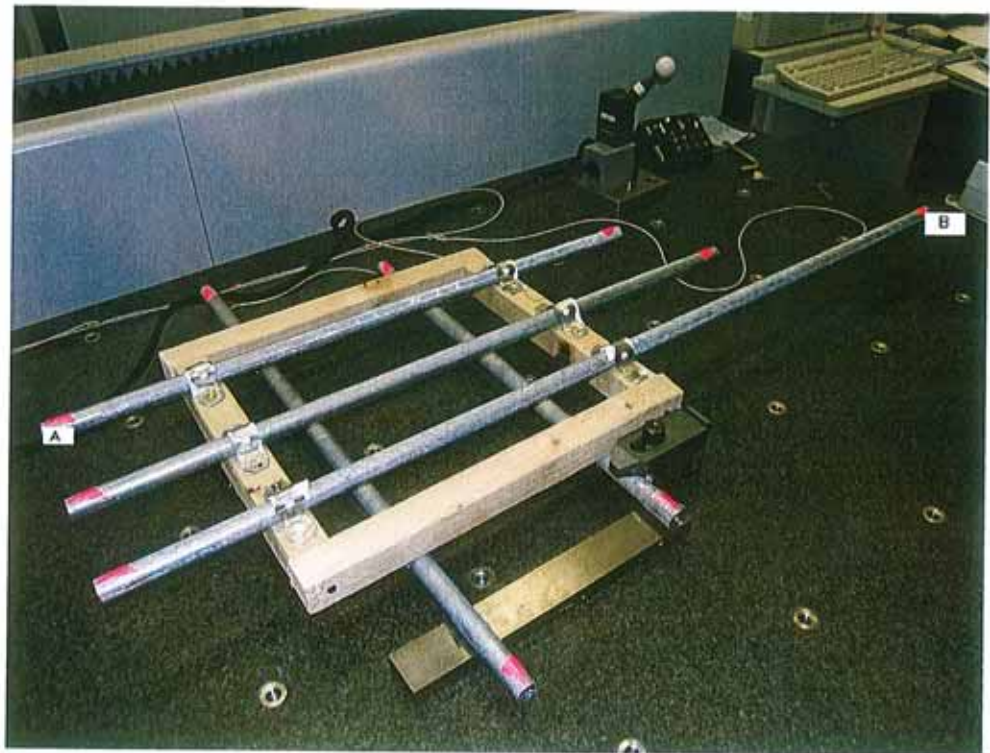


Figure 7.10. Pipes on table of CMM

Ten models of the pipes were then created in PhotoModeler using the same four photographs to create each model in order to allow for random error in the tagging of

points on a photograph. Points A and B marked in figure 7.10, have the largest distance between them, of all the points in the model. Therefore using their coordinates as found by the CMM and coordinate geometry, the distance between these points was found and used to scale each of the models. The length of each of the pipes was found in each of the models and these lengths averaged for the ten models. These average lengths are given in table 7A under PhotoModeler Length. The pipes were also measured ten times each using the tape measure and the averages of these lengths are given in table 7A, under Tape Length.

Actual Length /mm (CMM)	Average PhotoModeler Length /mm	Average Tape Length /mm
1101.479	1101.2	1101
764.057	763.9	764
702.302	702.3	702
680.560	680.2	680
553.381	552.7	553

Table 7A. Comparison of results for different methods of measuring.

7.2.1A PhotoModeler and Coordinate Measuring Machine

Figure 7.11 is a plot of the ten values found for each pipe from each of the ten PhotoModeler models plotted against the actual lengths of the pipes as found by the Coordinate Measuring Machine.

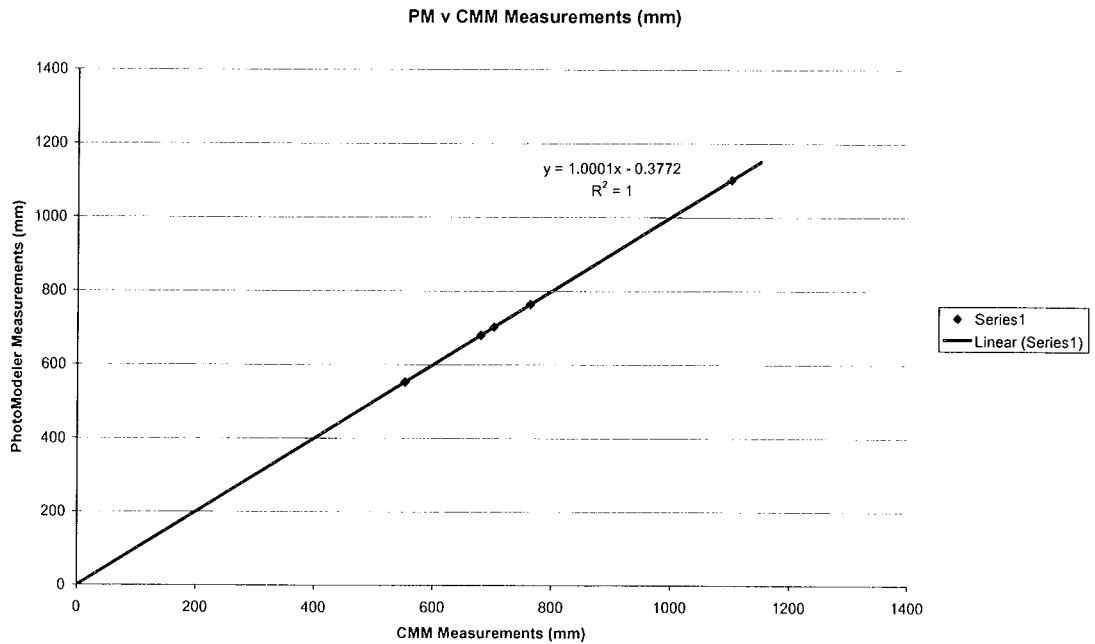


Figure 7.11 Plot of PhotoModeler measurements (PM) against the Coordinate Measuring Machine measurements (CMM)

Linear regression analysis of this data produces a slope of 1.0001, with a 95% confidence range of 0.9994 – 1.0009, and a P-value of 1.3×10^{-125} . The P-value is the probability of the slope value being by chance. A slope value of one and a P-value of zero means that the values on the x and y axes are equal. Therefore the regression confirms there is no statistically significant difference in the measurements obtained by a CMM and from a photogrammetric model [24].

Figure 7.12 is a plot of the differences between the PhotoModeler and the Coordinate Measuring Machine measurements (PM – CMM), plotted against the Coordinate Measuring Machine measurements. The differences are shown in blue and the mean difference for each length of pipe is shown in pink.

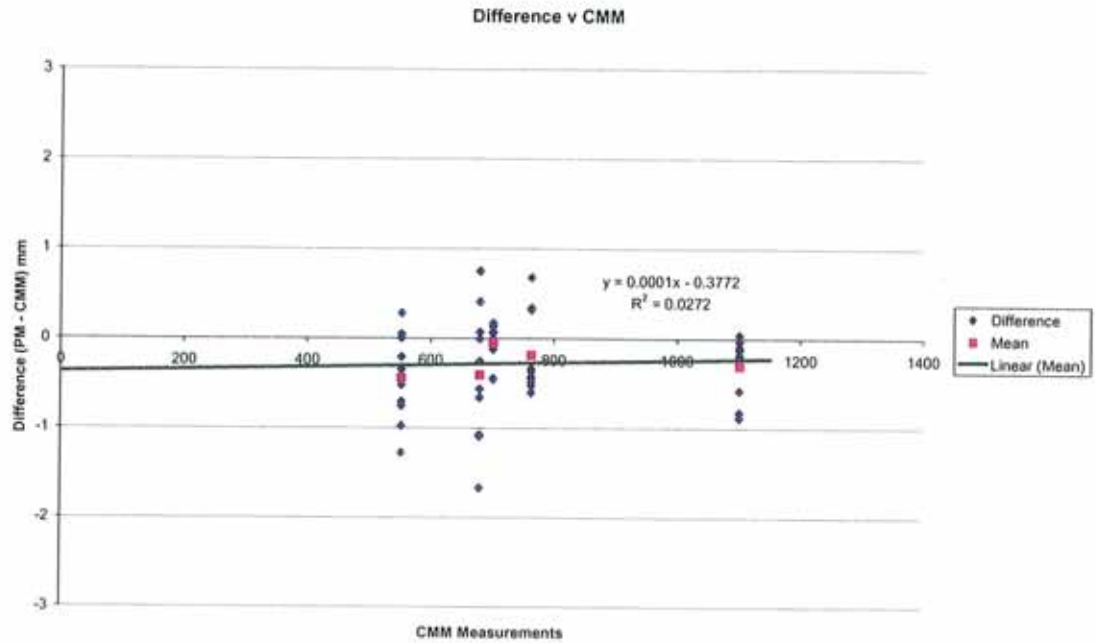


Figure 7.12 Plot of Difference (PM – CMM) against CMM measurements.

Linear regression analysis of this data gives a slope of 0.0001 and a 95% confidence range of -0.0006 – 0.0009. Therefore the accuracy of measurement with PhotoModeler is independent of length. However the mean value for the difference is statistically significant. For the fifty PhotoModeler measurements compared to the Coordinate Measuring Machine measurements the mean difference is -0.27mm and the standard deviation is 0.49mm. A t-test returned a value of -4.015. Therefore in this test experiment PhotoModeler produces a result that is less than the true (CMM) value of a length. The negative intercept value in the equation of the regression of figure 7.11, confirms that the difference between PhotoModeler and CMM is negative. Figures 7.13 A and B respectively show the histogram of the frequency and the cumulative distribution of the differences between PhotoModeler and Coordinate Measuring Machine measurements, showing that the data is normally distributed.

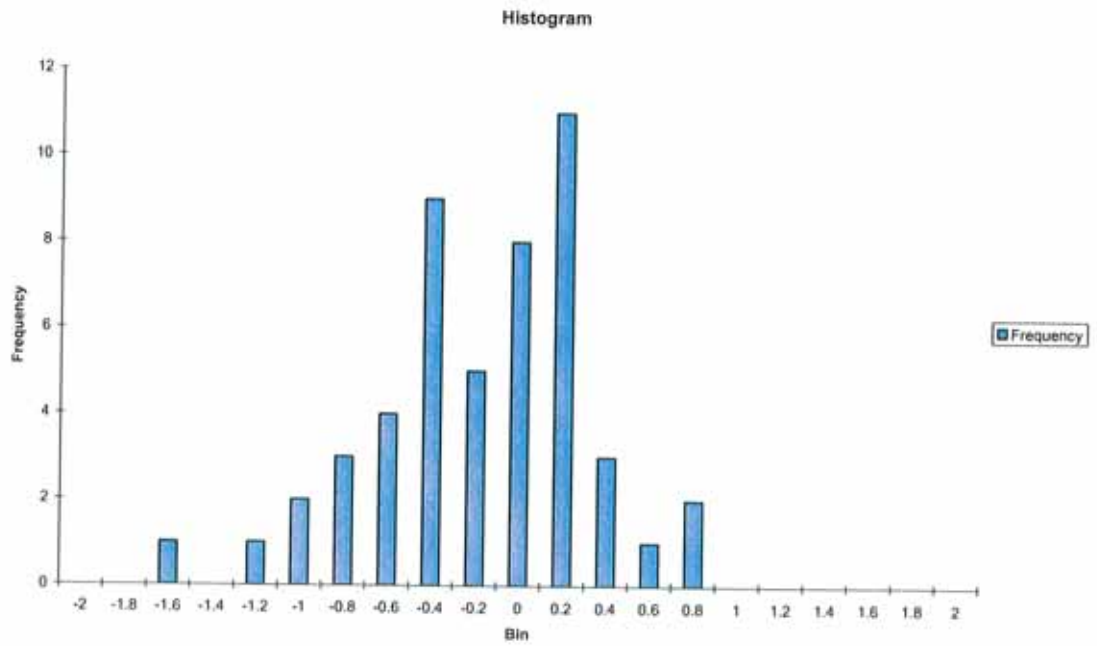


Figure 7.13A Frequency Histogram of Differences (PhotoModeler – CMM measurements)

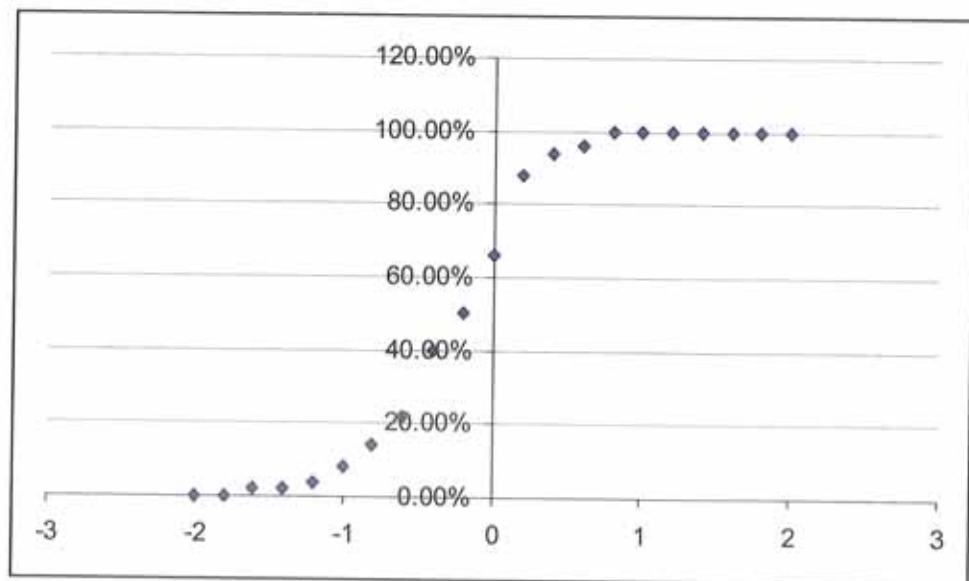


Figure 7.13B Cumulative Distribution of Differences (PhotoModeler – CMM measurements)

7.2.1B Tape measurements and Coordinate Measuring Machine

Figure 7.14 is a plot of the ten values found for each pipe using Tape measurements plotted against the actual lengths of the pipes as found by the Coordinate Measuring Machine.

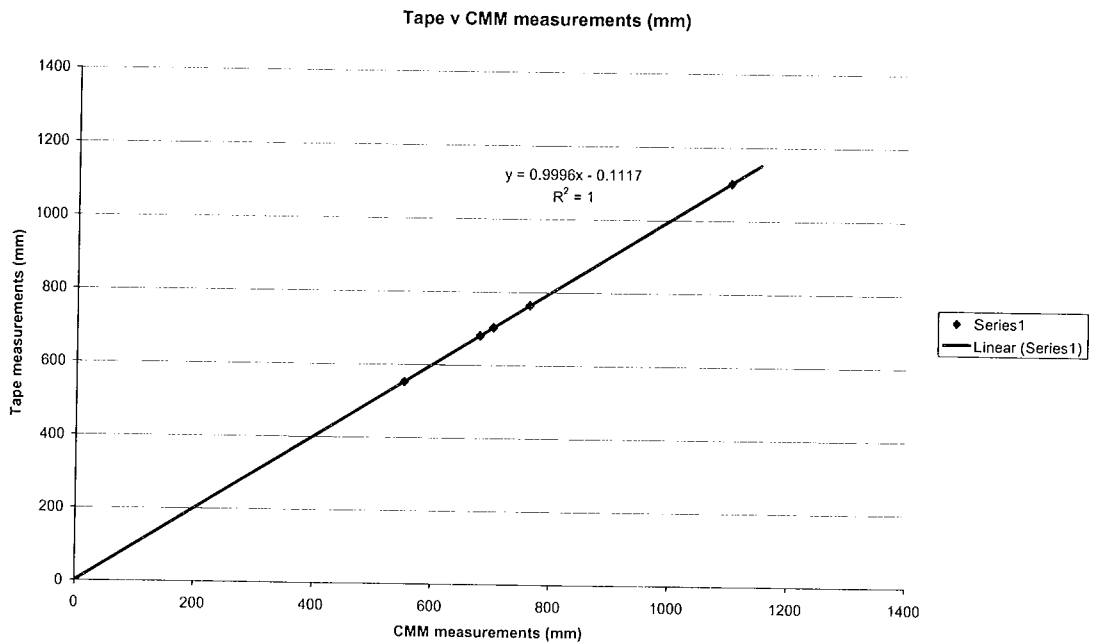


Figure 7.14 Plot of Tape measurements against the Coordinate Measuring Machine measurements (CMM)

Linear regression analysis of this data produces a slope of 0.9996, with a 95% confidence range of 0.9999 – 1.0002, and a P-value of 7.915×10^{-115} . Therefore the regression confirms there is no statistically significant difference between the measurements obtained by a CMM and a tape measure [24].

Figure 7.15 is a plot of the differences between the tape and the Coordinate Measuring Machine measurements (Tape – CMM), plotted against the Coordinate Measuring

Machine measurements. The differences are shown in blue and the mean difference for each length of pipe is shown in pink.

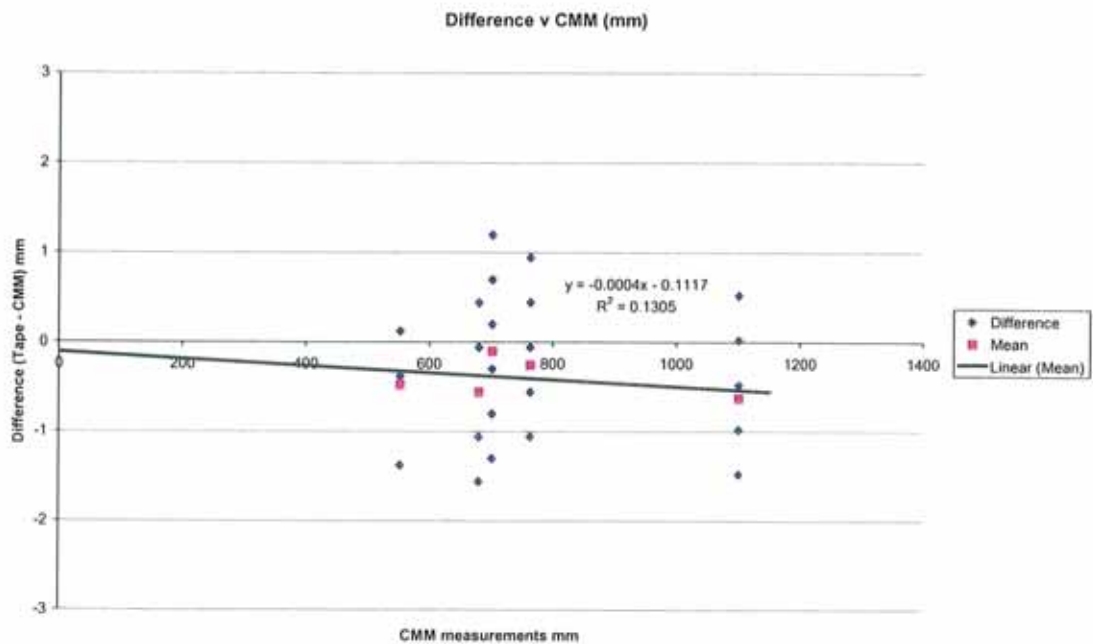


Figure 7.15 Plot of Difference (Tape – CMM) against CMM measurements.

Linear regression analysis of this data gives a slope of -0.0004 and a 95% confidence range of -0.0003 – 0.0018. Therefore measuring with Tape is independent of length. However in this case the mean value for the difference is insignificant. For the fifty tape measurements compared to the Coordinate Measuring Machine measurements the mean difference is -0.06mm and the standard deviation is 0.71mm. A t-test returned a value of -0.64. Therefore tape measurements and Coordinate Measuring Machine measurements of the same length are equal. The negative intercept value in the equation of the regression of figure 7.14, confirms that the difference between tape and CMM is negative. Figures 7.16 A and B respectively show the histogram of the frequency and the cumulative distribution of the difference between tape and Coordinate Measuring Machine measurements, again showing that the data is normally distributed.

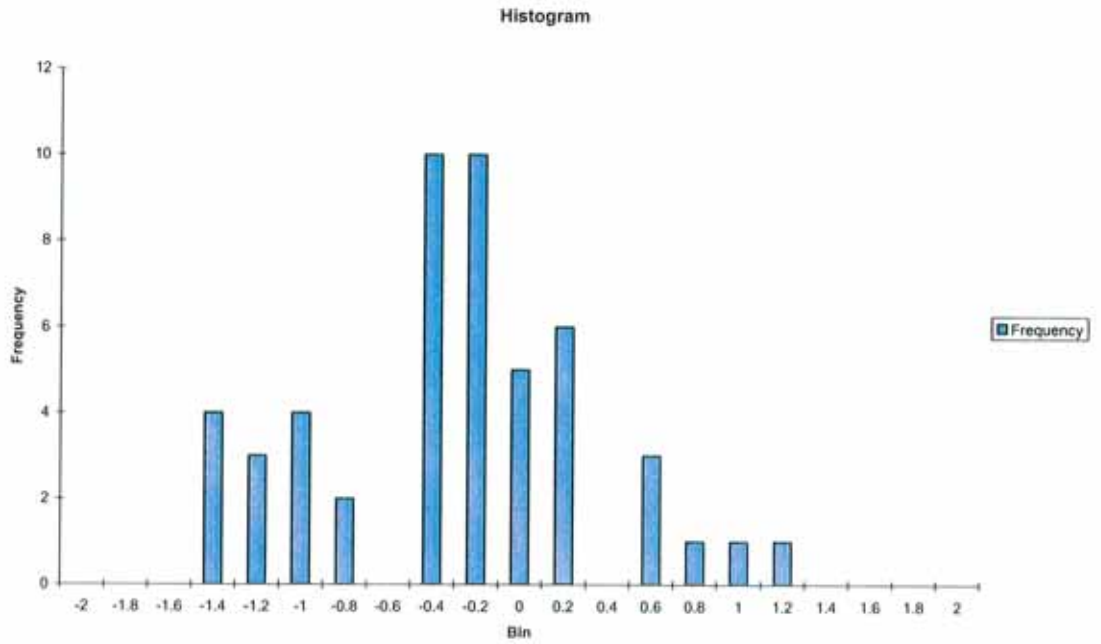


Figure 7.16A Frequency Histogram of Differences (Tape – CMM measurements)

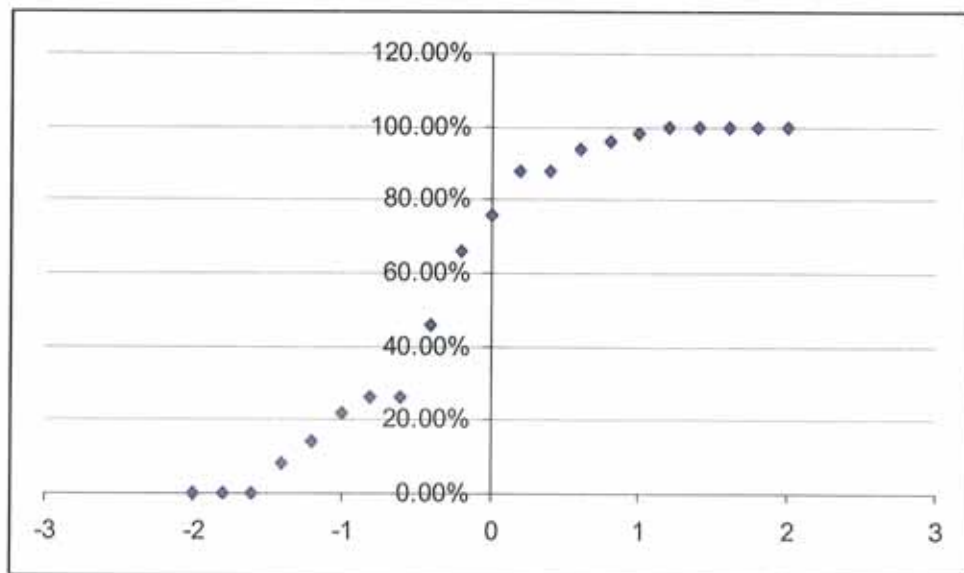


Figure 7.16B Cumulative Distribution of Differences (Tape – CMM measurements)

7.2.1C PhotoModeler and Tape Measurements (Short Lengths)

Figure 7.17 is a plot of the ten values found for each pipe from each of the ten PhotoModeler models created plotted against the actual lengths of the pipes as found by the tape measure.

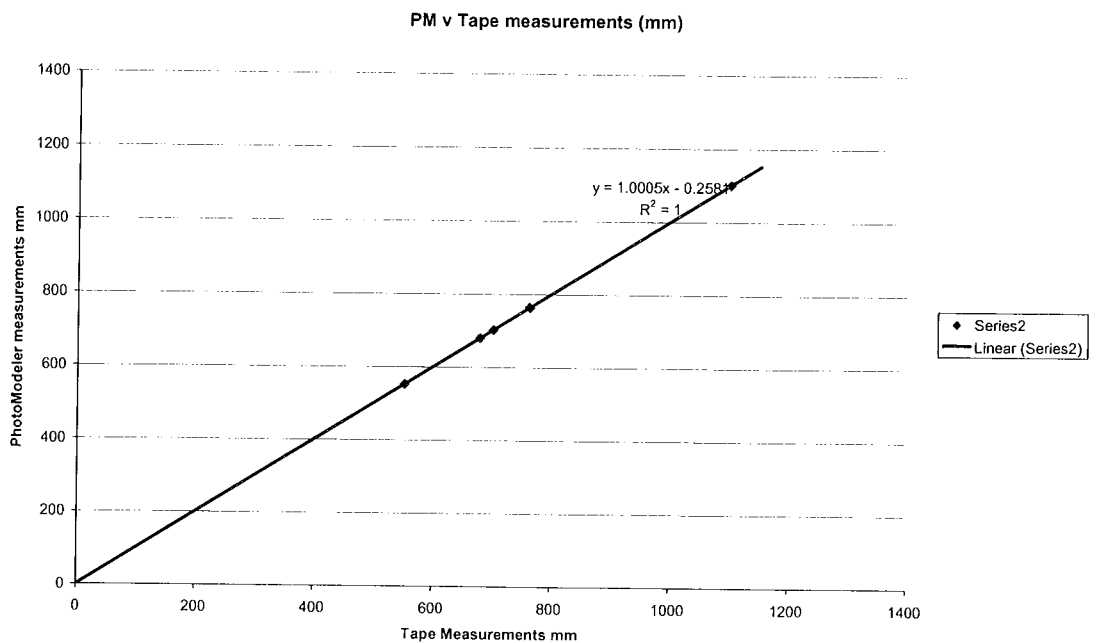


Figure 7.17 Plot of PhotoModeler measurements (PM) against the tape measure measurements

Linear regression analysis of this data produces a slope of 1.0005, with a 95% confidence range of 0.9994 – 1.0016, and a P-value of 8.11×10^{-118} . Therefore the regression confirms there is no significant difference in the measurements obtained by a tape measure or from a photogrammetric model [24].

Figure 7.18 is a plot of the differences between the PhotoModeler and the tape measurements (PM – tape), plotted against the tape measure measurements. The

differences are shown in blue and the mean difference for each length of pipe is shown in pink.

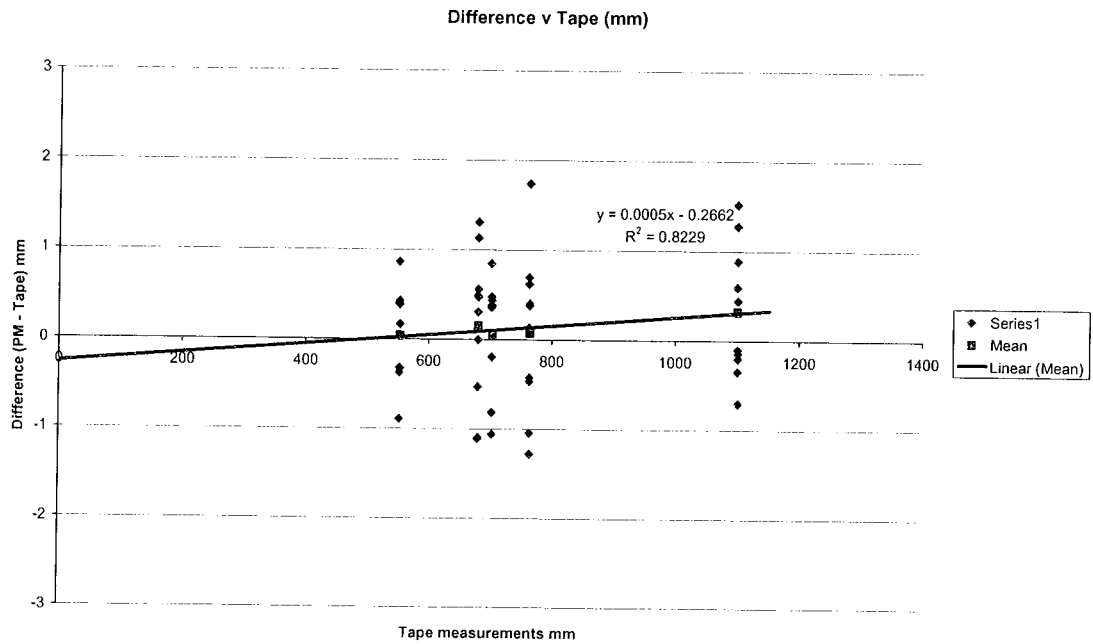


Figure 7.18 Plot of Difference (PM – Tape) against Tape measurements.

Linear regression analysis of this data gives a slope of 0.0005 and a 95% confidence range of -0.0006 – 0.0016. Therefore measuring with PhotoModeler is independent of length. Again in this case the mean value for the difference is insignificant. For the fifty PhotoModeler measurements compared to the tape measure measurements the mean difference is 0.13mm and the standard deviation is 0.71mm. A t-test returned a value of 1.28. Therefore in this experiment PhotoModeler and tape measurements are in agreement. Figures 7.19 A and B respectively show the histogram of the frequency and the cumulative distribution of the difference between PhotoModeler and tape measure measurements, which is normally distributed.

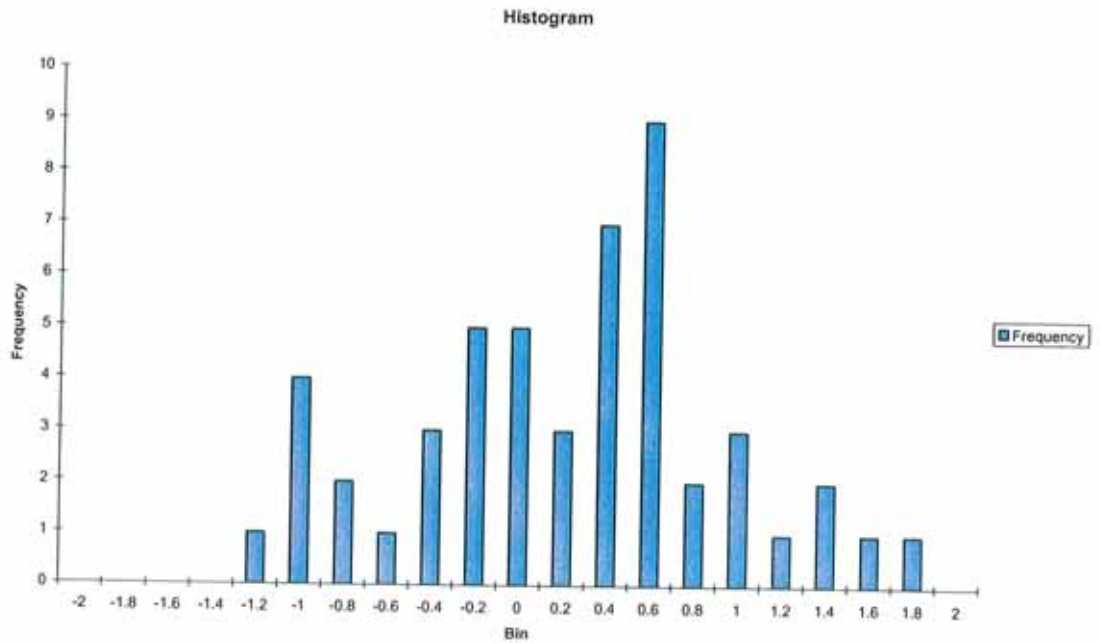


Figure 7.19A Frequency Histogram of Differences (PhotoModeler – Tape measurements)

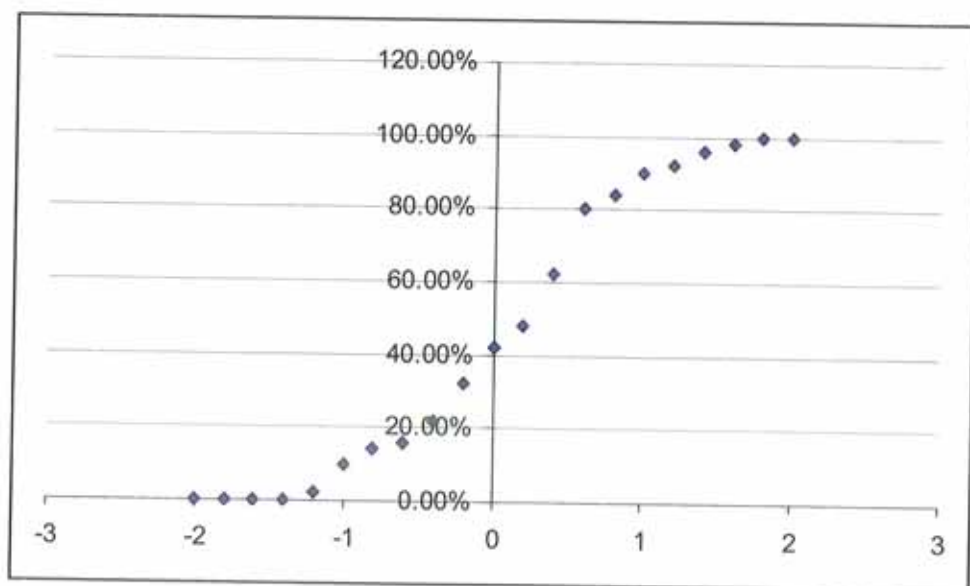


Figure 7.19B Cumulative Distribution of Differences (PhotoModeler – Tape measurements)

In the above experiments the lengths of the pipes that could be used were restricted by the size of the table of the Coordinate Measuring Machine. Further tests were carried

out with longer pipes more representative of vehicle dimensions. Since, as found above, there is no significant difference between tape and CMM measurements, and it is not possible to use a Coordinate Measuring Machine to take measurements in the field, tape measurements were taken to be the true values of dimensions in the remaining tests.

7.2.2 Long Pipes (Order of Magnitude of a Vehicle, Range 0.7m – 4m)

This experiment was completed using lengths of pipes with dimensions equivalent to those of vehicles, as this more accurately reflects the difficulties associated with photographing and modelling a vehicle, than the shorter pipes in the previous tests, since the entire object is not so clearly visible in more than two adjacent photographs. The pipes were arranged as in figure 7.20.



Figure 7.20 Arrangement of pipes with dimensions in order of magnitude of vehicles

Ten PhotoModeler models were created of these pipes. Each pipe was also measured ten times with the tape measure. Figure 7.21 shows the graph of the ten PhotoModeler measurements of every length in the arrangement plotted against the average tape measurement.

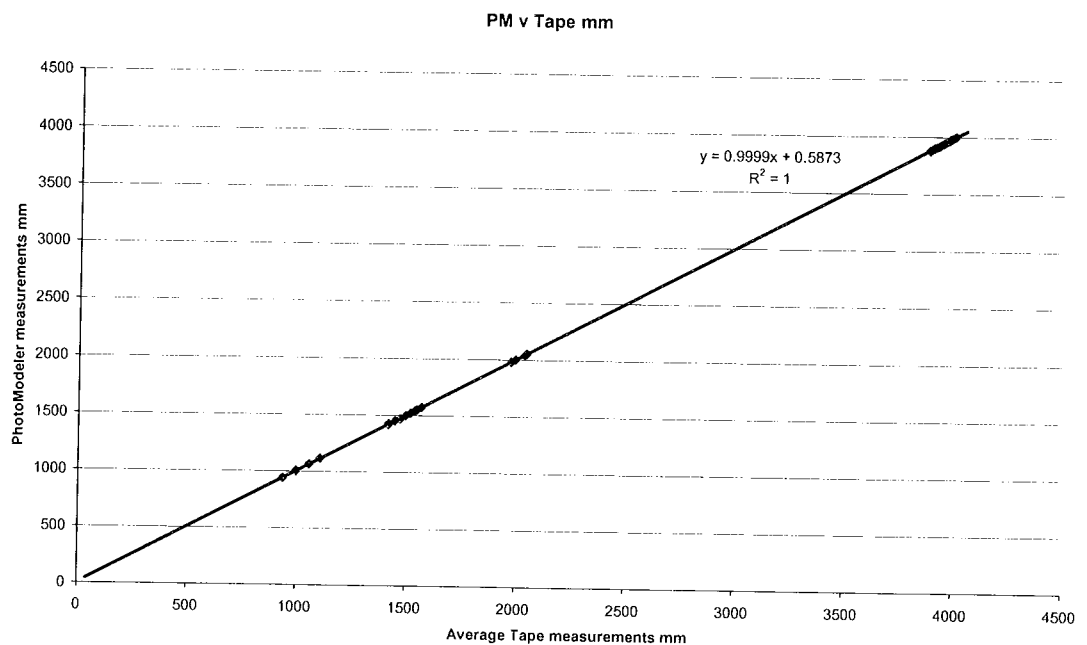


Figure 7.21 Plot of PhotoModeler measurements against average tape measurements for long pipes.

Linear regression analysis of this data produces a slope of 0.9999, with a 95% confidence range of 0.9996 – 1.0001, and a P-value of 0. Therefore the regression confirms there is no significant difference in the measurements obtained by a tape measure and by photogrammetry.

Figure 7.22 is a plot of the differences between the PhotoModeler and the average tape measurements (PM – tape), plotted against the average tape measurements. The differences are shown in blue and the mean difference for each length of pipe is shown in pink.

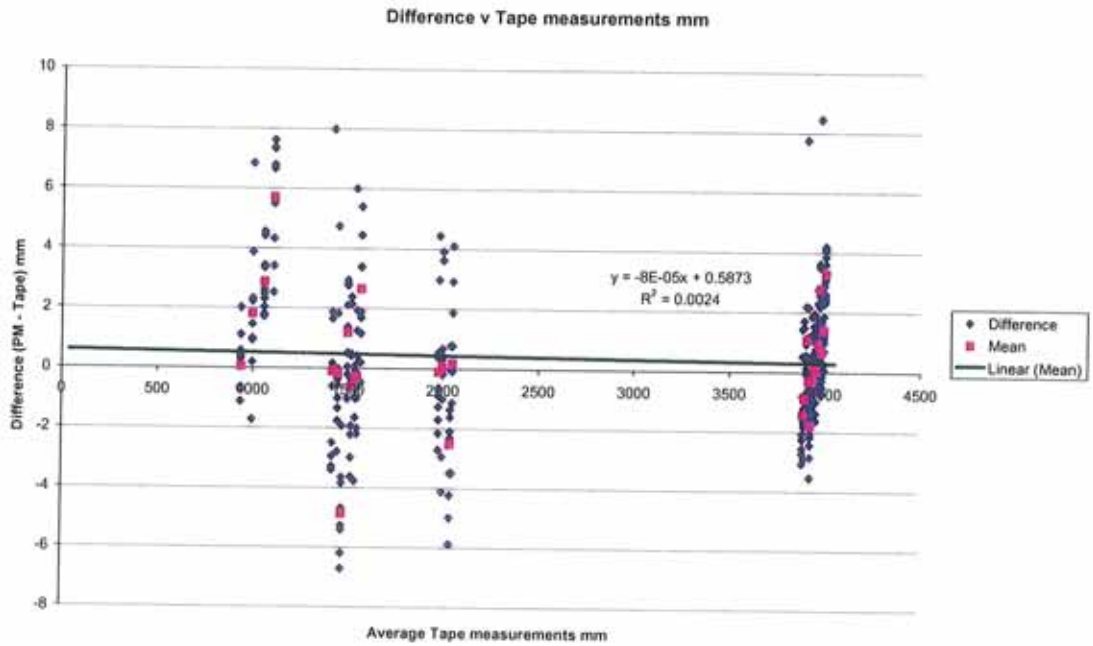


Figure 7.22 Plot of Difference (PM – Tape) against Tape measurements.

Linear regression analysis of this data gives a slope of -8×10^{-5} and a 95% confidence range of $-0.0003 - 0.0002$. Therefore PhotoModeler's measurement accuracy is independent of length. However the mean value for the difference is statistically significant. For the 290 PhotoModeler measurements compared to the tape measurements the mean difference is 0.39mm and the standard deviation is 2.59mm. A t-test returned a value of 2.54. Therefore in this experiment the results from PhotoModeler measures longer than the true (tape) value of a length. The positive intercept value in the equation of the regression of figure 7.21 confirms that the differences between PhotoModeler and tape measurements are positive. Figures 7.23 A and B respectively show the histogram of the frequency and the cumulative distribution of the differences between PhotoModeler and tape measurements, which are normally distributed.

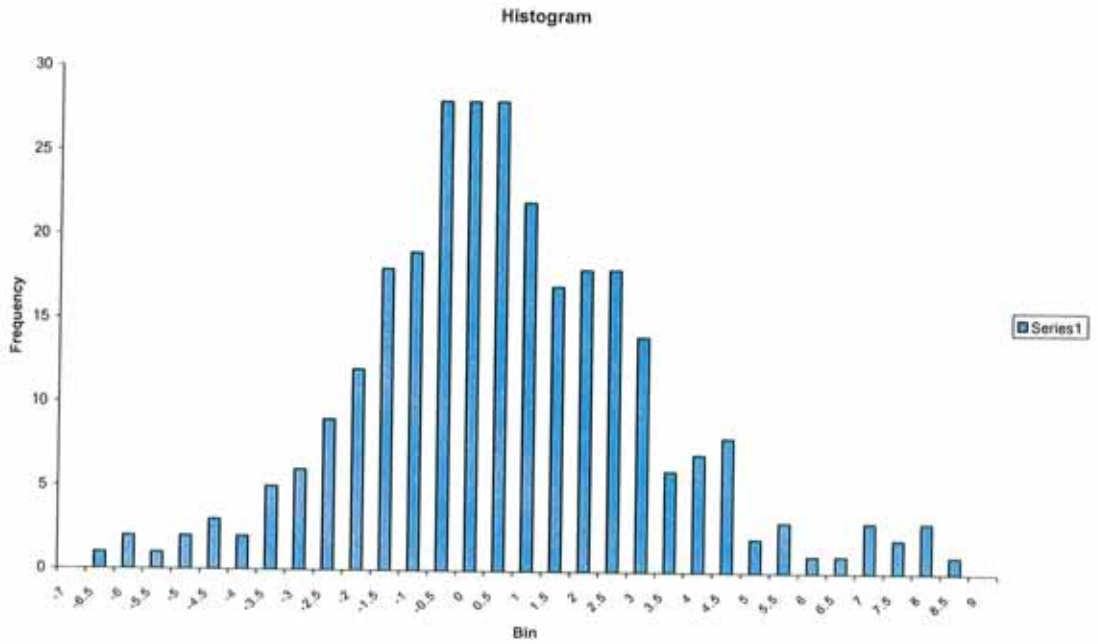


Figure 7.23A Frequency Histogram of Differences (PhotoModeler – Tape measurements) Long pipes

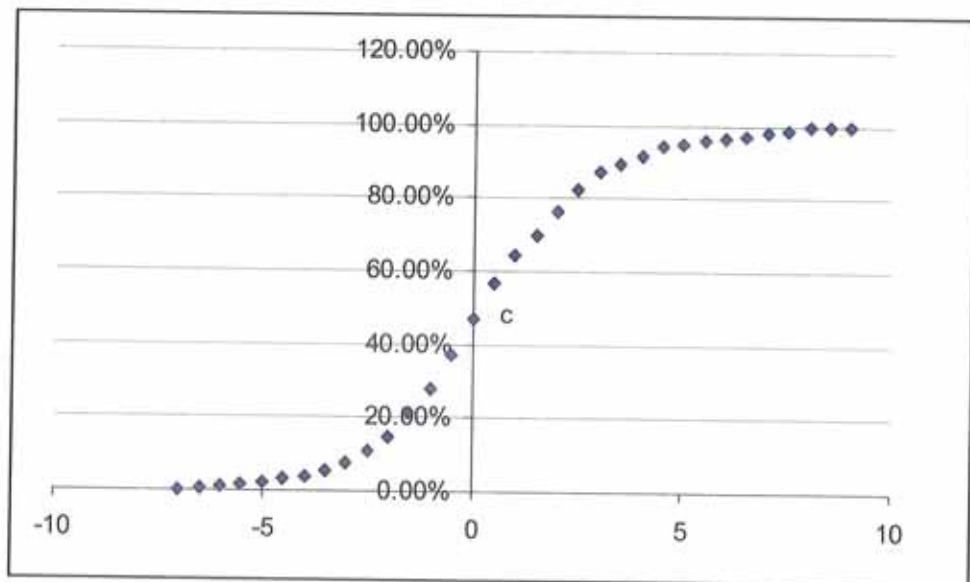


Figure 7.23B Cumulative Distribution of Differences (PhotoModeler – Tape measurements) Long pipes

Figure 7.24 is a plot of the combined data from the short and long pipe experiments. Specifically, the values found for each pipe from each of the models created in both the short and long pipe experiments are plotted against the tape measured lengths.

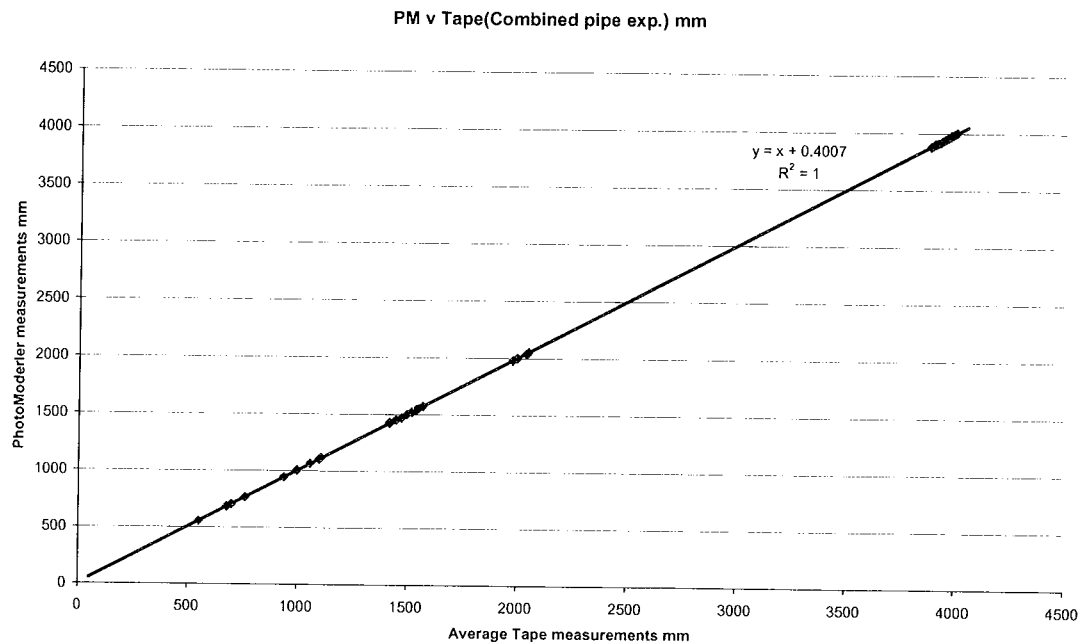


Figure 7.24 Plot of PhotoModeler measurements against average tape measurements, for both long and short pipes.

Linear regression analysis of this data produces a slope of 1, with a 95% confidence range of 0.9997 – 1.0001, and a P-value of 0. Therefore the regression confirms there is no significant difference in the measurements obtained by tape measurement and by photogrammetry [24].

Figure 7.25 is a plot of the differences between the PhotoModeler and the average tape measurements (PM – tape), plotted against the average tape measurements, for both the long and short pipes. The differences are shown in blue and the mean difference for each length of pipe is shown in pink.

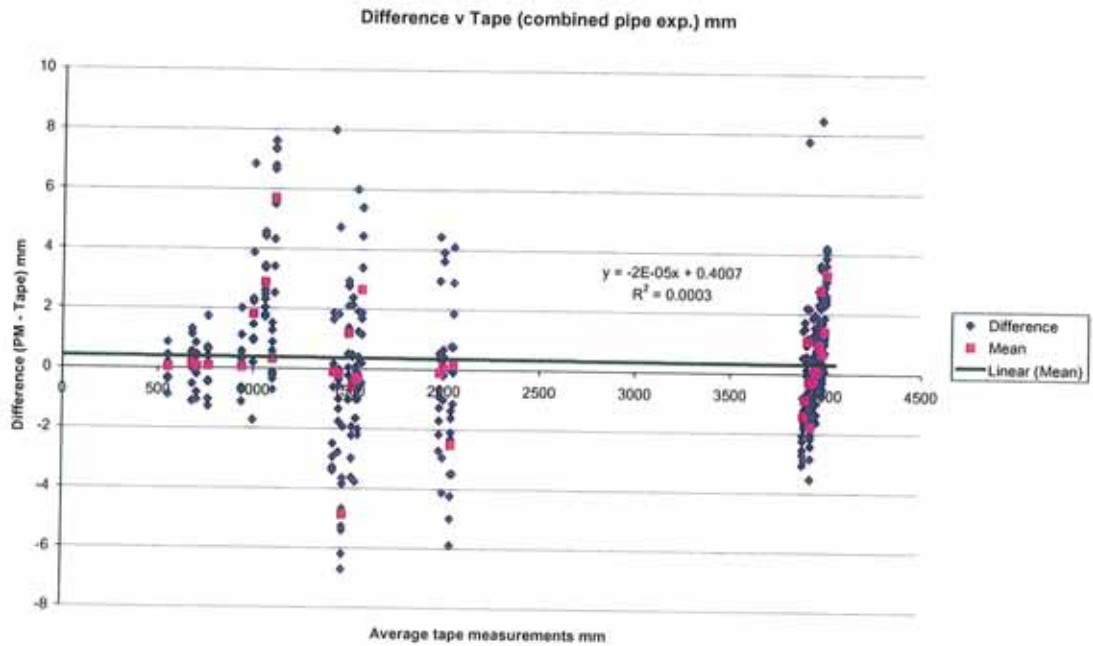


Figure 7.25 Plot of Difference (PM – Tape) against Tape measurements, for both long and short pipes.

Linear regression analysis of this data gives a slope of -2×10^{-5} and a 95% confidence range of $-0.0002 - 0.0002$. Therefore the measurement accuracy of PhotoModeler is independent of length. However the mean value for the difference is statistically significant, for the 340 PhotoModeler measurements compared to the tape measurements the mean difference is 0.35mm and the standard deviation is 2.41mm. A t-test returned a value of 2.67. Therefore in this experiment PhotoModeler produces results that are longer than the true (tape) values. The positive intercept value in the equation of the regression of figure 7.24 confirms that the differences between PhotoModeler and tape measurements are positive. Figures 7.26 A and B respectively show the histogram of the frequency and the cumulative distribution of the difference between PhotoModeler and tape measurements, which is normally distributed.

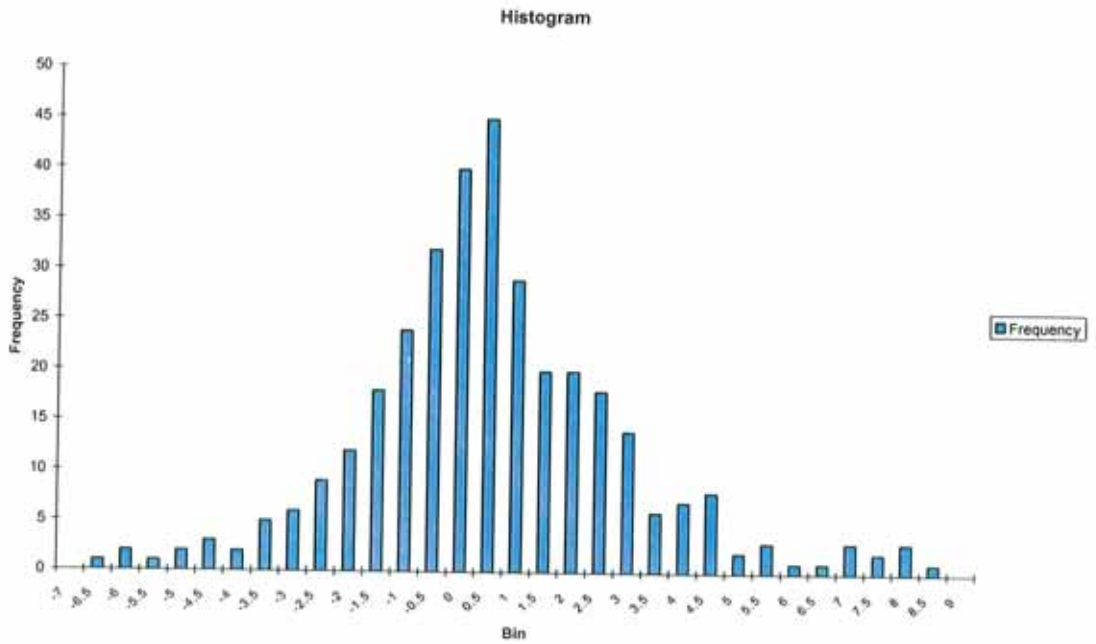


Figure 7.26A Frequency Histogram of Differences (PhotoModeler – Tape measurements) both Short and Long pipes

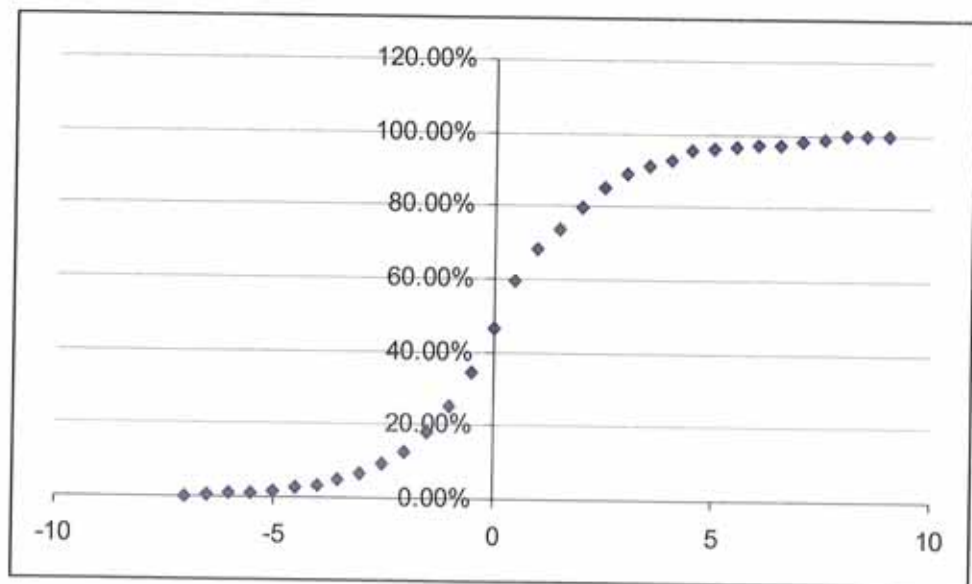


Figure 7.26B Cumulative Distribution of Differences (PhotoModeler – Tape measurements) both Short and Long pipes

7.2.3 Summary of Results of Modelling Simple Objects

Table 7B shows the results of the tests carried out when modelling simple objects i.e. pipes of various lengths.

	Mean Diff /mm	Std Dev /mm	t Test
PM - CMM (short pipes)	-0.27	0.49	-4.02
Tape - CMM (short pipes)	-0.06	0.71	-0.64
PM - Tape (short pipes)	0.13	0.71	1.28
PM - Tape (long pipes)	0.39	2.59	2.54
PM - Tape (both pipes)	0.35	2.41	2.67

Table 7B Summary of Pipe Results

From these results one can conclude that the tape measure used throughout these tests measured shorter lengths than the lengths obtained with the Coordinate Measuring Machine. t tests confirm that this is not statistically significant. However PhotoModeler also measured shorter than the Coordinate Measuring Machine, but the t test confirmed that this is significant. On the other hand PhotoModeler measured longer than the tape measure and the t tests confirm that this is also statistically significant. Therefore the standard deviation of 2.41mm should be included as the uncertainty when measuring lengths in the range of 0.5m to 4.0m (short and long pipes combined) on a simple object from a photogrammetric model, created with PhotoModeler. When a PhotoModeler measurement is being compared to a tape measurement, the longer length measurement by PhotoModeler should be accounted for and 0.35mm subtracted from the PhotoModeler measurement.

7.2.4 Comparison of Pipe measurements with Computational Model measurements

Figures 7.27 A and B compare the differences (PhotoModeler – Tape) found in the long pipe test with the computational differences (Calculated – Actual) found in the computational model programme. The computational model differences are in blue and the pipe differences are in pink. Figure 7.27A is the side-on computational model situation and figure 7.27B is the end-on computational model situation [24].

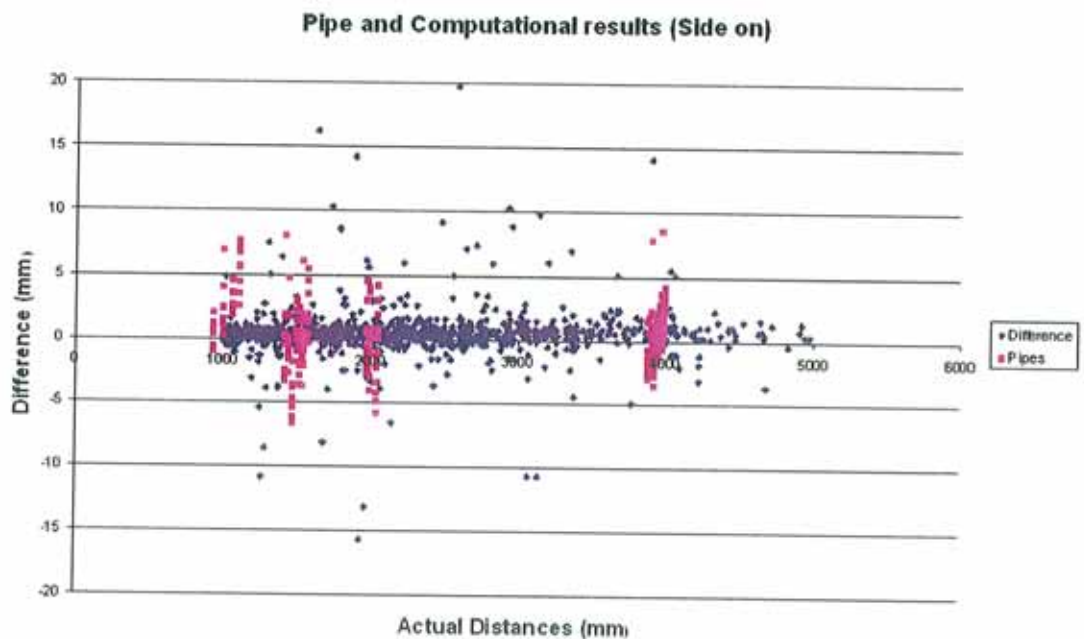


Figure 7.27A Difference (PM – True) against True length, Long pipe test (pink) and Computational Model side-on programme (blue).

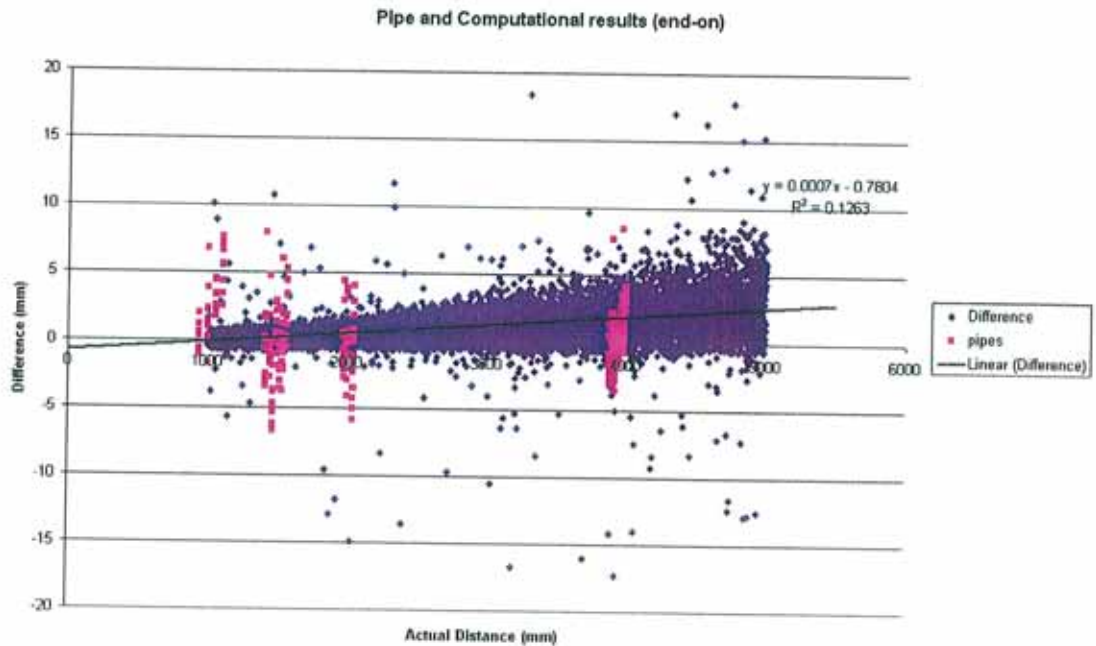


Figure 7.27B Difference (PM – True) against True length, Long pipe test (pink) and Computational Model end-on programme (blue).

It can be seen from figures 7.27 A and B that the range of values of the differences found in the pipe test is within the range of differences found in both computational model programmes. Therefore it can be concluded that the significant cause of the variation of the values of the lengths of the pipes is the mis-tagging error examined by the computational model test programmes. Figure 7.28 compares the cumulative distributions of the long pipe differences and the computational model differences for the end-on programme.

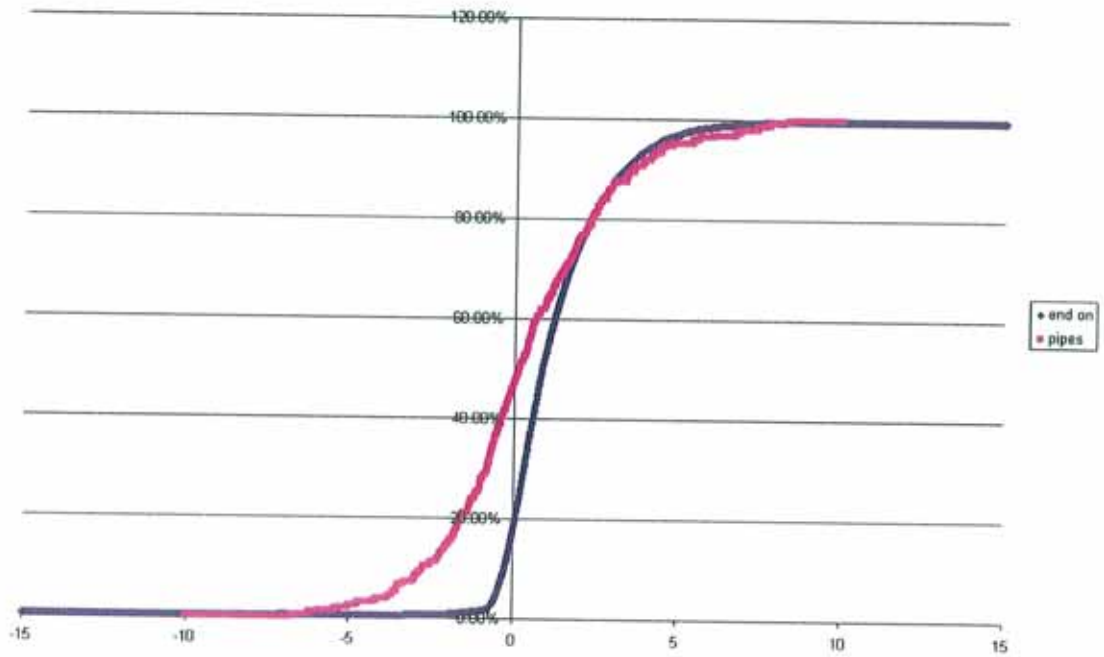


Figure 7.28 Cumulative distribution long pipe test and computational model end-on

The end-on computational model best reflects how the long pipes were modelled, as the pipes were perpendicular to the common area of the photographs used to create the models. The correlation between the distribution of results from the pipe and computational experiments in figure 7.28 shows that the error function programmed in the computational model is not a perfect representation of the error that occurs in actual use of photogrammetry.

7.3 Photogrammetric measurement of complex objects - vehicles.

Having established that a length in the order of magnitude of the dimensions of a vehicle can be modelled and measured accurately using PhotoModeler, the following experiment was carried out to establish the uncertainty in photogrammetric measurement of a complex object, such as a vehicle whose entire profile cannot be seen in a single photograph [57].

An undamaged vehicle was prepared for photographing, by placing targets on the vehicle's surface to outline its profile, and a 3m rule was placed next to the vehicle (providing a known distance to scale the models). The vehicle (fig 7.29) was photographed in various lighting conditions;

- Overcast (fig 7.29A) when the entire sky was covered with clouds.
- Sunny (fig 7.29B) when there were no clouds in the region of the sun.
- Dull (fig 7.29C) at sun set, the sun having just gone below the horizon.



Figure 7.29 Undamaged vehicle



Figure 7.29A Overcast Lighting Conditions



Figure 7.29B Sunny Lighting Conditions



Figure 7.29C Dusk Lighting Conditions

The overcast lighting conditions proved to be the best conditions to work with, as the photographs could be taken from any position around the vehicle without the problems of glare from the sun or the camera's flash, and it was naturally bright enough to allow the points of interest highlighted on the vehicle with targets, to be seen clearly in the photographs [57]. Ten models were created of the vehicle from the same set of photographs taken in each lighting condition. Various lengths and widths were measured from the models and were also measured on the vehicle itself with the tape measure.

7.3.1 Overcast Lighting Conditions

Figure 7.30 is a plot of the differences between the PhotoModeler and the average tape measurements (PM – tape), plotted against the average tape measurements, for the ten models created from the photographs taken in overcast lighting conditions. The

differences are shown in blue; the mean difference for each length of pipe is shown in pink and the standard deviation in yellow.

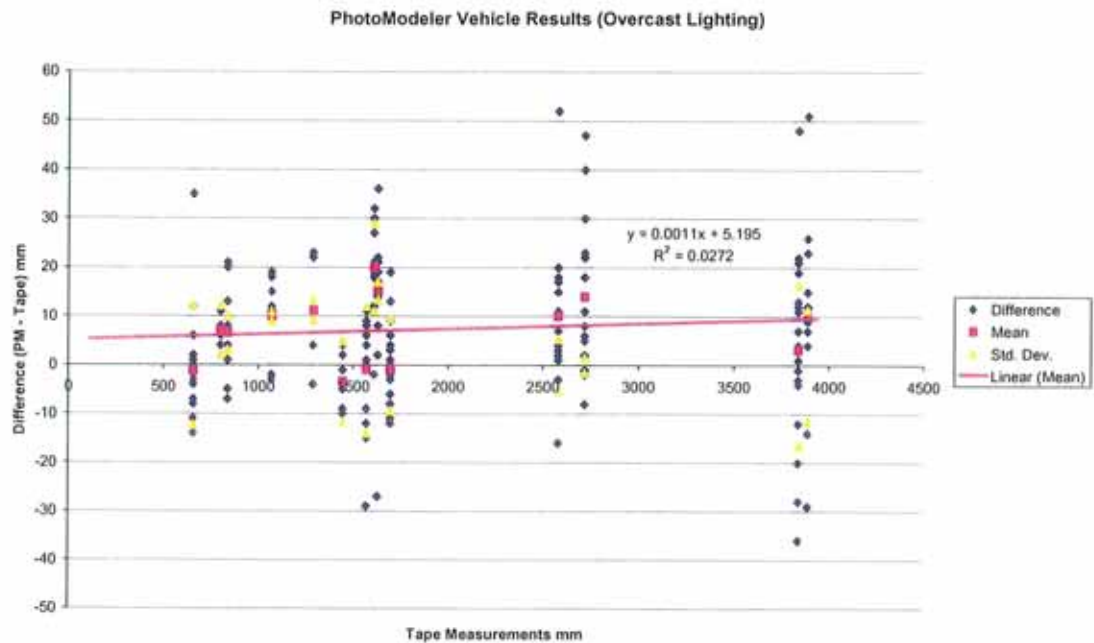


Figure 7.30 Plot of Difference (PM – Tape) against Tape measurements, for vehicle in overcast lighting conditions.

Linear regression analysis of this data gives a slope of 0.0011 and a 95% confidence interval of -0.0006 – 0.0036 therefore the measurement accuracy of PhotoModeler is independent of length. However the mean value for the differences is significant. For the 173 PhotoModeler measurements compared to the tape measurements the mean difference is 6.65mm and the standard deviation is 14.74mm. A t-test returned a value of 5.94. Therefore in this experiment PhotoModeler produces results that are longer than the true (tape) values [57]. Figures 7.31 A and B respectively show the histogram of the frequency and the cumulative distribution of the difference between PhotoModeler and tape measurements, which are normally distributed.

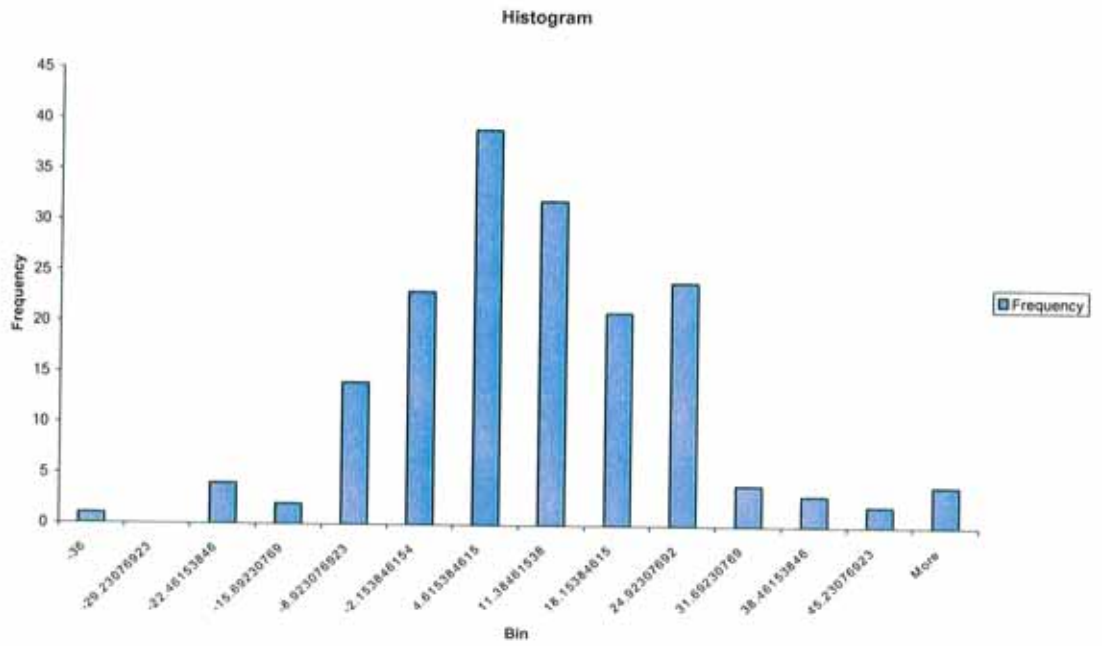


Figure 7.31A Frequency Histogram of Differences (PhotoModeler – Tape measurements) for Vehicle modelled in Overcast Lighting

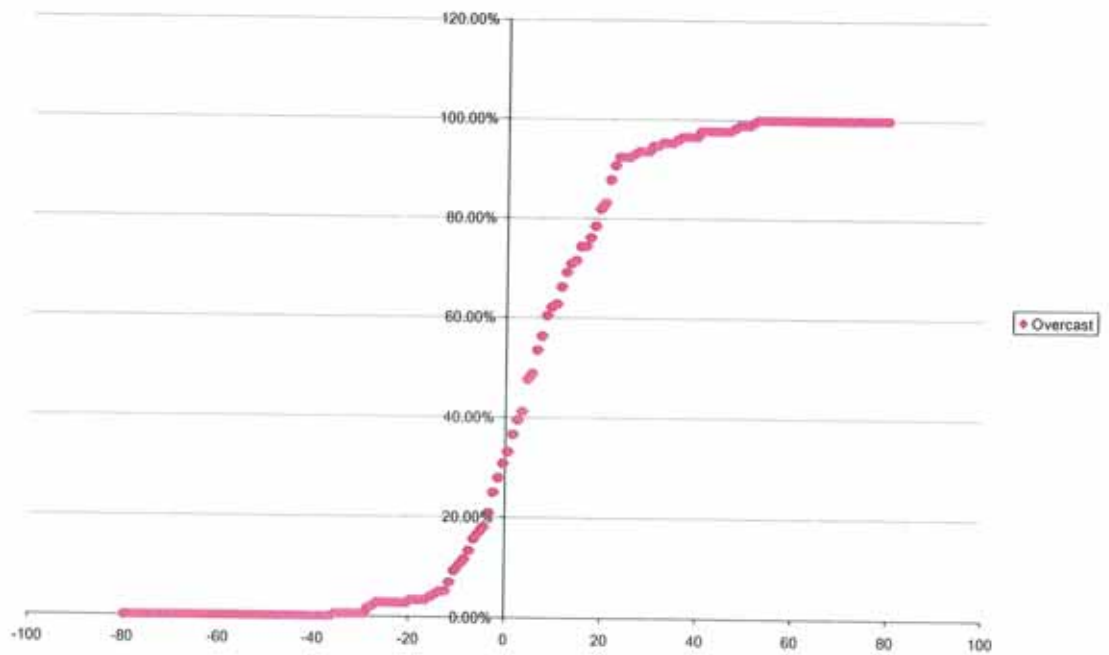


Figure 7.31B Cumulative Distribution for Vehicles modelled in Overcast Lighting

7.3.2 All Lighting Conditions

Figure 7.32 is a plot of the differences between the PhotoModeler and the average tape measurements (PM – tape), plotted against the average tape measurements, for the thirty models created from the photographs taken in the all lighting conditions. The differences are shown in blue; the mean difference for each length of pipe is shown in pink and the standard deviation in yellow.

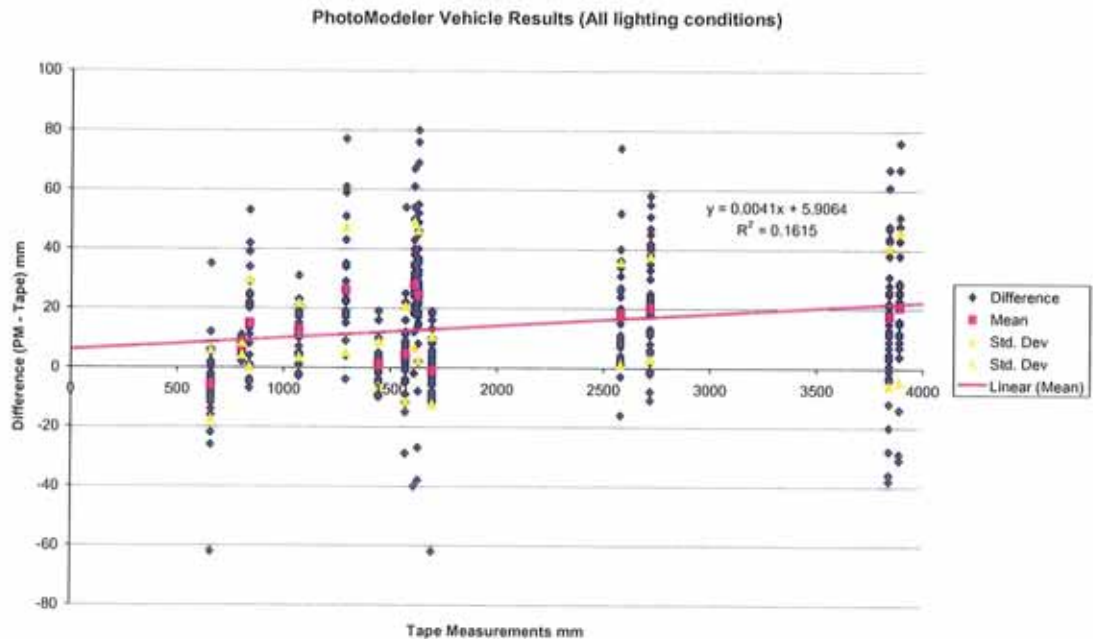


Figure 7.32 Plot of Difference (PM – Tape) against Tape measurements, for vehicle in all lighting conditions.

Linear regression analysis of this data gives a slope of 0.0041 and a 95% confidence interval of 0.0028 – 0.0062. The mean value of the differences is statistically significant from zero. For the 521 PhotoModeler measurements compared to the tape measurements the mean difference is 12.81mm and the standard deviation is 20.20mm. A t-test returned a value of 14.47. Therefore in this experiment PhotoModeler produces

results that are longer than the true (tape) values [57]. Figures 7.33 A and B respectively show the histogram of the frequency and the cumulative distribution of the difference between PhotoModeler and tape measurements, which are normally distributed.

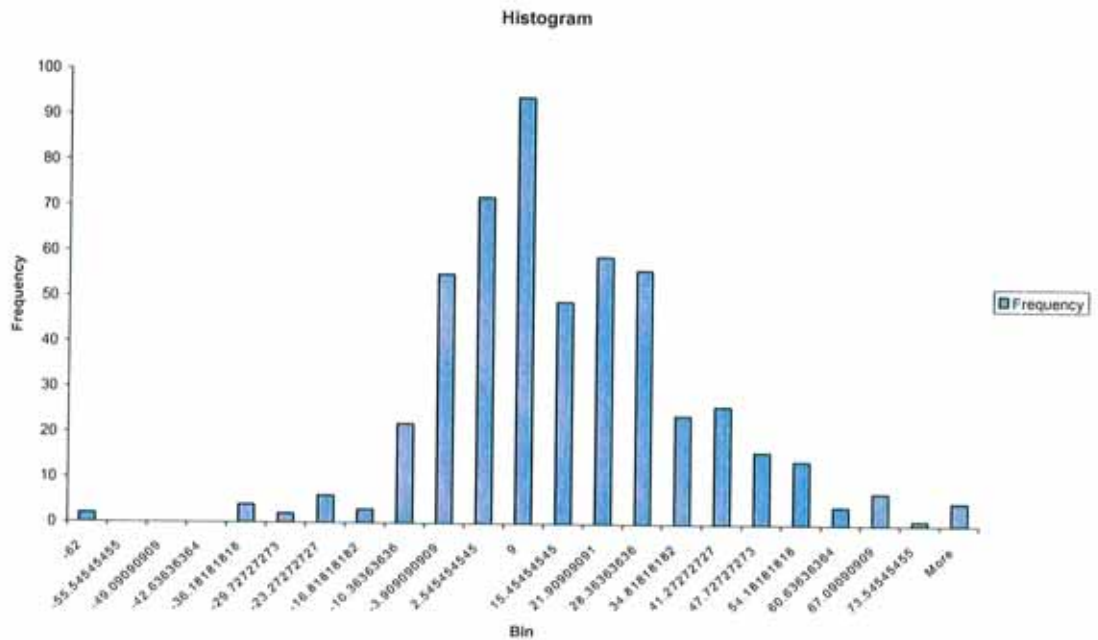


Figure 7.33A Frequency Histogram of Differences (PhotoModeler – Tape measurements) for Vehicles Modelled in All Lighting

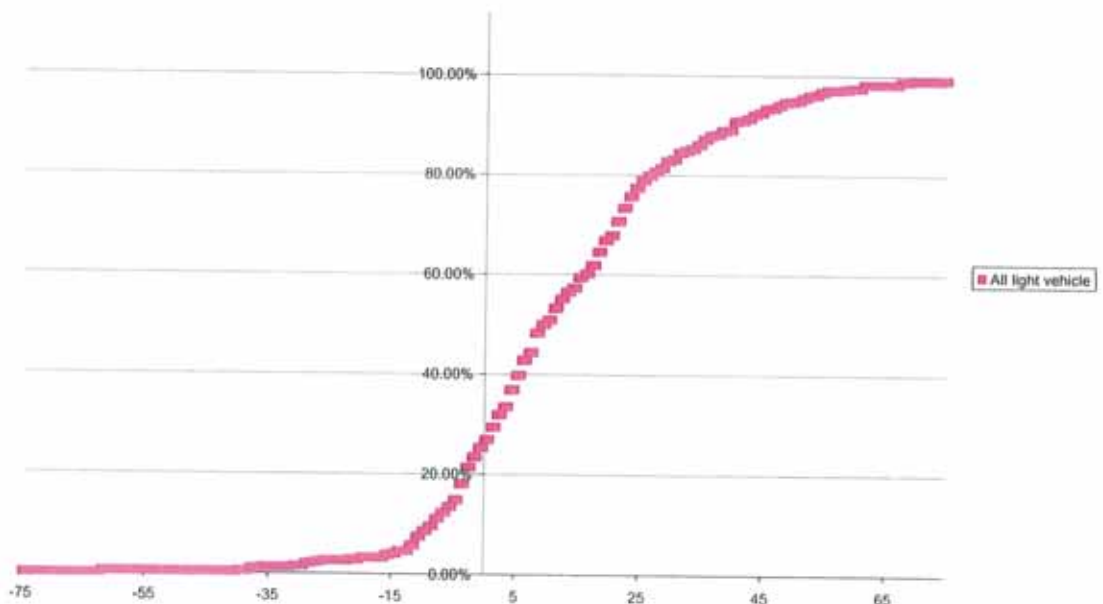


Figure 7.33B Cumulative Distribution for Vehicles modelled in All Lighting

7.3.3 Summary of Results of Modelling Complex Objects

Table 7C shows the results of the tests carried out when modelling complex objects, vehicles.

	Mean Diff /mm	Std Dev /mm	t Test
PM - Tape (overcast vehicle)	6.65	14.74	5.94
PM - Tape (all vehicles)	12.81	20.20	14.47

Table 7C Summary of Pipe Results

From these results one can conclude that PhotoModeler measures longer than the tape measure and the t tests confirm that this is statistically significant. Therefore the standard deviation of 20.20mm is the uncertainty of measuring lengths on a photogrammetric model of a vehicle, created with PhotoModeler and comparing them with tape measured lengths [57]. When a PhotoModeler measurement is being compared to a tape measurement, the longer length measurement by PhotoModeler, of 12.81mm, should be subtracted from the PhotoModeler measurement [57].

7.3.4 Comparison of Vehicle measurements with Computational Model measurements

The differences (PhotoModeler – Tape) found in the overcast lighting vehicle test are compared with the computational differences (Calculated – Actual) found using the computational model programme for the end-on situation. Figure 7.34, best represents how the vehicles are modelled, as the majority of lengths on the vehicle, are

perpendicular to the common area of the photographs. The computational model differences are in blue and the pipe differences are in pink.

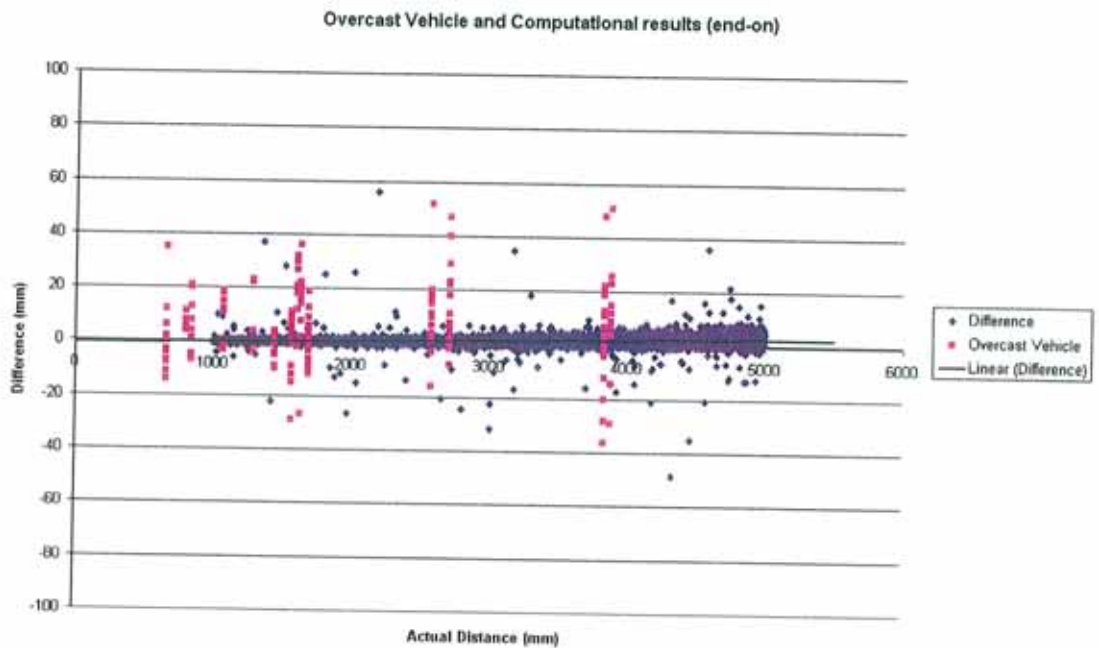


Figure 7.34 Comparison of Overcast Vehicle and Computational model, end-on results

It can be seen from figure 7.34 that the range of values of the differences found in the overcast vehicle modelling experiment is within the maximum differences found in the computational model programme. Therefore it can be concluded that the significant cause of the variation of the values of the lengths on the vehicle when modelled in overcast lighting conditions is the mis-tagging error examined in the computational model. Figure 7.35 compares the cumulative distributions of the overcast vehicle differences (pink) and the computational model differences (blue).

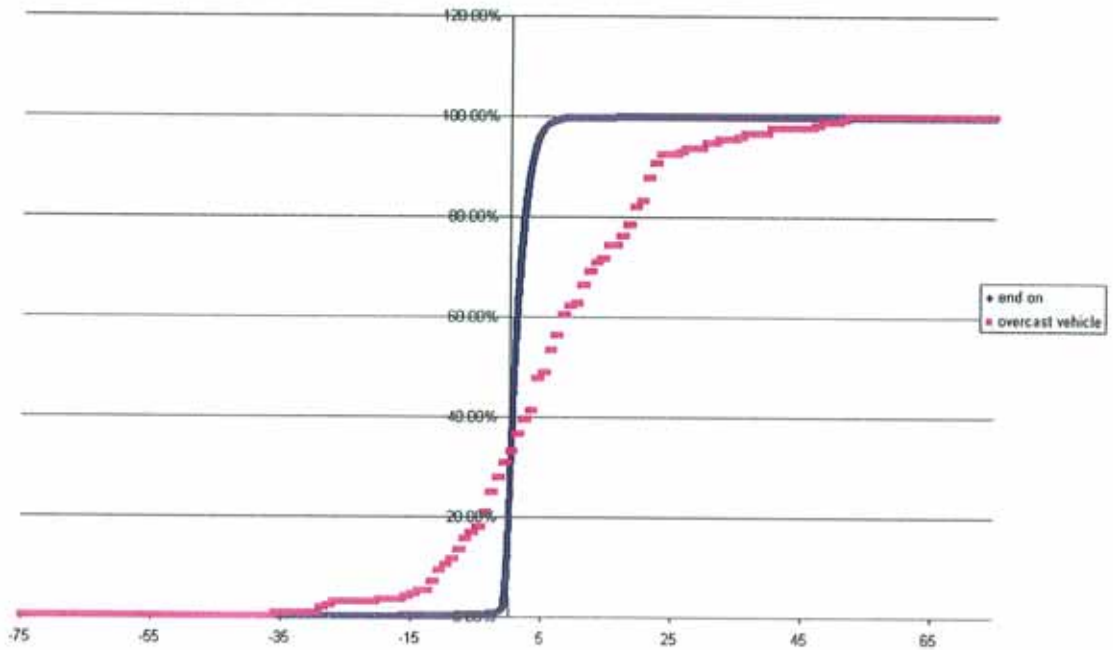


Figure 7.35 Cumulative Distributions for Overcast vehicle (pink) and Computational model, end-on (blue)

The differences (PhotoModeler – Tape) found in all lighting vehicle experiment are compared with the computational differences (Calculated – Actual) found using the computational model programme in figures 7.36. The computational model differences are in blue and the pipe differences are in pink.

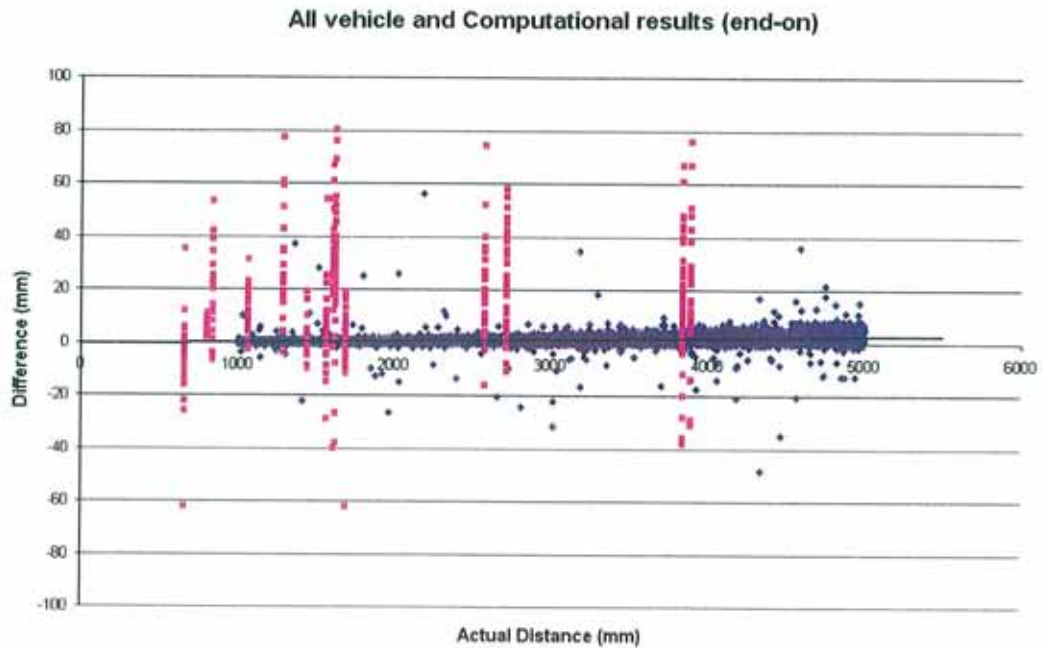


Figure 7.36 Comparison of All lighting Vehicle and Computational Model end-on results

It can be seen from figures 7.36 that the maximum values of the differences found in all lighting conditions vehicle modelling test are outside the maximum differences found in the computational model programme. Therefore it can be concluded that the significant cause of the variation of the values of the lengths on the vehicle when modelled in all lighting conditions is the mis-tagging error examined in the Matlab test programmes, but that the error in the programme should have been a larger error, increasing as the point of interest was further away from the camera. Figure 7.37 compares the cumulative distributions of all lighting vehicle differences (pink) and the computational model differences (blue).

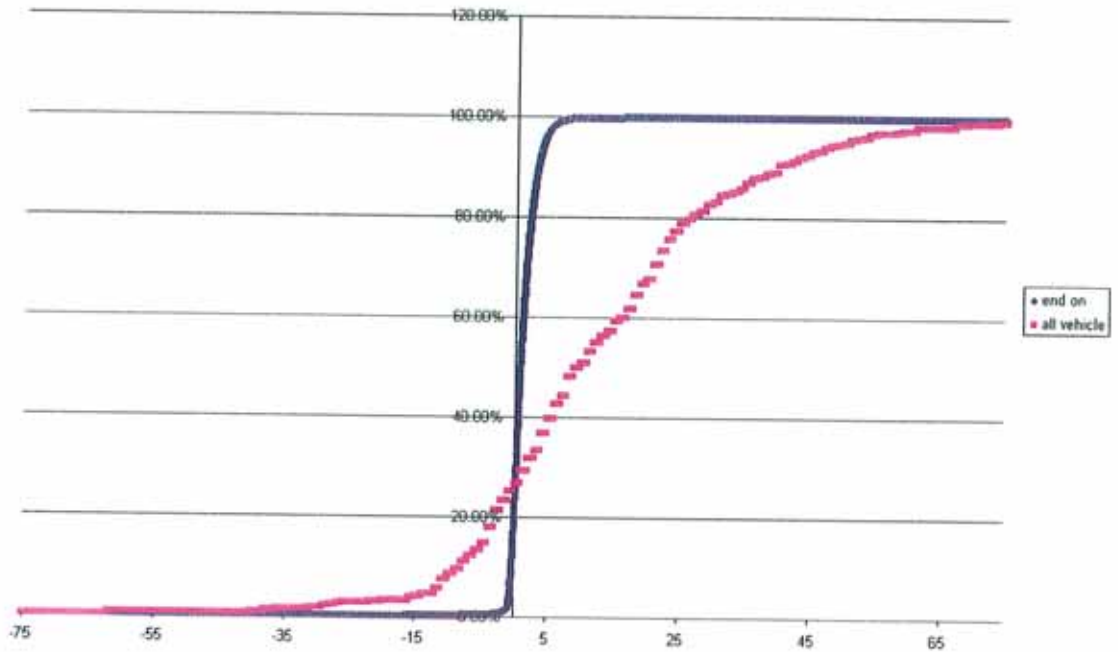


Figure 7.37 Cumulative Distributions for All vehicle (pink) and Matlab end-on (blue)

Another computational model programme was written for the end-on case, which had an increasing error on the tagging of the point as the true location of the point is further away from the cameras. Figure 7.38 shows the comparison of the cumulative distribution of the differences found in this increasing error programme (blue) with the differences found in the all lighting condition vehicle tests (pink).

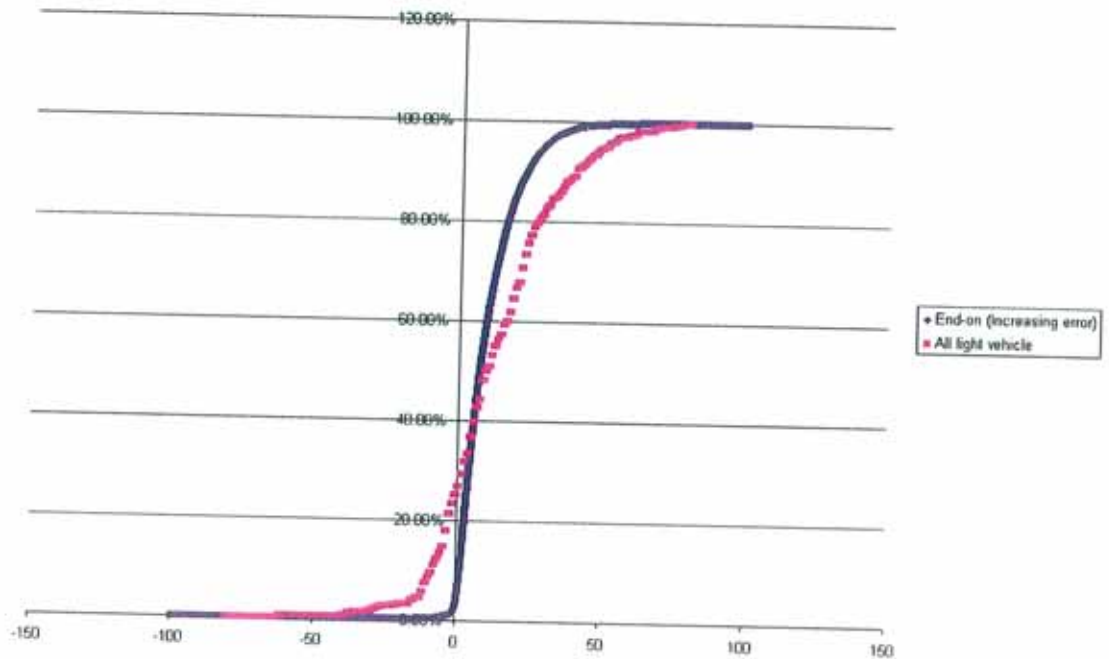


Figure 7.38 Cumulative Distributions for All vehicle (pink) and computational model end-on increasing error (blue)

There is a better correlation between the vehicle and computational model distributions in figure 7.38 than figure 7.37, therefore the increasing error in the computational model is a better representation of the error in using PhotoModeler. This reflects the difficulties when modelling, as when the points of interest are further away from the camera they become more difficult to identify and locate and therefore the mis-tagging error increases.

7.4 Consistency of Creating Photogrammetric Models with PhotoModeler

PhotoModeler has a merging function, (see section 6.5.3), which allows two or more models to be joined together to create a single model. Merging allowed the consistency

of PhotoModeler models to be checked. To establish that PhotoModeler produces consist models, the following experiment was carried out.

The models created during the experiment to establish the accuracy of modelling a vehicle in different light conditions (10 models for each lighting condition) were each merged with an eleventh model created in the same lighting condition [57]. In other words the models were matched / merged with themselves. The models were all of the same undamaged vehicle, but the eleventh model was treated as the original model and used as the base (selected first) model for the merge and the other ten models were each selected second. The merge was processed to create ten new models for each of the lighting conditions.

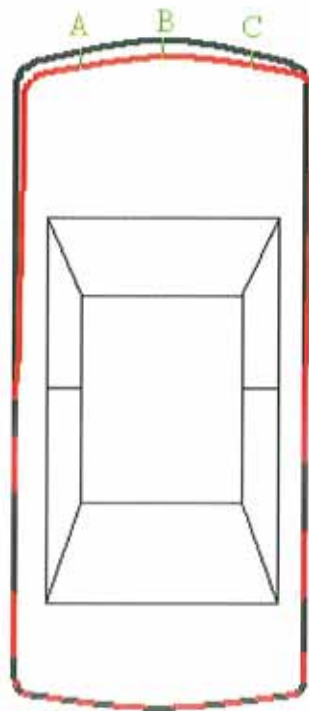


Figure 7.39 Merged vehicle models

The models were matched at points at the rear of the vehicle, figure 7.39. Three points were identified at the front of the vehicle and measurements were taken of the distances between the locations of these points on the merged models. Table 7D shows the difference between the locations of the points at the fronts of the models, A, B and C figure 7.39, within the ten merged models created under different lighting conditions [57].

	Number of Points	Mean / mm	Std. Dev./ mm	t Test
Overcast & Overcast	30	1.13	13.00	0.476
Sunny & Sunny	29	-1.97	11.86	0.910
Dusk & Dusk	29	1.21	12.40	0.530
All & All	88	0.14	12.40	0.060

Table 7D Results of remodelling test

From these results one can conclude that PhotoModeler creates consistent models the values of the t test confirm that the mean differences in the locations of points on the models are insignificant. However the standard deviations should be considered when modelling and measuring with PhotoModeler. 12.4mm is the uncertainty of measuring with PhotoModeler [57].

When the lengths obtained from the PhotoModeler models of vehicles were compared to the tape measurements, a standard deviation $\sigma_{Total} = 20.20\text{mm}$ of the differences was found. This standard deviation is a combination of the PhotoModeler, σ_{PM} , and tape, σ_{Tape} , standard deviations.

$$\sigma_{Total}^2 = \sqrt{\sigma_{PM}^2 + \sigma_{Tape}^2}$$

$$20.20^2 = \sqrt{12.40^2 + \sigma_{Tape}^2}$$

$$\sigma_{Tape} = 15.95mm$$

Bartlett et al [23] found a standard deviation of 0.025-ft or 7.62mm when measuring lengths of approximately 38.5-ft (11.7m) with a fibreglass tape measure. When comparing tape measurements to Coordinate Measuring Machine measurements for lengths ranging from 0.5m to 1m, the standard deviation was found to be 0.71mm. The high value of 15.95mm found when measuring vehicles with the tape measure may be as a result of errors in locating the start and end points of lengths on the vehicle.

From these experiments, the main conclusion is when using PhotoModeler to model vehicles, the standard deviation of 12.40mm should be applied to the measurements obtained from the model. Lengths less than 12.40mm cannot be confidently measured, therefore a lower limit is set. Crush measurements less than 12.40mm should not be measured using photogrammetric models.

Table 7E show the accuracy of measuring with photogrammetry of different objects as found by other researchers.

Researcher	Object Measured	Accuracy
Pappa et al [64]	Inflatable space antenna	1.3mm
Fedak [33]	Survey targets on a ship	2.9mm
Fenton et al [58]	Vehicle	3.0mm
Karvelis [59]	Rods with ball bearing targets	3.6mm
Switzer and Candrljic [60]	Survey targets on vehicle	5.0mm
Dierckx et al [61]	Vehicle / vehicle exhaust	8.0mm
Coyle et al [57]	Targets on vehicle	12.4mm
Rucoba et al [65]	Vehicle crush	14.6mm
Jechev [62]	Residential building	15.0mm
Lie [35]	Vehicle	30.0mm
Faig et al [36]	Vehicle frontal crush	40.0mm
Husher et al [63]	Accident scene	50.0mm
Tumbas and Smith [19]	Accident scene / vehicle	50.0mm

Table 7E Summary of photogrammetric accuracy

The accuracy of 12.40mm found in this research is within the range of accuracies found in previous studies. The study by Fenton et al [58] returned an accuracy of 3.0mm, a quarter of the accuracy found in this research, however Fenton et al only give measurements for a single vehicle and do not give details of how this value of accuracy was found. The study by Pappa et al [64] modelled and measured an inflatable space antenna. The antenna had a simple shape with outer diameter of 6.5m and was covered in retro-reflective targets, the centres of the targets were located on the images using the software's subpixel target identification option. Subpixel target identification was

examined during this research and found not to be suitable when modelling vehicles due to their complex shape. The study by Faig et al [36] measured frontal crush depth damage sustained by vehicles using photogrammetry and compared these measurements to ones obtained by an expert collision investigator. The average difference between photogrammetry and the expert (photogrammetry – expert) was 7.9mm with a standard deviation of 40mm. The positive average difference found by Faig et al [36], corresponds with the results found in the computational model, pipe modelling and vehicle modelling experiments as part of this research, photogrammetry measures longer than the true length of an object. Rucoba et al [65] measured the crush sustained by two vehicles involved in collisions, the photogrammetrically measured crush measurements were on average longer than the tape measurements by 14.6mm, again confirming the results found in the experiments completed during this research that photogrammetry measures longer than tape measurements.

Chapter 8 SPEED CALCULATIONS AND PHOTOGRAMMETRIC VEHICLE MODELS

The previous chapter determined that photogrammetry can be used to accurately model vehicles. This chapter evaluates the use of photogrammetry in practical collision damage measurement; it presents the results obtained from models created in PhotoModeler of the crush profiles, for vehicles that have been involved in collisions. Staged collisions were attended across Europe at a number of venues and events, which allowed the vehicles to be examined, photographed and measured before and after the collisions. Examination of vehicles involved in these collisions highlighted some limitations that have to be overcome to produce the best results from photogrammetry with PhotoModeler. As the undamaged vehicle was available for photographing before the collision, undamaged and damaged (before and after) models were created and merged together to show clearly the crush depth produced by the collision.

Photogrammetric models of undamaged and damaged vehicles can be superimposed, to show clearly the displacement between the original and crushed structure, i.e. the crush profile. Section 8.1 presents the crush profiles that it is possible to create using PhotoModeler. It also shows an example of the limitation of photogrammetry, i.e. only what is visible in the photographs can be included on the model. In section 8.2 the models of the vehicles involved in two-vehicle staged collisions are fitted together to give the orientation at the time of impact. The pre-impact speeds of the bullet vehicles for each of the collisions are estimated and compared to the recorded speeds. There are a number of methods for calculating speed from crush, which in general require six crush depth measurements from across the width of the damaged area of the vehicle.

These crush depth measurements can then be made from the crush profile. The method of estimating speed from crush chosen for this research is set out in detail in chapter 3 and is used to estimate the speeds of the bullet vehicles in section 8.2.

8.1 Photogrammetric Vehicle Models

This section describes crush profiles obtained from superimposed photogrammetric models of undamaged and subsequently damaged vehicles that were involved in on-road and staged collisions.

8.1.1 Saab 93 Side to Pole

The Saab 93 was placed on a sled and its driver's side collided with a rigid pole. Figure 8.1 shows the vehicle after the collision and figure 8.2 shows the merged before and after models of the vehicle.



Figure 8.1 Saab 93 that collide with a Pole

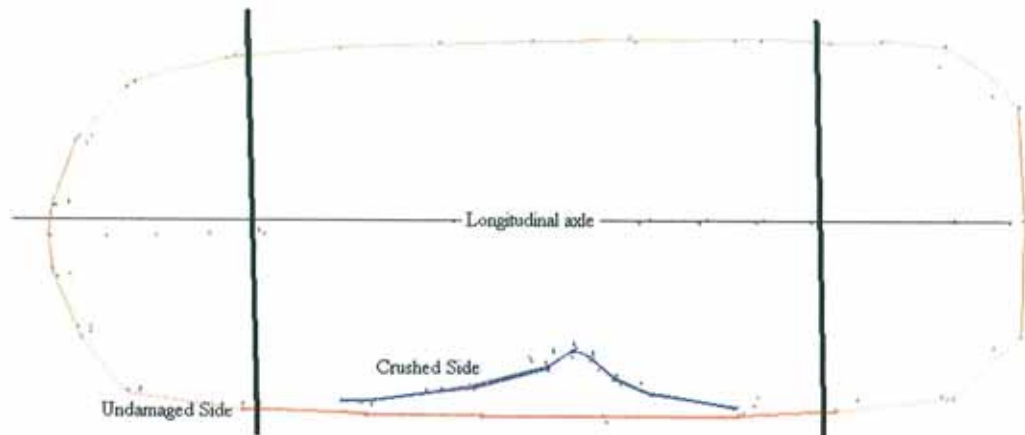


Figure 8.2 Merged before and after photogrammetric models of Saab 93

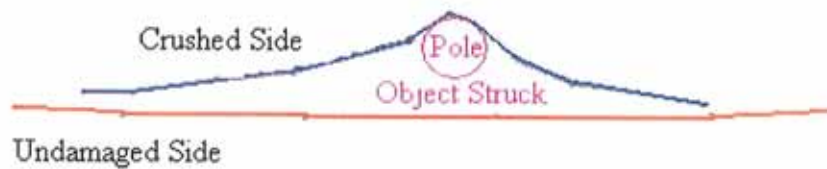


Figure 8.2A Crush damage sustained by Saab 93 and estimation of object struck

Figure 8.2A shows the crush damage and an estimation of the object struck by the vehicle. The pink circle in figure 8.2A, is the best circle that can be constructed from the indentation in the side of the Saab 93. The radius of this circle is 0.24m, the radius of the pole struck by the car is 0.254m, therefore this crush profile produces a very good estimation of shape and size of the object that was struck.

8.1.2 Saab 93 – Front

Figure 8.3 shows a Saab 93 convertible, which collided with a deformable barrier during a controlled offset collision with 40% of the front of the vehicle making direct contact with the barrier.



Figure 8.3 Saab 93 that collided with deformable barrier

The Saab 93 was photographed before and after collision with a deformable barrier. Figure 8.4 shows the merged before and after models. The red line represents the undamaged front of the vehicle, the blue line represents the damaged front bumper and the pink line represents the edge of the bumper bar. From this profile crush depths across the damaged front of the vehicle can be clearly seen and measured for use in the estimation of pre-impact speed. The crush profile (fig 8.4) shows that approximately 46% of the front bumper is crushed rearwards, the rest is projecting forwards, this is consistent with an offset frontal collision [7].

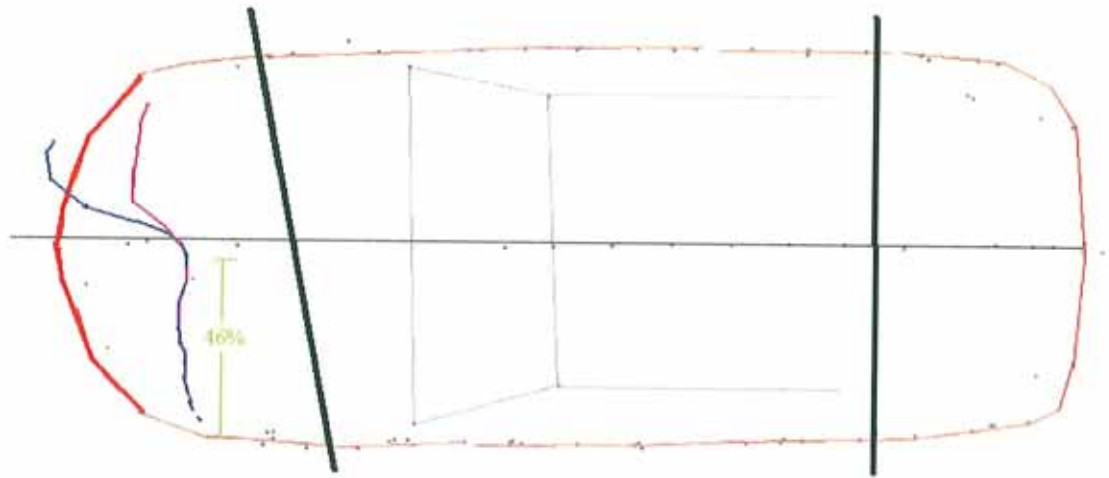


Figure 8.4 Merged before and after photogrammetric models of Saab 93

The above vehicles were crashed as part of EuroNCAP safety tests, at the TNO transport laboratory, Delft, Holland.

8.1.3 Toyota Corolla

A damaged Toyota Corolla was photographed and modelled. Figure 8.5 shows the damaged vehicle.



Figure 8.5 Toyota Corolla

An undamaged Corolla was also photographed and modelled. The damaged and undamaged models were then merged at points at the rear of the vehicle, as the rear was not damaged during the collision as shown in figure 8.6. Figure 8.6A shows the damaged vehicle along with an approximate depiction of the object that was struck, in this case the rear twin wheels of a truck. The blue line represents the undamaged front of the Corolla. The red line represents the damaged front and outlines the shape of the struck object, the twin wheels of a truck.

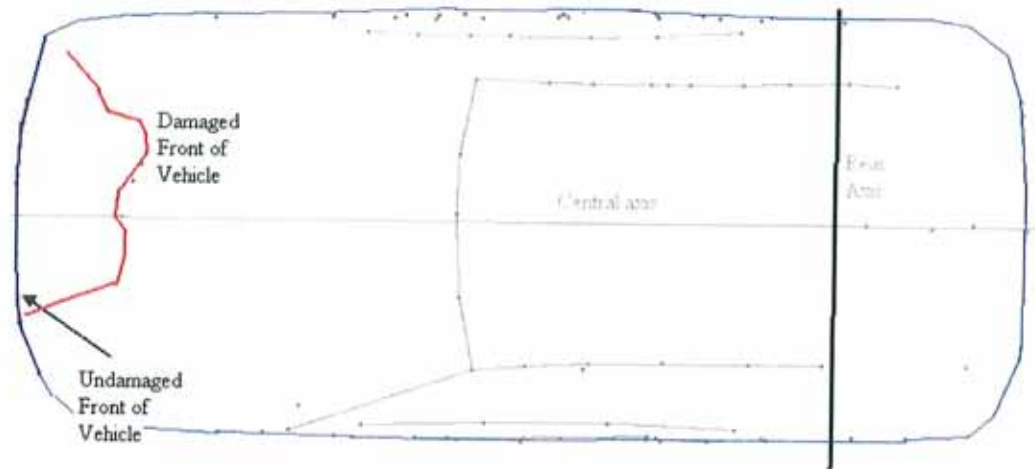


Figure 8.6 Merged before and after photogrammetric models of Corolla

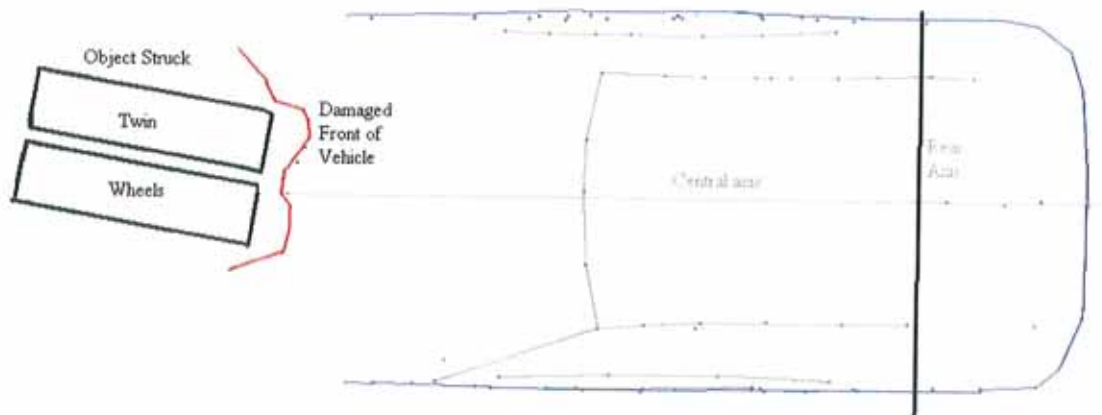


Figure 8.6A Crush damage sustained by Corolla and estimation of object struck

8.1.4 Opel Corsa

This vehicle is an example of a limitation of the approach of measuring crush depths using photogrammetry, only what is visible in the photographs can be included in the models and measured. This vehicle collided with another vehicle, in a T-style collision, the impact area of the target vehicle was the front wheel. This vehicle had hidden damage as the bumper had recovered after the collision, but the chassis and bumper bar

were damaged. The vehicle was photographed and measured with the bumper in place and also with the bumper removed (fig 8.7 and 8.8).



Figure 8.7 Opel Corsa (with Bumper, hiding extent of damage)

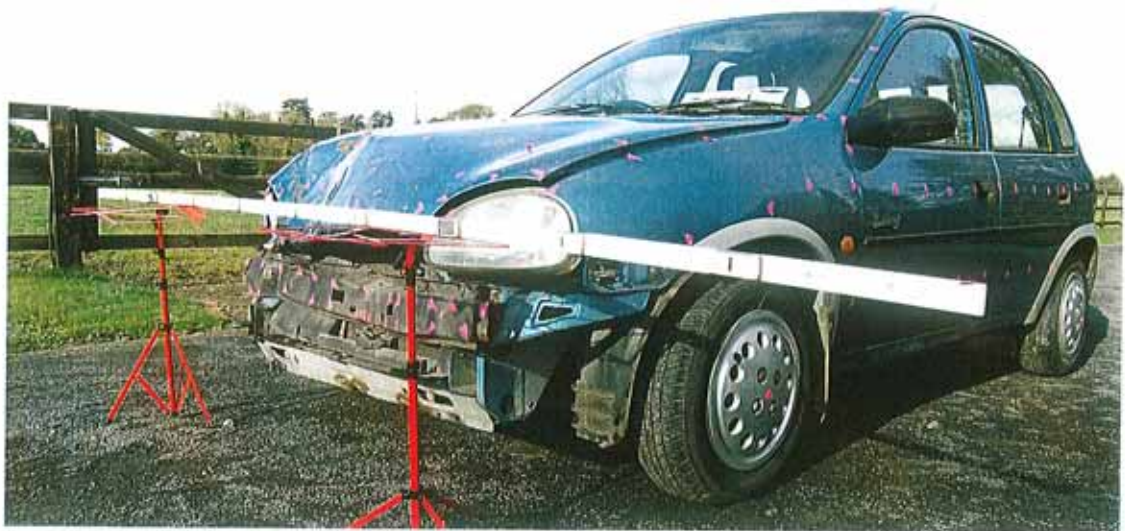
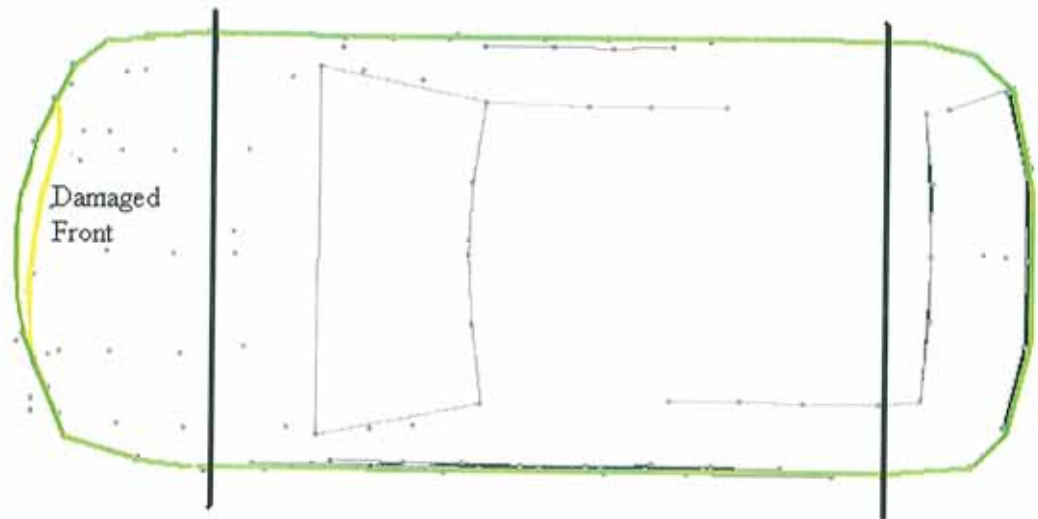
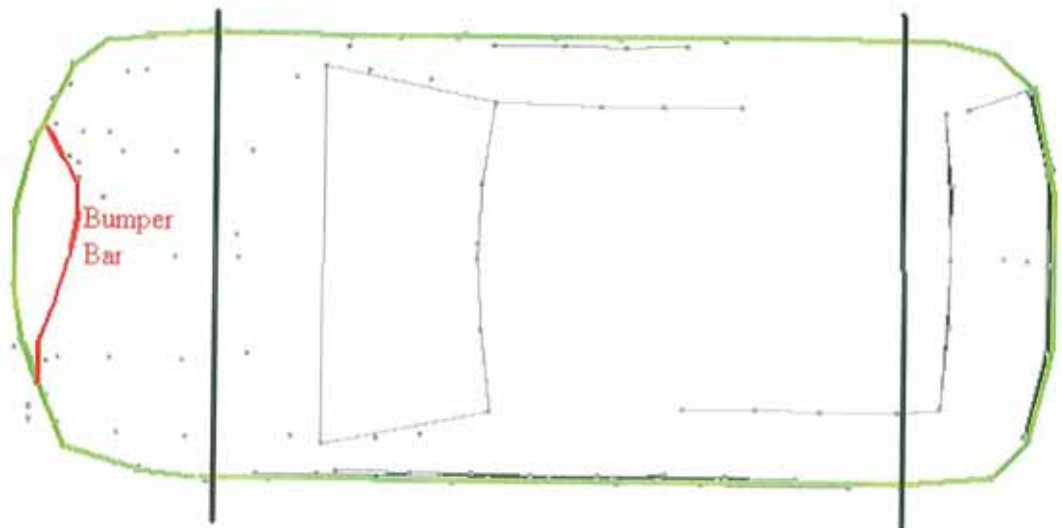


Figure 8.8 Opel Corsa (without Bumper, all damage visible)

The vehicle had previously been photographed undamaged allowing an undamaged model to be created. Two other models were created damaged with bumper and damaged without bumper. The undamaged model was merged with the damaged with bumper model (fig. 8.9A) and with the damaged without bumper model (fig. 8.9B).



**Figure 8.9A Merged before photogrammetric model and after with bumper
photogrammetric model of Corsa**



**Figure 8.9B Merged before photogrammetric model and after without bumper
photogrammetric model of Corsa**

The average crush depth measured from the model with the bumper is 0.048m and from the model without the bumper is 0.122m. The equation for Energy Equivalent Speed

$$(V_{EES} = 7.41 + 191.79 \left(\frac{\text{Average Crush}}{\text{Vehicle Length}} \right)^{\frac{2}{3}}),$$

the average crush depth from both models and the pre-impact length measured from the undamaged model (3.62m) were used to calculate the energy equivalent speed. It was underestimated by 8.5 km/h because the recovered bumper hid the true extent of the damage. Therefore the operator must ensure that during the examination and preparation of any vehicle before photographing that they check for hidden damage and remove any items that may obscure this damage from view.

8.2 Staged Two Vehicle Collisions, Orientation and Speed Calculations

The following section gives details of T-style staged collisions, where the longitudinal axes of the bullet and target vehicles have a 90° angle between them. In each case both vehicles were available for photographing before and after the collisions. Photogrammetric models were created from the photographs, these models were fitted together to give the orientation of the vehicles. Crush depth was measured from the models and used to estimate the pre-impact speed of the bullet vehicle in each collision.

Table 8A is a summary of the collision tests examined, the vehicles involved, their speeds and areas of the target vehicles that were struck during the impact.

Collision	Target Vehicle	Bullet Vehicle	Speed of Target km/h	Speed of Bullet km/h	Impact area on target
1	Jaguar XJ V6	Jaguar S-Type 2.5 V6	0.0 (Stationary)	49.4	Front Door
2	Opel Vectra 2.0i GL	Ford Mondeo 2.0i GT	58.0	38.0	Rear Wheel
3	Opel Vectra 2.0i 16V GT	Ford Mondeo 2.5i 24V	37.8	56.8	Rear Wheel
4	Opel Vectra 2.0i GLS	Ford Mondeo 2.0i 16V	41.1	42.1	Rear Wheel

Table 8A Summary of Collision Tests

8.2.1 Orientation of Vehicles

Each vehicle was photographed before and after the collision. Undamaged and damaged models were created for each vehicle from the photographs. The undamaged and damaged models were superimposed to produce a crush profile for each vehicle. The crush profiles of the vehicle at the level of the bumper of the bullet vehicle were printed, and the two profiles from each collision were adjusted and rotated until a best fit of their crush areas was obtained. Figures 8.10 – 8.13 show the models fitted together from each of these collisions.

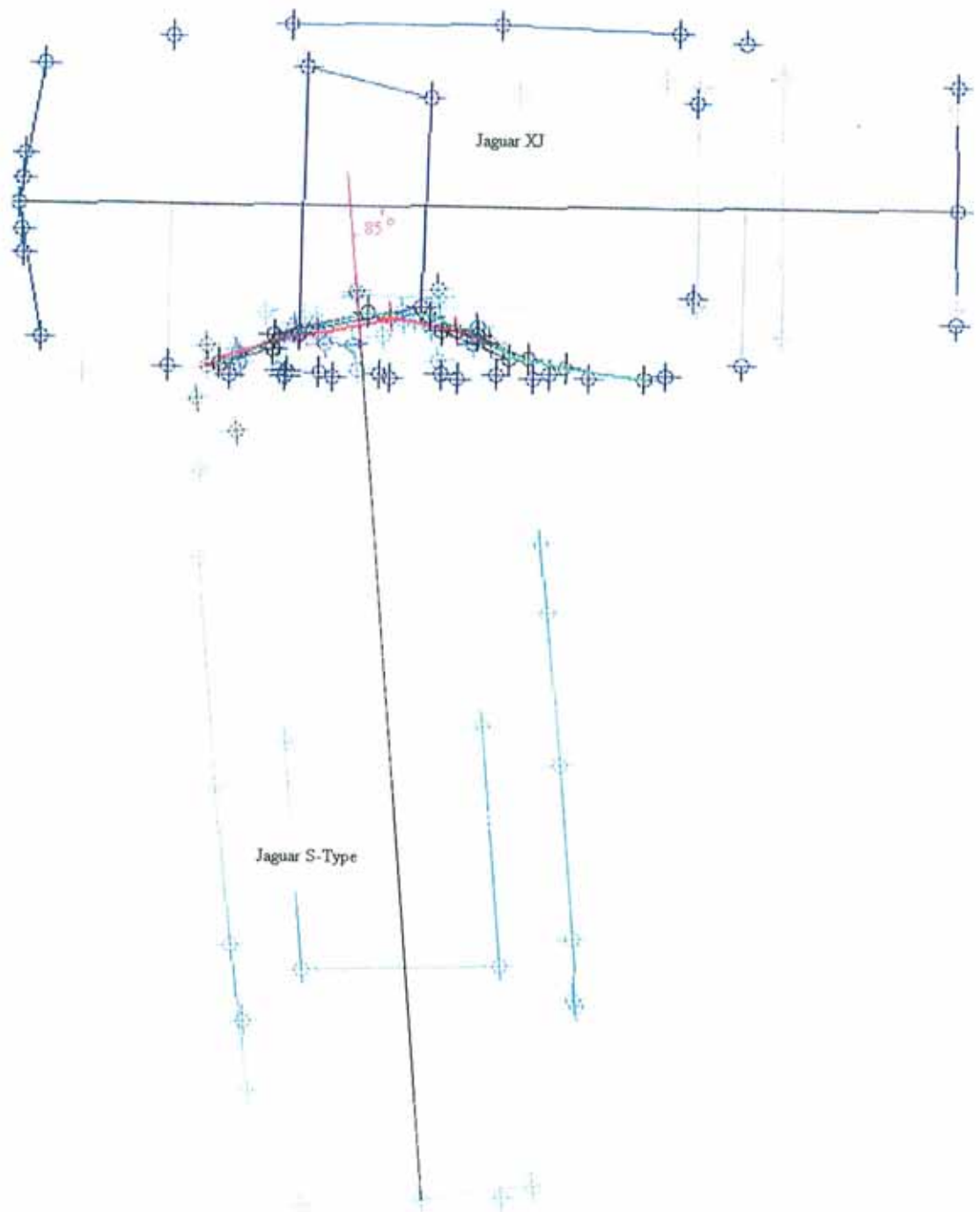


Figure 8.10 Collision 1 (Jaguar S-Type – Jaguar XJ)

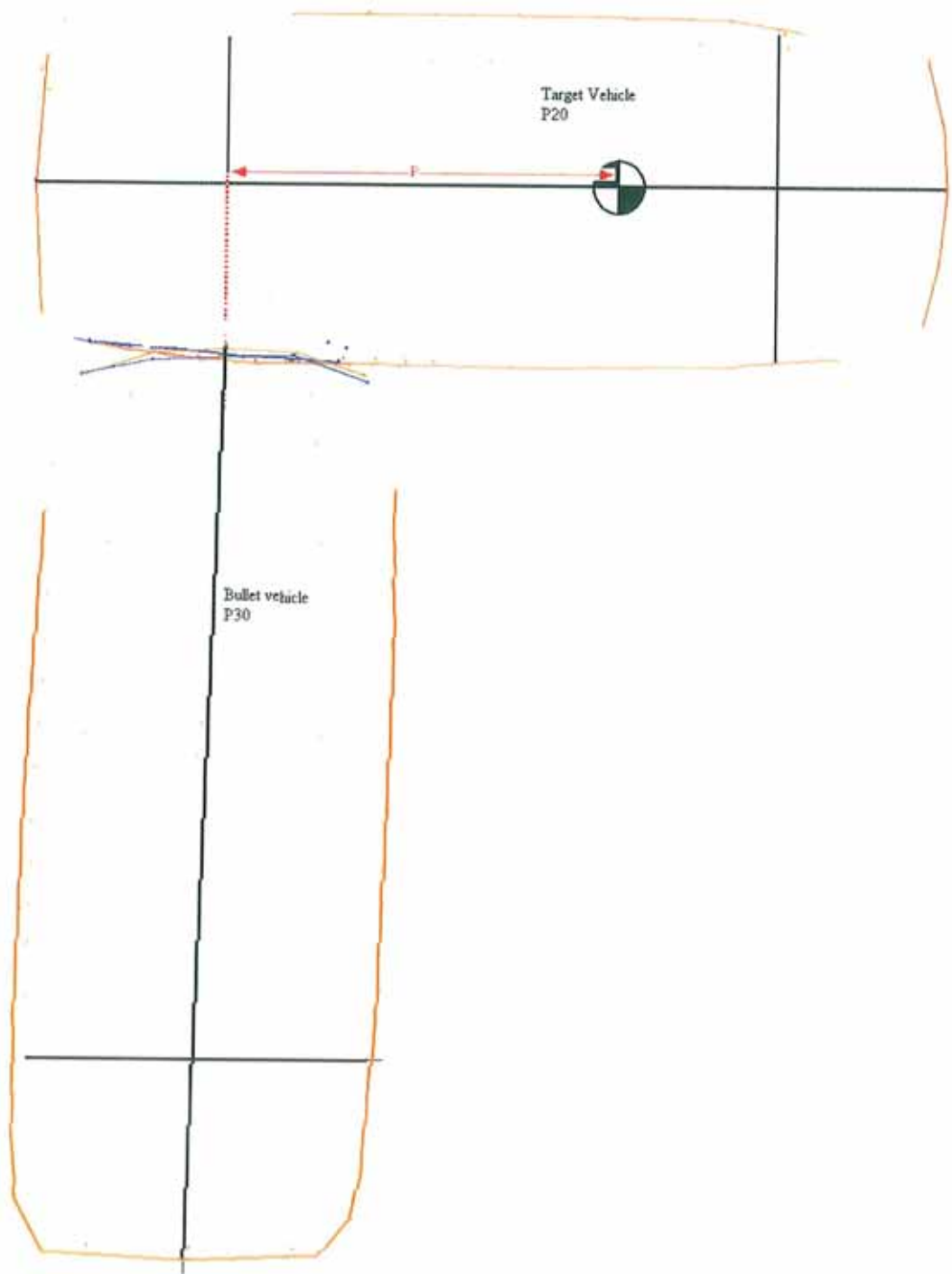


Figure 8.11 Collision 2 (Mondeo – Vectra)

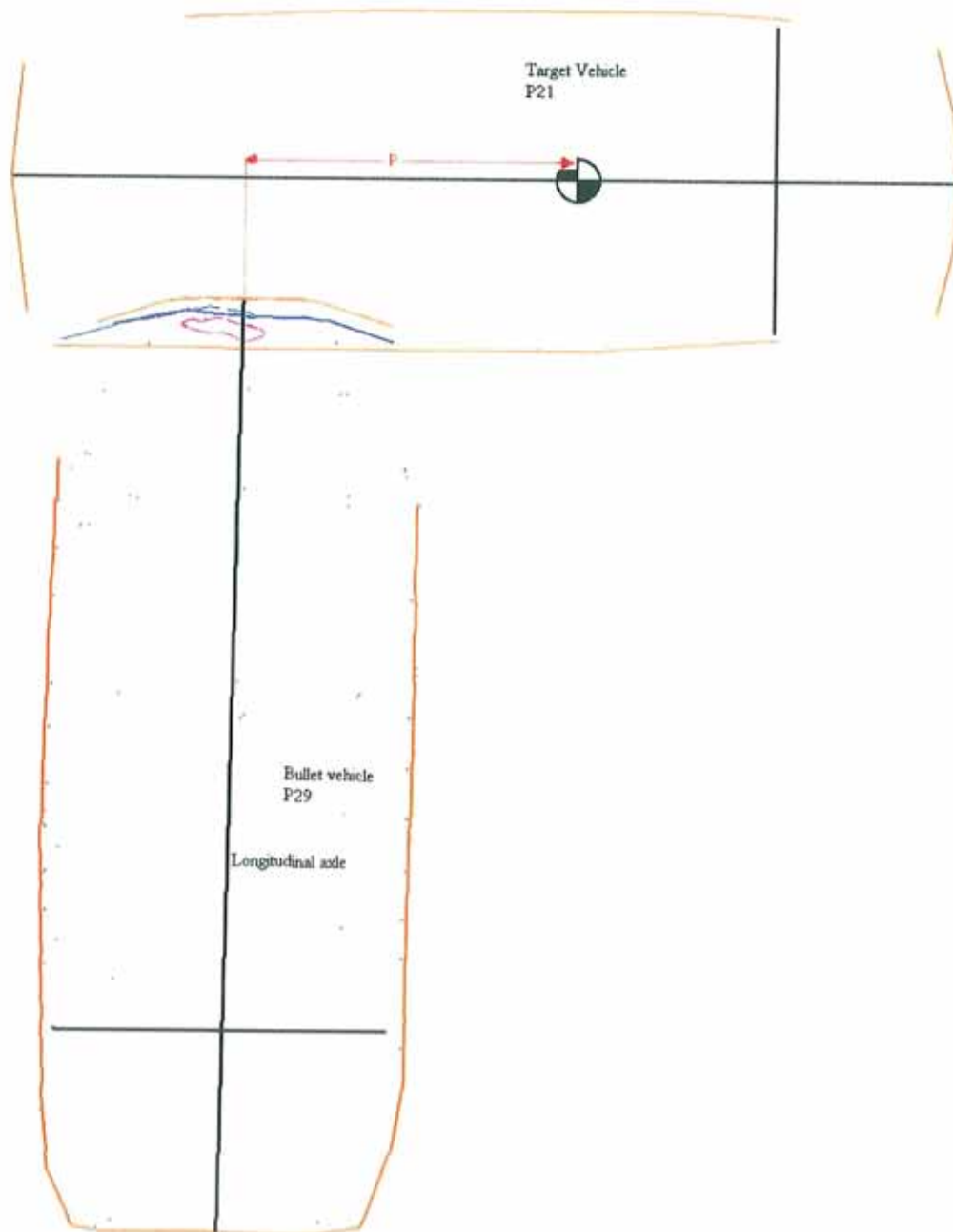


Figure 8.12 Collision 3 (Mondeo – Vectra)

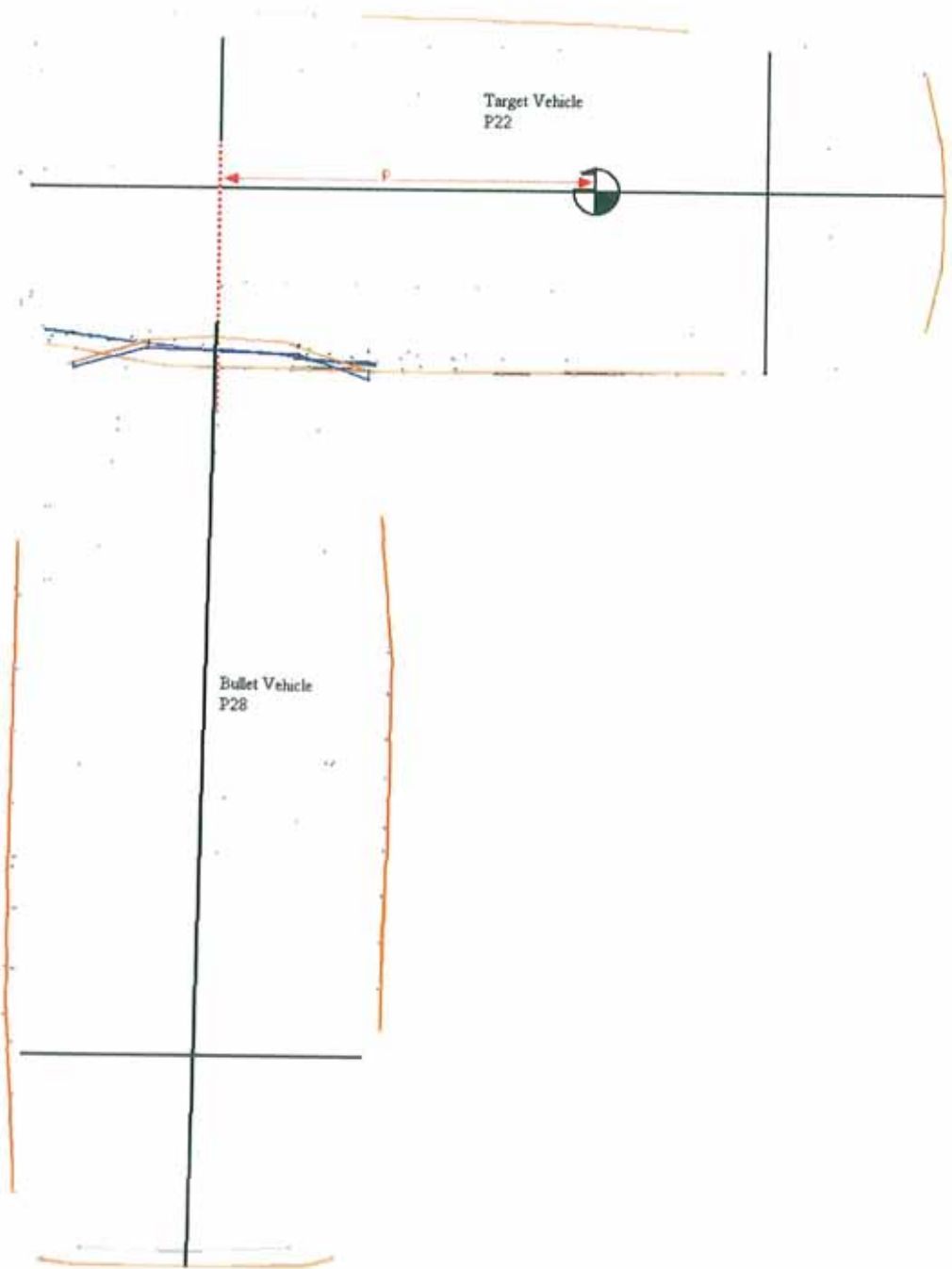


Figure 8.13 Collision 4 (Mondeo – Vectra)

Table 8B contains the angles of orientation between the longitudinal axes of the bullet and target vehicles for each of the collisions. The organisers of the staged collisions set-up the vehicles with 90° between the longitudinal axes of the bullet and target vehicles.

Collision	Actual Angle	Measured Angle	Difference
1	90°	85°	-5°
2	90°	91°	1°
3	90°	92°	2°
4	90°	93°	3°

Table 8B Orientation of Vehicles

A study by Ueyama et al [20] compared the orientation of vehicles using photogrammetric models with the orientation of the vehicles at their maximum engagement from high-speed footage of twelve collisions and found an accuracy of $\pm 5^\circ$.

Table 8B(i) shows Ueyama et al results for the T-style collisions they examined [20].

Ueyama Test	Actual Angle	Measured Angle	Difference
1	90°	90°	0°
5	90°	92°	2°
6	90°	90°	0°
8	90°	88°	-2°
9	90°	96°	6°
10	90°	94°	4°

Table 8B(i) Ueyama's Orientation of Vehicles

The above tables of results confirm that models created with PhotoModeler of a vehicle's deformation are a very useful tool in the orientation of the vehicles, which is a key step in the reconstruction of a collision.

8.2.2 Calculation of Speed of Bullet Vehicle

The crush depth was measured from the crush profile for each of the vehicles. These measurements along with other information (given in table 8C) were used to calculate the pre-impact speed for the bullet vehicle from each of the collisions. The method of estimating speed from crush damage was empirically developed by D P Wood, the method is discussed in chapter 3, the following are a summary of the equations used in the calculation of the speeds in this section. The full calculations are shown in appendix C.

Energy Equivalent Speed, V_{EES} , of the bullet vehicle is,

$$V_{EES} = 7.41 + 191.79 \left(\frac{\text{Average Crush}}{\text{Length}} \right)^{2/3}, \text{ and the Speed of bullet vehicle, } V, \text{ involved in}$$

$$\text{a T-style collision is } V = \left(\frac{M_k}{M_T} \right)^{1/2} \left(1 + \frac{\text{Crush}_{\text{Target}}}{\text{Crush}_{\text{Bullet}}} \right)^{1/2} V_{EES}, \text{ where } M_k \text{ is the unloaded}$$

mass of the bullet vehicle and M_T is the total combined mass of the bullet and target vehicles. $\text{Crush}_{\text{Target}}$ and $\text{Crush}_{\text{Bullet}}$ are the measurements of crush depths on the target and bullet vehicles, there are two possible ways of obtaining these values. A single measurement of crush can be measured along the direction of principal force of the collision (taken to be the central line of the bullet vehicle) when the vehicles have been orientated and fitted together; or the average crush depth from across the width of the damage, on both the target and bullet vehicles.

Collision	Curb Mass /kg	Total Mass /kg	Length Bullet /m	Ave. Crush Bullet/m	Ave. Crush Target/m	Single Crush Bullet/m	Single Crush Target/m
1	1564	860.45	4.887	0.036	0.200	0.071	0.330
2	1186	367.29	4.334	0.047	0.057	0.068	0.081
3	1282	380.49	4.307	0.100	0.141	0.109	0.119
4	1230	373.98	4.316	0.046	0.047	0.043	0.047

Table 8C Summary of Vehicle Measurements and Masses

In the previous chapter it was found that measurements obtained from a PhotoModeler model have a Standard Deviation of 12.4mm. When this Standard Deviation is applied to the values above, the results in table 8D and 8E are obtained for the average crush and single crush respectively [57]. The Standard Deviation for the average crush is

$$(\sigma_{ave} = \frac{\sigma_{modelling}}{\sqrt{N}})$$

the Standard Deviation due to modelling with PhotoModeler divided

by the square-root of the number of crush measurements taken from across the width of the damaged area.

Collision	Length Bullet /m	Standard Deviation /m	Ave. Crush Bullet/m	Standard Deviation /m	Ave. Crush Target/m	Standard Deviation /m
1	4.887	0.0124	0.036	0.0044	0.200	0.0038
2	4.334	0.0124	0.047	0.0056	0.057	0.0044
3	4.307	0.0124	0.100	0.0056	0.141	0.0039
4	4.316	0.0124	0.046	0.0056	0.047	0.0036

**Table 8D Average Crush Measurements and Standard Deviation due to measuring
from photogrammetric model**

Collision	Length Bullet /m	Standard Deviation /m	Single Crush Bullet/m	Standard Deviation /m	Single Crush Target/m	Standard Deviation /m
1	4.887	0.0124	0.071	0.0124	0.330	0.0124
2	4.334	0.0124	0.068	0.0124	0.081	0.0124
3	4.307	0.0124	0.109	0.0124	0.119	0.0124
4	4.316	0.0124	0.043	0.0124	0.047	0.0124

**Table 8E Single Crush Measurements and Standard Deviation due to measuring
from photogrammetric model**

The values presented in table 8C were used to calculate the pre-impact speeds of the bullet vehicles for both the average and single crush cases, for each collision.

A Monte Carlo simulation was run to find the range of pre-impact speed when the Standard Deviation due to measurement from a photogrammetric model (section 7.4) is

included. Tables 8F and 8G show the actual and calculated speeds of the bullet vehicle, the fiftieth percentile (when the values obtained from the simulation are sorted, this is the middle value) and the probable range of speeds found with the simulation (the twenty-fifth to seventy-fifth percentiles) for both the average and single crush. With the probable range the actual speed has a one in four chance of being below the range and a one in four chance of being above the range.

Collision	Actual Speed / km/h	50th Percentile / km/h	Standard Dev. / km/h	Probable Range / km/h
1	49.4	50.7	3.4	48.5 – 53.1
2	38.0	45.0	2.6	43.1 – 46.8
3	56.8	65.6	2.0	64.3 – 67.0
4	42.1	42.4	2.4	40.8 – 44.0

Table 8F Summary of Bullet Vehicle Pre-Impact Speeds (Average Crush), probable range due to standard deviation from photogrammetric modelling

Collision	Actual Speed / km/h	50th Percentile / km/h	Standard Dev. / km/h	Probable Range / km/h
1	49.4	47.0	4.2	44.6 – 49.9
2	38.0	44.8	3.7	42.4 – 47.2
3	56.8	61.2	2.9	59.3 – 63.2
4	42.1	42.6	5.9	39.2 – 44.9

Table 8G Summary of Bullet Vehicle Pre-Impact Speeds (Single Crush), probable range due to standard deviation from photogrammetric modelling

It can be seen from the above tables that the actual speed of the bullet vehicle falls within the probable range for the first and fourth case study and outside for the other two studies, for both average and single crush depth measurements.

Table 8H compares the actual crush to the values obtained for the fiftieth percentile of both the average and single crush Monte Carlo simulations.

Collision	Actual Speed / km/h	Ave. 50th Percentile / km/h	Single 50th Percentile / km/h	Ave. Diff. (Ave – Act) / km/h	Single Diff. (Sin. – Act) / km/h
1	49.4	50.7	47.0	1.3	-2.4
2	38.0	45.0	44.8	7.0	6.8
3	56.8	65.6	61.2	8.8	4.4
4	42.1	42.4	42.6	0.3	0.5

Table 8H Comparison of Average and Single Crush Speed Results

Table 8I shows the range of differences (Calculated – Actual) in the speeds, when the speed is calculated from the average crush or from the single crush measurement along the principal direction of force of the collision. The values returned by t-tests for this data are also shown.

	Difference / km/h	t-Test
(Average – Actual)	0.3 – 8.8	2.08
(Single – Actual)	-2.4 – +6.8	1.14

Table 8I Differences due to different crush measurement selection

Due to the small sample size, the values returned by the t-tests confirm that these differences are insignificant. There is no statistical difference in results obtained when crush depth is the average value of crush from across the damaged area or when it is a single measurement along the single line of the bullet vehicle on both the target and bullet vehicles.

The Standard Deviation in tables 8F and 8G is only the Standard Deviation of measuring with a photogrammetric model, as discussed in section 7.4. There is also a Standard Deviation associated with the formulae developed by D P Wood, which for a T-style collision is ± 5.5 mph (± 8.9 km/h) [7] [57]. When this Standard Deviation is included in a Monte Carlo simulation (appendix D) to find the range of probable speeds of the bullet vehicles, the results presented in tables 8J and 8K were found.

Collision	Actual Speed / km/h	50th Percentile / km/h	Standard Dev. / km/h	Probable Range / km/h
1	49.4	50.8	9.52	44.5 – 57.4
2	38.0	45.0	9.26	38.8 – 51.5
3	56.8	65.7	9.11	59.9 – 72.0
4	42.1	42.6	9.15	36.4 – 48.8

**Table 8J Summary of Bullet Vehicle Pre-Impact Speeds (Average Crush),
Standard Deviation due to photogrammetric modelling and speed calculation**

Collision	Actual Speed / km/h	50th Percentile / km/h	Standard Dev. / km/h	Probable Range / km/h
1	49.4	47.3	9.81	40.8 – 53.8
2	38.0	45.0	9.71	38.5 – 51.7
3	56.8	61.1	9.24	54.8 – 67.5
4	42.1	42.4	10.99	35.7 – 49.3

Table 8K Summary of Bullet Vehicle Pre-Impact Speeds (Single Crush), Standard Deviation due to photogrammetric modelling and speed calculation

It can be seen from the above results that when the Standard Deviation due to measuring and the formulae for calculating the speed are used to find a range of probable results, the actual speed of the bullet vehicle falls within the probable range for the first and fourth case study and outside for the other two studies, when average crush depth measurements from across the damaged area are used to calculate the speed. The actual speed of the bullet vehicle falls within the probable range for the first, third and fourth case studies and just outside for the second study, when the crush depth measurement is a single measurement along direction of the principal force of the collision. There is a one in four chance of the actual speed being below or above the probable range, as it is the range from the twenty-fifth percentile to the seventy-fifth percentile. Therefore the above results confirm that photogrammetric modelling of vehicles is a very good tool in the reconstruction of collisions.

Chapter 9 CONCLUSIONS

The aim of this research was to develop an accurate, fast and low cost method of measuring the damage caused to a vehicle during a collision. An accurate record of the damage sustained by a vehicle during a collision is of crucial importance in reconstructing the collision. Accident reconstruction aids in the understanding of what occurs during a collision enabling safety devices such as seat belts, airbags and ABS brakes, to be developed and improved, thus leading to better occupant protection. As accident reconstruction can determine the cause of a collision, this can expose driver error which in turn can help an investigator to determine if a driver is at fault. With improvements to and extended use of reconstruction techniques, drivers will be aware of the increased likelihood that they will be held accountable for a collision and as a consequence become safer drivers.

All collisions must obey the laws of physics, as discussed in chapter 2, in general vehicle collisions are inelastic (plastic) collisions. The kinetic energy is not conserved, but often vehicle collisions are totally inelastic, when the vehicles stick together after the collision and the velocities of the centres of gravity of the vehicles after the collision are the same. During a collision some of the pre-impact kinetic energy of the moving vehicle is converted to kinetic energy of deformation of the vehicle and converted to heat by frictional forces of the melting of the tyres and to acoustic energy in the sound made by the impact. The amount of remaining / residual damage sustained by the vehicle can be used to estimate the amount of energy absorbed and the total kinetic energy, and thus the pre-impact speed of the vehicle. As outlined in chapter 3 D P Wood [7] developed an empirical relationship between the amount of crush sustained

by a vehicle during a collision and the kinetic energy of the vehicle before the collision. In order to calculate the pre-impact speed using Wood's relationship, measurements of the crush depth, pre-impact vehicle length and the unloaded and loaded masses of the vehicles involved are required. There are a number of other methods of obtaining pre-impact speeds from crush also requiring crush and pre-impact measurements. There are a number of computer packages such as PC Crash, Ed Crash, which calculate the pre-impact speed. These packages usually require information about the orientations of the vehicles. Ueyama et al [20] studied twelve collisions that took place at road intersections. They found that photogrammetric models of vehicles crush at bumper level could be matched together and the angles of orientation of the vehicles with respect to one another could be found to within 5° of the true orientations, which were measured from footage of the collisions at the moment when the vehicles were at maximum engagement.

There are numerous of ways of measuring the crush damage sustained by a vehicle during a collision (as shown in chapter 4). Irrespective of the method of measurement used the operator must determine the damaged plane (i.e. front, rear or side of the vehicle) the width of the damaged area, and the height above ground at which damage should be measured. Traditionally crush depth has been measured by placing a reference line a set distance from the vehicle (generally at the estimated location of the undamaged vehicle's surface) and measuring from this line to the damaged surface. It has become more and more common for surveying instruments to be used to measure crush and record information at accident sites. Theodolites can be used to accurately obtain the coordinates of points on a vehicle's surface and around an accident site. However using a theodolite to record the coordinates of points that outline a damaged

vehicle's profile is very time consuming. Using a theodolite to obtain a detailed profile of a vehicle and its crush takes approximately 1.5 – 2 hours. Laser scanners can create three dimensional models of the surfaces of vehicles in moments. A laser scanner can produce a detailed model of a vehicle in approximately 15 minutes. However these instruments currently cost in the region of €250,000 to €500,000 while photogrammetric equipment can be purchased for €2,000. The Zurich City Police currently use a combination of laser scans and photogrammetric models to provide detailed records of collisions.

As explained in chapter 4 photogrammetric models require points on the object being modelled to appear in at least two photographs taken from different view points. When modelling a vehicle it is best practice to place targets on the vehicle's surface to highlight the points of interest that are to be included on the model, so that they can be accurately located and cross-referenced in the photographs. The targets can be placed on the vehicle and the required photographs taken in approximate 25 minutes. Photogrammetric equipment varies in price, from hundreds of euros to hundreds of thousands of euros. Photogrammetry was chosen as the technique to measure crush damage for this project as it immediately met two of the criteria set out for this project (speed and cost). It is fast; the data required can be collect in 25 minutes. It is low cost; the equipment needed (an over-the-counter Olympus C5060 digital camera and PhotoModeler a photogrammetric modelling software package) were purchased for less than €2000.

The remaining criterion was accuracy. In order to establish the accuracy of this photogrammetric technique, which used low cost over-the-counter equipment, a number of experiments were carried out, the details of which are set out in chapter 7.

A computational model was written (section 7.1) to examine the error associated with the mis-tagging of image points on two photographs. The programme randomly selected two object points in space and found the distance between them, this is the actual length. Then using the equation of a straight line and the coordinates of the principal point of the camera the locations of these points were found on the two photographs. An error of either -1, -2 or -3 pixels was then randomly select and added to the image locations, these new locations were the mis-tagged image points. The mis-tagged image points and the locations of the principal point of the camera when both photographs were taken were used to calculate the equations of straight lines. The points of intersection of these lines were the modelled locations of the object points. The distance between these points was the photogrammetric distance. This experiment found that on average the photogrammetrically measured distance between the two modelled points is longer than the actual distance between the points.

A further experiment compared Coordinate Measuring Machine measured lengths (considered to be the true lengths) with photogrammetrically measured lengths and with lengths measured using a tape measure. It was found for lengths in the range from 0.5m to 1m, that the average difference between photogrammetric and CMM measurements was -0.27mm (section 7.2.1A). This difference was found to be statistically significant and therefore photogrammetry produces values of distance that are less than those

produced by the CMM. The average difference between tape measurements and CMM measurements was found to be -0.06mm (section 7.2.1B).

This difference was found to be statistically insignificant and therefore Tape and CMM measurements can be considered equal. The average difference between photogrammetric and tape measurements was found to be 0.13mm (section 7.2.1C). This difference was found to be statistically significant and therefore photogrammetry produces distance values that are greater than the tape measurements; this concurs with the results from computational modelling (7.2.4).

An experiment comparing photogrammetrically measured lengths of pipes, with tape measurements for lengths from 0.7m to 4m , found the average difference between photogrammetric and tape measurements to be 0.39mm (section 7.2.2). This difference was found to be statistically significant and therefore photogrammetry produces results that are greater than the tape measurements, again concurring with the results from computational modelling. When the data from the previous two experiments were combined and analysed, the average difference between photogrammetric and tape measurements was 0.35mm (section 7.2.2). This difference was found to be statistically significant and therefore when a simple object is photogrammetrically modelled and its dimensions compared to tape measurements, 0.35mm should be subtracted from the photogrammetric measurements.

When the results of the above experiment were compared with the results from the computational model (section 7.2.4), the range of the differences (photogrammetric measured lengths – actual lengths) found in the pipe modelling experiment is within the

range of differences (measured lengths – actual lengths) found in the computational model. Therefore it can be concluded that the significant cause of the variation of the values of the lengths of the pipes is the mis-tagging error studied using the computational model.

A further experiment examined the capability of photogrammetry to model objects with complex shapes i.e. vehicles (section 7.3). Again the differences between photogrammetric and tape measurements were examined. The average difference was found to be 6.65 mm (section 7.3.1) when the vehicle was modelled from photographs taken in overcast lighting conditions. Overcast lighting is the best lighting for photographing vehicles, as there is no glare from the sun or the camera's flash, and it is naturally bright enough to see the points of interest on the vehicle's surface. When the differences between photogrammetric and tape measurements from all the models created in all lighting conditions were examined (section 7.3.2), the average difference was 12.81mm. This difference is statistically significant. Therefore when a vehicle is measured using a photogrammetric model and the results compared to tape measurements, 12.81mm should be subtracted from the photogrammetric measurement.

When the results of the above experiment are compared with the results from the computational model (section 7.3.4), the range of values of the differences (photogrammetric measured length – actual length) found in the vehicle modelling experiment is just larger than the range of differences (measured length – actual length) found in the computational model. It can be concluded that the significant cause of the variation of the values of the lengths on the vehicle when modelled in all lighting conditions is still the mis-tagging error, but that the error used in the programme should

have been increased with distance of the point of interest from the camera. A second computational programme was written, with error on the tagging of the point increasing with its distance from the camera. There was better agreement between the vehicle and computational model ranges of differences between actual and measured lengths. Therefore the increasing error in the computational model with distance from the camera is a better representation of the error in using photogrammetry. This reflects the reality when modelling, as when the points of interest are further away from the camera they become more difficult to identify and locate and therefore the mis-tagging error increases.

A final experiment examined the repeatability of modelling with PhotoModeler (section 7.4). Different models of the same vehicle were merged or superimposed with each other. The models were matched together at points at their rear and the displacements between points at the fronts of the models were measured. An insignificant mean value of 0.14mm was found for the differences in the locations of points between the two superimposed models. A standard deviation of 12.40mm was found. Therefore the uncertainty of modelling and measuring with PhotoModeler is $\pm 12.40\text{mm}$.

From this experiment, the main conclusion is that when using PhotoModeler to model vehicles, a standard deviation of 12.40mm should be applied to the measurements obtained from the model. Lengths and therefore crush depths of less than 12.40mm cannot be confidently measured using Photomodeler.

Having established that low cost photogrammetric equipment was capable of consistently modelling a vehicle, its capability of modelling the detail of the crush

damage sustained by a vehicle was studied. The first vehicle examined (8.1.1) was a Saab 93. When the crush damage was examined using the photogrammetric crush profile created, a circular indentation having a diameter of 24cm was found in the side of the vehicle. This vehicle had slid sideways into a pole whose diameter was 25.4cm. The second vehicle (8.1.2) was also a Saab 93. The crush profile of this vehicle showed that the front of the vehicle had been deformed rearwards. This vehicle struck a deformable barrier with 40% of the front of the vehicle making contact with the barrier. The crush profile showed that approximately 46% of the bumper was crushed rearwards; the rest projecting forwards, this is consistent with an offset frontal collision. A Toyota Corolla (8.1.3) was also modelled and its crush profile revealed the outline of a set of twin wheels. This vehicle had collided with the rear wheels of a truck. From these examples it is possible to see that photogrammetry is not only capable of modelling crush damage sustained by vehicles during collisions but the crush profile is detailed enough to also determine the dimensions and profile of the object struck.

An Opel Corsa (8.1.4) was modelled and this vehicle showed an example of a limitation of photogrammetric examination of vehicles. Following the impact the bumper structurally recovered and in so doing hid the extent of the damage sustained by the vehicle from view. Therefore the vehicle was photographed and modelled with and without its bumper and the crush depth measurements from both models were compared. The hidden crush damage caused an underestimation of the energy equivalent speed of 8.5 km/h. Therefore the operator must ensure that the true extent of the damage sustained by the vehicle is visible in all the photographs. Photogrammetric models can only model what appears in the photographs.

Four T-style staged collisions were reconstructed (section 8.2). The vehicles were photographed and modelled before and after the collisions. Crush profiles were created and printed so that the vehicles could be orientated with respect to one another at maximum engagement (8.2.1). The organisers of the collisions established a 90° angle between the longitudinal axes of the bullet and target vehicles. When the photogrammetric crush profiles were fitted together the angles of orientation ranged from 85° to 93°. This is consistent with results found by Ueyama et al [20] that the accuracy of vehicle orientation using photogrammetric models is $\pm 5^\circ$.

The crush depths and pre-impact lengths were measured from the same models and used in the equations developed by Wood (Chapter 3) to calculate the pre-impact speed of the bullet vehicles in all four collisions (Appendix C). A Monte Carlo simulation (Appendix D) was written to find the pre-impact speed when the standard deviation associated with photogrammetric measurement found in the earlier experiments, was included in the crush and length measurements. The simulation found the fiftieth percentile of the speed values and the probable range of speeds of the bullet car in each of the collisions (8.2.2). There is a one in four chance of the actual speed being below or above the probable range from the twenty-fifth percentile to the seventy-fifth percentile. Two methods of finding the values for the crush depth were used: a single measurement of crush along the direction of principal force of the collision (taken to be the central line of the bullet vehicle) when the vehicles have been orientated and fitted together and the average crush depth across the width of the damage, on both the target and bullet vehicles. The actual speed of the bullet vehicle fell within the probable range for the first and fourth collisions studied and outside for the other two collisions, for both crush measurement options (Tables 8F and 8G).

The calculated speeds (fiftieth percentile) for both options for measuring the crush depth were compared to the actual speeds of the collisions, and the differences between them were found to be statistically insignificant (Table 8I). Therefore either option can be used for the crush depth measurement.

The uncertainty associated with the equations developed by D P Wood [7] to calculate the speeds was also included in a Monte Carlo simulation. The actual speed of the bullet vehicle fell within the range for the first and fourth collisions studied and outside for the other two collisions, for the average crush measurement option (Table 8J). The actual speed of the bullet vehicle fell within the probable range for the first, third and fourth collisions studied and outside for the second collision, by 0.5km/h, for the single crush measurement option (Table 8K).

There is a one in four chance of the actual speed being below or above the probable range, as it is the range from the twenty-fifth percentile to the seventy-fifth percentile. Therefore the finding that actual speeds were within or very close to the probable range, confirms that photogrammetric modelling of vehicles is a very reliable tool in the reconstruction of collisions.

The minimum depth of crush that can confidently be measured from a photogrammetric model is 12.40mm. Using this limit, the length of an average family vehicle to be 4260mm and D P Wood's equation $V_{EES} = 7.41 + 191.79 \left(\frac{\text{Average Crush}}{\text{Length}} \right)^{2/3}$ can be used to find the lower limit of the pre-impact speed that can be found. The average

crush is generally found from six measurements made across the damaged area, therefore the standard deviation is 5.06mm. Using twice this standard deviation in the above equation returns a 95% confidence range of speeds of 7.41km/h – 10.83km/h. It follows that collisions involving a bullet vehicle travelling at closing speeds of less than 10.83km/h cannot confidently be reconstructed using photogrammetric models.

Digital photogrammetry with an over-the-counter digital camera and PhotoModeler photogrammetric software met the aim of this project, which was to develop an accurate, fast and low cost method of measuring the damage caused to a vehicle during a collision. The equipment, software and materials needed to measure the damage sustained by a vehicle during a collision, using the technique set out in this thesis, can be purchased for a total of less than €2000. The technique reduces the time spent with the vehicle by half, with no reduction in accuracy compared with other methods in current use.

The main conclusion that can be drawn from this work is that photogrammetry is a very useful tool in the reconstruction of vehicle collisions. It is a highly accurate measuring method, involving length measurement uncertainty of $\pm 12.4\text{mm}$. It requires only a short period of time to be spent with the vehicle, approximately twenty minutes. It produces a permanent record of the vehicle, which can be examined at any stage, even after the vehicle has been repaired or completely destroyed. It allows vehicles that are located in different places to be fitted together to give the orientations at the time of impact, with an accuracy of $\pm 5^\circ$.

References

- [1] National Roads Authority, "Road Accident Facts Ireland 2002", NRA, St. Martin's House, Dublin, 2003.
- [2] World Health Organisation Website, <http://www.who.int/whr/2003/en>
- [3] Evans Leonard, "Traffic Safety and the Driver", Van Nostrand Reinhold, New York, 1991.
- [4] Weaver H. Joseph, Brach Raymond, *Limitations of Momentum Methods for Accident Reconstruction, The Principles Underlying Current Accident Reconstruction Methods and the Factors limiting Their Application*, "Forensic Accident Investigation: Motor Vehicles", Bohan Thomas L., Damask Arthur C., Butterworth Michie (ed), Law Publishers, Charlottesville Virginia, 1995.
- [5] Damask Arthur C., *An Introduction to the Physics of Motor Vehicle Accidents, Applications of the Laws of motion to Accident Reconstruction*, "Forensic Accident Investigation: Motor Vehicles", Bohan Thomas L., Damask Arthur C., Butterworth Michie (ed), Law Publishers, Charlottesville Virginia, 1995.
- [6] Serway Raymond A., "Physics for Scientists and Engineers with Modern Physics", Fourth Edition, Saunders College Publishing 1996.
- [7] Wood Denis P., *Determination of Speed from Crush, The Damage Solution and Its Application in the Energy-Equivalent-Speed Model*, "Forensic Accident Investigation: Motor Vehicles", Bohan Thomas L., Damask Arthur C., Butterworth Michie (ed), Law Publishers, Charlottesville Virginia, 1995.
- [8] Wood Denis P., *Consideration of the Elastic Compressive Properties of Cars in Frontal Impact*, SAE paper 1999-01-0095, Society of Automotive Engineers, Inc., 1999.
- [9] Wood Denis P., Mooney Stephen, *Modelling of Car Dynamic Frontal Crush*, SAE paper 970943, Society of Automotive Engineers, Inc., 1997.

- [10] Huang Mathew, *Vehicle Crash Mechanics*, ISBN 0-8493-0104-1 page 446, CRC Press, 2002
- [11] Johnson W., Mamalis A. G., *Crashworthiness of Vehicles*, Mechanical Engineering Publications, London, England, 1978
- [12] <http://www.progressive.com/vehicle-resources/crash-ratings-videos.aspx> (June 2002)
- [13] Campbell K. L., *Energy Basis for Collision Severity*, SAE paper 740565, February 1974.
- [14] Danckert H., *Development of Crash Energy Management Solutions*, SAE paper 760793, February 1976.
- [15] Hofferbarth J., Tommassoni J., *A Study of Structural and Resistant Requirements for Automobile Crash Survival*, proceeding of the 3rd International Conference on Automobile Safety, pp 28-1 – 28-88, San Francisco California USA, July 15 – 17 1974.
- [16] Kahne C. J., *Effect of Car Size on the Frequency and Severity of Rollover Crashes*, proceeding of the 13th International ESV Conference, Paris France, December 1991.
- [17] Wood D. P., Glynn C., Simms C., *Frontal collision behaviour: Comparison of on board collision recorder data with car population characterises*, IJ Crash Vol. 10 No. 1 pp61 – 73, 2005
- [18] Wood Denis P., *A Model For The Frontal Impact Crashworthiness Of The Car Population*, SPT-4 -The Fourth International Conference on Structural Failure, Product Liability and Technical Insurance Vienna, Austria 6-9 July 1992.
- [19] Tumbas N. S., Smith R. A., *Measurement Protocol for Quantifying Vehicle Damage from an Energy Basis Point of View*, SAE Paper 880072, February 1988.

- [20] Ueyama M., Makishita H., Saito S., *Determination of Collision Configurations from Vehicle Deformation Patterns*, SAE paper 910127, Society of Automotive Engineers, Inc., 1991.
- [21] Coyle F., Toal V., Wood D. P., *Photogrammetric Reconstruction of Motor Vehicle Accidents*, Seminar proceedings Photogrammetry and Laser Scanning for Surveying and Recording Cultural Heritage, Dublin Institute of Technology, 26 January 2007.
- [22] <http://www.rudydegger.com/> (September 2002)
- [23] Bartlett Wade, Wright William, Masory Oren, Brach Raymond, Baxtor Al, Schmidt Bruno, Navin Frank, Stanard Terry, *Evaluating the Uncertainty in Various Measurement Tasks Common to Accident Reconstruction*, SAE paper 2002-01-0546, Society of Automotive Engineers, Inc. 2002.
- [24] Coyle F., Toal V., Wood D. P., *Photogrammetric Inaccuracies caused by Geometry of Modelling Process*, proposed paper, 2008.
- [25] Coyle F., Toal V., Wood D. P., *Motor Vehicle Crush Depth Measurement using Close – Range Digital Photogrammetry*, Conference proceedings International Symposium Modern Technologies, Education and Professional Practice in Geodesy and Related Fields, Sofia, 3 – 4 November 2005.
- [26] <http://www.leica-geosystems.com> (March 2005)
- [27] Arnold J., Braun M., “Argument for 3D-Scanning and 3D-Photogrammetry as Basis for Accident Reconstruction”, IRCOBI Conference paper – Graz (Austria) September 2004.
- [28] Demonstration of Riegl Laser Scanner, Dublin Institute of Technology, 25-26 October 2005.
- [29] <http://www.riegl.co.uk> (September 2005)
- [30] “Frequency Modulated Coherent Laser Radar Technology Description”, Leica-geosystems.
- [31] <http://www.3dscanner.co.uk> (March 2005)

[32] Egan Glenn, *Comparison of Industrial Measurement Techniques*, School of Surveying and Spatial Information Systems, The University of New South Wales, October 2002.

[33] Fedak Michael, *3D Measurement Accuracy of a Consumer-Grade Digital Camera and Retro-Reflective Survey Targets*, InSpec Engineering Services, West Vancouver, BC, Canada.

[34] Suthau T., Morè J., Wiedemann A., Franzen J., *Closed Range Photogrammetry with CCD Cameras and Matching Methods – Applied to the Fracture Surface of an Iron Bolt*, Technical University of Berlin, Department for Photogrammetry and Cartography.

[35] Lie, *Photogrammetric Measurements of Damaged Vehicles in Road Traffic Accidents*, pages 488 – 493, 12th International Technical Conference on Experimental Safety Vehicles, 1989.

[36] Faig W., Wilson F. R., King D., Shih T. Y., *Photogrammetric Solution for Vehicle – Damage Investigation*, Journal of Transportation Engineering, 1992.

[37] Mikhail Edward M., Bethel James S., McGlone J. Chris, *Introduction to Modern Photogrammetry*, John Wiley & Sons, Inc, New York, 2001.

[38] Cox Arthur, “Photographic Optics” Fifteenth Edition, Focal Press, London and New York, 1974.

[39] <http://library.thinkquest.org> The optics book (January 2003)

[40] Wolf P., “Elements of Photogrammetry with Air Photo Interpretation and Remote Sensing”, Second Edition, McGraw-Hill 1983.

[41] American Society of Photogrammetry, “Non-Topographic Photogrammetry” Second Edition, Editor in Chief, Karara H. M., 1989.

- [42] Ang Tom, "Advanced Digital Photography", Octopus Publishing Group Ltd., London, 2003.
- [43] Watson J., "Optoelectronics", Van Nostrand Reinhold (UK) Co. Ltd., 1988.
- [44] Langford Michael, "Advanced Photography" Sixth Edition, Focal Press, London and New York, 1998
- [45] Hedgecoe J., "The new manual of Photography", DK 2003.
- [46] Moffit F. H., Mikhail E. M., "Photogrammetry", Harper & Row 1980.
- [47] Atkinson K. B., "Close Range Photogrammetry and Machine Vision", Whittles 1996.
- [48] Operator's Manual D7 Metric Camera.
- [49] Operator's Manual Olympus C5060 Digital Camera.
- [50] "PhotoModeler Pro 4.0 User Manual", Eos Systems Inc., Vancouver, 2000
- [51] "PhotoModeler Pro 5.0 User Manual", Eos Systems Inc., Vancouver, 2003.
- [52] American Society of Photogrammetry, "Manual of Photogrammetry" Fourth Edition, Editor in Chief, Slama Chester C., 1980
- [53] Mooney Kevin, "Analytical Photogrammetry" lecture notes, Dublin Institute of Technology, 1998.
- [54] Coyle F., Toal V., Wood D. P., *The Suitability of Digital Photogrammetry with PhotoModeler Software for Accident Investigation*, Conference proceedings FISITA World Automotive Congress, Barcelona, May 23 - 27 2004, paper number F2004SC09.

- [55] Coyle F., Toal V., Wood D. P., *Photogrammetric Measurement of Motor Vehicle Crush Depth*, Conference proceedings 7th International Conference of the Institute of Traffic Accident Investigators, UK, November 12 - 13 2005, pages 113 – 120.
- [56] In conversation with Jim O'Donnell, National Metrology Laboratory, Dublin, 2003.
- [57] Coyle F., Toal V., Wood D. P., *Photogrammetrically Measured Vehicles and Resulting Speed Calculations*, proposed paper, 2008.
- [58] Fenton Stephen, Johnson Wendy, LaRocque James, Rose Nathan, Ziernicki Richard, *Using Digital Photogrammetry to Determine Vehicle Crush and Equivalent Barrier Speed (EBS)*, SAE paper 1999-01-0439, Society of Automotive Engineers, Inc., 1999.
- [59] Karvelis A. V., Rogers, M. W., Anderson C. E., Liubinskas A., *Computer-Aided 3-D Surface Reconstruction During High Speed Crush Events*, SAE paper 910320, February 1991.
- [60] Switzer D. A., Candrlie T. M., *Factors Affecting the Accuracy of Non-Metric Analytical 3-D Photogrammetry, using PhotoModeler*, SAE paper 1999-01-0451.
- [61] Dierckx B., De Veuster C., Guidault P-A., *Measuring a Geometry by Photogrammetry: Evaluation of the Approach in View of Experimental Modal Analysis on Automotive Structures*, SAE paper 2001-01-1473.
- [62] Jechev D., *Close-Range Photogrammetry with Amateur Camera*, GIS Sofia Ltd., Bulgaria
- [63] Husher S. E., Varat M. S., Kerkhoff J. F., *Survey of Photogrammetric Methodologies for Accident Reconstruction*, Proceedings of the Canadian Multidisciplinary Road Safety Conference VII; June 17 – 19 1991, Vancouver, British Columbia.
- [64] Pappa R. S., Giersch L. R., Quagliaroli J. M., *Photogrammetry of a 5m Inflatable Space Antenne With Consumer Digital Cameras*, NASA Langley Research Center,

George Washington University, University of Connecticut, USA,
(<http://www.photomodeler.com/products/photomodeler/documents/NASA.pdf>), April
2008.

[65] Rucoba R., Duran A., Carr L., Erdeljac D., *A Three-Dimensional Crush Measurement Methodology using Two-Dimensional Photographs*, SAE paper 2008-01-0163

Appendix A

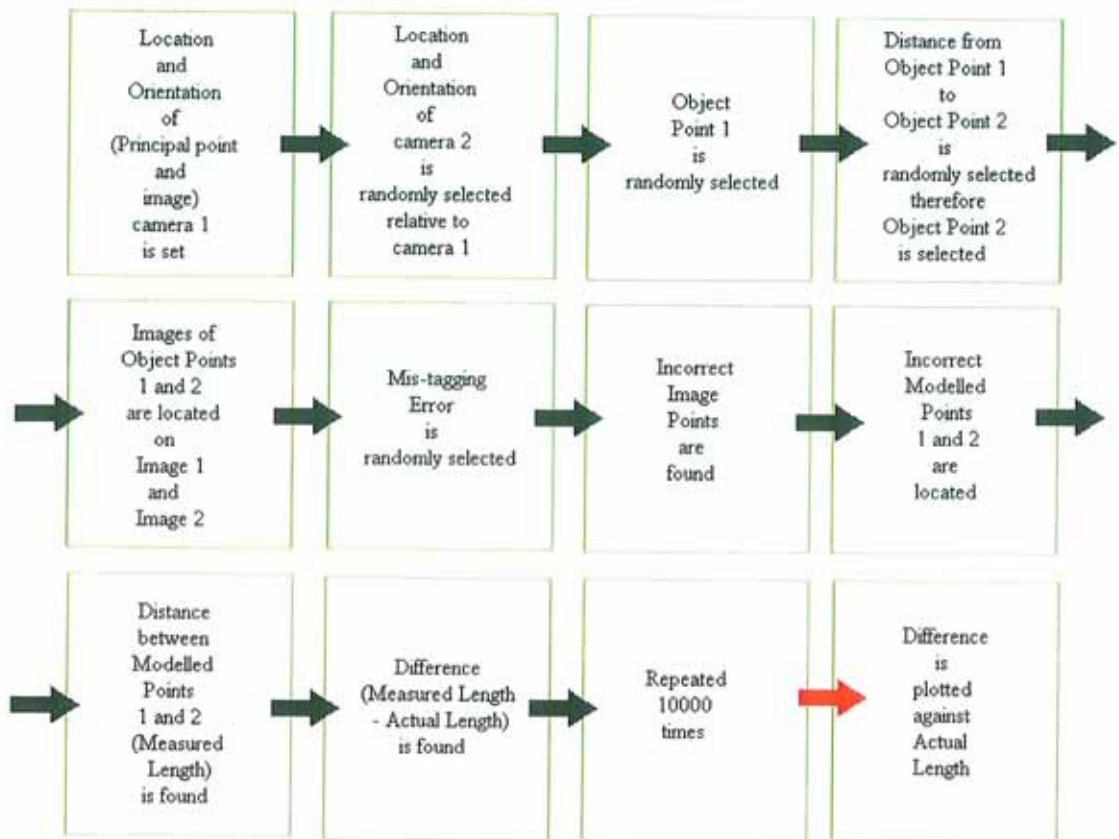


Figure 1. Flow Chart of Steps within Matlab Programme

Matlab Code for End on programme

```
%script to determine if there is a difference between true and measured
lengths
% ALL MEASUREMENTS IN MILLIMETERS (mm)
%location and orientation of camera 1
clear; close all;

pp1x=0;
pp1y=0;

Qf1=225*pi/180;

f=5.78; %focal length of camera lens.

iplx=0;
iply=(-1*f)/(cos((225-180)*pi/180));

%slope of image 1, angle of -45 to y axis
mip1=tan(-45*pi/180);

%equation of straight line that is image plane 1
```

```

%y-iply=mil*(x-iplx)

n=10000;

Qc=zeros(1,n);
Qf2=zeros(1,n);
Qr=zeros(1,n);
QL=zeros(1,n);
c=zeros(1,n);
r=zeros(1,n);
L=zeros(1,n);
Ex=zeros(1,n);
Fx=zeros(1,n);
Gx=zeros(1,n);
Hx=zeros(1,n);
Tx=zeros(1,n);
Ux=zeros(1,n);
Vx=zeros(1,n);
Wx=zeros(1,n);
Ey=zeros(1,n);
Fy=zeros(1,n);
Gy=zeros(1,n);
Hy=zeros(1,n);
Ty=zeros(1,n);
Uy=zeros(1,n);
Vy=zeros(1,n);
Wy=zeros(1,n);
areaA=zeros(1,n);
areaB=zeros(1,n);
cgxA=zeros(1,n);
cgyA=zeros(1,n);
cgxB=zeros(1,n);
cgyB=zeros(1,n);
Lm=zeros(1,n);
Lerr=zeros(1,n);

for i=1:n
    Qc(i)=(80+(100-80)*rand)*pi/180;
    Qf2(i)=(120+(150-120)*rand)*pi/180;
    Qr(i)=(15+(75-15)*rand)*pi/180;
    QL(i)=(140+(220-140)*rand)*pi/180;

    c(i)=1000+(3000-1000)*rand;
    r(i)=1000+(2000-1000)*rand;

    while r(i) >= c(i)
        c(i)=1000+(3000-1000)*rand;
        r(i)=1000+(2000-1000)*rand;
    end

    L(i)=1000+(5000-1000)*rand;

    %x,y coordinates of camera 2

    pp2x=c(i)*(cos(Qc(i)-(90*pi/180)));
    pp2y=-1*c(i)*(sin(Qc(i)-(90*pi/180)));

```

```

%equation of line that is image plane 2

%point on image plane 2

ip2x=pp2x;
ip2y=(-1*f)/(cos((180*pi/180)-Qf2(i)));

mip2=tan((180*pi/180)-Qf2(i)); %slope of image 2

%y=(mip2*x)-(mip2*ip2x)+ip2y

%x, y coordinates of point A

Ax=r(i)*(cos((90*pi/180)-Qr(i)));
Ay=r(i)*(sin((90*pi/180)-Qr(i)));

%equation of line through A and camera 1

mA1=(Ay-pp1y)/(Ax-pp1x); %slope

%y=(mA1*x)-(mA1*Ax)+Ay;

%equation of line through A and camera 2

mA2=(Ay-pp2y)/(Ax-pp2x); %slope

%y=(mA2*x)-(mA2*Ax)+Ay;

%x,y coordinates of image point A on image 1

iA1x=(-1*mip1*ip1x)+ip1y+(mA1*Ax)-Ay)/(mA1-mip1);
iA1y=(mip1*iA1x)-(mip1*ip1x)+ip1y;

%x,y coordinates of image point A on image 2

iA2x=(-1*mip2*ip2x)+ip2y+(mA2*Ax)-Ay)/(mA2-mip2);
iA2y=(mip2*iA2x)-(mip2*ip2x)+ip2y;

%x,y coordinates of point B

    bx=-1*L(i)*(sin((180*pi/180)-QL(i)));
    by=L(i)*(cos((180*pi/180)-QL(i)));

Bx=Ax+bx;
By=Ay+by;

%equation of line through B and camera 1

mB1=(By-pp1y)/(Bx-pp1x); %slope

%y=(mB1*x)-(mB1*Bx)+By;

%equation of line through B and camera 2

```



```

mB2=(By-pp2y)/(Bx-pp2x); %slope
%y=(mB2*x)-(mB2*Bx)+By);

%x,y coordinates of image point B on image 1
iB1x=(-1*mip1*ip1x)+ip1y+(mB1*Bx)-By)/(mB1-mip1);
iB1y=(mip1*iB1x)-(mip1*ip1x)+ip1y;

%x,y coordinates of image point B on image 2
iB2x=(-1*mip2*ip2x)+ip2y+(mB2*Bx)-By)/(mB2-mip2);
iB2y=(mip2*iB2x)-(mip2*ip2x)+ip2y;

%error on tagging a point on the image

err1=(2.43e-3+(8.34e-3*rand));
for err1=(7.99e-3:10.77e-3)
    err1=10.77e-3;
end
for err1=(5.21e-3:7.99e-3)
    err1=7.99e-3;
end
for err1=(2.43e-3:5.21e-3)
    err1=5.21e-3;
end

err2=(2.43e-3+(8.34e-3*rand));
for err2=(7.99e-3:10.77e-3)
    err2=10.77e-3;
end
for err2=(5.21e-3:7.99e-3)
    err2=7.99e-3;
end
for err2=(2.43e-3:5.21e-3)
    err2=5.21e-3;
end
err3=(-2.43e-3+(-8.34e-3*rand));
for err3=(-10.77e-3:-7.99e-3)
    err3=-10.77e-3;
end
for err3=(-7.99e-3:-5.21e-3)
    err1=-7.99e-3;
end
for err3=(-5.21e-3:-2.43e-3)
    err3=-5.21e-3;
end

err4=(-2.43e-3+(-8.34e-3*rand));
for err4=(-10.77e-3:-7.99e-3)
    err4=-10.77e-3;
end
for err4=(-7.99e-3:-5.21e-3)
    err4=-7.99e-3;
end

```

```

for err4=(-5.21e-3:-2.43e-3)
    err4=-5.21e-3;
end

%error location of A on image 1

ielA1x=iA1x-(err1*cos(45*pi/180));
ielA1y=iA1y+(err1*sin(45*pi/180));

%error location of A on image 2

ielA2x=iA2x+(err2*cos((180*pi/180)-Qf2(i)));
ielA2y=iA2y+(err2*sin((180*pi/180)-Qf2(i)));

%error location of B on image 1

ielB1x=iB1x-(err3*cos(45*pi/180));
ielB1y=iB1y+(err3*sin(45*pi/180));

%error location of A on image 2

ielB2x=iB2x+(err4*cos((180*pi/180)-Qf2(i)));
ielB2y=iB2y+(err4*sin((180*pi/180)-Qf2(i)));

%equation of line through ielA1 and camera 1, s1
ms1e=(ielA1y-pp1y)/(ielA1x-pp1x); %slope of s1

%equation of line through ielA2 and camera 2, s3
ms3e=(ielA2y-pp2y)/(ielA2x-pp2x); %slope of s3

%intersection of s1 and s3, E
Ex(i)=((-1*ms3e*ielA2x)+ielA2y+(ms1e*ielA1x)-ielA1y)/(ms1e-ms3e);
Ey(i)=(ms1e*Ex(i))-(ms1e*ielA1x)+ielA1y;

%equation of line through ielB1 and camera 1, k1
mk1e=(ielB1y-pp1y)/(ielB1x-pp1x); %slope of k1

%equation of line through ielB2 and camera 2, k3
mk3e=(ielB2y-pp2y)/(ielB2x-pp2x); %slope of k3

%intersection of k1 and k3, T

```

```

Tx(i) = ((-1*mk3e*ie1B2x)+ie1B2y+(mk1e*ie1B1x)-ie1B1y)/(mk1e-mk3e);
Ty(i) = (mk1e*Tx(i)) - (mk1e*ie1B1x)+ie1B1y;

%Distance from E to T is Lm (Lmeasured)
Lm(i) = sqrt(((Ex(i)-Tx(i))^2)+((Ey(i)-Ty(i))^2));

Lerr(i) = Lm(i) - L(i);
% Lerrsqr(i) = Lerr(i)^2;
% Lerr_rootsqr(i) = sqrt(Lerrsqr(i));
if Lerr(i) <= -100
    Qc(i) = (80+(100-80)*rand)*pi/180;
    Qf2(i) = (120+(150-120)*rand)*pi/180;
    Qr(i) = (15+(75-15)*rand)*pi/180;
    QL(i) = (140+(220-140)*rand)*pi/180;

    c(i) = 1000+(3000-1000)*rand;
    r(i) = 1000+(2000-1000)*rand;

    while r(i) >= c(i)
        c(i) = 1000+(3000-1000)*rand;
        r(i) = 1000+(2000-1000)*rand;
    end

    L(i) = 1000+(5000-1000)*rand;

    %x,y coordinates of camera 2

    pp2x = c(i)*(cos(Qc(i)-(90*pi/180)));
    pp2y = -1*c(i)*(sin(Qc(i)-(90*pi/180)));

%equation of line that is image plane 2

%point on image plane 2

ip2x = pp2x;
ip2y = (-1*f)/(cos((180*pi/180)-Qf2(i)));

mip2 = tan((180*pi/180)-Qf2(i)); %slope of image 2

%y = (mip2*x) - (mip2*ip2x) + ip2y

%x, y coordinates of point A

Ax = r(i)*(cos((90*pi/180)-Qr(i)));
Ay = r(i)*(sin((90*pi/180)-Qr(i)));

%equation of line through A and camera 1

mA1 = (Ay-pp1y)/(Ax-pp1x); %slope

%y = (mA1*x) - (mA1*Ax) + Ay;

```

```

%equation of line through A and camera 2
mA2=(Ay-pp2y)/(Ax-pp2x); %slope
%y=(mA2*x)-(mA2*Ax)+Ay;

%x,y coordinates of image point A on image 1
iA1x=(-1*mip1*ip1x)+ip1y+(mA1*Ax)-Ay)/(mA1-mip1);
iA1y=(mip1*iA1x)-(mip1*ip1x)+ip1y;

%x,y coordinates of image point A on image 2
iA2x=(-1*mip2*ip2x)+ip2y+(mA2*Ax)-Ay)/(mA2-mip2);
iA2y=(mip2*iA2x)-(mip2*ip2x)+ip2y;

%x,y coordinates of point B

    bx=-1*L(i)*(sin((180*pi/180)-QL(i)));
    by=L(i)*(cos((180*pi/180)-QL(i)));

Bx=Ax+bx;
By=Ay+by;

%equation of line through B and camera 1
mB1=(By-pp1y)/(Bx-pp1x); %slope
%y=(mB1*x)-(mB1*Bx)+By;

%equation of line through B and camera 2
mB2=(By-pp2y)/(Bx-pp2x); %slope
%y=(mB2*x)-(mB2*Bx)+By);

%x,y coordinates of image point B on image 1
iB1x=(-1*mip1*ip1x)+ip1y+(mB1*Bx)-By)/(mB1-mip1);
iB1y=(mip1*iB1x)-(mip1*ip1x)+ip1y;

%x,y coordinates of image point B on image 2
iB2x=(-1*mip2*ip2x)+ip2y+(mB2*Bx)-By)/(mB2-mip2);
iB2y=(mip2*iB2x)-(mip2*ip2x)+ip2y;

%error on tagging a point on the image
    err1=(2.43e-3+(8.34e-3*rand));
    for err1=(7.99e-3:10.77e-3)
        err1=10.77e-3;
    end
    for err1=(5.21e-3:7.99e-3)
        err1=7.99e-3;
    end
    for err1=(2.43e-3:5.21e-3)

```

```

    err1=5.21e-3;
end

err2=(2.43e-3+(8.34e-3*rand));
for err2=(7.99e-3:10.77e-3)
    err2=10.77e-3;
end
for err2=(5.21e-3:7.99e-3)
    err2=7.99e-3;
end
for err2=(2.43e-3:5.21e-3)
    err2=5.21e-3;
end
err3=(-2.43e-3+(-8.34e-3*rand));
for err3=(-10.77e-3:-7.99e-3)
    err3=-10.77e-3;
end
for err3=(-7.99e-3:-5.21e-3)
    err1=-7.99e-3;
end
for err3=(-5.21e-3:-2.43e-3)
    err3=-5.21e-3;
end

err4=(-2.43e-3+(-8.34e-3*rand));
for err4=(-10.77e-3:-7.99e-3)
    err4=-10.77e-3;
end
for err4=(-7.99e-3:-5.21e-3)
    err4=-7.99e-3;
end
for err4=(-5.21e-3:-2.43e-3)
    err4=-5.21e-3;
end

%error location of A on image 1
ie1A1x=iA1x-(err1*cos(45*pi/180));
ie1A1y=iA1y+(err1*sin(45*pi/180));

%error locatation of A on image 2
ie1A2x=iA2x+(err2*cos((180*pi/180)-Qf2(i)));
ie1A2y=iA2y+(err2*sin((180*pi/180)-Qf2(i)));

%error location of B on image 1
ie1B1x=iB1x-(err3*cos(45*pi/180));
ie1B1y=iB1y+(err3*sin(45*pi/180));

%error locatation of A on image 2

```

```

ielB2x=iB2x+(err4*cos((180*pi/180)-Qf2(i)));
ielB2y=iB2y+(err4*sin((180*pi/180)-Qf2(i)));

%equation of line through ielA1 and camera 1, s1
ms1e=(ielA1y-pp1y)/(ielA1x-pp1x); %slope of s1

%equation of line through ielA2 and camera 2, s3
ms3e=(ielA2y-pp2y)/(ielA2x-pp2x); %slope of s3

%intersection of s1 and s3, E
Ex(i)=((-1*ms3e*ielA2x)+ielA2y+(ms1e*ielA1x)-ielA1y)/(ms1e-ms3e);
Ey(i)=(ms1e*Ex(i))-(ms1e*ielA1x)+ielA1y;

%equation of line through ielB1 and camera 1, k1
mk1e=(ielB1y-pp1y)/(ielB1x-pp1x); %slope of k1

%equation of line through ielB2 and camera 2, k3
mk3e=(ielB2y-pp2y)/(ielB2x-pp2x); %slope of k3

%intersection of k1 and k3, T
Tx(i)=((-1*mk3e*ielB2x)+ielB2y+(mk1e*ielB1x)-ielB1y)/(mk1e-mk3e);
Ty(i)=(mk1e*Tx(i))-(mk1e*ielB1x)+ielB1y;

%Distance from E to T is Lm (Lmeasured)
Lm(i)=sqrt(((Ex(i)-Tx(i))^2)+((Ey(i)-Ty(i))^2));
Lerr(i)=Lm(i)-L(i);
end
if Lerr(i)>=100
    Qc(i)=(80+(100-80)*rand)*pi/180;
    Qf2(i)=(120+(150-120)*rand)*pi/180;
    Qr(i)=(15+(75-15)*rand)*pi/180;
    QL(i)=(140+(220-140)*rand)*pi/180;

    c(i)=1000+(3000-1000)*rand;
    r(i)=1000+(2000-1000)*rand;

    while r(i) >= c(i)
        c(i)=1000+(3000-1000)*rand;
        r(i)=1000+(2000-1000)*rand;
    end

    L(i)=1000+(5000-1000)*rand;

```

```

%x,y coordinates of camera 2

pp2x=c(i)*(cos(Qc(i)-(90*pi/180)));
pp2y=-1*c(i)*(sin(Qc(i)-(90*pi/180)));

%equation of line that is image plane 2

%point on image plane 2

ip2x=pp2x;
ip2y=(-1*f)/(cos((180*pi/180)-Qf2(i)));

mip2=tan((180*pi/180)-Qf2(i)); %slope of image 2

%y=(mip2*x)-(mip2*ip2x)+ip2y

%x, y coordinates of point A

Ax=r(i)*(cos((90*pi/180)-Qr(i)));
Ay=r(i)*(sin((90*pi/180)-Qr(i)));

%equation of line through A and camera 1

mA1=(Ay-pp1y)/(Ax-pp1x); %slope

%y=(mA1*x)-(mA1*Ax)+Ay;

%equation of line through A and camera 2

mA2=(Ay-pp2y)/(Ax-pp2x); %slope

%y=(mA2*x)-(mA2*Ax)+Ay;

%x,y coordinates of image point A on image 1

iA1x=(-1*mip1*ip1x)+ip1y+(mA1*Ax)-Ay)/(mA1-mip1);
iA1y=(mip1*iA1x)-(mip1*ip1x)+ip1y;

%x,y coordinates of image point A on image 2

iA2x=(-1*mip2*ip2x)+ip2y+(mA2*Ax)-Ay)/(mA2-mip2);
iA2y=(mip2*iA2x)-(mip2*ip2x)+ip2y;

%x,y coordinates of point B

bx=-1*L(i)*(sin((180*pi/180)-QL(i)));
by=L(i)*(cos((180*pi/180)-QL(i)));

Bx=Ax+bx;
By=Ay+by;

%equation of line through B and camera 1

mB1=(By-pp1y)/(Bx-pp1x); %slope

```

```

%y=(mB1*x) - (mB1*Bx) +By;

%equation of line through B and camera 2

mB2=(By-pp2y)/(Bx-pp2x); %slope

%y=(mB2*x) - (mB2*Bx) +By;

%x,y coordinates of image point B on image 1

iB1x=((-1*mip1*ip1x)+ip1y+(mB1*Bx)-By)/(mB1-mip1);
iB1y=(mip1*iB1x) - (mip1*ip1x)+ip1y;

%x,y coordinates of image point B on image 2

iB2x=((-1*mip2*ip2x)+ip2y+(mB2*Bx)-By)/(mB2-mip2);
iB2y=(mip2*iB2x) - (mip2*ip2x)+ip2y;

%error on tagging a point on the image
err1=(2.43e-3+(8.34e-3*rand));
for err1=(7.99e-3:10.77e-3)
    err1=10.77e-3;
end
for err1=(5.21e-3:7.99e-3)
    err1=7.99e-3;
end
for err1=(2.43e-3:5.21e-3)
    err1=5.21e-3;
end

err2=(2.43e-3+(8.34e-3*rand));
for err2=(7.99e-3:10.77e-3)
    err2=10.77e-3;
end
for err2=(5.21e-3:7.99e-3)
    err2=7.99e-3;
end
for err2=(2.43e-3:5.21e-3)
    err2=5.21e-3;
end
err3=(-2.43e-3+(-8.34e-3*rand));
for err3=(-10.77e-3:-7.99e-3)
    err3=-10.77e-3;
end
for err3=(-7.99e-3:-5.21e-3)
    err1=-7.99e-3;
end
for err3=(-5.21e-3:-2.43e-3)
    err3=-5.21e-3;
end

err4=(-2.43e-3+(-8.34e-3*rand));
for err4=(-10.77e-3:-7.99e-3)

```



```

    err4=-10.77e-3;
end
for err4=(-7.99e-3:-5.21e-3)
    err4=-7.99e-3;
end
for err4=(-5.21e-3:-2.43e-3)
    err4=-5.21e-3;
end

%error location of A on image 1

ie1A1x=iA1x-(err1*cos(45*pi/180));
ie1A1y=iA1y+(err1*sin(45*pi/180));

ie2A1x=iA1x+(err1*cos(45*pi/180));
ie2A1y=iA1y-(err1*sin(45*pi/180));

%error locatation of A on image 2

ie1A2x=iA2x+(err2*cos((180*pi/180)-Qf2(i)));
ie1A2y=iA2y+(err2*sin((180*pi/180)-Qf2(i)));

ie2A2x=iA2x-(err2*cos((180*pi/180)-Qf2(i)));
ie2A2y=iA2y-(err2*sin((180*pi/180)-Qf2(i)));

%error location of B on image 1

ie1B1x=iB1x-(err3*cos(45*pi/180));
ie1B1y=iB1y+(err3*sin(45*pi/180));

ie2B1x=iB1x+(err3*cos(45*pi/180));
ie2B1y=iB1y-(err3*sin(45*pi/180));

%error location of A on image 2

ie1B2x=iB2x+(err4*cos((180*pi/180)-Qf2(i)));
ie1B2y=iB2y+(err4*sin((180*pi/180)-Qf2(i)));

ie2B2x=iB2x-(err4*cos((180*pi/180)-Qf2(i)));
ie2B2y=iB2y-(err4*sin((180*pi/180)-Qf2(i)));

%equation of line through ie1A1 and camera 1, s1
ms1e=(ie1A1y-pp1y)/(ie1A1x-pp1x); %slope of s1

%equation of line through ie1A2 and camera 2, s3
ms3e=(ie1A2y-pp2y)/(ie1A2x-pp2x); %slope of s3

%intersection of s1 and s3, E
Ex(i)=((-1*ms3e*ie1A2x)+ie1A2y+(ms1e*ie1A1x)-ie1A1y)/(ms1e-ms3e);
Ey(i)=(ms1e*Ex(i))-(ms1e*ie1A1x)+ie1A1y;

```

```

%intersection of s2 and s3, G
Gx(i)=((-1*ms3e*ie1A2x)+ie1A2y+(ms2e*ie2A1x)-ie2A1y)/(ms2e-ms3e);
Gy(i)=(ms2e*Gx(i))-(ms2e*ie2A1x)+ie2A1y;

%equation of line through ie1B1 and camera 1, k1
mk1e=(ie1B1y-pp1y)/(ie1B1x-pp1x); %slope of k1
%equation of line through ie2B1 and camera 1, k2
mk2e=(ie2B1y-pp1y)/(ie2B1x-pp1x); %slope of k2
%equation of line through ie1B2 and camera 2, k3
mk3e=(ie1B2y-pp2y)/(ie1B2x-pp2x); %slope of k3

%intersection of k1 and k3, V
Vx(i)=((-1*mk3e*ie1B2x)+ie1B2y+(mk1e*ie1B1x)-ie1B1y)/(mk1e-mk3e);
Vy(i)=(mk1e*Vx(i))-(mk1e*ie1B1x)+ie1B1y;

%intersection of k1 and k4, U
Ux(i)=((-1*mk4e*ie2B2x)+ie2B2y+(mk1e*ie1B1x)-ie1B1y)/(mk1e-mk4e);
Uy(i)=(mk1e*Ux(i))-(mk1e*ie1B1x)+ie1B1y;

%Distance from At to Bt is Lm (Lmeasured)

Lm(i)=sqrt(((Ux(i)-Vx(i))^2)+((Uy(i)-Vy(i))^2));
Lerr(i)=Lm(i)-L(i);
end

end

save variables Qc Qf2 Qr QL c r L Lm Lerr;
m=100;
bin=(1000:40:5000);
for i=1:m
    ind=find(L>=bin(i)&L<bin(i+1));

    meanLerr(i)=mean(Lerr(ind));
    StDevLerr(i)=std(Lerr(ind));
end
j=(1040:40:5000);
save mean meanLerr StDevLerr;
figure(1); hold on; box on;
plot(L,Lerr,'k. ');
figure(2); hold on; box on;

```

```
plot(j,meanLerr,'k.');
```

```
A=meanLerr';  
B=Lerr';  
C=L';  
D=j';
```

```
dlmwrite('negerrendl.xls',B,'\t');  
dlmwrite('negerrendmeanl.xls',A,'\t');  
dlmwrite('negerrendLl.xls',C,'\t');  
dlmwrite('bins.xls',D,'\t');
```

Matlab Code for Side on programme

```
%script to determine if there is a difference between true and measured
lengths
% ALL MEASUREMENTS IN MILLIMETERS (mm)
%location and orientation of camera 1
clear; close all;

pp1x=0;
pp1y=0;

Qf1=225*pi/180;

f=5.78; %focal length of camera lens.

ip1x=0;
ip1y=(-1*f)/(cos((225-180)*pi/180));

%slope of image 1, angle of -45 to y axis
mip1=tan(-45*pi/180);

%equation of straight line that is image plane 1
%y-ip1y=mil*(x-ip1x)

n=10000;

Qc=zeros(1,n);
Qf2=zeros(1,n);
Qr=zeros(1,n);
QL=zeros(1,n);
c=zeros(1,n);
r=zeros(1,n);
L=zeros(1,n);
Ex=zeros(1,n);
Fx=zeros(1,n);
Gx=zeros(1,n);
Hx=zeros(1,n);
Tx=zeros(1,n);
Ux=zeros(1,n);
Vx=zeros(1,n);
Wx=zeros(1,n);
Ey=zeros(1,n);
Fy=zeros(1,n);
Gy=zeros(1,n);
Hy=zeros(1,n);
Ty=zeros(1,n);
Uy=zeros(1,n);
Vy=zeros(1,n);
Wy=zeros(1,n);
areaA=zeros(1,n);
areaB=zeros(1,n);
cgxA=zeros(1,n);
cgxA=zeros(1,n);
cgxB=zeros(1,n);
cgxB=zeros(1,n);
cgxB=zeros(1,n);
```

```

Lm=zeros(1,n);
Lerr=zeros(1,n);

for i=1:n
    Qc(i)=(80+(100-80)*rand)*pi/180;
    Qf2(i)=(120+(150-120)*rand)*pi/180;
    Qr(i)=(15+(75-15)*rand)*pi/180;
    QL(i)=(220+(320-220)*rand)*pi/180;

    c(i)=2000+(6000-2000)*rand;
    r(i)=500+(2500-500)*rand;
    L(i)=1000+(5000-1000)*rand;

    while (r(i)+L(i)) >= c(i)
        c(i)=2000+(6000-2000)*rand;
        r(i)=500+(2500-500)*rand;
        L(i)=1000+(5000-1000)*rand;
    end
end

```

The remainder of the code is the same as the code of the End on programme.

Matlab Code for End on programme with increasing error

The code for the increasing error is the same as for the End on programme, except for the selection of the pixel error which is given below.

```
%error on tagging a point on the image

    if(L(i)>1000&L(i)<=1500)
        pixerr=0;
    elseif(L(i)>1500&L(i)<=2000)
        pixerr=(1*2.78e-3);
    elseif(L(i)>2000&L(i)<=2500)
        pixerr=(2*2.78e-3);
    elseif(L(i)>2500&L(i)<=3000)
        pixerr=(3*2.78e-3);
    elseif(L(i)>3000&L(i)<=3500)
        pixerr=(4*2.78e-3);
    elseif(L(i)>3500&L(i)<=4000)
        pixerr=(5*2.78e-3);
    elseif(L(i)>4000&L(i)<=4500)
        pixerr=(6*2.78e-3);
    else
        pixerr=(7*2.78e-3);
    end

    err1=(2.43e-3+(8.34e-3*rand));
    for err1=((7.99e-3):(10.77e-3))
        err1=(10.77e-3);
    end
    for err1=((5.21e-3):(7.99e-3))
        err1=(7.99e-3);
    end
    for err1=((2.43e-3):(5.21e-3))
        err1=(5.21e-3);
    end

    err2=(2.43e-3+(8.34e-3*rand));
    for err2=((7.99e-3):(10.77e-3))
        err2=(10.77e-3);
    end
    for err2=((5.21e-3):(7.99e-3))
        err2=(7.99e-3);
    end
    for err2=((2.43e-3):(5.21e-3))
        err2=(5.21e-3);
    end

err3=(-2.43e-3+(-8.34e-3*rand)-pixerr);
    for err3=(-pixerr-10.77e-3):(-pixerr-7.99e-3))
        err3=(-pixerr-10.77e-3);
    end
    for err3=(-pixerr-7.99e-3):(-pixerr-5.21e-3))
        err3=(-pixerr-7.99e-3);
    end
end
```

```
for err3=(-pixerr-5.21e-3):(-pixerr-2.43e-3)
    err3=(-pixerr-5.21e-3);
end

err4=(-2.43e-3+(-8.34e-3*rand)-pixerr);
for err4=(-pixerr-10.77e-3):(-pixerr-7.99e-3)
    err4=(-pixerr-10.77e-3);
end
for err4=(-pixerr-7.99e-3):(-pixerr-5.21e-3)
    err4=(-pixerr-7.99e-3);
end
for err4=(-pixerr-5.21e-3):(-pixerr-2.43e-3)
    err4=(-pixerr-5.21e-3);
end
```

Appendix B

All measurements are in millimetres.

Measurements of short pipes obtained from Coordinate Measuring Machine (CMM), Tape measure and PhotoModeler models (PM)

CMM	Tape	PM
553.381	553	553.033
553.381	553	552.628
553.381	552	552.862
553.381	553	553.429
553.381	553	552.680
553.381	552	552.406
553.381	553.5	553.175
553.381	553	552.106
553.381	553	553.385
553.381	553.5	553.665
680.560	680	680.560
680.560	681	679.901
680.560	680	680.307
680.560	679.5	680.633
680.560	679	679.488
680.560	680	679.470
680.560	680	678.890
680.560	680	679.998
680.560	680.5	680.972
680.560	680	681.310
702.302	701	701.846
702.302	701.5	701.859
702.302	702	702.381
702.302	702.5	702.303
702.302	702	702.365
702.302	703.5	702.441
702.302	702	702.475
702.302	702	702.436
702.302	702.5	702.303
702.302	703	702.182
764.057	763	763.618
764.057	764	763.531
764.057	764	764.379
764.057	764	763.574
764.057	763	764.739
764.057	763	763.691
764.057	763.5	763.631
764.057	765	763.720
764.057	764.5	763.454
764.057	764	764.400
1101.479	1102	1101.298
1101.479	1100.5	1101.388
1101.479	1101.5	1101.300
1101.479	1101	1100.900
1101.479	1101.5	1101.356
1101.479	1101	1101.449

1101.479	1100	1100.598
1101.479	1101	1100.657
1101.479	1100	1101.520
1101.479	1100	1101.281

Measurements of Long Pipes obtained from PhotoModeler models.

939.250	1420.610	1520.990	1977.760	3878.550	3920.950	3963.330	4004.270
939.300	1422.260	1522.880	1977.500	3878.380	3920.370	3962.920	4003.480
939.360	1417.320	1518.570	1976.700	3879.040	3920.630	3962.410	4002.890
938.880	1417.660	1518.280	1976.240	3880.310	3922.290	3964.820	4004.020
940.570	1417.210	1517.520	1977.130	3879.580	3919.960	3962.790	4002.890
940.410	1418.110	1516.870	1975.690	3882.540	3922.580	3963.470	4004.490
940.300	1420.770	1520.130	1978.770	3878.040	3919.270	3961.850	4002.760
941.110	1422.480	1522.640	1981.370	3879.770	3922.120	3964.310	4004.610
939.250	1420.000	1520.020	1978.950	3878.850	3921.250	3963.070	4003.010
942.020	1428.580	1520.920	1982.850	3881.640	3920.760	3965.270	4004.580
1002.530	1447.970	1539.400	1999.370	3889.010	3931.650	3973.700	
1001.770	1454.040	1546.410	1998.510	3888.390	3931.400	3972.880	
998.580	1448.930	1540.190	1999.150	3888.510	3932.380	3974.080	
1001.240	1447.550	1538.750	1999.040	3889.280	3931.670	3975.130	
1000.500	1448.300	1538.750	1994.580	3888.380	3931.190	3971.940	
1001.290	1446.510	1536.630	1995.760	3891.930	3933.870	3979.960	
1001.280	1449.290	1540.500	1998.540	3887.300	3930.850	3972.780	
1002.630	1448.740	1540.320	2002.330	3889.410	3932.570	3975.020	
1004.180	1449.000	1539.690	1997.690	3889.290	3931.220	3972.980	
1007.140	1451.130	1540.090	2002.620	3891.710	3930.360	3974.340	
1063.140	1467.790	1549.620	2038.780	3902.030	3942.030	3983.170	
1064.260	1468.430	1551.450	2038.990	3902.550	3942.050	3982.210	
1062.020	1467.930	1549.520	2036.860	3900.510	3942.420	3982.360	
1061.430	1471.280	1552.130	2036.100	3902.180	3943.550	3983.160	
1061.510	1467.010	1548.200	2037.600	3900.330	3941.160	3982.000	
1062.320	1466.490	1548.000	2035.210	3903.800	3944.470	3984.180	
1063.060	1467.010	1549.200	2039.730	3901.560	3940.950	3981.780	
1064.130	1469.360	1550.610	2041.060	3902.750	3944.050	3985.290	
1062.180	1469.550	1550.350	2039.470	3901.730	3941.800	3982.660	
1061.740	1468.520	1550.030	2041.870	3909.360	3943.840	3984.900	
1116.070	1499.850	1571.100	2049.820	3911.190	3952.760	3994.860	
1116.770	1502.750	1574.800	2051.780	3910.980	3950.340	3993.710	
1111.930	1499.600	1569.600	2050.670	3910.780	3951.250	3995.300	
1114.900	1501.180	1572.780	2050.090	3911.820	3952.490	3994.260	
1112.820	1500.300	1570.570	2046.410	3910.490	3950.070	3994.000	
1113.740	1498.780	1568.940	2046.420	3913.980	3953.280	3993.280	
1114.990	1501.920	1572.790	2049.970	3910.050	3950.710	3993.070	
1116.190	1502.610	1573.850	2054.010	3911.570	3952.240	3995.910	
1116.740	1500.320	1571.290	2048.760	3911.220	3951.340	3994.150	
1117.020	1502.570	1574.800	2052.820	3912.990	3952.930	3995.580	

Measurements of Vehicle Dimensions obtained from Tape measure and PhotoModeler models.

Tape	PM	Tape	PM	Tape	PM
658	646	1696	1697	2719	2721
658	694	1696	1687	2719	2731
658	663	1696	1694	2719	2744
658	674	1696	1682	3841	3852
658	647	1696	1695	3841	3829
658	651	1696	1689	3841	3860
658	658	1696	1698	3841	3819
658	653	1696	1684	3841	3857
658	662	2580	2593	3841	3831
658	652	2580	2597	3841	3861
658	649	2580	2584	3841	3843
658	654	2580	2626	3841	3859
658	652	2580	2609	3841	3822
658	650	2580	2577	3841	3847
658	656	2580	2601	3841	3833
658	654	2580	2581	3841	3867
658	656	2580	2590	3841	3818
658	650	2580	2573	3841	3847
1636	1634	2580	2585	3841	3826
1636	1619	2580	2569	3841	3852
1636	1639	2580	2593	3841	3838
1636	1630	2580	2567	3841	3850
1636	1634	2719	2756	3841	3818
1636	1625	2719	2732	3890	3904
1636	1642	2719	2754	3890	3883
1636	1631	2719	2723	3890	3918
1636	1633	2719	2743	3890	3872
1636	1619	2719	2714	3890	3906
1696	1689	2719	2738	3890	3884
1696	1722	2719	2753	3890	3913
1696	1697	2719	2736	3890	3894
1696	1703	2719	2712	3890	3908
1696	1696	2719	2729	3890	3871
1696	1683	2719	2729		
1696	1702	2719	2752		
1696	1693	2719	2714		
1696	1702	2719	2724		
1696	1685	2719	2707		
1696	1692	2719	2725		

Differences in locations of points on merged vehicle models.

-2	-27	12	-10
-27	11	-24	21
16	8	12	8
-8	6	-11	-12
6	-8	16	2
-5	10	9	-15
13	18	-7	6
18	5	-6	6
10	-13	6	-11
8	-7	-7	19
2	-3	8	-8
-26	9	-23	20
10	-23	-11	8
-8	20	-13	-10
-6	-10	-8	-1
-7	16	-4	-12
12	6	-6	4
18	-4	10	-10
7	-5	10	16
-10	6	-14	-8
3	-5	24	19
-10	2	-9	-10

Appendix C

Collision 1 Jaguar Collision

In this collision the two vehicles were a Jaguar S-Type V8 and a Jaguar XJ V8. The XJ was stationary (the target vehicle) and the S-Type (the bullet) with the use of a pulley system was driven into the side of the XJ at a recorded speed of 49.4km/h. Both vehicles had a driver and front seat passenger.

Figure 1 shows the S-type after the collision. Figure 2 shows the final positions of the vehicles after the collision.



Figure 1 The Jaguar S-Type, after the collision



Figure 2 The vehicles after the collision.

The undamaged and damaged models of both vehicles were created. The residual crush depths were then measured from the models. The crush depths measured on the bullet vehicle (S-Type) were 0.015m, 0.006m, 0.038m, 0.085m, 0.062m, 0.022m, 0.038m, 0.022m. Therefore the average residual crush depth, $C_{res} = 0.036m$. Pre-impact length, $l = 4.877m$, as provided by the vehicle specifications was used to scale the model.

The energy equivalent speed, of the bullet vehicle was found to be;

$$V_{EES} = 4.6 + 119.1 \left(\frac{C_{res}}{l} \right)^{2/3}$$

$$V_{EES} = 4.6 + 119.1 \left(\frac{0.036}{4.877} \right)^{2/3}$$

$$V_{EES} = 9.12 \text{ mph} = 4.07 \text{ m/s}$$

The loaded mass of bullet car, $m_l = 1734\text{kg}$ (as given by organisers), the mass of load = 170kg (mass of two crash test dummies, 85kg each), therefore the unloaded mass of the bullet car, $m_k = 1564\text{kg}$.

Therefore the energy of bullet vehicle, E_b is;

$$E_b = \frac{1}{2} m_k (V_{EES})^2$$

$$E_b = \frac{1}{2} 1564 (4.07)^2$$

$$E_b = 12976.61 \text{ J}$$

Figure 3 shows the target vehicle after the collision.



Figure 3 The Jaguar XJ, after the collision

The residual crush depths of the target vehicle were measured from the merged models of the before and after models created in PhotoModeler, and found to be 0.09m, 0.163m, 0.271m, 0.17m, 0.143m, 0.119m, 0.209m, 0.337m, 0.322m, 0.239m, 0.141m. The average residual crush depth, $C_{res} = 0.2m$.

Also at the event the crush depths were measured manually by Robert Sproat, Crash Analyst, Birmingham Automotive Safety Centre, School of Engineering, University of Birmingham. Mr. Sproat and his team measured the crush depth using a very similar method to the reference base-line technique; and found the crush depths to be 0cm (at rear wheel), 4cm, 15cm, 37cm, 25cm, 0cm (at front wheel). Figure 4 is a diagram of Mr. Sproat's measurements plotted onto the PhotoModeler model, and allowing for the fact that their reference line was placed against the vehicle's tyres and therefore was slightly offset from the vehicle, the profiles of the crush damage are a very good match.



Figure 4 PhotoModeler model of Jaguar XJ with manual measurements shown.

The mass of the Jaguar XJ = 1708kg. M_T , is the equivalent mass of the energy absorbing structure (central impact), i.e. the combined mass of the two vehicles.

$$M_T = \frac{m_{bullet} \times m_{target}}{m_{bullet} + m_{target}}$$

$$M_T = \frac{1734 \times 1708}{1734 + 1708}$$

$$M_T = 860.45kg$$

The total energy absorbed in this collision, E , when the average values found for crush depth on both the bullet (\bar{d}_{bullet}) and target (\bar{d}_{target}) vehicles is used is;

$$E = E_b \left(1 + \frac{\bar{d}_{target}}{\bar{d}_{bullet}} \right)$$

$$E = 12976.61 \left(1 + \frac{0.200}{0.036} \right)$$

$$E = 85068.89J$$

The speed of the bullet vehicle, V , was then found to be;

$$E = \frac{1}{2} M_T V^2$$

$$85068.89 = \frac{1}{2} 860.45 V^2$$

$$V = 14.06m/s = 50.62km/h$$

The calculated pre-impact speed of the bullet car is 50.62km/h; the measured pre-impact speed was 49.4km/h, which is a difference of 1.22km/h or 2.5%.

The total energy absorbed in this collision, E , when the crush depth values found at the point of impact on both the bullet (d_{bullet}) and target (d_{target}) vehicles is used. d_{target} is the depth of damage at the point of contact on the target vehicle = 0.33m, and d_{bullet} is the depth of damage at the point of contact on the bullet vehicle = 0.071m

$$E = E_b \left(1 + \frac{d_{target}}{d_{bullet}} \right)$$

$$E = 12976.61 \left(1 + \frac{0.33}{0.071} \right)$$

$$E = 73290.43J$$

The speed of the bullet vehicle, V , was found to be;

$$E = \frac{1}{2} M_r V^2$$

$$73290.43 = \frac{1}{2} 860.45 V^2$$

$$V = 13.05m/s = 46.98km/h$$

The calculated pre-impact speed of the bullet car is 46.98km/h; the measured pre-impact speed was 49.4km/h, which is a difference of -2.42km/h or -4.9%.

Mondeo and Vectra (3 Collisions)

Three staged eccentric collisions were carried out between a Ford Mondeo and an Opel Vectra using a pulley system. Figures 5 and 6 show the style of Mondeos and Vectras that were crashed in the collisions. The collisions were arranged so that the longitudinal axis of the bullet vehicles (Mondeo) and the rear wheel axle of the target vehicles (Vectra) were aligned when the vehicles made contact, in these three collisions.



Figure 5 Ford Mondeo



Figure 6 Opel Vectra

Collision 2 Mondeo and Vectra

In this collision the Mondeo was the bullet car with a recorded speed of 38 km/h and the target vehicle, the Vectra had a recorded speed of 58 km/h. The Mondeo was photographed before and after the collision; models were created and overlaid. Figure 7 shows the overlaid damaged and undamaged models of the Mondeo involved in the first collision.

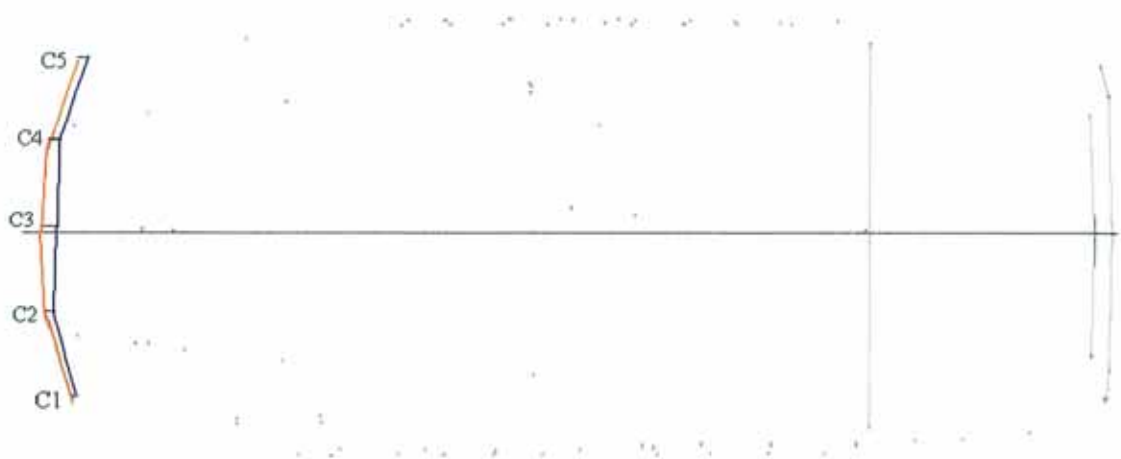


Figure 7 Overlaid damaged and undamaged models of the Mondeo (Collision 1)

The following measurements were made on the Mondeo model: Crush Depth: 0.051m, 0.052m, 0.068m, 0.037m, 0.027m. Average Crush Depth, $C_{res} = 0.047m$. Pre-impact length = 4.334m. Pre-impact width = 1.721m.

The Energy Equivalent Speed of the Mondeo was found to be

$$V_{EES} = 4.6 + 119.1 \left(\frac{C_{res}}{l} \right)^{\frac{2}{3}}$$

$$V_{EES} = 4.6 + 119.1 \left(\frac{0.047}{4.334} \right)^{\frac{2}{3}}$$

$$V_{EES} = 10.435mph = 4.663m/s$$

Therefore the energy of bullet vehicle was

$$E_b = \frac{1}{2} m_k (V_{EES})^2$$

$$E_b = \frac{1}{2} 1186(4.663)^2$$

$$E_b = 12893.94J$$

The unloaded mass of bullet car, $m_k = 1186kg$.

The Opel Vectra was also photographed before and after the collision; models were created from these photographs, and figure 8 shows the overlaid model of the damaged

and undamaged Vectra. The centre of gravity, the longitudinal axis and wheel axle are shown. P is the distance from the centre of gravity to the rear wheel axle.

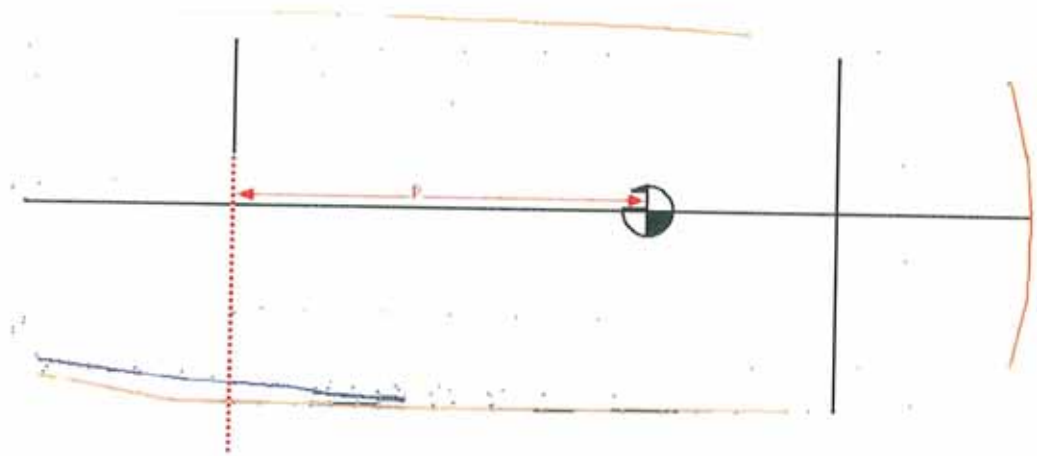


Figure 8 Overlaid damaged and undamaged models of the Vectra (Collision 1)

The following measurements were made on the model: Pre-impact length = 4.1168m.
Pre-impact width = 1.696m.

The collision is eccentric, as the point of impact was not at the point where the longitudinal axis of the bullet vehicle is in line with the centre of gravity of the target vehicle, and the mass of the target vehicle must be adjusted. The point of impact was along the rear axle; the distance from the centre of gravity of the Vectra to the rear axle, $p = 1.69\text{m}$ and the distance from the point of impact to the longitudinal axis of the target vehicle, $q = 0.85\text{m}$. The mass of target car = 1152kg, (the Radius of gyration)², $k^2 = \frac{0.931}{12}(l^2 + w^2) = 0.0776(4.168^2 + 1.696^2) = 1.57$, therefore the adjusted mass, m_{te} is

$$m_{te} = m_t \left(\frac{k^2 + q^2}{k^2 + q^2 + p^2} \right)$$

$$m_{te} = 1162 \left(\frac{1.57 + 0.85^2}{1.57 + 0.85^2 + 1.69^2} \right)$$

$$m_{te} = 512.9\text{kg}$$

The mass of bullet car = 1260kg. M_T , is the equivalent mass of the energy absorbing structure, i.e. the combined mass of the two vehicles.

$$M_T = \frac{m_{bullet} \times m_{te}}{m_{bullet} + m_{te}}$$

$$M_T = \frac{(1260)(512.9)}{1260 + 512.9}$$

$$M_T = 364.5kg$$

The total energy absorbed in this collision, E , when the average values found for crush depth on both the bullet (\bar{d}_{bullet}) and target (\bar{d}_{target}) vehicles is used is;

$$E = E_b \left(1 + \frac{\bar{d}_{target}}{\bar{d}_{bullet}} \right)$$

$$E = 12893.94 \left(1 + \frac{0.057}{0.047} \right)$$

$$E = 28531.27J$$

The pre-impact speed of bullet vehicle, V , is

$$E = \frac{1}{2} M_{total} V^2$$

$$28531.27 = \frac{1}{2} (364.5) V^2$$

$$V = 12.51m/s = 45km/h$$

The calculated speed of the bullet vehicle is 45 km/h, while the speed recorded on the day was 38 km/h, a difference of 7 km/h or 18.4%.

The total energy absorbed in this collision, E , when the crush depth values found at the point of impact on both the bullet (d_{bullet}) and target (d_{target}) vehicles is used.

Crush depth at point of impact, $d_{bullet} = 0.068m$, $d_{target} = 0.081m$.

$$E = E_b \left(1 + \frac{d_{target}}{d_{bullet}} \right)$$

$$E = 12893.94 \left(1 + \frac{0.081}{0.068} \right)$$

$$E = 28252.9J$$

The pre-impact speed of bullet vehicle, V , is

$$E = \frac{1}{2} M_{total} V^2$$

$$28252.9 = \frac{1}{2} (364.5) V^2$$

$$V = 12.45 m / s = 44.8 km / h$$

The calculated speed of the bullet vehicle is 44.8 km/h, while the speed recorded on the day was 38 km/h, a difference of 6.8 km/h or 17.9%.

Collision 3 Mondeo and Vectra

In this collision the Mondeo, the bullet car had a recorded speed of 56.8 km/h and the target vehicle, the Vectra had a recorded speed of 37.8 km/h. The vehicles were photographed before and after the collision.

Models of the Mondeo were created and overlaid. The following measurements were made on the model: Crush Depth: 0.104m, 0.101m, 0.109m, 0.095m, 0.093m. Average Crush Depth, $C_{res} = 0.1004m$. Pre-impact width = 4.307m.

The Energy Equivalent Speed of the Mondeo was found to be

$$V_{EES} = 4.6 + 119.1 \left(\frac{C_{res}}{l} \right)^{2/3}$$

$$V_{EES} = 4.6 + 119.1 \left(\frac{0.1004}{4.307} \right)^{2/3}$$

$$V_{EES} = 14.32 mph = 6.39 m / s$$

Therefore the energy of bullet vehicle was

$$E_b = \frac{1}{2} m_k (V_{EES})^2$$

$$E_b = \frac{1}{2} 1282 (6.39)^2$$

$$E_b = 26248.15 J$$

The Opel Vectra was also photographed before and after the collision; models were created from these photographs, and the models of the damaged and undamaged Vectra were overlaid. The following measurements were made on the model: Pre-impact length = 4.345m. Pre-impact length = 1.668m.

As the point of impact was not in line with the centre of gravity of the target vehicle, the collision is eccentric and the mass of the target vehicle must be adjusted. The point of impact was along the rear axle; the distance from the centre of gravity of the Vectra to the rear axle, $p = 1.69\text{m}$ and the distance from the point of impact to the longitudinal axis of the target vehicle, $q = 0.834\text{m}$. The mass of target car = 1162kg, (the Radius of gyration)², $k^2 = \frac{0.931}{12}(l^2 + w^2) = 0.0776(4.345^2 + 1.668^2) = 1.68$, therefore the adjusted mass, m_{te} is

$$m_{te} = m_t \left(\frac{k^2 + q^2}{k^2 + q^2 + p^2} \right)$$

$$m_{te} = 1162 \left(\frac{1.68 + 0.834^2}{1.68 + 0.834^2 + 1.576^2} \right)$$

$$m_{te} = 568.1\text{kg}$$

The mass of bullet car = 1358kg. M_T , is the equivalent mass of the energy absorbing structure, i.e. the combined mass of the two vehicles.

$$M_T = \frac{m_{bullet} \times m_{te}}{m_{bullet} + m_{te}}$$

$$M_T = \frac{(1358.00)(568.1)}{1358.00 + 568.1}$$

$$M_T = 400.58\text{kg}$$

The total energy absorbed in this collision, E , when the average values found for crush depth on both the bullet (\bar{d}_{bullet}) and target (\bar{d}_{target}) vehicles is used is;

$$E = E_b \left(1 + \frac{\bar{d}_{target}}{\bar{d}_{bullet}} \right)$$

$$E = 26248.15 \left(1 + \frac{0.141}{0.1004} \right)$$

$$E = 62890.7\text{J}$$

The pre-impact speed of bullet vehicle, V , is

$$E = \frac{1}{2} M_{Total} V^2$$

$$62890.7 = \frac{1}{2} (400.58) V^2$$

$$V = 17.72 m / s = 63.8 km / h$$

The calculated speed of the bullet vehicle is 63.8 km/h, while the speed recorded on the day was 56.8 km/h, a difference of 7 km/h or 12.3%.

The total energy absorbed in this collision, E , when the crush depth values found at the point of impact on both the bullet (d_{bullet}) and target (d_{target}) vehicles is used. Crush depth at point of impact, $d_{bullet} = 0.158m$, $d_{target} = 0.119m$

The total energy of the collision was found to be;

$$E = E_b \left(1 + \frac{d_{target}}{d_{bullet}} \right)$$

$$E = 26248.15 \left(1 + \frac{0.119}{0.109} \right)$$

$$E = 54713J$$

The pre-impact speed of bullet vehicle, V , is

$$E = \frac{1}{2} M_{Total} V^2$$

$$54713 = \frac{1}{2} (400.58) V^2$$

$$V = 16.53 m / s = 59.5 km / h$$

The calculated speed of the bullet vehicle is 59.5 km/h, while the speed recorded on the day was 56.8 km/h, a difference of 2.7 km/h or 4.7%.

Collision 4 Mondeo and Vectra

In this collision the Mondeo, the bullet car had a recorded speed of 42.1 km/h and the target vehicle was the Vectra with a speed of 41.1 km/h. The Mondeo was photographed before and after the collision. Undamaged and damaged models were

created and overlaid. The following measurements were made on the model of the bullet vehicle's crush profile: Crush Depth: 0.061m, 0.042m, 0.043m, 0.039m, 0.043m. Average Crush Depth, $C_{res} = 0.0456m$. Pre-impact length = 4.316m.

The Energy Equivalent Speed of the Mondeo was found to be

$$V_{EES} = 4.6 + 119.1 \left(\frac{C_{res}}{l} \right)^{2/3}$$

$$V_{EES} = 4.6 + 119.1 \left(\frac{0.0456}{4.316} \right)^{2/3}$$

$$V_{EES} = 10.34mph = 4.62m/s$$

Therefore the energy of bullet vehicle was

$$E_b = \frac{1}{2} m_k (V_{EES})^2$$

$$E_b = \frac{1}{2} 1230(4.62)^2$$

$$E_b = 13126.8J$$

The unloaded mass of bullet car, $m_k = 1230kg$.

The Opel Vectra was also photographed before and after the collision; models were created from these photographs and the models of the damaged and undamaged Vectra were overlaid. The following measurements were made on the model: Pre-impact length = 4.259m. Pre-impact width = 1.686m.

Again the point of impact was not in line with the centre of gravity of the target vehicle, therefore the collision is eccentric and the mass of the target vehicle must be adjusted. The point of impact was along the rear axle; the distance from the centre of gravity of the Vectra to the rear axle, $p = 1.69m$ and the distance from the point of impact to the longitudinal axis, $q = 0.843m$. The mass of target car = 1170kg, (the Radius of gyration)², $k^2 = \frac{0.931}{12} (l^2 + w^2) = 0.0776(4.259^2 + 1.686^2) = 1.63$, therefore the adjusted mass, m_{te} is

$$m_{te} = m_b \left(\frac{k^2 + q^2}{k^2 + q^2 + p^2} \right)$$

$$m_{te} = 1170 \left(\frac{1.63 + 0.843^2}{1.63 + 0.843^2 + 1.57^2} \right)$$

$$m_{te} = 569.87 \text{ kg}$$

The mass of bullet car = 1306kg. . M_T , is the equivalent mass of the energy absorbing structure, i.e. the combined mass of the two vehicles.

$$M_T = \frac{m_{bullet} \times m_{te}}{m_{bullet} + m_{te}}$$

$$M_T = \frac{(1306)(569.87)}{1306 + 569.87}$$

$$M_T = 396.75 \text{ kg}$$

The total energy absorbed in this collision, E , when the average values found for crush depth on both the bullet (\bar{d}_{bullet}) and target (\bar{d}_{target}) vehicles is used is;

$$E = E_b \left(1 + \frac{\bar{d}_{target}}{\bar{d}_{bullet}} \right)$$

$$E = 13126.8 \left(1 + \frac{0.047}{0.0456} \right)$$

$$E = 26656.62 \text{ J}$$

The pre-impact speed of bullet vehicle, V , is

$$E = \frac{1}{2} M_{Total} V^2$$

$$26656.62 = \frac{1}{2} (396.75) V^2$$

$$V = 11.59 \text{ m/s} = 41.73 \text{ km/h}$$

The calculated speed of the bullet vehicle is 41.73 km/h, while the speed recorded on the day was 42.1 km/h, a difference of -0.37 km/h or 0.9%.

The total energy absorbed in this collision, E , when the crush depth values found at the point of impact on both the bullet (d_{bullet}) and target (d_{target}) vehicles is used. Crush depth at point of impact, $d_{bullet} = 0.043\text{m}$, $d_{target} = 0.047\text{m}$.

The total energy of the collision was found to be;

$$E = E_b \left(1 + \frac{d_{target}}{d_{bullet}} \right)$$

$$E = 13126.8 \left(1 + \frac{0.047}{0.043} \right)$$

$$E = 27474.7 J$$

The pre-impact speed of bullet vehicle, V , is

$$E = \frac{1}{2} M_{total} V^2$$

$$27474.7 = \frac{1}{2} (396.75) V^2$$

$$V = 11.77 m/s = 42.37 km/h$$

The calculated speed of the bullet vehicle is 42.37 km/h, while the speed recorded on the day was 42.1 km/h, a difference of 0.27km/h or 0.6%.

Appendix D

Matlab Code for Monte Carlo Simulation, speed calculations with standard deviation due to measuring from a photogrammetric model

```
clear; close all;

Mk = 1564; Mt = 860.45; Unloaded Mass of bullet vehicle and Combined
total mass of both vehicles.
Lmean = 4.877; Lstd = 0.0124; Pre-impact length of vehicle and standard
deviation due to measuring from a photogrammetric model
db_ave_mean = 0.036; db_ave_std = 0.0044; Average crush depth of bullet
vehicle and standard deviation due to measuring from a photogrammetric
model
dtmean = 0.33; dtstd = 0.0124; single crush depth measurement on target
vehicle and standard deviation due to measuring from a photogrammetric
model

dbmean = 0.071; dbstd = 0.0124; single crush depth measurement on bullet
vehicle and standard deviation due to measuring from a photogrammetric
model

for i = 1:10000
    db_ave = db_ave_mean + randn*db_ave_std;
    L = Lmean + randn*Lstd;
    dt = dtmean + randn*dtstd;
    db = dbmean + randn*dbstd;

    Vees = 7.407 + 191.79*(db_ave/L)^(2/3);

    Vccs(i) = ((Mk/Mt)^0.5) * ((1+dt/db)^0.5) * Vees;
end

Vccs = sort(Vccs);

maxVccs = max(Vccs);
minVccs = min(Vccs);
meanVccs = mean(Vccs);
stdVccs = std(Vccs);
Vccs50 = Vccs(10000*0.5);
Vccs2pt5 = Vccs(10000*0.025);
Vccs97pt5 = Vccs(10000*0.975);
Vccspt1 = Vccs(10000*0.001);
Vccs99pt9 = Vccs(10000*0.999);
Vccs25 = Vccs(10000*0.25);
Vccs75 = Vccs(10000*0.75);

clc

disp(['Mean Vccs: ' num2str(meanVccs) '.'])
disp(' ')
disp(['50%ile Vccs: ' num2str(Vccs50) '.'])
disp(' ')
disp(['Standard Deviation of Vccs: ' num2str(stdVccs) '.'])
disp(' ')
```

```

disp(['Min and Max Vccs: ' num2str(minVccs) ' and ' num2str(maxVccs)
     '.'])
disp(' ')
disp(['Overall Range of Vccs: ' num2str(Vccspt1) ' to '
     num2str(Vccs99pt9) '.'])
disp(' ')
disp(['95% Range of Vccs: ' num2str(Vccs2pt5) ' to ' num2str(Vccs97pt5)
     '.'])
disp(' ')
disp(['Probable Range of Vccs: ' num2str(Vccs25) ' to ' num2str(Vccs75)
     '.'])

figure(1); hold on; box on; grid on;
set(gca,'fontsize',16)
xlabel('Vccs (kph)'); ylabel('Cumulative Frequency')
plot(Vccs,(1:10000)./10000,'k','linewidth',2)

```

%The following values for the masses of the vehicles were obtained from the collision organiser, the values for lengths and crush were obtained from photogrammetric models. New figures were inserted in the programme for the different vehicles.

```
clear; close all;
```

```
Mk = 1564; Mt = 860.45;
Lmean = 4.877; Lstd = 0.0124;
db_ave_mean = 0.036; db_ave_std = 0.0044;
dtmean = 0.2; dtstd = 0.00378;

for i = 1:10000
    db_ave = db_ave_mean + randn*db_ave_std;
    L = Lmean + randn*Lstd;
    dt = dtmean + randn*dtstd;
    db = db_ave_mean + randn*db_ave_std;

    Vees = 7.407 + 191.79*(db_ave/L)^(2/3);

    Vccs(i) = ((Mk/Mt)^0.5) * ((1+dt/db)^0.5) * Vees;

Vccs2(i) = Vccs(i)+randn*8.86;
end

Vccs = Vccs2;
Vccs = sort(Vccs);

maxVccs = max(Vccs);
minVccs = min(Vccs);
meanVccs = mean(Vccs);
stdVccs = std(Vccs);
Vccs50 = Vccs(10000*0.5);
Vccs2pt5 = Vccs(10000*0.025);
Vccs97pt5 = Vccs(10000*0.975);
Vccspt1 = Vccs(10000*0.001);
Vccs99pt9 = Vccs(10000*0.999);
Vccs25 = Vccs(10000*0.25);
Vccs75 = Vccs(10000*0.75);

clc

disp(['Mean Vccs: ' num2str(meanVccs) '.'])
disp(' ')
disp(['50%ile Vccs: ' num2str(Vccs50) '.'])
disp(' ')
disp(['Standard Deviation of Vccs: ' num2str(stdVccs) '.'])
disp(' ')
disp(['Min and Max Vccs: ' num2str(minVccs) ' and ' num2str(maxVccs)
'.'])
disp(' ')
disp(['Overall Range of Vccs: ' num2str(Vccspt1) ' to '
num2str(Vccs99pt9) '.'])
disp(' ')

```



```
disp(['95% Range of Vccs: ' num2str(Vccs2pt5) ' to ' num2str(Vccs97pt5)
' .'])
disp(' ')
disp(['Probable Range of Vccs: ' num2str(Vccs25) ' to ' num2str(Vccs75)
' .'])

figure(1); hold on; box on; grid on;
set(gca,'fontsize',16)
xlabel('Vccs (kph)'); ylabel('Cumulative Frequency')
plot(Vccs,(1:10000)./10000,'k','linewidth',2)
```

List of Publications

Coyle F., Toal V., Wood D. P., “Photogrammetry Research at Dublin Institute of Technology”, **Impact**, the Journal of the Institute of Traffic Accident Investigators, UK, Spring/August 2002, Vol. 11, pages 29-31.

Coyle F., Toal V., Wood D. P., *Accuracy of Photogrammetry and PhotoModeler in Investigation of Low Speed Collisions*, Conference proceedings 6th International Conference of the Institute of Traffic Accident Investigators, UK, September 26 –29 2003, pages 93 – 103.

Coyle F., Toal V., Wood D. P., *The Suitability of Digital Photogrammetry with PhotoModeler Software for Accident Investigation*, Conference proceedings FISITA World Automotive Congress, Barcelona, May 23 - 27 2004, paper number F2004SC09.

Coyle F., Toal V., Wood D. P., *Motor Vehicle Crush Depth Measurement using Close – Range Digital Photogrammetry*, Conference proceedings International Symposium Modern Technologies, Education and Professional Practice in Geodesy and Related Fields, Sofia, 3 – 4 November 2005.

Coyle F., Toal V., Wood D. P., *Photogrammetric Measurement of Motor Vehicle Crush Depth*, Conference proceedings 7th International Conference of the Institute of Traffic Accident Investigators, UK, November 12 - 13 2005, pages 113 – 120.

Coyle F., Toal V., Wood D. P., *Photogrammetric Reconstruction of Motor Vehicle Accidents*, Seminar proceedings Photogrammetry and Laser Scanning for Surveying and Recording Cultural Heritage, Dublin Institute of Technology, 26 January 2007.